Photoconductive Terahertz Emitters and Detectors for the Operation with 1550 nm Pulsed Fiber Lasers

Dissertation

zur Erlangung des

Doktorgrades der Naturwissenschaften

(Dr. rer. nat.)

dem Fachbereich Physik der

Philipps-Universität Marburg

vorgelegt von

Björn Globisch

aus Damme

Marburg, 2017

Vom Fachbereich Physik der Philipps-Universität Marburg
als Dissertation angenommen am: 06.03.2017

Erstgutachter: Prof. Dr. Martin Koch

Zweitgutachter: Prof. Dr. Martin Schell

Tag der mündlichen Prüfung: 09.03.2017

Hochschulkennziffer: 1180

Abstract

In this thesis, photoconductive terahertz (THz) emitters and detectors suitable for the excitation with femtosecond laser pulses centered on 1550 nm are investigated. The motivation for this study is the development of cost-efficient, flexible and rapid THz time-domain-spectroscopy (TDS) systems for the application in growing fields like non-destructive testing (NDT) and in-line process monitoring. In order to achieve this goal, the physics of the generation and detection of THz radiation in photoconductors is investigated. The combination of experimental data with the analytic modeling of the carrier dynamics in THz photoconductors allows for a detailed understanding of the interplay between the growth conditions of the photoconductor and the properties of the fabricated THz device.

In this work, three different photoconductive materials were studied as THz emitters and detectors. All these photoconductors contain layers of the ternary semiconductor indium gallium arsenide (InGaAs). When InGaAs is grown lattice matched to an indium phosphide (InP) substrate, the material can be excited by erbium doped femtosecond fiber lasers with a central wavelength around 1550 nm. Therefore, InGaAs is a predestinated absorber in photoconductive THz emitters and detectors.

Aside from the common InGaAs layers, the photoconductors investigated in this thesis feature essentially different electrical and optical properties. The reason is that theoretical models and experimental results obtained within the last two decades revealed different demands on photoconductors for THz emitters and detectors. On the detector side, a sub-picosecond electron lifetime is required for the detection of broadband THz radiation with high dynamic range. In contrast, photoconductive materials for THz emitters require high breakdown fields and carrier mobility, whereas the electron lifetime is of minor importance. Therefore, the first part of this work is dedicated to the development of InGaAs-based photoconductors for THz emitters and receivers.

Photoconductors with sub-picosecond electron lifetimes were obtained by low-temperature growth of InGaAs with molecular beam epitaxy (MBE). At temperatures below 300 °C the growth is non-stoichiometric and arsenic antisites are incorporated as point defects into the lattice. When these antisites are ionized they serve as fast trapping and recombination centers. In this work, it is shown that the concentration of the (ionized) antisites can be controlled by the growth temperature, by using an additional p-dopant (beryllium), and by the temperature and the duration of a post-growth annealing step. Electron lifetimes as short as 140 fs were obtained. The precise adjustment of all these parameters allowed for the design and the fabrication of THz receivers with a spectral bandwidth of up to 6 THz and a peak dynamic range exceeding 95 dB.

For THz emitters, a high mobility, which is generally equivalent to a low defect density, is required in order to enable the efficient acceleration of the photoexcited carriers in the electric field applied to the emitter. Due to the high density of defects, low-temperature-grown (LTG) InGaAs based photoconductors are not the material of choice for THz emitters. Instead, a material comprising almost defect free layers of InGaAs surrounded by InAlAs barriers containing a high density of deep defects was used. These properties were achieved at growth temperatures close to 400 °C in a MBE system. At those temperatures, alloying forms deep defects inside the InAlAs layers, whereas InGaAs grows almost defect free. A THz-power of up to 112 µW ± 7 µW was measured for emitters fabricated from this photoconductor, which is an increase by a factor of 100 compared to emitters made of the LTG material.

By combining the optimized photoconductive emitters and receivers compact THz-TDS systems with up to 6 THz bandwidth and 90 dB peak dynamic range were realized. In addition, an all fiber-coupled THz spectrometer with kHz measurement rate as well as a fully fiber-coupled near-field imaging system with a lateral resolution of 100 µm was demonstrated with these optimized photoconductive devices.

However, a critical disadvantage of individual THz emitter and detector devices appears when THz-TDS measurements are performed in reflection geometry. Since many applications in NDT and in-line process monitoring allow only one side access to the sample under test, reflection measurements are the common use-case of THz-TDS in these fields. In this thesis, a fiber-coupled, monolithically integrated THz transceiver was developed, which combines the emitter and the receiver on a single photoconductive chip. As the photoconductor, Be-doped LTG-InGaAs/InAlAs with 0.5 ps electron lifetime was used in order to enable a broadband detection. The optical coupling of the transceiver was realized with the help of a polymer waveguide chip. With a bandwidth of 4.5 THz and a peak dynamic range larger than 70 dB this THz transceiver showed a significant performance increase compared to previous transceiver concepts (2 THz bandwidth and 50 dB peak dynamic range).

In order to further increase the performance of THz transceivers a novel photoconductor had to be developed, which combines the required properties of THz emitters and detectors in the same material. For this purpose, iron (Fe) doped InGaAs grown by MBE was investigated. At growth temperatures close to 400 °C iron could be incorporated homogenously up to concentrations of 5×10^{20} cm^{-3}. The resulting material combined sub-picosecond electron lifetime with high breakdown fields and high mobility. Applied as a photoconductive emitter, 75 µW ± 5 µW of radiated THz power were measured. As a detector, THz pulses with a bandwidth of up to 6 THz and a peak dynamic range of 95 dB were obtained. Hence, Fe-doped InGaAs has not only the potential to replace the relatively complex state-of-the art photoconductors, it also bears great potential for future integrated THz devices.

In conclusion, the systematic study of the electrical properties and the carrier dynamics in InGaAs-based photoconductive materials led to significant improvements of individual THz emitter and detector devices. The detectable bandwidth was increased by 50 % from below 4 THz to 6 THz and the emitted THz power was enhanced by a factor of 100. Further, the knowledge from these studies was exploited for the fabrication of a fiber-coupled, monolithically integrated THz transceiver with a 4.5 THz bandwidth and 70 dB peak dynamic range. These results are a significant increase in THz performance compared to previous transceiver concepts (2 THz bandwidth and 50 dB dynamic range). In order to allow for further improvements of THz transceivers and integrated THz devices, Fe-doped InGaAs was investigated as a photoconductive emitter and detector. Due to the unique combination of sub-picosecond electron lifetime, high resistivity (> 2 Ω cm) and high mobility (> 900 $cm^2V^{-1}s^{-1}$) Fe-doped InGaAs showed a performance comparable to the optimized THz photoconductors. Hence, the results presented in this work pave the way for compact and integrated THz devices for applications in industrial environments.

Zusammenfassung

In dieser Dissertation werden photoleitende Halbleiter zur Erzeugung und zur Detektion von Terahertz (THz) Strahlung untersucht, die mithilfe von Erbium-dotierten Faserlasern betrieben werden können. Das Ziel dieser Untersuchungen ist die Entwicklung von kostengünstigen, stabilen und kompakten THz Zeitbereichsspektrometern, die für Anwendungen in der zerstörungsfreien Materialprüfung und der industriellen Prozesskontrolle geeignet sind. Dabei ist das detaillierte Verständnis der physikalischen Prozesse bei der Erzeugung und Detektion von THz Strahlung die Voraussetzung für die gezielte Optimierung des THz Photoleiters. Durch ausführliche Messreihen in Verbindung mit analytischen Modellen der Ladungsträgerdynamik werden in dieser Arbeit die elektrischen und dynamischen Eigenschaften von Photoleitern mit der Leistungscharakteristik der daraus hergestellten THz Emitter und Detektoren verknüpft.

Diese Arbeit analysiert drei unterschiedliche Materialkonzepte für photoleitende THz Emitter und Detektoren, wobei alle diese Photoleiter Schichten des ternären Halbleiters Indiumgalliumarsenid (InGaAs) enthalten. InGaAs ist der ideale Absorber für Femtosekundenpulse mit einer Zentralwellenlänge um 1550 nm, da die Bandlücke dieses Materials, bei gitterangepasster Komposition zu InP, mit der Energie der infraroten Laserpulse übereinstimmt, die von einem Erbium-dotierten Faserlaser emittiert werden.

Abgesehen von den InGaAs-Absorberschichten unterscheiden sich die untersuchten photoleitenden Materialien signifikant in ihren elektrischen und optischen Eigenschaften. Dies ist durch die deutlich unterschiedlichen Anforderungen bedingt, die photoleitende THz Sender und Empfänger an ein optimales Halbleitermaterial stellen. Während beim Empfänger eine Ladungsträgerlebensdauer unterhalb einer Pikosekunde für die breitbandige Detektion von THz Strahlung unbedingt erforderlich ist, benötigen photoleitende Sender vor allem eine hohe Ladungsträgermobilität und eine hohe Durchbruchfeldstärke. Die Ladungsträgerlebens-dauer muss lediglich klein gegenüber der Pulswiederholrate des Lasers sein. Daher wurde im ersten Teil dieser Arbeit zunächst jeweils ein Photoleiterkonzept für die Anwendung als THz-Emitter bzw. THz-Detektor untersucht.

Photoleiter mit einer Ladungsträgerlebensdauer unterhalb von 1 ps wurden mithilfe des Niedrigtemperaturwachstums in einer Molekularstrahlepitaxieanlage (MBE) hergestellt. Bei Wachstumstemperaturen unterhalb von 300 °C wird zunehmend Überschuss Arsen (As) als Substitutionsdefekt in das InGaAs-Kristallgitter eingebaut. Diese As-Punktdefekte bilden schnelle Einfang- und Rekombinationszentren, wenn sie durch einen p-Dotierstoff ionisiert werden. Die im Rahmen dieser Arbeit durchgeführten Studien konnten zeigen, dass die Konzentration der ionisierten As-Substitutionsdefekte durch die Wachstumstemperatur, durch die Konzentration des p-Dotierstoffs Beryllium und durch die Temperatur und die Dauer eines

an das eigentliche Wachstum angeschlossenen Ausheilschritts gezielt beeinflusst werden kann. Elektronenlebensdauern bis hinunter zu 140 fs konnten so erreicht werden. Mithilfe der THz Empfänger, die aus dem optimierten Photoleiter hergestellt wurden, konnten Pulse mit einer Bandbreite von 6 THz und einem maximalen Dynamikbereich von mehr als 95 dB detektiert werden.

Um eine möglichst effiziente Beschleunigung der Ladungsträger im photoleitenden THz Emitter zu erreichen, ist eine hohe Mobilität erforderlich, was im Allgemeinen gleichbedeutend mit einer möglichst geringen Defektdichte ist. Das durch das Niedrigtemperaturwachstum hergestellte Photoleitermaterial enthält aufgrund der kurzen Ladungsträgerlebensdauer allerdings eine hohe Defektdichte, wodurch dieses Material als THz Emitter nicht optimal ist. Im Rahmen dieser Arbeit wurde ein photoleitendes Material als THz Emitter erforscht, welches aus nahezu defektfreien InGaAs Schichten besteht, die eine hohe Mobilität gewährleisten, und von Schichten aus Indiumaluminiumarsenid (InAlAs) umgeben sind, die eine hohe Konzentration tiefliegender Störstellen aufweisen. Durch dieses Prinzip sind die THz Erzeugung in den InGaAs-Schichten und die Ladungsträgerrekombination in den InAlAs-Schichten räumlich voneinander getrennt. Die oben beschriebenen Eigenschaften konnten bei Wachstumstemperaturen um 400 °C in einer MBE erreicht werden. Durch Legierungsentmischung bilden sich in diesem Temperaturbereich tiefe Störstellen im InAlAs, während InGaAs nahezu defektfrei wächst. THz-Sender, die aus diesem Photoleiter hergestellten wurden, emittieren eine mittlere Leistung von bis zu 112 µW ± 7 µW. Im Vergleich zu THz-Emittern, die auf niedrigtemperaturgewachsenen Photoleitern basieren, entspricht dies einer Leistungserhöhung um den Faktor 100.

Durch die Kombination der optimierten THz-Emitter und THz-Detektoren konnte ein fasergekoppeltes THz System mit einer Bandbreite von 6 THz und einem Dynamikbereich von mehr als 90 dB realisiert werden. Außerdem haben die verbesserten photoleitenden Komponenten die Entwicklung von Spektrometern mit Messraten im kHz-Bereich sowie fasergekoppelte Nahfeldmesssysteme mit einer lateralen Auflösung von 100 µm ermöglicht.

Die Verwendung von diskreten und individuell optimierten THz-Sendern und Empfängern stellt sich bei Messungen in Reflexionsanordnung als sehr unvorteilhaft heraus, da der resultierende THz Strahlengang komplex und verlustbehaftet ist. Viele Anwendungen in Bereichen der zerstörungsfreien Materialprüfung erfordern jedoch THz-Reflexionsmessungen, da die zu untersuchenden Bauteile lediglich von einer Seite zugänglich sind. Für dieses Anwendungsgebiet ist daher ein THz-Messkopf erforderlich, welcher sowohl den Sender als auch den Empfänger enthält und orthogonal zur Bauteiloberfläche betrieben werden kann. Im Rahmen dieser Arbeit wurde ein solcher THz-Transceiver entwickelt, bei dem Sender und Empfänger in einem Abstand von lediglich 45 µm auf demselben photoleitenden Chip monolithisch integriert wurden. Der verwendete Photoleiter besteht aus einer Be-dotierten

InGaAs/InAlAs Struktur mit einer Ladungsträgerlebensdauer von 0.5 ps, um einen breitbandigen THz-Empfänger im Transceiver zu ermöglichen. Die optische Faserkopplung wurde mithilfe eines Polymerwellenleiters realisiert. Mit einer Bandbreite von 4.5 THz und einem maximalen Dynamikbereich von mehr als 70 dB ist dieser Transceiver eine erhebliche Verbesserung bestehender Konzepte, die lediglich eine maximale Bandbreite von 2 THz und einen Dynamikbereich von 50 dB ermöglichten. Somit ist der hier vorgestellte Transceiver ein vielversprechender Ansatz für die Anwendung der THz-Spektroskopie in Bereichen der zerstörungsfreien Materialprüfung.

Um die Leistungsfähigkeit von THz Transceivern weiter zu steigern, ist jedoch ein photoleitendes Material erforderlich, welches sowohl die optimalen Eigenschaften eines THz-Senders als auch die eines THz-Empfängers in nur einem Halbleiter kombiniert. Vor dieser Arbeit war ein solches Material für eine Anregungswellenlänge um 1550 nm noch nicht bekannt. Im Rahmen der vorliegenden Dissertation wurde eisendotiertes (Fe) InGaAs als geeigneter Photoleiter identifiziert, mit dem eine Ladungsträgerlebensdauer von 300 fs, eine Mobilität von mehr als 900 $cm^2V^{-1}s^{-1}$ und ein elektrischer Widerstand oberhalb von 2 kΩ cm erreicht werden können. Photoleitende THz-Sender, die aus Fe-dotiertem InGaAs hergestellt wurden, emittierten eine THz-Leistung von bis zu 75 µW ± 5 µW. THz-Pulse mit einer Bandbreite von bis zu 6 THz und einem Dynamikbereich von mehr als 95 dB wurden mithilfe von Fe-dotierten InGaAs Empfängern detektiert. Somit erreicht eisendotiertes InGaAs die THz-Eigenschaften optimierter, individueller Photoleiter und ist daher ein vielversprechendes Material für zukünftige integrierte THz Bauteile.

Durch die systematische Analyse der elektrischen und dynamischen Eigenschaften von THz-Photoleitern auf der Basis von InGaAs wurden in dieser Arbeit deutliche Verbesserungen sowohl auf Sender- als auch auf der Empfängerseite erzielt. Die detektierte Bandbreite konnte von ca. 4 THz auf 6 THz erhöht werden, und die vom Sender emittierte THz-Leistung wurde um den Faktor 100 gesteigert. Für THz-Reflexionsmessungen wurde erstmals ein monolithisch integrierter, fasergekoppelter Transceiver mit einer Bandbreite von 4.5 THz entwickelt. Dieser Transceiver ist ein kompakter Messkopf, der mithilfe kommerziell erhältlicher THz-Spektrometer in der zerstörungsfreien Materialprüfung eingesetzt werden kann. Um die Leistungsfähigkeit von THz-Transceivern weiter zu steigern wird allerdings ein Photoleiter benötigt, welcher die optimalen Eigenschaften eines Senders und eines Empfängers in einem Material vereint. Im Rahmen dieser Arbeit wurde gezeigt, dass eisendotiertes InGaAs durch die Kombination von ultraschnellem Ladungsträgereinfang, hohem elektrischen Widerstand und hoher Ladungsträgermobilität die THz-Leistungscharakteristik optimierter Sender- und Empfänger erreicht. Somit sind die Ergebnisse dieser Dissertation ein wichtiger Schritt für die Anwendung der THz Technologie im industriellen Umfeld.

Acknowledgements

I would like to express my gratitude to all people who made this work possible by giving me the opportunity to work in my field of research and by supporting me in many different ways.

First of all I would like to thank Prof. Dr. Martin Schell, Dr. Bernd Sartorius and Dr. Thorsten Göbel for giving me the opportunity to conduct my research on THz photoconductors in the photonic components department of the Fraunhofer Institute for Telecommunications, Heinrich Hertz Institute, in Berlin. I was able to become an active member of the scientific community by participating in conferences, exhibitions and workshops, which I highly appreciate.

With the same gratitude I would like to thank Prof. Dr. Martin Koch for being my doctoral adviser and for giving me access to the experimental facilities of his group at the University of Marburg. Further, I am very grateful for a lot of fruitful discussions and helpful advices concerning my research.

I would like to express special thanks to Dr. Roman J. B. Dietz for the great collaboration and the endless discussions about semiconductors, carrier dynamics and THz spectroscopy. I would also like to thank Dr. Thorsten Göbel for the confidence in my work, for the freedom I was given to conduct my research in the THz group and for a lot of essential advices.

I am very grateful for the support from my colleagues Dr. Helmut Roehle and Dr. Dennis Stanze. Many thanks to my former master students and actual colleagues Simon Nellen and Robert Kohlhaas for the support and the fruitful discussions about actual and future experiments. I would like to thank Dr. Harald Künzel, Jutta Böttcher and Rudi Gibis for their expertise in molecular beam epitaxy and for all the good advices concerning growth parameters, defect concentrations and surface morphology.

I would also like to address many thanks to Dr. Nico Vieweg, Dr. Anselm Deninger (Toptica photonics AG) and Dr. Ole Peters (Menlosystems GmbH) for the great collaboration in our joint research projects and for the successful commercialization of the THz technology. I thank Prof. W. Ted Masselink, Dr. Mykhaylo Semtsiv and David Alcer from the Humboldt University as well as Dr. Andreas Steiger (Physikalisch Technische Bundesanstalt, PTB) and Werner Bohmeyer (Sensor- und Lasertechnik GmbH) for the great collaboration. Special thanks to Christian Lammers and Philipp-Henrik Richter from Philipps University Marburg for many important experiments.

I would like to thank my family and my friends for all their support and the essential distraction. Last but not least, I express my highest gratitude to my partner Kristin for her support, her patience, and all her love, without which this work would not have been possible.

Contents

1 Introduction

The first experiments with terahertz (THz) radiation, which is commonly regarded as the frequency interval of 100 GHz – 10 THz, were already conducted at the beginning of the 20th century by H. Rubens, M. Czerny and W. Woltersdorff [1]–[3]. At that time, the so-called *Reststrahlenmethode* was applied in order to extract radiation with a wavelength between 15 µm – 100 µm (20 THz – 3 THz) from the spectrum of a gas mantle [1], [2]. However, it took another 60 years until the development of the first femtosecond pulse laser in the 1980s allowed for the generation of coherent THz radiation [4]. The reason for the long time delay arises from the fact that the generation of THz radiation is relatively difficult. Electronic oscillators are rather inefficient at frequencies above 100 GHz and lasers, which are commonly used for generating coherent infrared radiation, cannot be operated at room temperature in the THz frequency range [5]. Thus, the first generation and detection of coherent THz radiation relied on an optoelectronic technique. A femtosecond laser source was applied in order to induce a transient current in a light-sensitive, biased semiconductor [4].

Until today, several techniques for the generation and detection of THz radiation have been developed. THz quantum cascade lasers (QCLs) [6], high frequency electronics relying on non-linear mixing, and photoconductive emitters and detectors can be used to generate and detect continuous wave (CW) THz-radiation [7], [8]. Pulsed THz signals, containing a broad spectrum ranging from 100 GHz to several THz, can be obtained by frequency mixing in non-linear crystals and air plasmas as well as by optoelectronic generation techniques using photoconductive devices [9], [10]. Since a plurality of processes in physics, chemistry, material science, and biology are related to THz frequencies, THz spectroscopy has become a versatile and important tool in these fields [9], [11]–[17].

However, one of the current challenges of the THz technology is the transfer from purely scientific studies to applications in out-of-the-lab environments [18]. Among all the aforementioned possibilities to generate and detected THz radiation, time-domain spectroscopy (TDS) based on photoconductive emitters and detectors is a promising technique to enable this technology transfer. The main advantages of THz-TDS include the operation at room temperature, the relative compact design, and the high bandwidth. Until recent years, photoconductive THz-TDS relied on titanium-sapphire (Ti:sapph) femtosecond lasers in combination with low-temperature grown (LTG) GaAs emitters and detectors [19], [20]. The main drawbacks of these systems are the relatively high cost of the Ti:sapph laser and the emission wavelength centered on 780 nm. The latter requires free-space optics for guiding the femtosecond pulse to the respective THz antenna, since optical fiber technology is hardly available in the 800 nm wavelength range. This circumstance leads to sensitive, inflexible and bulky setups, which impeded the use of photoconductive THz-TDS outside the laboratory.

With the development of ytterbium and erbium doped femtosecond fiber lasers, emitting at 1030 nm and 1550 nm, respectively, all fiber-coupled, compact, and more cost effective THz systems came into close reach. Apart from the femtosecond laser, photoconductive materials which are both sensitive to the infrared pulses and suitable for THz emission and detection had to be developed. In the last decades, several photoconductive materials have been proposed as promising candidates [21]. These include iron-doped or iron implanted InGaAs [22]–[24], LTG-InGaAs [25], [26], Be-doped LTG-InGaAs/InAlAs superlattices [27]–[29], ErAs:InGaAs superlattices [30], and LTG-GaAsSb [31]. Compared to photoconductors made of LTG-GaAs the performance of all these materials suitable for the excitation with 1550 nm radiation has to be improved significantly. Therefore, novel concepts and specific improvements are required, in order to obtain compact, all fiber-coupled and flexible THz-TDS systems.

The aim of this work is the development of photoconductive THz-emitter and detector antennas suitable for the excitation with femtosecond pulses centered around 1550 nm. Here, the main field of research is understanding the interplay between the epitaxial growth conditions, the material properties and the carrier dynamics in the THz antenna itself. Thereby, the work can be divided into two parts. In the first part, two different photoconductive materials are studied as individual THz emitters and detectors, respectively. In this context, the present work is the direct continuation of the work of Dr. Roman J. B. Dietz [32]. In the second part, photoconductors for integrated THz devices are investigated. A fiber-coupled THz transceiver with a bandwidth of 4.5 THz is demonstrated, comprising the THz emitter and detector in close proximity to each other on the same photoconductive chip. Further, iron (Fe) doped InGaAs grown by Molecular Beam Epitaxy (MBE) at temperatures close to 400 °C is studied as THz emitter and detector. This unique photoconductive material combines the sub-picosecond electron lifetime of state-of-the-art detectors with the high mobility and the high breakdown field of state-of-the-art emitter materials. Therefore, InGaAs:Fe is a promising material for future integrated THz devices.

This work is a dissertation by publications. Thus, it summarizes the author's main findings in the field of photoconductive THz antennas and combines the results in a closed, descriptive form. Each chapter highlights the main results and gives immediate references to the relevant publications of the author.

2 Background

2.1 Photoconductive THz generation and detection

This section gives a brief overview of the main mechanisms involved in the generation and detection of THz radiation in photoconductors. Several excellent and extensive reviews have been published on this topic [9], [10], [21], [33]–[35]. Thus, this section is restricted to those aspects, which are most relevant in the remainder of this work.

In photoconductive THz-TDS the broad spectral bandwidth of a femtosecond laser pulse is translated into a broadband electromagnetic pulse by applying a photoconductive switch as the optical-to-electrical converter. When an external bias field is applied to the photoconductive emitter, the optically excited electrons and holes generate a transient current in the photoconductor, which is radiated into free space [36]. One of the simplest models, which describes the THz generation, is the Drude model of carrier transport. In this framework the current density can be described as follows [33], [35], [37]

$$j(t) = -e\, n(t) v(t). \tag{2.1}$$

Here, $n(t)$ and $v(t)$ are the concentration of electrons in the conduction band (CB) of the photoconductor and their velocity, respectively. The constant e denotes the elementary charge. Since the effective mass of CB-electrons is significantly higher than the effective mass of valence band (VB) holes in the most common III-V photoconductors, the main contribution to the transient current originates from CB-electrons. Thus, this analysis is restricted to electrons only. The dynamic equations describing the time dependence of n and v can be expressed as (see for example [38]):

$$\frac{dn}{dt} = G(t) - \frac{n(t)}{\tau_e}\,, \tag{2.2}$$

$$\frac{dv}{dt} = -\frac{v(t)}{\tau_s} + \frac{e}{m_e^*}\left(E_{bias} - \frac{P(t)}{\eta e}\right), \tag{2.3}$$

$$\frac{dP}{dt} = -\frac{P(t)}{\tau_r} + j(t). \tag{2.4}$$

In Eq. (2.2) the term $G(t)$ represents the generation of electrons by the femtosecond laser pulse and the second term on the right hand side denotes the electron trapping with the time constant τ_e. Eq. (2.2) is a rather simple description of the dynamic trapping process in photoconductors. In the remainder of this work, Eq. (2.2) will be adapted to the investigated photoconductive material. In Eq. (2.3) the electron velocity increases due to the external bias field E_{bias}, whereas scattering processes, denoted by the electron scattering time τ_s, and the (dynamic) screening of the bias field decrease the velocity $v(t)$. The screening itself is modeled via the time dependent

polarization $P(t)$, which builds up proportional to the current density $j(t)$ and decays due to carrier recombination, which is modeled by the time constant τ_r. In Eq. (2.3), the effective electron mass is represented by m_e^* and η is a geometrical factor [9], [39], [40]. By solving the set of Eqs. (2.2) - (2.4), the transient current density $j(t)$ can be determined. According to Maxwell's theory of electromagnetism, the far field of an electric dipole is proportional to the time derivate of the transient current [4].

$$E_{THz}(t) \propto \frac{dj(t)}{dt}. \tag{2.5}$$

Hence, the carrier dynamics inside the photoconductive material determines the properties of the radiated THz pulse.

The electric field of the emitted THz pulse can be detected by photoconductive sampling with an antenna structure similar to the emitter. Thereby, the photoconductive receiver is illuminated with a portion of the femtosecond pulse train, which was used for the illumination of the photoconductive emitter. The incoming THz pulse serves as the bias field of the photoconductive receiver. With the help of an optical delay line the electric field of the THz pulse is sampled successively by the receiver. Hence, the current induced inside the photoconductive receiver can be described by the convolution of the incoming THz pulse $E_{THz}(t)$ and the response function of the receiver antenna $g(t)$ [9], [41]

$$J(t) \propto E_{THz}(t) * g(t). \tag{2.6}$$

Here, the carrier dynamics inside the photoconductive receiver can be described in analogy to the dynamical processes inside the emitter (see Eqs. (2.2) -(2.4)). In order to point out the need of an ultra-short electron lifetime in photoconductive THz-receivers, Eq. (2.6) is analyzed in two limit cases.

In the first regime, the response function of the photoconductive receiver $g(t)$ is regarded as a delta-function, which means that the duration of the exciting laser pulse and the lifetime of the photocarriers is much lower than the duration of the incoming THz pulse. In that case, the current induced inside the photoconductive receiver is directly proportional to the electric field of the THz pulse, such that the frequency response of the receiver can be written as [41]

$$J(\omega) \propto E_{THz}(\omega). \tag{2.7}$$

Hence, this regime describes the optimal photoconductive receiver, which resembles every frequency component of the incoming THz pulse.

In the opposite regime, the receiver is assumed to be an integrating detector, in which the lifetime of the photoexcited carriers exceeds the duration of the incoming THz pulse by far. In this case, the frequency response of the photoconductive receiver can be written as [9]

$$J(\omega) \propto E_{THz}(\omega)/\omega\,. \tag{2.8}$$

Note that $J(\omega)$ decays stronger for higher frequencies, such that the receiver becomes more and more insensitive for higher THz frequencies. Since high THz frequencies are especially important for applications in NDT and broadband THz spectroscopy, this analysis underlines the importance of an ultrafast current response in photoconductive THz receivers, in order to obtain undistorted and broadband THz pulses.

The desired properties of broadband photoconductive antennas, which will serve as a guideline throughout this work, can be summarized as follows:

- ❒ High absorption coefficient for the femtosecond laser pulse, in order to obtain high concentrations of exited carriers in the photoconductor (see Eq. (2.2)).
- ❒ High carrier mobility, for the efficient acceleration and deceleration of the optically excited carriers.
- ❒ High breakdown fields, especially in the photoconductive emitter, for applying high external bias fields.
- ❒ Ultrashort carrier lifetime, especially in the photoconductive receiver, for the detection of broadband THz pulses (see Eq. (2.6) and Eq. (2.7)).

In general, high mobility and ultrashort carrier lifetime are opposed quantities. The carrier lifetime is commonly reduced by the incorporation of (ionized) point defects as trapping and recombination centers. However, the probability for carrier scattering increases with the density of these defects, which in turn reduces the carrier mobility. Hence, one of the principal challenges for the design of efficient THz photoconductors is the precise adjustment of these material properties. Therefore, the aim of the investigations presented throughout this work is to link the material parameters with the performance of the respective THz antenna.

2.2 Experimental techniques

In this section the experimental techniques employed frequently throughout this work are briefly introduced. Unless otherwise stated, the data presented in the following sections were acquired with the experimental setups described below.

2.2.1 Time-resolved Differential transmission

Time-resolved differential transmission (DT) is a powerful tool to characterize the dynamics of excited carriers in semiconductors [42]. A DT experiment is a pump-probe experiment, in which a strong pump pulse excites electron-hole pairs in a semiconductor. Due to the limited density of states in the CB and the VB of the photoconductor, the transmission of a weak probe pulse is increased directly after the excitation by the pump. When the transmission of the probe pulse is recorded as a function of the time delay between the pump and the probe pulse, the

transmission change is a direct measure for the population dynamics in the CB and – under certain conditions – in the VB of the photoconductor under test. The time dependent transmission can be modeled by the following equation:

$$T(t) = T_0 \exp\left(-\alpha L \frac{n(t)}{N_0}\right). \tag{2.9}$$

Here, T_0 is the transmission of the sample without any optical excitation, αL is the absorption length, N_0 represents the total density of states in the CB of the photoconductor and $n(t)$ is the time dependent occupation of the CB. Hence, the differential transmission $\Delta T/T_0$ reads:

$$\frac{\Delta T}{T_0} = \frac{T(t) - T_0}{T_0} = \exp\left(-\alpha L \frac{n(t)}{N_0}\right) - 1. \tag{2.10}$$

In Eq. (2.10) one observes that the differential transmission is a direct measure for the time dependent occupation of the CB $n(t)$. In the remainder of this work, rate equation models will be used in order to describe $n(t)$ for the photoconductive materials under test.

The time resolution of the DT experiment depends on the duration of the optical excitation pulse. Therefore, femtosecond lasers are employed in order to measure the carrier dynamics on sub-picosecond timescales. The DT-setup used throughout this work is schematically drawn in Fig. 2.1. It comprises a femtosecond fiber laser (C-Fiber, Menlo Systems GmbH) with a central frequency around 1550 nm, a pulse repetition frequency of 100 MHz and a pulse duration of 90 fs (FWHM). The two fiber-coupled output ports of the laser are used for the pump and the probe pulse, respectively. A computer controlled optical delay line generates the time delay between the pump and the probe pulse. The average optical power of the two pulses can be adjusted by a fiber-coupled optical attenuator (Agilent N7752 A). In order to avoid the direct interference of the optical beams at the sample surface, pump and probe beam are orthogonally polarized. The angle of incidence measures 15 ° with respect to

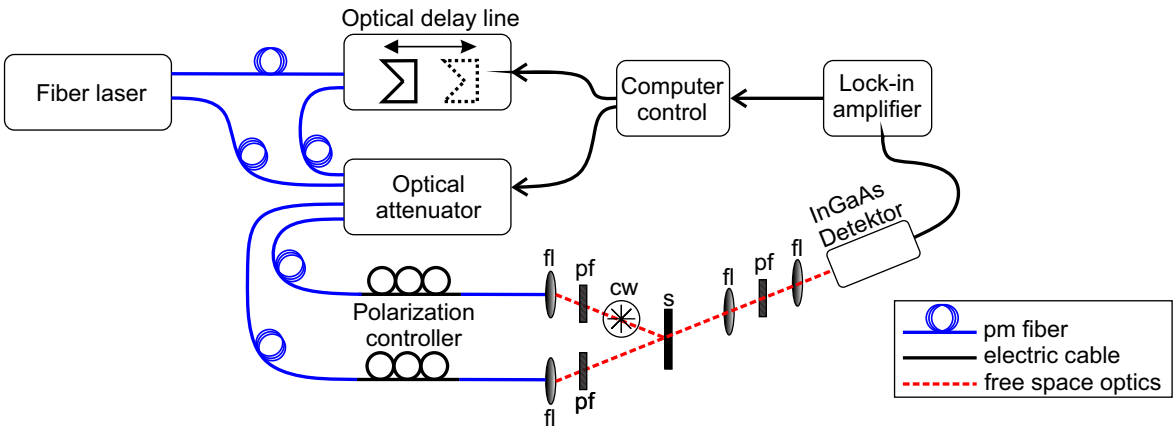

Fig. 2.1. Schematic of the time-resolved differential transmission setup. The abbreviations denote: fl – focusing lens, pf – polarization filter, cw – chopper wheel, s – sample.

the surface normal. Lock-in detection is used to measure the differential transmission of the probe beam. In order to avoid the illumination of the InGaAs photodetector with light from the intense pump pulse that was scattered at the backside of the sample into the direction of the detector, an additional polarization filter (pf) is mounted in front of the detector. The $1/e^2$-spot diameter of the pump beam measures approx. 15 µm. Thus, carrier densities of up to 4×10^{18} cm^{-3} can be excited with the laser power provided by the system. In order to avoid any influence of the probe pulse on the carrier dynamics, the pump pulse is at least a factor of 10 more intense than the probe pulse.

2.2.2 THz spectroscopy

The THz antennas fabricated from the photoconductive materials investigated in this work were characterized in a THz-TDS setup based on the schematic drawing in Fig. 2.2. A fiber laser providing pulses with a duration of 100 fs and 100 MHz repetition frequency was used for the optical excitation. The optical delay line as well as the data acquisition was part of a commercially available THz time-domain spectrometer [43]. The operation mode of this system was identical for all THz experiments: 1000 pulse traces with a length of 70 ps each were averaged for a single measurement. The acquisition time of a single pulse trace measured 60 ms, leading to a total acquisition time of 60 s for a single measurement. No lock-in amplification was used in the THz experiments. The optical illumination power of the fiber-coupled THz emitter (THz-Tx) and receiver (THz-Rx) was controlled by a fiber-coupled optical attenuator. The THz emitters are commonly biased with a DC voltage supplied by an external voltage source. Unless otherwise stated, the THz path consisted of two 90 °-off-axis parabolic mirrors (OPMs) with a focal length of 3 inch and a diameter of 2 inch for the collimation and the focusing of the THz beam. The total length of the THz path measured 25 cm, and all THz measurements were performed in ambient air. Unless otherwise stated, the antenna structure of the photoconductive THz emitter is a mesa-structured [29] strip-line antenna with a gap-width of 100 µm. The THz receiver contains a mesa-structured $\lambda/2$ dipole antenna with a 10 µm wide mesa and a dipole length of 25 µm.

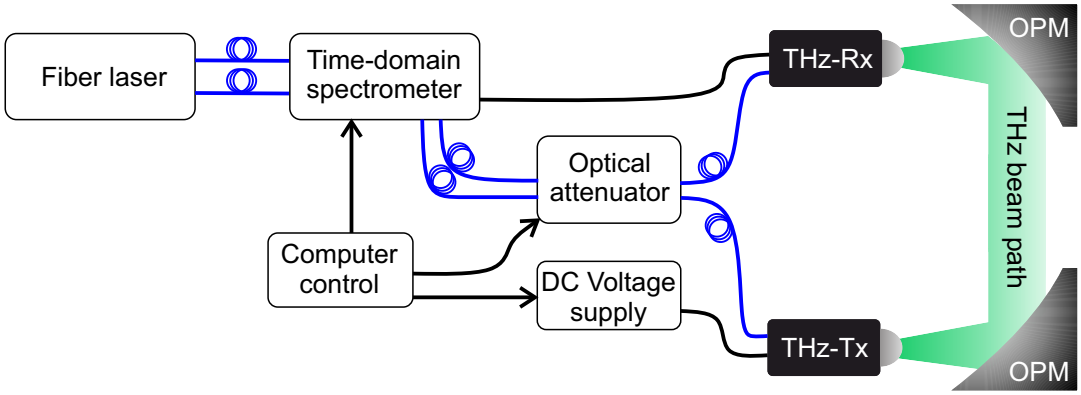

Fig. 2.2. Schematic of the THz time domain spectroscopy setup. OPM – 90 °-off-axis parabolic mirror.

3 THz receivers made of low-temperature grown InGaAs/InAlAs

In this section, beryllium (Be) doped InGaAs/InAlAs heterostructures grown at low temperatures (< 250 °C) in a MBE system are investigated as photoconductive receivers for THz-TDS. The main focus is on the influence of the growth conditions on the electrical properties, the carrier dynamics, and the resulting performance as a photoconductive THz receiver. In particular, the effect of Be-doping and post-growth annealing of the material is systematically studied. The variation of these parameters allowed for a specific manipulation of the resistivity and the residual carrier concentration of the photoconductor by more than three orders of magnitude. By combining time-resolved differential transmission measurements with a rate equation model the processes of electron trapping and electron-hole recombination were investigated. Due to the fundamental understanding of the material properties, optimized photoconductive THz receivers with a bandwidth of up to 6 THz and a dynamic range exceeding 95 dB were fabricated. These devices have become one of the key components in state-of-the-art, fiber-coupled THz-TDS systems based on the 1550 nm technology [43]. Before the main findings are discussed in Sec. 3.2 - 3.5 an overview of the current research on low-temperature grown (LTG) III-V semiconductors is given in the next subsection. The results discussed in this paragraph are based on the publications [II], [III] and [VI].

3.1 Low-temperature grown III-V semiconductors

Low-temperature growth is a key technique to fabricate THz photoconductors with sub-picosecond lifetimes. This subsection summarizes the results obtained by previous studies and identifies open questions. Since low-temperature growth was first established for the binary semiconductor GaAs, the properties of LTG-GaAs are compared with LTG-InGaAs based materials.

In the last 30 years, the interplay of growth temperature, post-growth annealing, and doping with beryllium was studied extensively in LTG-GaAs [44], [45]. The main findings are the following: At temperatures below 300 °C the growth of GaAs is non-stoichiometric due to the incorporation of As atoms on Ga lattice sites [46], [47]. These defects are called arsenic antisites (As_{Ga}) and their concentration increases for decreasing growth temperatures. At T_G = 200 °C, As_{Ga} concentrations above 10^{20} cm^{-3} were reported [46], [47]. The energy level of the As_{Ga} defects is approx. 0.75 eV below the conduction band minimum and, therefore, almost mid-bandgap in GaAs [48]. The conductivity of as-grown LTG-GaAs is determined by hopping conductivity in this deep-defect band [48], [49]. When LTG-GaAs is annealed after the growth process at temperatures above 300 °C the excess arsenic precipitates and forms arsenic clusters, whereas the size and the spacing of these clusters depends on the duration and the temperature

of the annealing process [49]–[54]. Due to the precipitation of As_{Ga} the resistivity of LTG-GaAs increases as the probability of hopping conductivity decreases exponentially with the distance of the defect sites [53], [55]. In addition, the arsenic precipitates form Schottky-barriers in the material, which further increases the resistivity [56], [57]. During the annealing process, As_{Ga} defects diffuse via gallium vacancies (V_{Ga}), which are incorporated during the growth process in concentrations of up to 10^{18} cm^{-3} [50], [58]–[60].

In addition to these effects on the electrical properties, low-temperature growth has a great impact on the carrier lifetime of GaAs. Positively charged arsenic antisites (As_{Ga}^{+}) are effective recombination centers with relatively large capture cross sections for electrons $\sigma_e = 7 \times 10^{-15}$cm^2 and holes $\sigma_e = 6 \times 10^{-17}$cm^2, respectively [44], [61]. The ionization of As_{Ga} defects is caused by gallium vacancies in as-grown LTG-GaAs [62]. Electron lifetimes as short as 100 fs were obtained in as-grown LTG-GaAs, whereas the electron lifetime increases for annealed samples due to the precipitation of (ionized) antisite defects [53], [61], [63].

The precipitation of arsenic antisites could be significantly reduced when LTG-GaAs was p-doped with beryllium during the growth process [47], [58], [64]. The small Be dopants reduce the lattice strain caused by the As_{Ga} defects, which is the principal driving force of the As-precipitation [65]. Initially, Be-As complexes were suggested in order to explain the anneal stability of Be-doped LTG-GaAs [49]. However, these complexes have not been found in the material, yet [47].

In summary, the growth temperature, the duration and the temperature of the annealing process, and the Be-doping concentration determine the properties of LTG-GaAs. The optimization and tuning of these parameters allowed for the fabrication of THz photoconductors, suitable for the excitation with femtosecond pulses from a Ti:sapph laser centered at 780 nm [9], [21].

When low-temperature growth is applied to the ternary semiconductor $In_{0.53}Ga_{0.47}As$, which can be grown lattice matched to an InP substrate, As_{Ga} defects are incorporated in LTG-InGaAs for growth temperatures below 300 °C [66], [67] (In the remainder of this work we use the abbreviation InGaAs for $In_{0.53}Ga_{0.47}As$.). In analogy to LTG-GaAs, the concentration of As_{Ga} increases with decreasing growth temperatures and can reach a fraction of approx. 1 % of the total number of As Atoms in the lattice, which corresponds to 10^{20} cm^{-3} [66], [68]. The fundamental difference between As_{Ga} defects in LTG-GaAs and LTG-InGaAs is the energy level of the defect. Whereas it is almost mid-bandgap in LTG-GaAs the ionization energy in uncompensated LTG-InGaAs is 30 – 40 meV [66], [68]. The important consequence is that a considerable amount of the As_{Ga} defects is thermally ionized at room temperature, i.e. As_{Ga} defects act as donors in LTG-InGaAs, which results in n-conductive material with carrier concentrations in the 10^{17} cm^{-3} range for growth temperatures around 200 °C [66]. Fig. 3.1 shows the residual electron concentration n and the resistivity R of as-grown InGaAs with a

thickness of 1 µm determined by room temperature Hall measurements as a function of the growth temperature in the MBE. The increase of the carrier concentration for lower growth temperatures due to the incorporation of As_{Ga} defects can be clearly seen. As a consequence, the resistivity of the material is lower than 0.01 Ω cm. Due to these unfavorable electrical properties, as-grown LTG-InGaAs is not directly applicable as THz photoconductor.

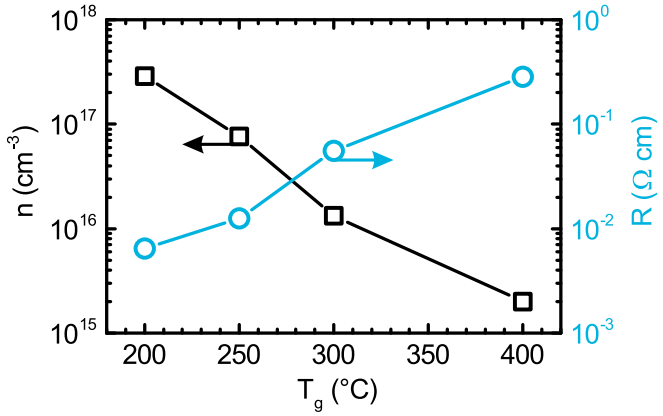

Fig. 3.1. Residual electron concentration (black squares) and resistivity (blue circles) of 1 µm LTG-InGaAs grown on top of an InP substrate as a function of the growth temperature T_g in the MBE determined by room temperature Hall measurements. The increase of *n* for lower growth temperatures is caused by an augmented incorporation of As_{Ga} defects, which are partially ionized at room temperature.

In contrast to LTG-GaAs, post-growth annealing of LTG-InGaAs cannot increase the resistivity nor decrease the residual electron concentration considerably, although arsenic precipitates are formed [44], [67], [68]. The reason is the fundamentally different origin of the conductivity of as-grown LTG-InGaAs compared to as-grown LTG-GaAs. In the latter case the dominant mechanism is hopping conductivity between mid-bandgap As_{Ga} defects, whereas thermally ionized As_{Ga} defects cause the conductivity of LTG-InGaAs. Since the probability of hopping conductivity decreases exponentially with the distance between the defect sites, annealing has a great impact on the electrical properties of LT-GaAs. In LTG-InGaAs, this effect is much smaller, since the probability of thermal ionization is directly proportional to the defect concentration.

In order to reduce the residual electron concentration in LTG-InGaAs the material is commonly p-doped with beryllium [69]. Thereby, the resistivity can be increased to 10 – 100 Ω cm and the residual electron concentration decreases to 10^{14} cm^{-3} [25], [28]. In order to increase the resistivity of the material even more, multiple quantum wells (MQWs) consisting of up to 100 periods of $In_{0.53}Ga_{0.47}As/In_{0.52}Al_{0.48}As$ can be grown. Due to the high bandgap energy E_G = 1.45 eV of InAlAs the material is transparent for 1550 nm radiation. In addition, the resistivity of as-grown InAlAs is several orders of magnitudes higher than the resistivity of InGaAs. Therefore, the effect of these InAlAs barriers is purely compensatory as the LT-defects in these barriers trap residual electrons from the adjacent InGaAs [28], [70]. The thickness of the InGaAs layer used in former studies measured typically 8 nm - 12 nm whereas the InAlAs-thickness varied between 7 nm – 10 nm. For Be-doped LTG-InGaAs/InAlAs heterostructures a resistivity of several 100 Ω cm was reported [27], [28].

Apart from the purely compensatory effect, Be has a great impact on the carrier dynamics after the optical excitation. When the doping concentration exceeds the residual electron concentration of LTG-InGaAs, the conductivity remains electron-like – even for Be doping concentrations of 2×10^{18} cm^{-3} [61], [71]. The reason is that Be dopants tend to ionize additional antisite defects, which increases the concentration of fast trapping centers in LTG-InGaAs [68]. The carrier dynamics as well as the performance as photoconductive THz emitter and detector of Be-doped LTG-InGaAs/InAlAs (MQWs) were studied by several groups. The main findings are:

- The electron lifetime can be reduced to below 1 ps for Be doping concentrations between 8×10^{17} cm^{-3} and 2×10^{18} cm^{-3} [27], [72]–[74]. An electron lifetime as short as 230 fs was reported by Biermann and coworkers [74].

- As a photoconductive emitter and detector a bandwidth of 3 - 4 THz and a peak dynamic range of 60 dB was reported in THz-TDS. [28], [29], [75].

At the beginning of this work, the following properties of LTG-InGaAs/InAlAs MQWs were not unambiguously resolved:

- The details of the carrier dynamics especially regarding the carrier recombination and its influence on the performance as a THz receiver.

- The influence of annealing on the electrical and optical properties of the material. Several groups reported an increase of the electron lifetime after annealing [71], [74], [76] whereas others observed a lifetime decrease [77].

Since only a fundamental understanding of the material properties allows for a precise optimization of the photoconductive devices, the unresolved points were systematically analyzed and optimized in this work.

3.2 Influence of beryllium doping

The results presented in this subsection are based on the publications [II] and [III]. It is demonstrated that the concentration of fast trapping defects in LTG-InGaAs/InAlAs MQWs can be systematically influenced by the beryllium doping concentration. A rate equation model is employed in order to describe the details of the carrier dynamics. Afterwards, THz antennas were fabricated from these samples and the fundamental influence of the Be-doping concentration on the performance as a receiver in THz-TDS is shown.

In total, five 2-inch wafers grown at a substrate temperature of 130 °C in an MBE system with nominal Be-doping concentrations of 0.3×10^{18} cm^{-3} - 4.0×10^{18} cm^{-3} were investigated. The layer structure consisted of 100 periods of 12 nm InGaAs wells and 8 nm InAlAs barriers. Both

wells and barriers were homogenously Be doped. All samples were annealed for 60 min. at 500 °C inside the growth chamber of the MBE under arsenic overpressure in order to avoid out-diffusion. The impact of the annealing process on the material properties is discussed in Sec. 3.4 and publication [VI].

In publication [II], the details of the carrier trapping and carrier recombination in the material were investigated by pump-power dependent differential transmission (DT) measurements with femtosecond laser pulses centered on 1550 nm (see Sec. 2.2.1). A rate equation model, which accounted for the limited number of fast trapping and recombination centers in the material, was expanded in three limit cases in order to separate the processes of electron trapping, the recombination of trapped electrons and holes and the saturation of trapping defects for high concentrations of optically excited carriers. The derived equations (see Sec. 3.3) were applied to fit the experimental data in the three aforementioned regimes. The results reveal that the Be doping concentration is a direct measure for the concentration of ionized As_{Ga} defects (As_{Ga}^{+})which serve as fast electron traps in the material. Photoexcited electrons are trapped by As_{Ga}^{+} and recombine with holes trapped by ionized Be dopants (Be^{-}). Electron trapping times as low as 150 fs were measured. The electron capture cross section of the As_{Ga}^{+} defects was calculated as $\sigma_e = 2 \times 10^{-14}$ cm^2 from the DT-signals.

After this comprehensive study of the carrier dynamics in Be-doped LTG-InGaAs/InAlAs MQWs photoconductive antennas were fabricated from the same samples in order to reveal the influence of the material properties on the performance as a receiver in THz-TDS (see publication [III]). In analogy to the dynamical experiments the receivers were operated in different regimes, characterized by the ratio of excited carriers and available trapping and recombination centers. The main findings are:

- The saturation of trapping centers, characterized by a higher concentration of optically excited carriers than available trapping centers, leads to a faster roll-off in the THz spectrum (see Fig. 3 of publication [III]).

- The receiver noise current I_N is dominated by Nyquist noise, which is anti-proportional to the square-root of the average resistivity R of the material

$$I_N \propto \sqrt{R^{-1}}\,.$$

  Hence, short electron lifetimes lead to low receiver noise as electrons and holes recombine promptly after the optical excitation (see Fig. 5 of publication [III]).

- The THz peak-to-peak amplitude detected by the receiver decreases for higher Be doping since the probability of ionized impurity scattering increases for higher doping concentrations (see Fig. 2 of publication [III]).

- By optimized Be doping, THz receivers with a bandwidth of 6 THz and more than 90 dB dynamic range were demonstrated (see Fig 8 of publication [III]).

The aforementioned results point out the well-known trade-off between a fast electron lifetime and a high detector current in THz-TDS. On the one hand, high Be doping leads to electron lifetimes as short as 140 fs and reduces the Nyquist noise in the receiver. On the other hand, ionized impurity scattering increases for higher doping concentration, which decreases the amplitude of the detected THz pulses. Hence, a careful adjustment of the Be doping concentration is required in order to design photoconductive receivers for THz-TDS capable to detect high THz amplitudes with both high bandwidth und high dynamic range. Fig. 3.2 shows the normalized power spectrum detected with a THz receiver fabricated from a LTG-InGaAs/InAlAs MQW with a nominal Be doping concentration of 4.0×10^{18} cm^{-3}. As the THz emitter, a fiber-coupled module comprising a high-mobility emitter was used (see Sec. 4 and publication [IV]). The emitter bias measured 120 V and the optical power at the emitter was 25 mW. Details of the experimental setup are described in Sec. 2.2.2. Note that the bandwidth and the maximum dynamic range of the spectrum exceed 6 THz and 80 dB, respectively. These results were the highest reported values for a system operated with 1550 nm pulses at the time of publication and underline the competitiveness of this technology compared to photoconductors based on 800 nm excitation.

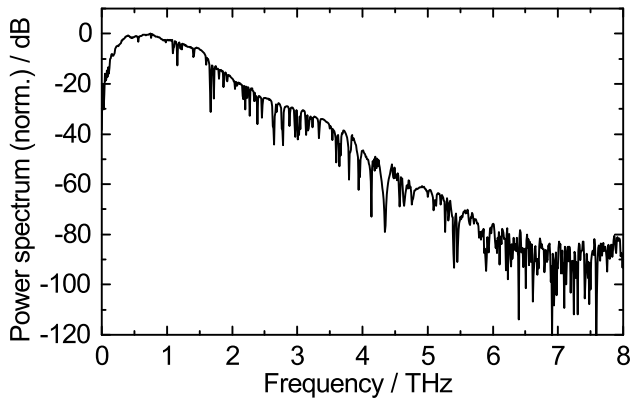

Fig. 3.2. Normalized power spectrum detected by a THz detector fabricated from LTG-InGaAs/InAlAs with a Be doping concentration of 4×10^{18} cm^{-3}. The receiver was illuminated with 16 mW optical power. The spectrum is obtained by averaging 10000 pulse trace with a length of 70 ps. The total acquisition time was 10 min. As THz emitter, a fiber-coupled high mobility photoconductor was used (see publication [IV]). The emitter was biased with 120 V and the optical power measured 25 mW. The THz measurement was done in ambient air. This figure was taken from publication [III].

3.3 Transient carrier dynamics

In this section the rate-equation model of the carrier dynamics in Be-doped LTG-InGaAs/InAlAs MQWs is described. The basic assumptions of the asymptotic analysis as well as the comparison of the analytic equations and the experimental data is presented. The explicit derivation of the equations can be found in publication [II] and the supplemental material therein. The experimental set-up of the pump-power dependent differential transmission experiments is described in Sec. 2.2.1.

The time dependent differential transmission of a sample can be described by Eq. (2.10). Here, the time dependent occupation of the conduction band $n(t)$ determines the decay time of the DT signal. In order to model the transient carrier dynamics in Be-doped LTG-InGaAs/InAlAs MQWs the following assumptions are made: The optical pump pulse creates a population of n electrons in the conduction band and h holes in the valence band. Electrons are trapped by ionized arsenic antisite defects, whereas holes are trapped by ionized Be dopants. The recombination of trapped electrons and holes is modeled as a two particle process between neutral arsenic antisites and neutral Be dopants. In order to describe this process mathematically four dynamic variables are needed: the concentration of electrons in the conduction band $n(t)$, the concentration of occupied electron traps $n_T(t)$, which is equivalent to the concentration of occupied As_{Ga}^{+} defects, the concentration of occupied hole traps n_{Be}, which corresponds to the concentration of neutral Be dopants, and the concentration of valence band holes $h(t)$.

$$\frac{dn}{dt} = G(t,n) - \frac{n}{\tau_e}\left(1 - \frac{n_T}{N_{As}^+}\right) \tag{3.1}$$

$$\frac{dn_T}{dt} = \frac{n}{\tau_e}\left(1 - \frac{n_T}{N_{As}^+}\right) - B_R(N_{As} - N_{As}^+ + n_T)n_{Be} \tag{3.2}$$

$$\frac{dn_{Be}}{dt} = \frac{h}{\tau_e}\left(1 - \frac{n_{Be}}{N_{As}^+}\right) - B_R(N_{As} - N_{As}^+ + n_T)n_{Be} \tag{3.3}$$

$$\frac{dh}{dt} = G(t,n) - \frac{h}{\tau_h}\left(1 - \frac{n_{Be}}{N_{As}^+}\right) \tag{3.4}$$

In Eqs. (3.1) - (3.4) the quantities N_{As} and N_{As}^+ denote the concentration of neutral and positively ionized As_{Ga} defects. The term $G(t,n)$ describes the optical excitation by the femtosecond pump pulse. The time dependence can be described by a Gaussian function and the density dependence arises from the limited total density of states in the conduction band. The factors $(1 - n_T/N_{As}^+)$ and $(1 - n_{Be}/N_{As}^+)$ account for the limited density of electron and hole traps. Here, the total concentration of available electron and hole traps is identical to N_{As}^+. It is shown later on that this assumption holds true since the concentration of ionized arsenic antisites is determined by the Be doping concentration for all samples discussed in this work. The term $B_R(N_{As} - N_{As}^+ + n_T)n_{Be}$ describes the recombination of trapped electrons and trapped holes, whereas $(N_{As} - N_{As}^+ + n_T)$ is the time-dependent concentration of neutral As_{Ga} defects and B_R symbolizes the two particle recombination coefficient, which is proportional to the overlap of the wavefunctions of the two bound trap states. The parameters τ_e and τ_r desribe the (unsaturated) electron and hole lifetimes.

Since the numerical solution of Eqs. (3.1) - (3.4) would require a large number of fit parameters, we expanded the equations in three limit cases in order to extract the unknown quantities. By varying the energy of the optical pump pulse, the ratio between excited carriers and available

trapping centers was directly influenced. This ratio is the main parameter for the subsequent analysis.

I. The unsaturated regime

In the unsaturated regime the density of electrons and holes excited by the pump pulse is at least one order of magnitude lower than the density of available trapping centers. In that case the terms $(1 - n_T/N_{As}^+)$ and $(1 - n_{Be}/N_{As}^+)$ in Eq. (3.1) and Eq. (3.4) are very close to unity, since the occupation of trapping centers n_T, n_{Be} is small compared to the density of available trapping sites N_{As}^+. Therefore, Eq. (3.1) reduces to

$$\frac{dn}{dt} \approx G(t,n) - \frac{n}{\tau_e}. \tag{3.5}$$

The time and density dependence of $G(t,n)$ can be neglected since the duration of the pump pulse measures only 90 fs in our experiments, and the density of excited carriers in the unsaturated regime is small compared to the total density of states in the conduction band. Hence, the solution of the Eq. (3.5) decreases mono-exponentially with decay time τ_e. In order to induce this regime experimentally we used the lowest optical pump power that generated a detectable DT signal. The density of excited carriers in this regime measured 3×10^{16} cm^{-3}. The normalized DT signals of the samples with nominal Be doping concentration of 0.3×10^{18} cm^{-3}, 0.9×10^{18} cm^{-3}, 2.0×10^{18} cm^{-3} and 4.0×10^{18} cm^{-3} are shown in Fig. 3.3. Note that all signals decay mono-exponentially whereas the decay time decreases from 3.3 ps for a Be doping concentration of 0.3×10^{18} cm^{-3} to 0.15 ps for a doping concentration of 4.0×10^{18} cm^{-3}. The dashed blue lines in Fig. 3.3 are exponential fits to the data. The calculated decay time τ_e is plotted as a function of the Be doping concentration in

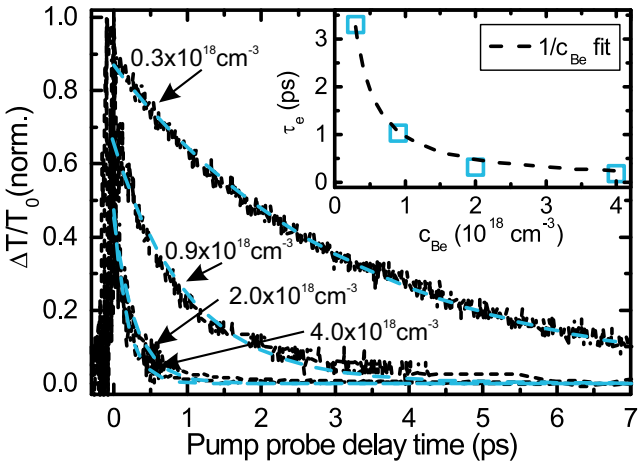

Fig. 3.3. Normalized differential transmission signal of samples with a nominal Be doping concentration of 0.3×10^{18} cm^{-3}, 0.9×10^{18} cm^{-3}, 2.0×10^{18} cm^{-3} and 4.0×10^{18} cm^{-3} for unsaturated excitation. The density of carriers excited by the pump pulse was 3×10^{16} cm^{-3} for all measurements. The dashed blue lines are mono-exponential fits to the data. The carrier lifetime τ_e is plotted as a function of the Be doping concentration c_{Be} in the inset. The dashed black line highlights the decrease of τ_e proportional to the Be doping concentration. This figure was adopted from publication [II] and slightly modified.

the inset. It can be clearly seen that the decay time decreases anti-proportional to the Be-doping concentration. The dashed black line in the inset is a $1/c_{Be}$ fit, which highlights the aforementioned anti-proportionality. Thus, the electron capture time τ_e is directly determined

by the concentration of Be dopants due their ability to ionize As_{Ga} defects. By applying the Shockley-Read-Hall relation of carrier capture [78]

$$\sigma_e = (v_{th}^e c_{Be} \tau_e)^{-1}, \tag{3.6}$$

the electron capture cross section of the ionized arsenic antisite is determined as $\sigma_e = 2 \times 10^{-14}$ cm^2. This value is about a factor of two higher than the capture cross section of As_{Ga}^+ defects in LTG-GaAs $\sigma_e = 7 \times 10^{-15}$ cm^2 determined in previous investigations [61]. Since the energy level of the As_{Ga} defects in LTG-InGaAs is closer to the conduction band than the energy level of the As_{Ga} defects in LTG-GaAs the electron trapping is supposed to be faster in LTG-InGaAs. For the calculation of σ_e the thermal velocity of electrons in InGaAs $v_{th}^e = 5.5 \times 10^7$ cm/s was used [79].

II. Partial trap filling

In the regime of partial trap filling, the density of optically excited carriers has the same magnitude as the concentration of trapping defects. In that case, the trapping centers start to fill up quickly after the optical excitation such that the terms $(1 - n_T/N_{As}^+)$ and $(1 - n_{Be}/N_{As}^+)$ are smaller than unity. Further, it is assumed that the process of carrier trapping is a much faster than the carrier recombination. This assumption is justified since the energetic distance from the conduction band to a bound trap state is much lower than the energetic distance for electron-hole recombination between bound trap states. Therefore, carrier trapping requires less phonons in order to fulfill energy and momentum conservation than electron hole-recombination, which in turn increases the probability of electron capture compared to electron-hole recombination [80]–[84]. Thus, the recombination terms in Eq. (3.2) and Eq. (3.3) can be neglected and the equations can be solved analytically [II]. The following relation is obtained for the time dependent electron concentration in the conduction band:

$$n(t) \approx n_{ex} \exp\left\{-\left(1 - \frac{n_{ex}}{N_{As}^+}\right)\frac{t}{\tau_e}\right\}. \tag{3.7}$$

Here, n_{ex} denotes the total concentration of optically excited electrons, which means that $n(t)$ decays mono-exponentially with a rescaled decay time

$$\tau_{pt} \equiv \tau_e \left(1 - \frac{n_{ex}}{N_{As}^+}\right)^{-1}. \tag{3.8}$$

Note that τ_{pt} increases with the concentration of optically excited electrons n_{ex}, such that the carrier capture is slower for higher optical excitation.

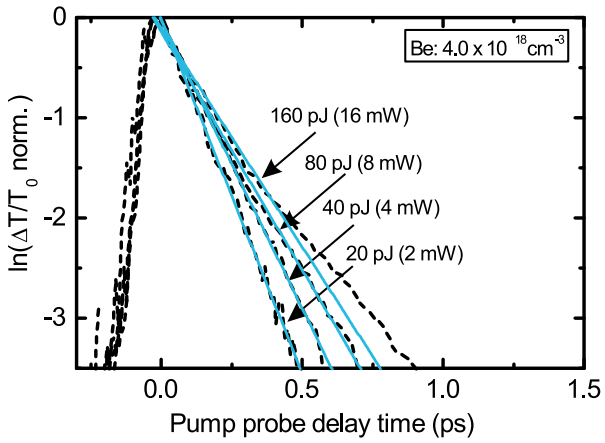

Fig. 3.4. Natural logarithm of the normalized differential transmission of the sample with nominal Be doping concentration of 4.0×10^{18} cm^{-3} for an increasing concentration of optically excited carriers. The plots are labeled by the energy (average optical power) of the pump pulse. The signal decay time increases for higher pulse energies due to partial trap filling. This figure was adopted from publication [II] and slightly modified.

In the experiments, the energy of the pump pulse was successively increased in order to observe the transition between the unsaturated regime and the regime of partial trap filling. Fig. 3.4 shows the natural logarithm of the normalized differential transmission of the LTG-InGaAs/InAlAs MQW structure with a Be-doping concentration of 4.0×10^{18} cm^{-3} for increasing pump pulse energies. For the lowest energy (20 pJ) the signal decay is mono-exponential with a decay time of 0.15 ps. This corresponds to the unsaturated electron capture time. When the pump pulse energy is successively increased, the signal decay remains mono-exponential with decay times of 0.17 ps and 0.21 ps for energies of 40 pJ and 80 pJ, respectively, as predicted by Eq. (3.8). For the highest pulse energy (160 pJ) a deviation from the mono-exponential decay can be clearly seen, indicating that the assumptions made for the regime of partial trap filling are no longer fulfilled.

III. The saturated regime

In the saturated regime, the concentration of optically excited electrons is large compared to the density of trapping centers. The result is a DT signal, which consists of two components: an initially fast decay corresponding to the electron capture in As_{Ga}^{+} defects directly after the excitation and a slow component, which describes the recombination of trapped electrons with holes. Since carrier trapping is much faster than carrier recombination, the traps fill up gradually and finally almost every trapping site is occupied by an electron. In this case, the remaining conduction band electrons can only be trapped, if a trapped electron has recombined with a trapped hole. Therefore, the electron dynamic in the conduction band is completely determined by the electron-hole recombination. In order to expand Eqs. (3.1) - (3.4) in this regime the relations $(1 - n_T/N_{As}^{+}) \ll 1$ and $(1 - n_{Be}/N_{As}^{+}) \ll 1$ were used, i.e. it was assumed that the trapping sites n_T and n_{Be} are almost completely filled. In that case, electrons and holes, which have recombined with each other, are almost instantaneously replaced by another free electron/hole from the CB/VB. Thus, the population of the trapping sites is clamped to its maximum as long as the saturation condition holds. In this case it can be shown that the population of the conduction band decays linearly with time [II]

$$n^{sat}(t) \approx n_0^{sat} - B_r N_{As}^{+} N_{As} t. \tag{3.9}$$

Here, n_0^{sat} symbolizes the residual electron concentration in the conduction band when the complete saturation of trapping centers begins. The important point in Eq. (3.9) is the dependence of the recombination process on the concentration of ionized antisites N_{As}^{+}. This means that the recombination process becomes faster, when the concentration of ionized antisites, which is equivalent to the Be doping concentration, increases.

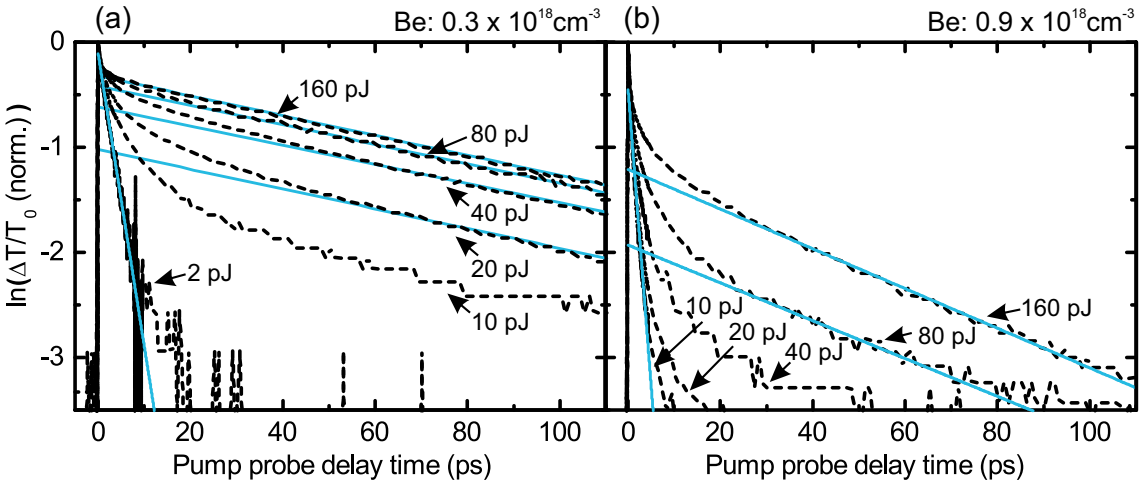

Fig. 3.5. Natural logarithm of the normalized differential transmission of the 0.3×10^{18} cm^{-3} (a) and 0.9×10^{18} cm^{-3} (b) doped samples. Each curve is labeled by the energy of the optical pump pulse. Solid blue lines indicate linear fits to the data. The saturation of trapping centers for increasing pulse energies is clearly seen. This figure was adopted from publication [II] and slightly modified.

In the experiments, the two samples with the lowest Be doping concentration are investigated, since the effect of trap saturation is larger for a lower concentration of trapping centers. Fig. 3.5 (a) and (b) show the natural logarithm of the normalized differential transmission of the samples with Be doping concentrations of 0.3×10^{18} cm^{-3} and 0.9×10^{18} cm^{-3} for increasing pump pulse energies. In both cases the transition from the unsaturated to the completely saturated regime can be clearly identified, whereas the saturation is stronger for the sample with lower doping. For the highest pump pulse energies (80 pJ and 160 pJ) the signal decay is mono-exponential for pump probe delay times larger than 5 ps. This is the regime of trap saturation, which is described by Eq. (3.9). The blue lines are linear fits to the mono-exponential part of the signals. One directly observes that the slope of the linear fit is independent of the pump pulse energy but depends only on the Be doping concentration. This is directly predicted by Eq. (3.9), due to its dependency on the concentration of trapping sites N_{As}^{+}.

In conclusion, the results of pump-power dependent DT measurements on Be-doped LTG-InGaAs/InAlAs MQWs were successfully described by expanding a rate equation model in three limit cases. This comprehensive study of the carrier dynamics was a prerequisite for the understanding of the THz performance of these structures studied in publication [III]. In

addition, the same asymptotic techniques were employed in Sec. 6.3 and publication [VIII] in order to describe the carrier dynamics in iron-doped InGaAs.

3.4 Influence of annealing

Apart from the growth temperature, which influences the overall density of antisite defects in LTG-InGaAs/InAlAs, and the Be-doping concentration, which determines the concentration of ionized arsenic antisites, post-growth annealing is an important mechanism to design the material properties of the future THz photoconductor. Extensive annealing studies were performed in publication [VI]. The central aim of that paper was to answer the question of how annealing of LTG-InGaAs/InAlAs MQWs determines the electron lifetime. Recently published results reported a lifetime decrease after annealing [77], several different groups observed a lifetime increase due to the precipitation of As_{Ga} defects [71], [74], [76].

We investigated the influence of the annealing time at a fixed temperature (isothermal annealing) and the influence of the annealing temperature at a constant duration of the annealing process (isochronal annealing) on the electrical and optical properties of the material. The layer structure was identical to the layout of the samples investigated in the last two subsections: An InAlAs buffer layer with a thickness of 700 nm was grown on top of a 2-inch semi-insulating InP:Fe substrate. Afterward, 100 periods of 12 nm InGaAs and 8 nm InAlAs were grown at a substrate temperature of 130 °C. The samples were Be-doped with concentrations of 8×10^{17} cm^{-3} – 12×10^{18} cm^{-3}. The composition of all layers was lattice matched to the InP substrate, which was verified by XRD rocking curves.

For the isothermal annealing, samples with a nominal Be doping concentration of 1×10^{18} cm^{-3} were annealed at 500 °C inside the MBE growth chamber for 15, 30, 60 and 120 minutes. For the isochronal annealing, three 2-inch wafers with nominal Be doping concentrations of 8×10^{17} cm^{-3}, 4×10^{18} cm^{-3}, and 12×10^{18} cm^{-3} were grown by MBE. After growth, the samples were removed from the MBE growth chamber and cleaved into eight pieces, which were individually annealed for 60 min. at 500 °C, 525 °C, 550 °C, 575 °C, 600 °C, 650 °C, and 700 °C in an MOVPE system. One sample of each wafer was not annealed. The reason for the ex-situ annealing is the achievable arsenic and phosphorous overpressure, which is higher in a MOVPE system than in a MBE. The As and P flux measured 100 sccm up to 600 °C-annealing and 200 sccm for higher temperatures. All samples were analyzed by room temperature Hall measurements and pump-power dependent differential transmission. The main findings are:

- After isothermal annealing between 15 min. – 120 min. the resistivity of the material increased by a factor of 4; the electron lifetime increased by approximately 50 % from 0.9 ps – 1.3 ps (see Fig. 1 of publication [VI]).

- Isochronal annealing for 60 min. at 600 °C increased the resistivity by three orders of magnitude whereas the residual electron concentration decreased by approx. the same amount.

- The electron lifetime increased up to a factor of 4 after isochronal annealing at 600 C. The influence of the annealing on the electron lifetime is stronger for samples with lower Be doping concentrations.

These findings are illustrated in Fig. 3.6. The resistance (a), the residual electron concentration (b) and the unsaturated electron lifetime (c) are plotted semi-logarithmically as a function of the inverse annealing temperature for the isochronally annealed samples. The annealing temperature of the unannealed reference samples was set to 20 °C. The color coding of the plots is as follows: black squares, blue circles, and green triangles correspond to LTG-InGaAs/InAlAs samples with a nominal Be doping concentration of 0.8×10^{18} cm^{-3}, 4.0×10^{18} cm^{-3}, and 12.0×10^{18} cm^{-3}, respectively. The dashed lines are linear fits to the data. In Fig. 3.6 (a) and Fig. 3.6 (b) the increase of the resistance and the decrease of the residual electron concentration for higher annealing temperatures can be clearly seen. In these semi-logarithmic plots, the linear dependence of the resistance and the residual electron concentration on the inverse annealing temperature indicates a thermally activated diffusion process (Arrhenius plot). In analogy to the results of annealed LTG-GaAs, these findings can be explained by the diffusion of arsenic antisites via Gallium vacancies and the formation of arsenic precipitates [49]–[51], [58]. The precipitates are supposed to form Schottky-barriers in the material, which explains the increase of the resistance shown in Fig. 3.6 (a). Another strong argument in favor of this interpretation is the dependence of the electron lifetime on the annealing temperature. In Fig. 3.6 (c) the electron lifetime increases for all doping concentrations when the annealing temperature is increased. Hence, the concentration of fast trapping centers, i.e. As_{Ga}^{+} defects, is lower for samples annealed at higher temperatures. When As_{Ga}^{+} defects precipitate during the annealing process their concentration decreases and the electron lifetime of the annealed samples increases. In addition, one clearly observes that the slope of the linear fits in Fig. 3.6 (c) depends on the Be doping concentration. Thus, the activation energy for the diffusion of As_{Ga} defects is higher for samples with higher Be doping. The same trend was observed in annealing studies of Be-doped LTG-GaAs and was finally explained by the small Be dopants, which relax the lattice strain due to the high concentration of arsenic antisites in the material [65]. In conclusion, the results show unambiguously that the annealing of Be-doped LTG-InGaAs/InAlAs MQWs increases the electron lifetime of the material. In addition, resistance and residual electron concentration can be efficiently adjusted by the duration and the temperature of the annealing process.

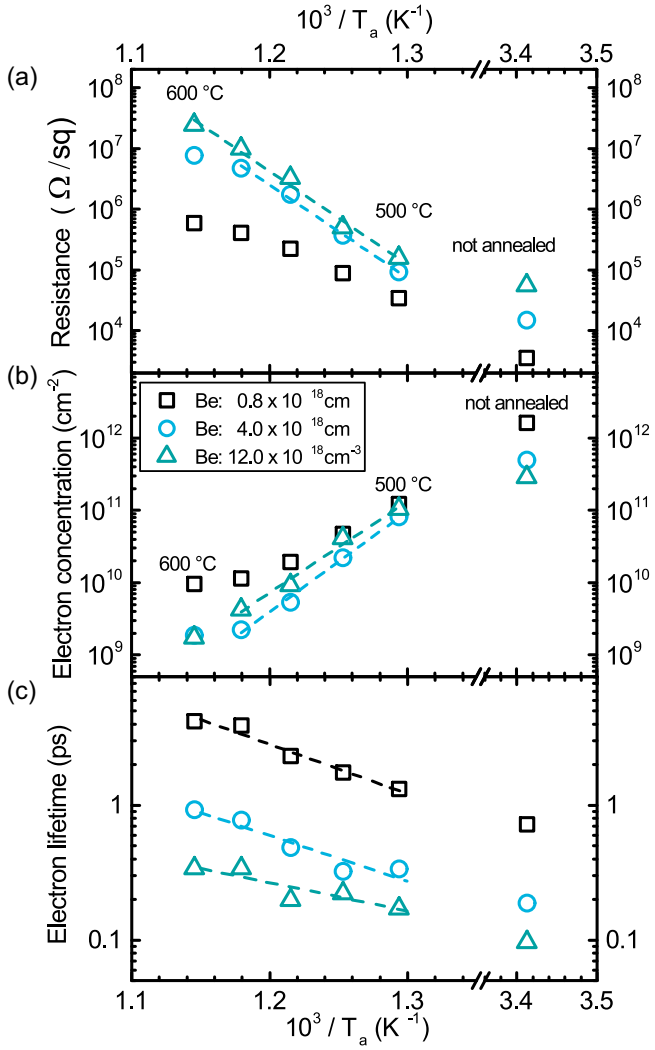

Fig. 3.6. (a) Semi-logarithmic plot of the resistance and (b) the residual electron concentration determined by room-temperature Hall measurements as a function of the inverse temperature of the isochronal annealing. All samples comprise the same layer structure and were grown at 130 °C by MBE. Black squares, blue circles, and green triangles correspond to nominal Be doping concentrations of 0.8×10^{18} cm^{-3}, 4.0×10^{18} cm^{-3}, and 12.0×10^{18} cm^{-3}. Dashed lines are linear fits to the data indicating a thermally activated diffusion. (c) The unsaturated electron lifetime determined by differential transmission measurements is plotted semi-logarithmically as a function of the inverse annealing temperature. The carrier density excited by the pump pulse was 6.5×10^{16} cm^{-3} for all measurements, which is significantly lower than the Be-doping concentration of all samples. Thus, the electron lifetimes correspond to the unsaturated regime described in Sec. 3.3. A lifetime of 140 fs was measured for a doping concentration of 12×10^{18}cm^{-3}. The annealing temperature of the unannealed samples was set to 20 °C in all plots. This figure is based on Fig. 2 and Fig. 3 of publication [VI].

The detailed understanding of the influence of the Be doping and the annealing on the electrical and optical properties of the photoconductor was exploited to influence and optimize the properties of receivers for THz-TDS. Table 3.1 summarizes the growth conditions, the electrical properties and the electron lifetime of three wafers grown for the fabrication of photoconductive receiver antennas. Note that the electron lifetime of all samples is below 0.3 ps. In this case, the saturation of trapping centers is avoided even at high optical excitation of the THz receiver. Thus, the influence of the electrical parameters on the performance of THz receivers could be studied without losing the broadband detection capability of the devices.

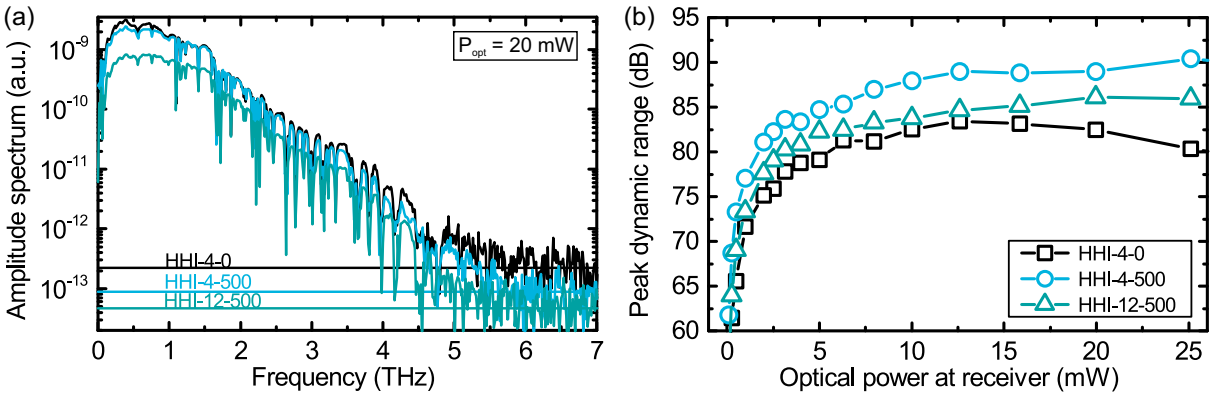

Fig. 3.7 (a) Amplitude spectra detected by the THz photoconductive receivers fabricated from the samples in Table 3.1. The horizontal lines indicate the noise level, which was determined by averaging the spectral amplitudes from 7.5 THz – 10 THz. (b) Peak dynamic range as a function of the optical illumination power at the receivers. All measurements were performed in the TDS setup described in Sec. 2.2.2. As emitter, a fiber-coupled module containing an undoped InGaAs/InAlAs photoconductor (see Sec. 4) was applied. Bias voltage and optical power of the emitter measured 120 V and 20 mW, respectively.

The receiver antennas were structured as $\lambda/2$-dipoles with a length of 25 µm and a 10 µm-wide photoconductive mesa. The antennas were characterized in the TDS setup described in Sec. 2.2.2. As emitter, a fiber-coupled high mobility InGaAs/InAlAs heterostructure (see Sec. 4) was employed. The bias voltage of the emitter measured 120 V and the optical illumination power was fixed at 20 mW for all measurements. Fig. 3.7 (a) shows the amplitude spectra, which were neither shifted with respect to each other nor normalized. Thus, the observable differences are attributed to different material properties. First, one observes that each spectrum features a bandwidth of more than 5 THz, which is explained by the sub-picosecond lifetime of each material. The noise level of each spectrum, which was determined as the average of all spectral amplitudes in the range of 7.5 THz – 10 THz, is highlighted as a horizontal line in Fig. 3.7 (a). Note that the spectrum detected by the photoconductor with the highest doping (HHI-12-500) has the lowest noise level. Generally, the detector noise correlates with the resistivity ρ of the photoconductor (see Table 3.1).

Table 3.1. Growth parameters, electrical properties and electron lifetimes of the samples used for the fabrication of the THz photoconductive receiver antennas. The symbols denote: c_{Be} – Be doping concentration; T_A – annealing temperature; ρ – Hall resistance; n_e – residual electron concentration; μ_e – electron mobility; τ_e – unsaturated electron lifetime.

Name	c_{Be} (10^{18} cm^{-3})	T_a (°C)	ρ (Ω / sq)	n_e (10^{11} cm^{-2})	μ_e (cm^2 V^{-1} s^{-1})	τ_e (ps)
HHI-4-0	4.0	-	1.5×10^4	8.1	517	0.16
HHI-4-500	4.0	500	1.1×10^5	1.1	517	0.27
HHI-12-500	12.0	500	3.3×10^5	0.9	194	0.14

In Fig. 3.7 (b) the peak dynamic range of the receivers is compared for an increasing optical illumination power. HHI-4-500, the sample with a Be-doping concentration of 4×10^{18} cm^{-3} and a 500 °C-annealing shows the highest values for all excitation densities. Due to the high noise of HHI-4-0, the dynamic range of this receiver is the lowest of all samples. Although the high doping concentration of HHI-12-500 leads to the lowest noise level of all receivers (see Fig. 3.7 (a)), the high concentration of ionized antisites and Be dopants in the material increases the probability of ionized impurity scattering. This in turn decreases the peak-to-peak amplitude of the detected THz signal, which explains the intermediate peak dynamic range of this sample. (For further discussions of the results see publication [VI])

In conclusion, the results of the last subsections demonstrated that photoconductive receivers with a bandwidth of up to 6 THz and a peak dynamic range exceeding 90 dB can be fabricated from Be-doped LTG-InGaAs/InAlAs MQWs by exploiting the complex interplay between growth temperature, Be-doping concentration and post-growth annealing. In the next subsection, Be-doped LTG-InGaAs/InAlAs photoconductors are used to fabricate THz near-field probe tips. These devices allow for THz images with sub-wavelength resolution.

3.5 Application: THz Near-field detector

In this subsection we report on the development of a THz near-field detector based on Be-doped LTG-InGaAs/InAlAs photoconductors. The results were discussed extensively in publication [V].

Near-field imaging offers the possibility to increase the spatial resolution of THz images into the deep subwavelength range [85]. By employing metallic apertures, a spatial resolution of 10 µm at 1 THz was demonstrated [86]. THz imaging of nanoscopic structures was enabled by scanning near-field optical microscopy (SNOM) systems, which use atomic-force-microscope tips as scattering elements for THz radiation [87]. Photoconductive (PC) near-field detectors based on free-standing cantilever microstructures made of LTG-GaAs have been developed as a relatively simple alternative to the aforementioned approaches [88]. With a resolution of a few micrometers PC near-field detectors range between the metallic apertures and the scattering type near-field microscopes. The PC approach bears great potential for future applications of high resolution conductivity measurements on solar cells [89]. However, PC near-field detectors based on LTG-GaAs have to be illuminated with femtosecond pulses centered on 800 nm for efficient device operation. This impedes the use of compact, stable and cost-effective THz-TDS systems relying on fiber-optical technologies.

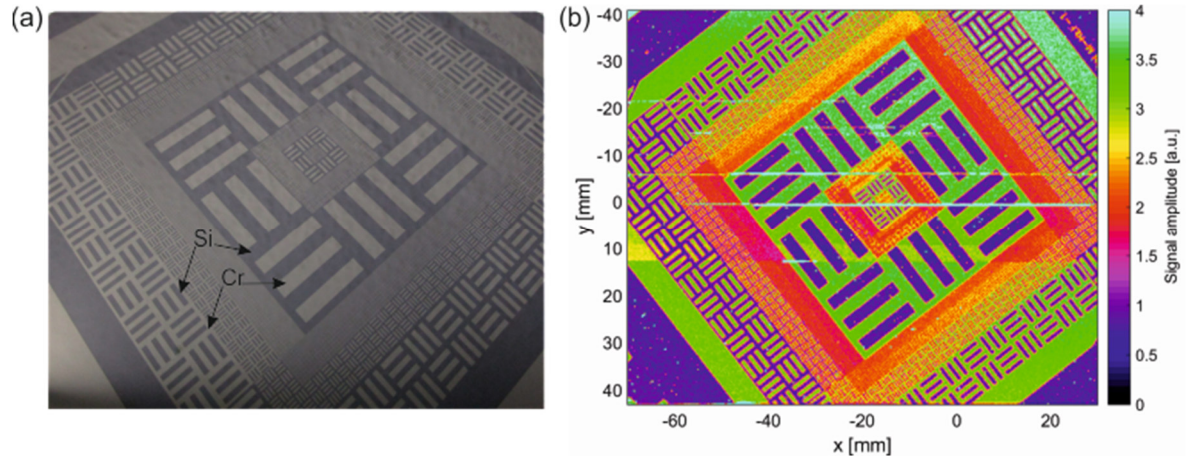

Fig. 3.8. (a) Optical micrograph of a high resistivity float zone (HRFZ) silicon wafer. The light structures of the image consist of chromium with a thickness of 40 nm, which was lithographically structured after deposition on the silicon wafer (dark structures). (b) Near-field image of the wafer shown in (a) recorded with a commercially available THz-TDS system together with the novel PC probe-tip. The image consists of 500000 pixels. For each pixel a THz pulse trace with a duration of 25 ps was acquired within 20 ms. This figure was adopted from publication [V] and slightly modified.

In publication [V] the first PC THz near-field microprobe for the operation at 1550 nm and, therefore, directly compatible with a fully fiber-coupled THz-TDS system was demonstrated. This development combines the sub-wavelength spatial resolution of a near-field detector with state-of-the art time-domain spectroscopy, which allows for a fully fiber-coupled coherent near-field imaging system.

The microprobe itself was made of an optimized Be-doped LTG-InGaAs/InAlAs photoconductor with a carrier lifetime of 0.5 ps (see Fig. 2 of publication [V]). Gold electrodes forming a resonant near-field antenna were structured on top of the free standing photoconductive cantilever. A 5-µm-wide photosensitive gap is located at the very tip of the antenna. Prior to the application as a near-field microprobe, the device was used as a PC detector in a standard (far-field) THz-TDS system in order to verify the correct operation of the device. With a spectral bandwidth of 2 THz, the performance of the novel microprobe was competitive to PC near-field detectors based on LT-GaAs (see Fig. 4 of publication [V]).

In the THz near-field imaging experiment the conductivity of a 6-inch high resistivity float zone (HRFZ) silicon wafer was investigated, comprising lithographically structured 40 nm-thick chromium thin-films on its topside. A photograph of the wafer is shown in Fig. 3.8 (a). The Cr layer is structured to a grid of bars with different sizes, ranging from a few micrometers to several millimeters. The total area measures 100 mm × 85 mm. The wafer was mounted on a motorized xyz-translation stage, which allowed for a continuous movement of the sample between the fiber-coupled THz emitter and the PC microprobe. During the scanning, an optical height sensor was employed in order to keep the distance between the near-field detector and the sample constant. The sample was scanned with a lateral resolution of 250 µm in a vertical distance of approx. 120 µm. For each of the 500000 pixels, a THz pulse trace with a duration

of 25 ps was acquired in 20 ms. While the amplitude of the transmitted THz pulse is mainly determined by the conductivity of the Cr-layer, the phase of the THz signal provides information about the substrate thickness. In previous near-field imaging setups, relying on LT-GaAs based microprobes, amplitude and phase information were commonly not available for each pixel due to the lack of fast scanning TDS spectrometers. By using a commercially available THz-TDS system relying on 1550 nm technology [43], the full information of the THz pulse could be provided at every sampling point.

The structures of the photograph in Fig. 3.8 (a) are nicely reproduced in the THz image Fig. 3.8 (b). Here, light green to red color refers to areas of high-THz transmission (HRFZ silicon substrate) while violet to black color indicates low-THz transmission corresponding to those parts covered with the Cr thin-film. The horizontal light-blue lines in the THz image are measurement artifacts. In order to evaluate the lateral resolution limit of the microprobe, a high resolution image of a small wafer area was acquired. Here, the sample-to-detector distance was reduced to 15 µm and the lateral resolution was increased to 20 µm. Structures with a width of 100 µm were nicely resolved in this image (see Fig. 6 of publication [V]).

The results of this subsection underline that photoconductive near-field imaging systems can be significantly improved with respect to the measurement speed as well as the provided information by using THz-TDS systems relying on 1550 nm technology.

4 THz emitters based on undoped InGaAs/InAlAs MQWs

In this section, THz emitters based on InGaAs/InAlAs multiple quantum wells (MQWs) grown at temperatures around 400 °C by MBE are investigated. This photoconductor exploits the spatial separation of THz generation and carrier trapping, which leads to a material with high carrier mobility and increased THz output power. At growth temperatures around 400 °C the InGaAs layers are almost free of defects, whereas the adjacent InAlAs layers contain deep-level recombination centers. Thus, optically excited carriers are efficiently accelerated in the InGaAs layers until they are trapped by the defects in the adjacent InAlAs. Due to the low defect concentration, the electron mobility in the InGaAs layers is significantly higher than in Be-doped LTG-InGaAs/InAlAs photoconductors. THz-emitters fabricated from these undoped InGaAs/InAlAs MQWs emit broadband THz pulses with a bandwidth up to 6 THz and an average THz power above 0.1 mW. This corresponds to a 100-fold increase in THz-power compared to THz-emitters based on LTG-InGaAs/InAlAs. The results presented in this section are based on publications [I] and [IV].

4.1 Introduction

Previous theoretical and experimental studies revealed that the demands on photoconductors for THz emitters and detectors are essentially different. In 1997, Tani and coworkers compared semi-insulating GaAs (SI-GaAs) with a carrier lifetime of several hundred picoseconds and LTG-GaAs with a carrier lifetime below 1 ps as a photoconductive THz emitter [39]. The radiation spectra of these two different emitter materials were almost identical, which indicated that an ultra-short carrier lifetime is of minor importance in photoconductive emitters. The only constraint on the carrier lifetime is given by the repetition frequency of the femtosecond laser source, which is typically on the order of 100 MHz. The carriers excited by one laser pulse have to have recombined until the next pulse hits the antenna. Thus, carrier lifetimes of several hundred picoseconds are acceptable for THz-emitters. These findings were explained by the fact that the high frequency components of the THz pulse are mainly created by the rising of the photocurrent right after the excitation by the ultrashort laser pulse instead of the falling current caused by carrier scattering, carrier trapping, and carrier recombination [37]. Several studies confirmed the results of Tani and coworkers [90]–[93].

In general, photoconductors with longer carrier lifetimes feature a significantly higher electron mobility compared to their short carrier lifetime counterparts. A sub-picosecond lifetime is achieved by incorporating point defects as trapping and recombination centers into the material (see Sec. 3). These defects are commonly ionized and, therefore, they act as scattering centers, which reduce the carrier mobility. Since a high mobility is required for the efficient acceleration of photoexcited carriers in the bias field of the emitter, higher THz powers can be generated with photoconductors comprising longer carrier lifetimes.

In order to obtain a high mobility material with carrier lifetimes on the order of 100 ps the following concept was studied in the remainder of this chapter. The THz generation, i.e. the absorption of the infrared light and the carrier acceleration, was spatially separated from the carrier trapping and the recombination in the photoconductor.

In 2011, Dietz and coworkers proposed a photoconductor consisting of up to 100 periods of undoped InGaAs and InAlAs layers with a thickness of 12 nm and 8 nm, respectively, grown by MBE at a substrate temperature of 400 °C [94]. The InGaAs layers were almost free of defects at that growth temperature. Especially, antisite defects and other deep centers are not incorporated into InGaAs at 400 °C [66]. In contrast, the InAlAs layers contained high concentrations of deep-level defects at that growth temperature [95]–[98]. The origin of these defects is a non-stoichiometric alloying due to the temperature dependent surface kinetic of the Al atoms [95]. This leads to areas with a diameter of about 35 Å inside the InAlAs layers where the material is more InAs-like than in the surrounding InAlAs [96]. The activation energy E_A = 0.6 – 0.7 eV of these defects was determined via deep-level transient spectroscopy (DLTS [99]) [95], [97]. Hence, the deep-level defects in InAlAs are located below the conduction band (CB) minimum of InGaAs in the heterostructures proposed by Dietz and coworkers [94]. Therefore, optically excited electrons in the CB of InGaAs can be trapped by the defects in the adjacent InAlAs layers. A schematic band diagram of a single InGaAs layer arranged between two InAlAs barriers is shown in Fig. 4.1. The discontinuities of the CB and the VB in InGaAs/InAlAs heterostructures were taken from Ref. [100]. Thus, the photoconductive concept presented in Fig. 4.1 is supposed to spatially separate the optical excitation in the InGaAs layers from the carrier trapping and recombination in the InAlAs. In Ref. [94] the authors demonstrated that THz emitters fabricated this photoconductive material comprised a 6-fold higher optical-to-THz conversion efficiency than emitters consisting of LTG-InGaAs/InAlAs operated under the same conditions [94].

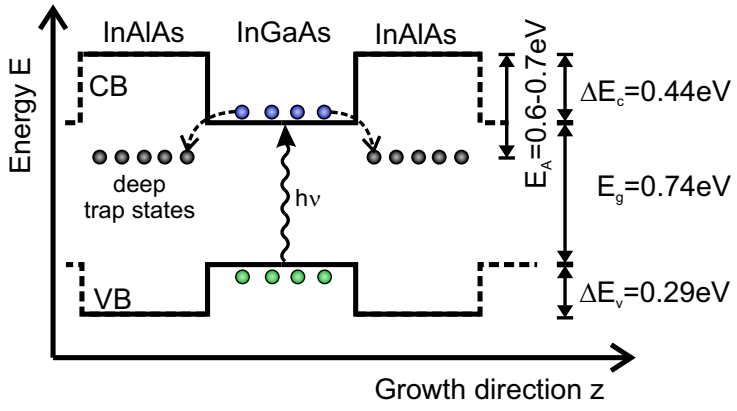

Fig. 4.1. Schematic band diagram of a single InGaAs layer sandwiched between InAlAs barriers. The band gap energy of InGaAs E_G, the band discontinuities of the valence band (VB) and the conduction band (CV) $\Delta E_{V/C}$ as well as the activation energy E_A of the deep trap states are given. Blue and green circles denote photoexcited electrons and holes, respectively. The electron trapping occurs in the InAlAs layers, which is indicated by dashed arrows.

The findings of Dietz and coworkers [94] are the starting point of the investigations and improvements described in this section. The influence of the growth temperature and the

thickness of the InAlAs layers on the transient carrier dynamics and the performance of THz photoconductive emitters were studied in publication [I]. The main findings are:

- The carrier lifetime is a function of the thickness of the InAlAs barrier. The larger the barrier thickness (up to a maximum around 8 nm), the lower the carrier lifetime of the material (see Fig. 3 of publication [I]). These results show unambiguously that the carriers are trapped by defects inside the InAlAs layer.

- The carrier lifetime shows a minimum for growth temperatures around 375 °C, indicating the highest concentration of the alloying defects close to that temperature.

- The emitted THz spectrum is broadband for growth temperatures around 375 °C, comparable to Be-doped LTG-InGaAs/InAlAs emitters (see Fig. 4 of publication [I])

- The emitted THz power is a factor of 100 higher than the power emitted by Be-doped LTG-InGaAs/InAlAs THz emitters (see Fig. 5 of publication [I]).

In publication [IV] a calibrated power detector was employed in order to determine the absolute THz power emitted by a photoconductor consisting of 100 periods of 12 nm InGaAs and 16 nm InAlAs grown at 375 °C in an MBE. An average THz power of 112 µW ± 7 µW was measured, which is among the highest values published for THz emitters designed for the illumination with 1550 nm laser pulses. To the best of our knowledge the power measurement conducted in publication [IV] is the first calibrated power measurement of a THz emitter for TDS with a detector traceable to a national standard. Hence, these measurements set the standard for all subsequent power measurements of THz-TDS emitters.

The high THz output power of the undoped InGaAs/InAlAs based photoconductors are the prerequisite for THz-TDS systems with high measurements speed. By combining the high power emitters and an electrically controlled optical sampling (ECOPS) system, an all fiber-coupled THz-TDS system with kHz measurement rate could be realized [101].

In the next subsections, the optical and THz properties of the emitter material are discussed in more detail.

4.2 Optical properties

In publication [I] three sample series were investigated in order to unambiguously show that the carrier trapping occurs in the InAlAs barrier layers. Table 4.1. summarizes the layer structures of the investigated samples. In T_g series 1 and T_g series 2 the growth temperature was varied between 325 °C – 450 °C and 350 °C – 425 °C, respectively, whereas the remaining growth parameters were kept constant. In the d_B series the growth temperature was kept constant at 375 °C while the thickness of the InAlAs layers was changed between 2 nm and 16 nm. The multi-quantum well structures were grown on top of an InAlAs buffer with a thickness of 777 nm. The substrate was semi-insulating InP:Fe with a thickness of 350 µm. The surface morphology of all samples was controlled by differential interference contrast microscopy in combination with XRD rocking curves. All samples were single-crystal with clearly resolved superlattices of the intended thickness.

Table 4.1. Sample series investigated in publication [I]. The symbols denote: T_g – growth temperature, d_{InGaAs} – thickness of the InGaAs layers, d_{InAlAs} – thickness of the InAlAs layers, repetitions – number of multi-quantum wells consisting of an InGaAs and an InAlAs layer.

Name	T_g (°C)	d_{InGaAs} (nm)	d_{InAlAs} (nm)	repetitions
T_g series 1	325 – 450	12	8	30
T_g series 2	350 – 425	12	8	100
d_B series	375	12	2 – 16	100

The carrier lifetime was determined by optical differential transmission (DT) measurements with femtosecond pulses centered on 1550 nm (see Sec. 2.2.1). Fig. 4.2 shows the natural logarithm of the normalized differential transmission signals for the samples of T_g series 2. Each plot is labeled by the growth temperature of the corresponding sample. For comparison, the DT signal of a Be-doped LTG-InGaAs/InAlAs heterostructure with the same layer structure as the samples from T_g series 2 is shown (T_g= 130 °C). One clearly observes that the signal decay time increases with growth temperature. The dashed blue lines are linear fits to the data for pump-probe delay times above 2 ps.[1] The extracted electron lifetime τ_2 is plotted as a function of the growth temperature T_g in Fig. 4.2 (b). In this plot, the electron lifetime of T_g

[1] The initially fast decay of the DT signals for pump-probe delay times below 2 ps is explained by the thermalization of hot carriers in the conduction band of InGaAs via phonon emission. We did not find any significant correlation between the duration of this fast signal decay and the growth temperature or the InAlAs barrier thickness. Therefore, this fast decay is neglected in the remainder of this thesis. For a more detailed discussion see publication [I].

series 1 (empty squares) and T_g series 2 (full squares) are shown. Full and dashed lines are guides to the eye.

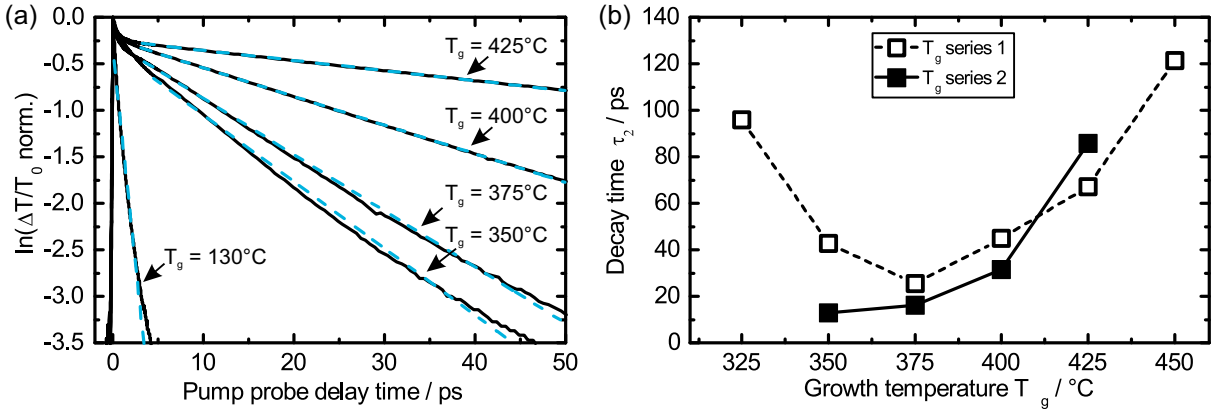

Fig. 4.2. Natural logarithm of the normalized differential transmission for the samples of T_g series 2 (a). The signal comprises a fast decaying component, which is independent of the growth temperature and a slowly decaying component, which strongly depends on T_g. Dashed blue lines are linear fits to the slowly decaying component. The calculated decay constant is plotted as a function of the growth temperature for T_g series 1 and T_g series 2 in (b). This figure is a combination of Fig. 1 and Fig. 2 from publication [I].

The electron lifetime τ_2 depends strongly on the growth temperature. The T_g series 1 shows a pronounced minimum for T_g = 375 °C whereas the electron lifetime of T_g series 2 is the smallest at T_g = 350 °C. Although the samples of T_g series 1 and T_g series 2 are nominally identical, the observed differences of τ_2 are attributed to an uncertainty of the real growth temperature. In the MBE used for the material growth the substrate surface temperature could not be measured directly. Instead, the growth temperature was determined by interpolating from the temperature of the oxide desorption from the InP substrate, which occurs at 520 °C, to the desired growth temperature. This results in a temperature uncertainty, which is estimated to $\Delta T \approx 15$ °C since T_g series 1 and T_g series 2 were not grown in direct succession. Nevertheless, Fig. 4.2 clearly demonstrates that the growth temperature influences the lifetime of optically excited electrons in the InGaAs layer.

In addition to the lifetime studies presented in publication [I], the dependence of the defect density on the growth temperature was investigated by temperature dependent photoluminescence (PL) measurements on T_g series 1 [102]. In analogy to the carrier lifetime shown in Fig. 4.2 (b), the PL intensity shows a pronounced minimum for T_g = 375 °C (see Fig. 3 of Reference [102]), which is a clear indicator for the highest defect density at this growth temperature. Furthermore, the PL-linewidth is broadened for T_g = 375 °C (see Fig. 3 of Reference [102]). In summary, these results underline the strong dependence of the defect density in the InGaAs/InAlAs MQWs on the growth temperature with a pronounced maximum around 375 °C.

In order to demonstrate that the trapping defects are located inside the InAlAs, the carrier lifetime τ_2 was analyzed as a function of the InAlAs layer thickness (see d_B series in Table 4.1).

In Fig. 4.3, the carrier lifetime τ_2 is plotted against the InAlAs thickness for all samples of the d_B series.

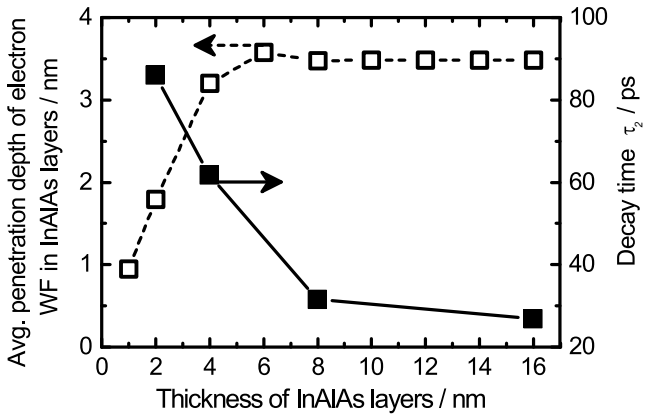

Fig. 4.3. Average penetration depth of the electron wavefunction into the InAlAs layer and the decay time τ_2 of the differential transmission signal as a function of the InAlAs layer thickness. This figure is based on Fig. 3 from publication [I].

Note that the carrier lifetime decreases from above 80 ps for an InAlAs thickness of 2 nm to about 30 ps for a thickness of 8 nm. Since the absolute number of trapping defects increases with the InAlAs thickness these findings support the assumption that the electron capture occurs inside the InAlAs layers. However, samples with 16 nm thick InAlAs layers show a minor decrease of the electron lifetime, although the layer thickness doubles from 8 nm to 16 nm (see Fig. 4.3). This effect can be explained by the limited penetration depth of the wavefunction of CB electrons in InGaAs into the InAlAs layers. Due to the conduction band discontinuity $\Delta E_c = 0.44$ eV (see Fig. 4.1), the excess energy of a photoexcited electron in the conduction band of InGaAs is not sufficient for a direct transfer into the InAlAs layer. Therefore, the electron wavefunction decays exponentially at the barrier between the InGaAs and the InAlAs layers. Hence, CB electrons in InGaAs can only be trapped by defects in the InAlAs layer when the overlap of the electron wavefunction and the defect wavefunction is nonzero. In order to verify this explanation, the 1D Schrödinger equation for 30 periods of the MQW structure with different InAlAs layer thicknesses was solved numerically and the averaged penetration depth of the electron wavefunction into the InAlAs was calculated by summing over all positions in the barrier with nonzero wavefunctions in the first sub-band of the MQW structure. The result is shown as open squares in Fig. 4.3. The penetration of the wavefunction into the InAlAs barrier has its maximum for an InAlAs thickness of 6 nm. Hence, CB electrons in InGaAs cannot reach defects sites, which are located more than 6 nm from the InGaAs/InAlAs interface. Therefore, the electron lifetime decreases only slightly when the InAlAs thickness is increased from 8 nm to 16 nm.

In summary, the results of this subsection show that the optical absorption and the carrier trapping are spatially separated by the material concept depicted schematically in Fig. 4.1. In the next subsection these photoconductors are employed as emitters in THz-TDS.

4.3 THz results and absolute power measurements

In this subsection the undoped InGaAs/InAlAs MQW structure with spatially separated layers for the THz generation and the carrier trapping is investigated as a photoconductive emitter in THz-TDS.[2] The results are based on publication [I], in which THz emitters fabricated from Be-doped LTG-InGaAs/InAlAs and undoped InGaAs/InAlAs MQWs were compared. The main findings are:

- The THz power generated by undoped InGaAs/InAlAs emitters is up to a factor of 100 higher than the average THz power from LTG emitters (see Fig. 7 of publication [I]).
- The THz spectra of both types of emitters are comparable. The bandwidth exceeds 4.5 THz and the spectral roll-off is essentially equal for both emitter types. (see Fig. 4 (b) of publication [I]).

The significantly higher THz power of the undoped InGaAs/InAlAs MQWs is attributed to an increased mobility in the InGaAs layers. An electron mobility higher than 2000 $cm^2V^{-1}s^{-1}$ was measured for the undoped MQWs whereas the electron mobility of typical LTG materials is in the range of 200 $cm^2V^{-1}s^{-1}$ [94], [III]. The mobility increase was enabled by moving the trapping defects from the InGaAs to the adjacent InAlAs layers. Moreover, these results underline that the generation of broadband THz pulses is not essentially determined by the carrier lifetime in the photoconductive material. In agreement with the findings of Tani and coworkers [39], the results of publication [I] show that photoconductors with an electron lifetime of several tens of picoseconds allow for the generation of broadband THz pulses.

The combination of undoped InGaAs/InAlAs emitters and Be-doped LTG-InGaAs/InAlAs MQWs (see Sec. 3) enabled all fiber-coupled THz spectrometers with a bandwidth of up to 6 THz and a peak dynamic range above 90 dB [43], which is the state-of-the-art in commercially available THz-TDS systems. However, the comparison of THz-TDS systems from different manufactures remains a challenging task since these systems are commonly characterized by the dynamic range at certain frequencies, which depends on the experimental geometry, the measurement speed and the precision of the optical delay line. Hence, the dynamic range is not only determined by the performance of the photoconductive antennas such that additional parameters are required for an independent characterization.

[2] Due to the electron lifetime in the range of several tens of picoseconds, the material is inappropriate as a THz receiver. Tani and coworker compared SI-GaAs and LT-GaAs as a photoconductive receiver for the illumination with 800 nm radiation and found that the long carrier lifetime of SI-GaAs increased the receiver noise significantly compared to LT-GaAs receivers [122]. In analogy to the results presented by Tani and coworkers we found the same behavior for the undoped InGaAs/InAlAs MQWs.

In order to enable the direct comparison of the generated THz power of photoconductive emitters, we demonstrated, to the best of our knowledge, the first calibrated absolute power measurement of photoconductive emitters for THz-TDS [IV]. These experiments were conducted with a novel pyroelectric thin-film detector, which was developed by Sensor- und Lasertechnik (SLT) and calibrated to a national standard by the German national metrology institute (Physikalisch-Technische Bundesanstalt, PTB). Due to a spectrally flat absorption from 100 GHz to 5 THz and a power sensitivity down to 1 µW, these detectors are well suited for absolute power measurements of photoconductive THz emitters [103]–[106].

In publication [IV], the THz output of a fiber-coupled emitter fabricated from an undoped InGaAs/InAlAs MQW structure grown at 375 °C comprising 100 periods of 12 nm InGaAs and 16 nm InAlAs layers was analyzed. First, the predicted spectrally flat absorption of the pyroelectric thin-film detector was verified by THz transmission measurements. The pyroelectric detector was set in the focal point of a THz transmission setup, consisting of four 90 ° off-axis parabolic mirrors with a focal length of 3-inch. A fiber-coupled THz emitter module, containing the above mentioned photoconductive material and a fiber-coupled THz receiver containing a Be-doped LTG-InGaAs/InAlAs receiver antenna, were operated together with a commercially available THz-system [43]. The average optical power at the emitter and the detector was 20 mW and the bias voltage of the emitter was set to 120 V. The measurements were performed under nitrogen purge in order to eliminate water vapor absorption from the THz spectrum. The lower panel of Fig. 4.4 shows the THz power spectra calculated by Fast Fourier Transformation (FFT). The light blue line indicates the transmission through the pyroelectric thin-film and the black line serves as the reference spectrum acquired without any sample inside the THz beam path.

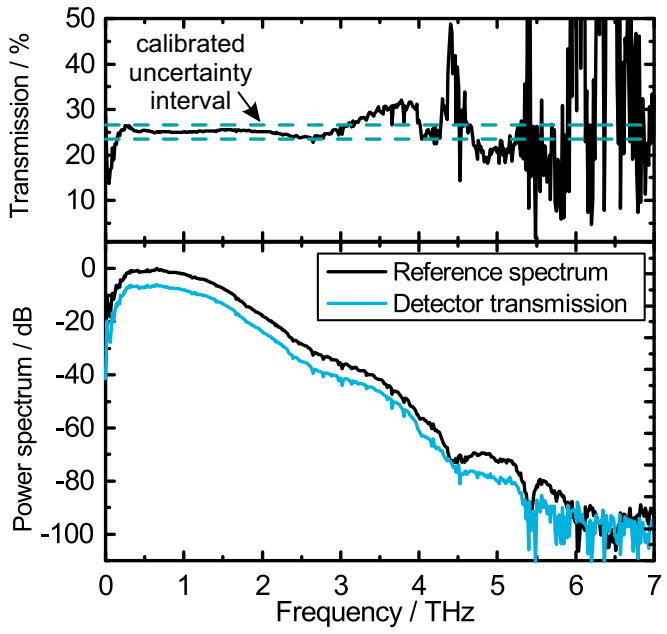

Fig. 4.4. Results of the THz transmission experiments on the pyroelectric thin-film. The power spectra (lower panel) were calculated via fast Fourier transformation (FFT) of the corresponding THz pulses. The light-blue line shows is the signal transmitted through the pyroelectric film and the black line serves as the reference spectrum without any sample in the THz beam path. Measurements were performed under dry nitrogen purge. The spectra are normalized to the maximum of the reference spectrum. The THz transmission (upper panel) is the quotient of the transmitted and the reference spectrum. By design, the transmission is supposed to measure 25 % in units of power. The dashed green lines indicate the uncertainty interval derived from the detector calibration. This figure is based on Fig. 2 from publication [IV].

The broadband THz emission of the photoconductive emitter with a bandwidth of more than 5 THz can be clearly seen. By design, the transmission through the pyroelectric thin-film measures 25 % in units of power, since 25 % of the incoming THz radiation is reflected at the surface of the thin-film and 50 % is absorbed by the material itself [103]. In order to verify the 25 % transmission, the ratio of the detector transmission and the reference spectrum was calculated and plotted in the upper panel of Fig. 4.4. Here, the dashed green lines indicate the uncertainty interval derived from the calibration uncertainty of the pyroelectric detector (see publication [IV]). From 100 GHz to 3.2 THz the transmission amounts to 25 % ± 1.6 %, which is clearly inside the calibrated uncertainty. For higher frequencies, artefacts originating from residual water vapor absorption lead to a deviation from the 25 % transmission. Nevertheless, these results verify the spectral flatness of the pyroelectric thin-film for the frequency interval, in which the highest THz power is generated by the emitter.

Next, the calibrated absolute THz power emitted by the fiber-coupled emitter was measured. In order to ensure that the detector signal exclusively stems from the emitted THz radiation, possible sources of unwanted signals were systematically ruled out. The details of these measures are explained extensively in publication [IV]. The absolute THz power calculated from the calibrated sensitivity of the pyroelectric detector (160 V/W ± 10 V/W) is plotted as a function of the applied bias voltage and the optical power at the emitter in Fig. 4.5 (a) and (b), respectively. In Fig. 4.5 (a) the THz power increases from below 1 µW at 30 V bias to more than 70 µW at 120 V bias voltage. For an optical illumination power above 30 mW the emitted THz power exceeds 0.1 mW (see Fig. 4.5 (b)). This corresponds to an optical-to-THz conversion efficiency of 0.33%.

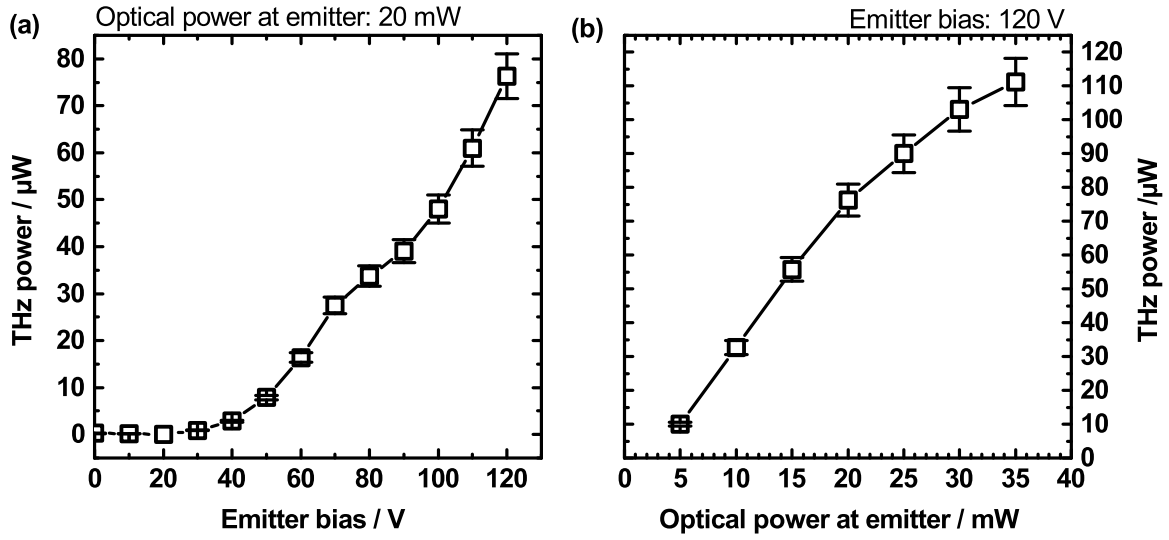

Fig. 4.5. (a) Calibrated THz power as a function of the bias voltage and (b) the optical illumination power at the fiber-coupled THz emitter. Error bars were calculated from the calibrated sensitivity of the pyroelectric detector measuring 160 V/W ± 10 V/W. This figure is based on Fig. 5 from publication [IV].

In conclusion, it was demonstrated that broadband THz pulses with an average power of up to $112\,\mu W \pm 7\,\mu W$ can be generated by THz emitters fabricated from undoped LTG-InGaAs/InAlAs MQW structures grown at temperatures close to 375 °C in an MBE. This material exploits the spatial separation of THz generation and carrier trapping. Inside the high-mobility InGaAs layers, photoexcited carriers are efficiently accelerated leading to the emission of strong THz pulses. The carrier trapping and recombination occurs inside the adjacent InAlAs layers, which contain deep-level defects caused by nonstoichiometric alloying at temperatures around 375 °C [95], [96], [98]. These emitters are one of the key components in state-of-the-art THz-TDS systems [43], [101].

5 Integrated THz transceiver

In the two previous sections the photoconductive materials for emitters and detectors in THz-TDS were optimized separately. Be-doped LTG-InGaAs/InAlAs MQWs with electron lifetimes between 140 fs – 500 fs served as broadband THz receivers with a bandwidth of 6 THz and a maximum dynamic range exceeding 90 dB (see Fig. 3.2). Undoped InGaAs/InAlAs grown by MBE at substrate temperatures between 375 °C and 400 °C was used as a photoconductive emitter of broadband THz pulses with a calibrated power of up to 112 µW ± 7 µW (see Fig. 4.5).

However, most of the applications of THz-TDS in fields like non-destructive testing (NDT) and in-line process monitoring allow only one-side access to the sample under test, which requires measurements in reflection geometry. When individual THz emitters and detectors are employed for these measurements, either an angled THz beam path or a THz beam splitter is required. Both concepts lead to bulky and complex setups. Therefore, an integrated THz device, i.e. a THz transceiver, which combines THz emitter and detector on the same photoconductive chip, is highly desired. On the one hand, the transceiver would enable reflection measurements under normal incidence to the sample surface, which reduces the complexity of the THz beam path. On the other hand, the size of the sensor head could be significantly downscaled allowing for compact and ready-to-use devices.

THz transceivers were investigated for the first time in the year 2000 by Tani and coworkers [107]. The authors employed a single photoconductive dipole-antenna, made of LTG-GaAs, for the generation and the detection of THz radiation suitable for THz reflection measurements under normal incidence to the sample surface. Since then, THz transceivers have been studied by several research groups and the investigated transceiver concepts can be divided into two groups:

- Transceivers employing the same photoconductive gap for THz emission and detection [107]–[109].
- Transceivers comprising spatially separated photoconductive antennas for THz emission and THz detection, which are arranged in close proximity to one another on the same chip [110], [111].

The main advantage of the first concept is that only a single photoconductive gap has to be illuminated by the femtosecond laser. This allows for a rather simple optical (fiber) coupling. However, the bias voltage, which is required to drive the THz-emitter, and the residual carriers originating from the optical excitation of the emitter, increase the noise of the THz receiver.

Therefore, the maximum dynamic range obtained with this transceiver concept was limited to 50 dB and the highest bandwidth measured 2 THz only [107]–[109].

This unwanted crosstalk is significantly reduced by the second concept, where emitter and detector are spatially separated. The challenge of this approach is the optical coupling of the individual photoconductive gaps. Since the diameter of a stripped single-mode fiber measures typically 125 µm, the spatial separation of emitter and detector on the transceiver is predetermined by this value, when the fibers are directly attached to the chip. In THz-TDS, the emitted THz pulse contains frequencies from 100 GHz – 6 THz, which corresponds to wavelengths between 50 µm – 3000 µm. When the spatial separation of emitter and detector on a transceiver chip is within this wavelength range, distortions of the THz pulse and unwanted resonances in the THz spectrum decrease the performance of the transceiver [110]. In previous studies, THz transceivers with a spatial separation of emitter and detector around 500 µm [110] and 250 µm [111] showed a bandwidth of 2 THz and a peak dynamic range of 40 dB. Since individual photoconductive antennas feature a bandwidth of up to 6 THz and a peak dynamic range exceeding 90 dB, the capability of THz transceivers has to be significantly improved for competitive performance.

In order to overcome the aforementioned limitations a photoconductive transceiver chip was designed, on which the emitter and the detector are separated by 45 µm only (see publication [VII]). The optical fiber coupling was enabled by employing a polymer waveguide chip, which reduced the spacing of two polarization maintaining fibers from 500 µm at the front facet of the waveguide chip to 45 µm at the rear facet (see Fig. 5.1 (b)). The transceiver chip was attached to a hyper-hemispheric high-resistivity float zone (HRFZ) silicon lens, butt-coupled to the polymer chip, and integrated into a cylindrical housing with a diameter of 25 mm. With a bandwidth of 4.5 THz and a peak dynamic range higher than 70 dB, this transceiver concept is a significant improvement compared to all results published previously [107]–[111].

Since the transceiver combines an emitter and a detector on the same chip, a photoconductor suitable for the emission *and* the detection of THz radiation had to be employed. For this purpose, the most important material property is the electron lifetime. For THz receivers, a sub-picosecond electron lifetime is the prerequisite for the detection of broadband THz pulses (see Sec. 3). In contrast, undoped InGaAs/InAlAs with a lifetime of several tens of picoseconds allowed for significantly higher THz powers compared to photoconductors with ultrashort lifetimes (see Sec. 4). However, in case of a THz transceiver a sub-picosecond lifetime is beneficial for both THz emitters and receivers. Due to the close proximity of emitter and detector on the transceiver chip, long-living carriers are a potential source of low-frequency radiation, which increases the receiver noise. Therefore, the transceiver chip studied in publication [VII] was fabricated from LTG-grown Be-doped InGaAs/InAlAs.

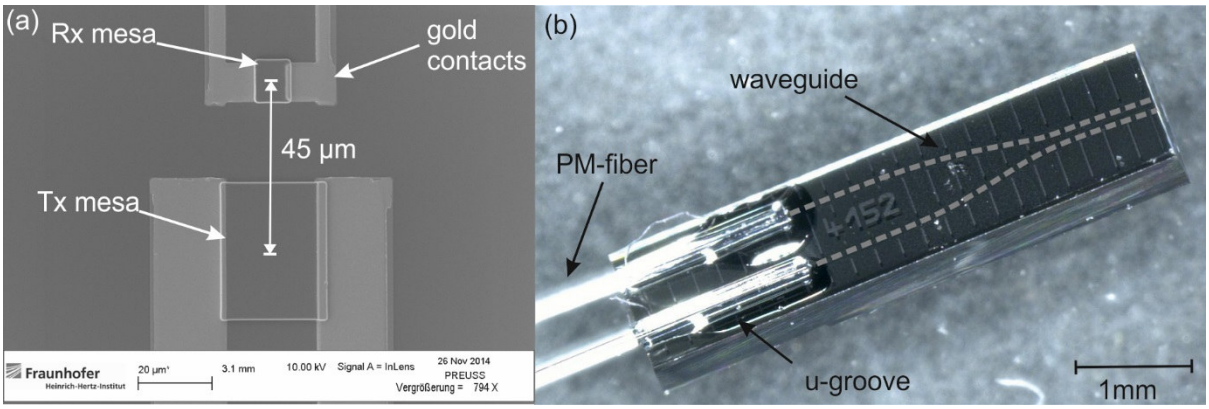

Fig. 5.1. (a) Scanning electron micrograph of the transceiver chip. The emitter (Tx) and detector (Rx) mesa comprise an active area of 25 µm × 40 µm and 10 µm × 15 µm, respectively. The distance between Rx and Tx measures 45 µm. (b) Optical micrograph of the polymer waveguide chip. Two stripped PM-fibers with a diameter of 125 µm are mounted in two u-grooves with a pitch of 500 µm. Optical waveguides lead from the tip of each u-groove to the facet of the chip and reduce the distance between the optical beams from 500 µm to 45 µm. For the optical coupling, the polymer waveguide chip is butt-coupled to the transceiver. This figure is based on Fig. 1 from publication [VII].

The photoconductor comprised an (unsaturated) electron lifetime of 0.5 ps, which was verified by transient differential transmission measurements (see Sec. 2.2.1). The emitter and the detector gap of the transceiver were mesa structured by chemically assisted ion beam etching (CAIBE) [29] and measured 25 µm × 40 µm and 10 µm × 15 µm, respectively. A scanning electron micrograph of the transceiver chip is shown in Fig. 5.1 (a). The receiver comprises a dipole antenna with a dipole length of 25 µm, whereas the emitter is contacted by a strip-line antenna. An optical micrograph of the polymer waveguide chip is depicted in Fig. 5.1 (b). The waveguides, which were lithographically structured into the polymer, are highlighted by dashed lines. The total size of the chip is 4 mm × 1 mm. Details about the polymer and the design of the fiber-coupled module can be found in Ref. [112] and publication [VII]. The fiber-coupled THz transceiver was operated in a THz reflection setup consisting of a 90 ° off-axis parabolic mirror in order to collimate the emitted THz beam and a plane, gold-coated mirror. The total length of the THz path was 15 cm and the measurements were conducted in ambient air. The average optical power at the emitter and the detector was set to 20 mW and the emitter was biased with a constant voltage of 35 V. The signal acquisition and the THz-TDS system are described in detail in Sec. 2.2.2. Fig. 5.2 (a) is an excerpt of the detected pulse trace. One observes a pronounced peak and subsequent undulation due to the water vapor absorption of the ambient air. In particular, features of increased cross-talk between the emitter and the detector are not observed. The corresponding power spectrum with a bandwidth exceeding 4.5 THz and a peak dynamic range higher than 70 dB is shown in Fig. 5.2 (b).

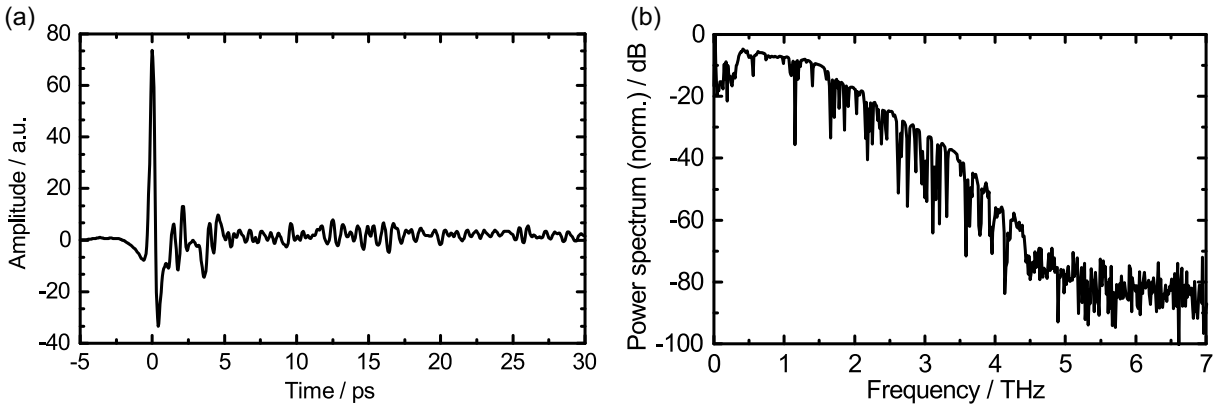

Fig. 5.2. (a) Pulse trace and (b) corresponding FFT spectrum detected with the fiber-coupled THz transceiver in reflection geometry. The emitter and detector mesa of the transceiver were illuminated with 20 mW of average optical power. The emitter bias measured 35 V. The THz optics comprised a 90 ° off-axis parabolic mirror for the collimation of the THz beam and a plane, gold-coated mirror as the reflector. The total path length measured 15 cm. The pulse trace shown in (a) is an average of 1000 individual pulse traces. The total acquisition time was 60 s. This plot is based on Fig. 2 of publication [VII].

In addition to the operation of the transceiver in THz-TDS, the radiation pattern of the THz transceiver was compared to the radiation pattern of an individual fiber-coupled emitter in publication [VII]. Very similar radiation patterns were obtained, which underlines that the spatial separation of the emitter and the detector on the transceiver chip does not distort the emitted THz beam. Details of these measurements can be found in publication [VII].

In conclusion, the demonstrated transceiver concept is a versatile tool for THz reflection measurements. Due to the optical fiber coupling it is directly compatible to commercially available THz-TDS systems. A bandwidth of 4.5 THz together with a peak dynamic range of more than 70 dB are the highest values reported for integrated THz transceivers so far.

Although this fiber-coupled transceiver is a great improvement of previously suggested transceiver concepts, the employed photoconductor is an essential compromise. By using Be-doped LTG-InGaAs/InAlAs the main attention was laid on a sub-picosecond electron lifetime, in order to reduce the crosstalk between the emitter and the detector. However, the results of Sec. 4 indicate that the emitted THz power of optimized photoconductive emitters can be significantly higher than the THz power generated in Be-doped LTG-InGaAs/InAlAs. Therefore, a single photoconductor with a performance competitive to individual THz emitters and detectors is required, in order to close the performance gap between the THz transceiver and individual devices. In the following section it is shown that iron doped InGaAs grown by MBE at temperatures close to 400 °C combines the properties of high power emitters and broadband THz detectors in the same photoconductor. Hence, this material is extremely useful for the development of future THz transceivers.

6 THz Emitters and detectors made of iron doped InGaAs

In Sec. 5, fiber-coupled THz transceivers comprising spatially separated emitter and detector mesas on a single photoconductive chip were demonstrated as a versatile device for THz reflection measurements. Due to the compact design as well as the simple THz beam path these transceivers bear great potential to replace discrete emitter and detector devices. In addition, compact and easy-to-use sensor heads may permit novel THz applications in the future.

However, the main drawback of the transceiver presented in Sec. 5 is the photoconductive material. In Sec. 4 it was shown that the emitted THz power of an optimized photoconductive emitter can be up to a factor of 100 higher than the THz power of Be-doped LTG-InGaAs/InAlAs emitters employed for the transceiver. Hence, photoconductors for THz transceivers with competitive performance to individual emitters *and* detectors have to combine the following properties in a single material:

- ❒ High resistivity in order to apply high bias fields at the emitter
- ❒ High electron mobility for efficient THz generation and detection
- ❒ Sub-picosecond electron lifetime for a broadband THz receiver and low crosstalk

Prior to this thesis, a single photoconductive material that is both sensitive to 1550 nm excitation and that combines all the aforementioned properties was not identified.

In publication [VIII] we demonstrated that iron doped InGaAs (InGaAs:Fe) grown by MBE at temperatures around 400 °C fulfills the desired properties far better than any other photoconductor presented to date. A Hall resistivity higher than 2 kΩ cm, a Hall mobility of almost 1000 $cm^2V^{-1}s^{-1}$ and an (unsaturated) electron lifetime of 0.3 ps was obtained for InGaAs:Fe. Thus, this photoconductor combines the sub-picosecond electron lifetime of the optimized receiver material presented in Sec. 3 with the high resistivity and the high mobility of the optimized emitters (see Sec. 4). Consequently, Fe-doped InGaAs showed competitive performance to state-of-the art photoconductive emitters *and* detectors in THz-TDS. A THz power up to 75 µW ± 5 µW was measured for InGaAs:Fe emitters and THz pulses with a bandwidth of up to 5.5 THz and a peak-dynamic range higher than 90 dB were detected by InGaAs:Fe receivers. Therefore, this material bears great potential for future integrated THz devices. In the remainder of this section the key results are summarized. The extensive discussion can be found in publication [VIII].

6.1 Previous results on InGaAs:Fe

In the last decades, iron doping of InGaAs has been studied by several groups. Due to shallow impurities, as-grown InGaAs is n-conductive with a residual electron concentration around 10^{15} cm^{-3} [66]. Since Fe dopants form mid-bandgap acceptors in InGaAs, iron doping is a well-established technique for obtaining semi-insulating InGaAs layers [113]–[116]. The activation energy of substitutional iron in InGaAs is well known and measures $E_A = 0.35\text{eV} \pm 0.02$ eV, which is almost mid-bandgap [115]–[117].

The first application of iron implanted InGaAs as a THz photoconductor was published by Suzuki and coworkers in 2005. The authors fabricated a detector antenna, sensitive to the excitation with 1.56 µm femtosecond lasers, and demonstrated THz pulses with a bandwidth of 2 THz [22]. In 2010 and 2011, iron doped InGaAs grown by metal-organic vapor phase epitaxy (MOVPE) was applied as a THz emitter and detector, respectively [23], [24]. A resistivity of several kΩ cm and a bandwidth of up to 2.5 THz were reported. In addition, the authors found that samples with a lower Fe doping concentration showed superior performance as THz photoconductor than samples with higher doping. These results were explained by the compensatory effect of iron dopants in MOVPE grown InGaAs. Since iron serves as a deep acceptor, the conductivity of the material changes from n-type to p-type, when the residual electron concentration is entirely compensated by the Fe dopants. In agreement with the modelling of Tell and coworkers [115], the authors of Ref. [24] and Ref. [23] observed the transition from n-type to p-type InGaAs for Fe doping concentrations between 10^{17} cm^{-3} – 10^{18} cm^{-3}. Therefore, doping levels slightly below 10^{17} cm^{-3} led to the highest resistivity in MOVPE-grown InGaAs:Fe and, therefore, the best performance as a THz photoconductor.

In publication [VIII] it is shown that Fe-doped InGaAs grown by MBE at temperatures close to 400 °C has essentially different electrical and optical properties than those reported for Fe-doped InGaAs grown by MOVPE at temperatures around 650 °C – 680 °C [23], [24]. These results are attributed to different kinetics at the substrate surface due to the lower growth temperature in the MBE. The main findings of this investigation are summarized in the next subsections.

6.2 Electrical properties

In publication [VIII], InGaAs samples with nominal Fe-doping concentrations between 3×10^{16} cm^{-3} and 5×10^{20} cm^{-3} were investigated. The layer structure of the samples comprised a nominally undoped 700 nm-InAlAs buffer layer, which was grown on top of a 2-inch, 350 µm thick, semi-insulating InP:Fe substrate. The homogenously doped InGaAs:Fe layers with a thickness of 1.0 µm - 1.2 µm were grown on top of the InAlAs buffer.

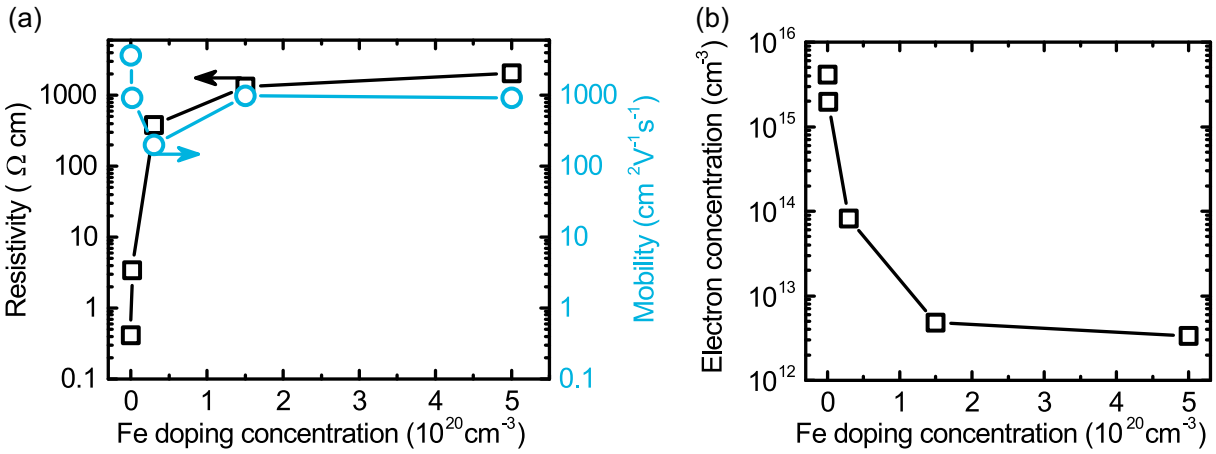

Fig. 6.1. (a) Resistivity, mobility, (b) and residual carrier concentration determined by room-temperature Hall measurements as a function of the Fe doping concentration. Note that the conductivity is electron-like even for doping concentrations above 10^{20} cm^{-3}.

The growth temperature was set between 350 °C - 450 °C. All samples were single-crystal with sharp and clearly resolved peaks in the XRD rocking curves. In interference contrast microscopy a slightly rough surface was observed for all samples whereas the roughness did not increase for higher Fe doping. The nominal doping concentrations were verified by Secondary Ion Mass Spectroscopy (SIMS). The doping profile was homogenous inside the InGaAs layer with a sharp drop at the interface to the undoped InAlAs buffer (see Fig. 1 in publication [VIII]).

The electrical properties of the samples were determined by room temperature hall measurements and are summarized in Table 6.1. The Hall resistivity and the Hall mobility are shown as a function of the Fe doping concentration Fig. 6.1 (a). The resistivity increases from values below 1 Ωcm for the undoped InGaAs samples to 2038 Ω cm for the

Table 6.1 Growth temperature (Tg), doping concentration (cFe), residual electron concentration (nHall) and resistivity (ρ) of the iron doped InGaAs samples. The doping concentration was determined by secondary ion mass spectroscopy measurements and corresponds to the total density of Fe dopants.

Sample name	T_G (°C)	c_{Fe} (cm^{-3})	n_{Hall} (cm^{-3})	ρ (Ω cm)
Fe5e20	350	5.0×10^{20}	3.4×10^{12}	2038.0
Fe2e20	400	1.5×10^{20}	4.8×10^{12}	1328.0
Fe3e19	400	3.0×10^{19}	8.2×10^{13}	379.0
Fe1e18	450	1.0×10^{18}	2.0×10^{15}	3.0
undoped	350	n.i.d.	4.0×10^{15}	0.4

highest Fe doping concentration (5×10^{20} cm^{-3}). This is a huge contrast to the results obtained for MOVPE grown InGaAs:Fe. In the latter case, the resistivity decreased for doping concentrations above 10^{17} cm^{-3}.

The mobility in Fig. 6.1 (a) decreases from values above 4000 cm^{2}V^{-1}s^{-1} of the undoped InGaAs to 918 cm^{2}V^{-1}s^{-1} for a doping concentration of 5×10^{20} cm^{-3}, which is a comparably high mobility for doping densities in the range of 10^{20} cm^{-3}. In Fig. 6.1 (b) the residual electron concentration is plotted as a function of the Fe doping concentration. Here, the large difference between MOVPE and MBE grown InGaAs:Fe is clearly observable. The conductivity type of the MBE grown samples remains electron-like for all doping concentrations. In particular, the residual electron concentration of the highest doped samples measures 3.4×10^{12} cm^{-3}, which is close to the intrinsic value of InGaAs at room temperature (6.7×10^{17} cm^{-3}). Hence, the concentration of electrically active dopants in MBE grown InGaAs is below 10^{17} cm^{-3}, even at Fe doping concentrations above 10^{20} cm^{-3}. Higher concentrations of electrically active dopants would result in p-conductive material, which is not observed (see Ref. [115]). The remaining Fe dopants are electrically inactive forming interstitials or clusters.

In order to determine the activation energy of the electrically active Fe dopants, temperature dependent Hall measurements between 300 K and 400 K were performed. The residual electron concentration of sample Fe3e19 is shown as an Arrhenius plot in Fig. 6.2 The activation energy $E_A = 0.33$ eV is determined by assuming an uncompensated material such that the relation $n \propto \exp(E_A/(2k_BT))$ can be employed [118]. These results agree well with the activation energy of substitutional iron dopants in InGaAs determined in previous studies [115]–[117]. Hence, the electrically active dopant is indeed the substitutional iron.

In analogy to the annealing experiments presented in Sec. 3.4, the thermal stability of the Fe doped samples was studied by ex-situ annealing at 550 °C and 600 °C in an MOVPE system under arsenic and phosphorous atmosphere. In room-temperature Hall measurements no essential changes of the electrical properties before and after annealing were observed. The blue circles in Fig. 6.2 show the Arrhenius plot of the residual electron concentration of the 600 °C-annealed sample. One clearly observes that the unannealed and the annealed samples feature the same residual carrier concentrations and the same activation energy. Hence, the iron dopants in MBE grown InGaAs:Fe occupy thermally stable positions in the lattice.

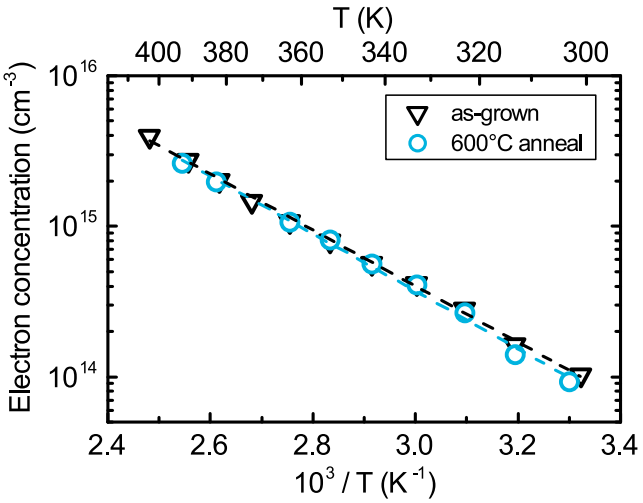

Fig. 6.2. Residual electron concentration determined by Hall measurements as a function of the inverse temperature in the range between 300 °C and 400 °C. Black triangles correspond to an as-grown sample with nominally doping concentration of 3×10^{19}cm^{-3}. Blue circles denote the residual carrier concentration after annealing for 60 min. at 600 °C in an MOVPE system under As and P stabilized atmosphere. The dashed lines are linear fits to the data. An activation energy of $E_A = 0.33$ eV was calculated. This figure was adopted from publication [VIII].

6.3 Transient carrier dynamics

In this subsection the concentration of active trapping defects as well as the capture cross section of electrons and holes in MBE-grown InGaAs:Fe is determined. In analogy to the experiments discussed in detail in Sec. 3.3, pump power dependent differential transmission measurements with femtosecond pulses centered on 1550 nm were conducted. Details of the experimental setup are given in Sec. 2.2.1.

The procedure for extracting the relevant parameters from the experiments is analog to the procedure described in Sec. 3.3. A rate equation model was expanded in the *unsaturated regime*, the regime of *partial trap filling* and the *saturated regime*. The rate equations, which were used to describe the carrier dynamics in InGaAs:Fe, read:

$$\frac{dn}{dt} = G - \frac{n}{\tau_e}\left(1 - \frac{n_T}{N_T^0}\right) \tag{6.1}$$

$$\frac{dn_T}{dt} = \frac{n}{\tau_e}\left(1 - \frac{n_T}{N_T^0}\right) - \frac{n_T}{\tau_r}. \tag{6.2}$$

Here, the dynamic variables $n(t)$ and $n_T(t)$ denote the concentration of electrons in the conduction band of InGaAs and the occupation of trapping centers, respectively. It will be shown that the density of trapping centers is related to the concentration of Fe dopants. The remaining parameters in Eq. (6.1) and Eq. (6.2) are the electron lifetime τ_e, the total density of available trapping centers N_T^0, the electron-hole recombination time τ_r and the generation term G, accounting for the optical excitation of carriers by the pump pulse. For InGaAs:Fe samples only a single trapping defect is assumed, which simplifies the rate equations significantly as compared to Eqs. (3.1) - (3.4). The asymptotic analysis of Eqs. (6.1) - (6.2) was performed in direct analogy to the procedure presented in Sec. 3.3. The details can be found in publication [VIII]. In the following, the analytic expressions are directly compared with the experimental findings.

I. The unsaturated regime

In this regime, the concentration of available trapping centers exceeds the concentration of excited carriers such that $n(t)$ decays mono-exponentially with the time constant τ_e. In the experiment, the energy of the optical pump pulse was set to 2 pJ, corresponding to 5×10^{16} cm^{-3} of excited electrons. The transient DT-signals were recorded for samples with Fe doping concentrations of a) 5×10^{20} cm^{-3}, b) 2×10^{20} cm^{-3}, c) 3×10^{19} cm^{-3}, and d) 1×10^{18} cm^{-3}. The natural logarithm of the normalized signals is shown in Fig. 6.3 (a). As expected for the unsaturated regime signals a) and b) show an essentially mono-exponential decay. In particular, the signal decay is much faster for higher Fe doping concentrations, which indicates that the electron trapping is directly connected to the Fe doping of the samples. However, signals c) and d) corresponding to doping concentrations of 3×10^{19} cm^{-3} and 1×10^{18} cm^{-3} show explicit features of trap saturation: An initially fast decay followed by a second slower decaying component. This finding is unexpected since it indicates that not all Fe dopants serve as fast trapping centers in InGaAs:Fe. In order to quantify the percentage of active trapping centers the regime of partial trap filling was investigated.

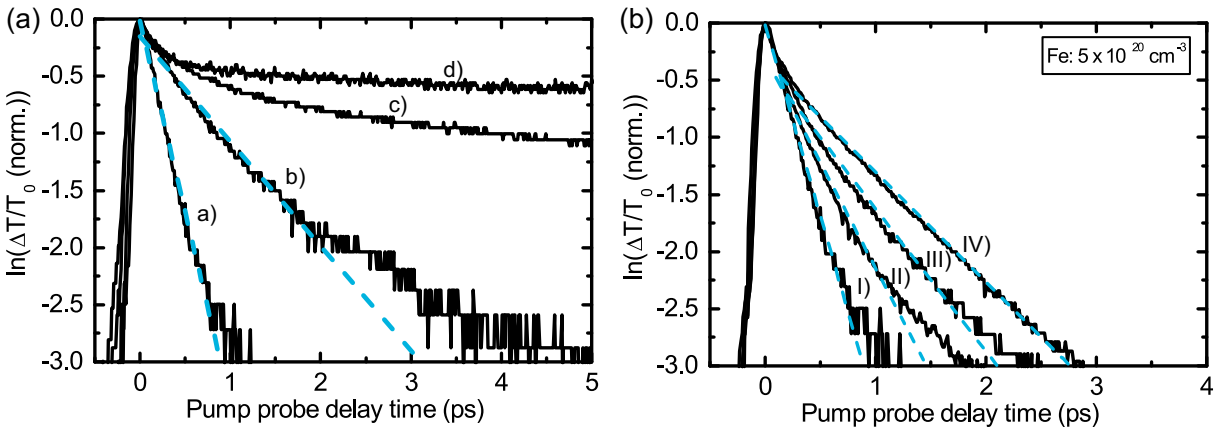

Fig. 6.3. (a) Natural logarithm of the differential transmission signal for samples Fe5e20 a), Fe2e20 b), Fe3e19 c) and Fe1e18 d) for an excited carrier density of 5×10^{16} cm^{-3}. Dashed blue lines are linear fits to the data. (b) Natural logarithm of the differential transmission signal of sample Fe5e20 for different carriers densities excited by the pump pulse: I) 5×10^{16} cm^{-3}, II) 5×10^{17} cm^{-3}, III) 1×10^{18} cm^{-3}, IV) 2×10^{18} cm^{-3}. Due to partial trap filling the signal decay time increases for higher excitation densities. Figures were taken from publication [VIII].

II. Partial trap filling

In the regime of partial trap filling, the density of excited carriers and available trapping centers have to be of the same magnitude. If this requirement is fulfilled the solution of Eqs. (6.1) – (6.2) can be written as (see Sec. 3.3 and publication [VIII]):

$$n(t) \approx n_{ex} \exp\left\{-\frac{t}{\tau_{pt}}\right\}, \tag{6.3}$$

where n_{ex} is the total density of optically excited electrons and τ_{pt} is a normalized decay time, reading $\tau_{pt} \equiv \tau_e(1 - n_{ex}/N_T^0)^{-1}$. Since τ_{pt} depends on the density of excited carriers n_{ex} and

the total density of trapping centers N_T^0 one can extract N_T^0 from two independent DT measurements with a different density of excited carriers n_{ex}. These measurements are shown exemplarily for sample Fe5e20 in Fig. 6.3 (b). The density of exited electrons measures I) 5×10^{16} cm^{-3}, II) 5×10^{17} cm^{-3}, III) 1×10^{18} cm^{-3}, and IV) 2×10^{18} cm^{-3}. As predicted by Eq. (6.3), the signal decay is mono-exponential. The dashed lines in Fig. 6.3 (b) are linear fits to the data. From the obtained normalized decay times τ_{pt} the total density of trapping centers in sample Fe5e20 was determined to $N_T^0 = (1.9 \pm 0.7) \times 10^{18}$ cm^{-3}. The uncertainty is obtained by averaging the values of N_T^0 of measurements II) - IV). Note that the calculated value of N_T^0 corresponds to a fraction of approx. 0.5 % of all Fe dopants in sample Fe5e20, which underlines that only a small fraction of all dopants serves as a trapping defect in InGaAs:Fe. The nature of the trapping defect could not be determined so far, since additional experiments like electron paramagnetic resonance (EPR) would be required. In the remainder of this work, it is assumed that the concentration of active trapping defects represents 0.5 % of all Fe dopants in the samples. This assumption allowed us to determine the capture cross section for electrons from the results obtained so far. Together with the Shockley-Read-Hall relation of carrier capture (see Eq. (3.6)) we calculated $\sigma_e = 3.8 \times 10^{-14}$ cm^2. This value is approximately two orders of magnitude higher than previously published results of iron in InGaAs, which can be directly explained by the fact that only 0.5 % of all Fe dopants serve as fast trapping centers.

III. The Saturated regime

In the saturated regime, the density of excited carriers exceeds the density of fast trapping centers by far, such that the electron dynamic in the conduction band $n(t)$ is completely determined by the recombination process of trapped electrons. Therefore, the relation $n(t) \propto \exp(-t/\tau_r)$ holds in the saturated regime (see publication [VIII]). The recombination lifetime τ_r, which can be interpreted as the hole trapping time, is determined by a mono-exponential fit to the saturation tail of the DT signals. In the experiments, this regime was induced by exciting 2×10^{18} cm^{-3} of electrons with the optical pump pulse. By fitting the saturation tail of each signal and evaluating the decay constant τ_r it could be shown that the recombination becomes faster for higher Fe doping concentrations. Thus, the recombination of trapped electrons occurs from defects related to the Fe dopants.

In conclusion, pump power dependent DT experiments were performed in order to show that Fe doped InGaAs grown by MBE features electron lifetimes as short as 0.3 ps. The measurements also revealed that approx. 0.5 % of all Fe dopants act as fast trapping centers in the material. Thus, doping concentrations of 10^{20} cm^{-3} were required in order to obtain sub-picosecond electron lifetimes in InGaAs, which is inevitable for broadband photoconductive THz detectors.

6.4 THz results

Due to the combination of high resistivity (≈ 2 kΩ cm), high mobility (> 900 $cm^2 V^{-1}s^{-1}$) and ultrashort carrier lifetime (< 1 ps) MBE grown InGaAs:Fe with doping concentrations in the range of 10^{20} cm^{-3} promises competitive THz performance to state-of-the-art photoconductive emitters *and* detectors. Thus, we compared photoconductive antennas fabricated from Fe-doped InGaAs to the specialized detectors and emitters described in Sec. 3 and Sec. 4, respectively.

6.4.1 THz emitters

The InGaAs:Fe based THz emitters were fabricated as mesa-structured [29], strip-line antennas with 25 µm wide gaps. The undoped InGaAs/InAlAs counterpart consists of a mesa-structured 100 µm-wide strip-line antenna, since the output power of these emitters is significantly higher for 100 µm wide gaps [I].

In Fig. 6.4 (a), the absolute THz power detected by a calibrated pyroelectric detector [103], [104] is plotted as a function of the bias voltage at the emitter. Black squares correspond to the InGaAs:Fe emitter and blue circles symbolize the undoped InGaAs/InAlAs material of Sec. 4. The data of the undoped InGaAs/InAlAs material is identical to Fig. 4.5 and publication [IV]. Note that the maximal THz power of the InGaAs:Fe emitter measures 75.6 µW ± 4.7 µW whereas the undoped InGaAs/InAlAs emitter emits 76.3 µW ± 4.8 µW. Thus, InGaAs:Fe is indeed competitive to the state-of-the-art THz emitters. Due to the combination of high mobility, high resistivity and sub-picosecond electron lifetime, the InGaAs:Fe emitter allows bias voltages up to 150 V, which corresponds to an electric bias field of 60 kV/cm. In contrast, the undoped InGaAs/InAlAs is commonly operated at 12 kV/cm in order to avoid any damage of the device. In InGaAs:Fe emitters the average current through the photoconductor is about a factor of 10 lower than in InGaAs/InAlAs based emitters. Since the main cause of device failure is the current through the photoconductor and the resulting Joule heating, the breakdown field of InGaAs:Fe emitters is significantly higher than the breakdown field of undoped InGaAs/InAlAs.

In addition to the absolute THz power, the bandwidth of the THz pulse generated by the two different emitters was compared. For this experiment, the emitters were operated in the THz-TDS setup described in Sec. 2.2.2. A fiber-coupled THz module comprising a Be-doped LTG-InGaAs/InAlAs photoconductive antenna served as the THz receiver. The optical excitation power at the emitter and the receiver measured 20 mW. In Fig. 6.4 (b), the power spectrum of the InGaAs:Fe emitter biased with 150 V is compared to the power spectrum of the undoped

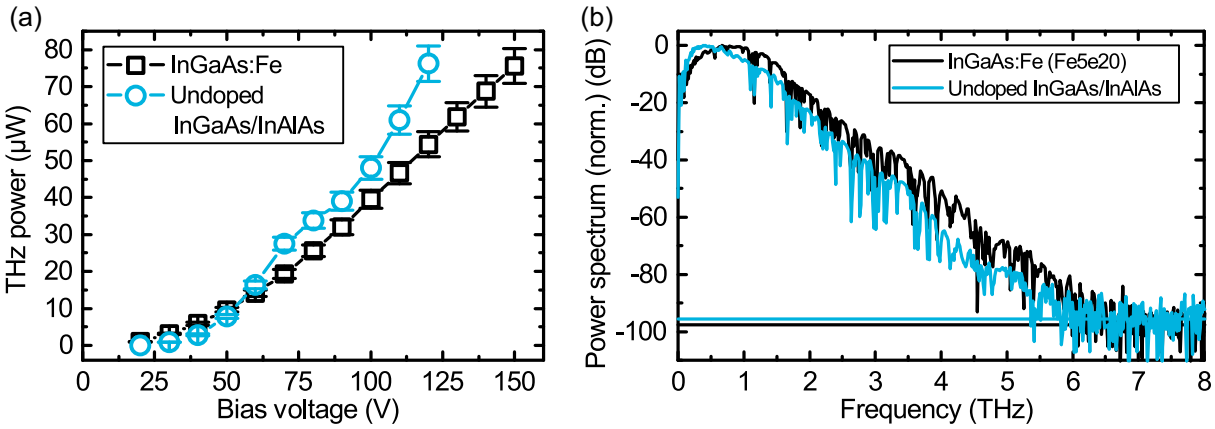

Fig. 6.4. (a) Absolute THz power detected by a calibrated pyroelectric detector as a function of the bias voltage for an InGaAs:Fe (blue squares) and a state-of-the-art photoconductive emitter (blue circles). (b) Comparison of the power spectra of the two different emitter materials. As receiver, a fiber-coupled THz module containing a Be-doped LTG InGaAs/InAlAs receiver was used. The optical power at the emitter and the receiver measured 20 mW, respectively. Both emitters were operated such that the emitted THz power was equal for both devices, i.e. the bias voltage of the InGaAs:Fe emitter measured 150 V whereas the undoped InGaAs/InAlAs emitter was biased with 120 V. The horizontal lines correspond to the spectral noise level, which was calculated by averaging the spectral amplitudes between 7.5 THz – 10 THz. Details of the experimental setup can be found in Sec. 2.2.2.

InGaAs/InAlAs emitter with 120 V bias. Under these conditions, the emitted THz power is identical for both emitters (see Fig. 6.4 (a)). Both spectra show a bandwidth of 6 THz with a peak dynamic range higher than 95 dB. However, the spectrum of the InGaAs:Fe emitter contains a larger amount of high frequency components than the corresponding undoped InGaAs/InAlAs emitter. In addition, the frequency with the highest spectral power is shifted towards higher frequencies for the InGaAs:Fe emitter. Note that the dynamic range in the interval from 1 THz – 5 THz is up to 10 dB higher compared to the state-of-the-art emitter. These results underline that InGaAs:Fe has the potential to replace the undoped InGaAs/InAlAs devices in fiber-coupled TDS systems operating at 1550 nm central wavelength.

6.4.2 THz receivers

The THz receiver antennas were structured as a $\lambda/2$-dipole with a dipole length of 25 µm and a 10 µm-wide photoconductive mesa. The THz-TDS setup described in Sec. 2.2.2 was used for the characterization. As emitter, a fiber-coupled THz module containing an undoped InGaAs/InAlAs MQW structure, described in Sec. 4 and publication [IV], was used. A THz receiver made of sample Fe5e20 was compared with a state-of-the-art THz receiver antenna consisting of Be-doped LTG-InGaAs/InAlAs. In Fig. 6.5 (a) the power spectrum detected by the respective receivers are plotted for an average illumination power of 20 mW. One clearly observes that the spectral bandwidth of both receiver materials exceeds 5.5 THz with a peak dynamic range higher than 90 dB. The sub-picosecond electron lifetime of both materials guarantees this broadband detection capability. In analogy to the emitter results presented in

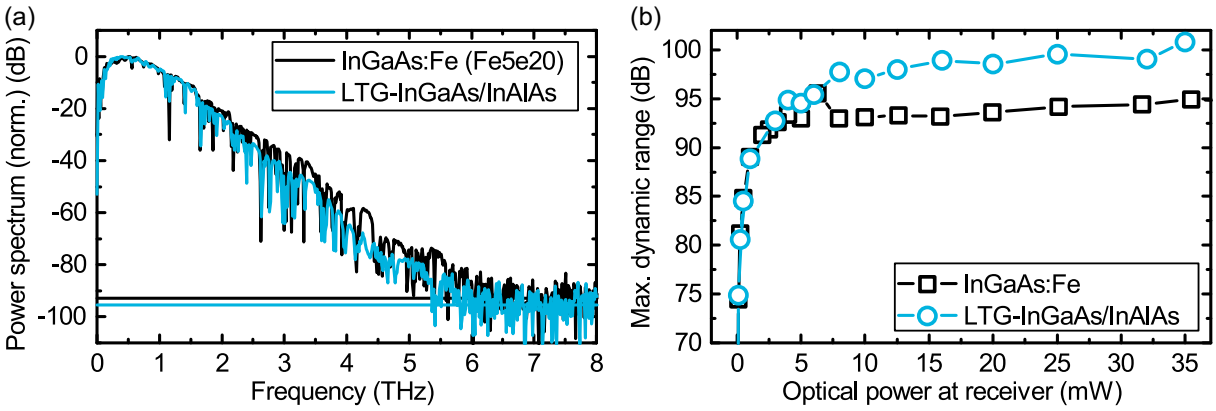

Fig. 6.5 (a) Normalized power spectrum calculated by FFT of the corresponding pulse traces for an InGaAs:Fe receiver (black) and a state-of-the-art photoconductive detector based on Be-doped LTG-InGaAs/InAlAs (blue). The horizontal lines indicate the noise level of the signals, obtained by averaging the spectral components between 7.5 THz – 10 THz. The detectors were illuminated with an average optical power of 20 mW. The fiber-coupled emitter was a state-of-the-art emitter presented in section 4 and publication [IV]. The operation conditions were V_b = 120 V and P_{opt} = 20 mW. The THz measurements were performed with the setup described in Sec. 2.2.2. (b) Maximum dynamic range of the two TDS-receivers as a function of the optical power at the receiver.

the last subsection, the spectrum of the InGaAs:Fe receiver contains a higher fraction of high frequency components: in the frequency interval between 2 THz and 5 THz the dynamic range of InGaAs:Fe is up to 10 dB higher than the dynamic range of the Be-doped LTG-InGaAs/InAlAs counterpart. The increased electron mobility and the higher Hall resistivity is assumed as one of the reasons for the superior performance of InGaAs:Fe photoconductive detectors. The high dark resistivity translates into a low noise-level (see publications [III], [VI]), whereas the mobility of almost 900 $cm^2V^{-1}s^{-1}$ allows for the efficient acceleration of carriers in the bias field of the incoming THz pulse. In Fig. 6.5 (b) the peak dynamic range of the two receiver materials is plotted as a function of the optical excitation power at the receiver. In both cases the peak dynamic range exceeds 90 dB for average optical powers between 5 mW and 35 mW. In combination with the superior spectral roll-off of the InGaAs:Fe receivers (see Fig. 6.5 (a)) these results underline the suitability of InGaAs:Fe THz receivers in future THz-TDS systems.

In conclusion, iron-doped InGaAs grown by MBE at temperatures close to 400 °C was investigated as a photoconductive emitter and detector in THz-TDS. Due to the unique combination of high mobility, high resistivity and ultra-short electron lifetime, this material shows competitive or even superior performance to specialized photoconductive emitter and receiver materials. InGaAs:Fe bears not only the potential to replace existing photoconductors in THz-TDS systems, it also paves the way for fully-competitive, integrated THz devices.

7 Summary and Outlook

In the present thesis, the physical properties of photoconductive terahertz (THz) antennas for the excitation with 1550 nm femtosecond laser pulses were investigated. The overall goal was the development of efficiency enhanced photoconductive emitters and detectors suitable for the integration into fully fiber-coupled THz-TDS systems. Thereby, the understanding of the underlying physical processes involved in the generation and detection of THz radiation in photoconductors as well as the analysis of the interplay between growth conditions, material properties and THz performance was the main objective. In the first part of this thesis two different material concepts for THz-photoconductors were developed and optimized: one being particularly designed as a receiver for pulsed THz systems and one optimized as an emitter. In the second part, a fiber-coupled THz-transceiver, containing the THz-emitter and detector on the same photoconductive chip, was developed. This integrated device is a promising concept for THz reflection measurements, which are one of the main applications of THz-TDS in industrial environments. In this context, iron doped-InGaAs was studied as a novel photoconductive material, which can be applied as THz-emitter and receiver. Therefore, it is a promising photoconductor for future integrated THz devices. In this section, the main results of this thesis are summarized and an outlook on possible future work is given.

Beryllium (Be) doped low-temperature grown (LTG) InGaAs/InAlAs was investigated as a photoconductive receiver in Sec. 3. The main focus was the description of the transient carrier dynamics after the optical excitation by a femtosecond laser pulse. By applying a rate equation model, which was expanded asymptotically in different limit cases, the role of the intentionally incorporated defects could be identified. It was found that optically excited electrons are trapped by ionized arsenic antisite defects (As_{Ga}^{+}) and recombine with holes trapped by ionized Be dopants. The density of the trapping and recombination centers can be precisely adjusted by the doping concentration and the duration and the temperature of a post-growth annealing step. With the help of time-resolved differential transmission measurements (see Sec. 2.2.1) it was further shown that annealing at temperatures above 500 °C reduces the density of fast trapping centers, which suggests the formation of arsenic precipitates. Previous investigations have not obtained unambiguous results on this topic. Carrier lifetimes as low as 140 fs were obtained for doping concentrations of 1.2×10^{19} cm^{-3} and annealing for 60 min. at 500 °C. Furthermore, the influence of the density of recombination centers in the material on the performance as a receiver in THz-TDS was studied. The frequency response as well as the noise of the receiver is strongly influenced by the density of recombination centers. The precise adjustment of all material parameters led to broadband receivers with a bandwidth of 6 THz and a peak dynamic range above 95 dB.

In Sec. 4, THz-emitters with spatially separated photoconductive and recombination regions were investigated. For this purpose, InGaAs was embedded into barriers of InAlAs grown at temperatures close to 400 °C in an MBE. In that temperature range, the photoconductive InGaAs layers are almost defect free, resulting in high carrier mobility, whereas the InAlAs contains deep-level defects, due to alloying. Time-resolved differential transmission experiments on samples with different InAlAs thickness revealed that the carrier recombination occurs indeed inside the InAlAs. In general, the carrier lifetime of this photoconductor measured 10 ps – 100 ps, which renders them inappropriate as THz receivers. However, in agreement with previous studies on long-lifetime photoconductors, the undoped InGaAs/InAlAs heterostructures were extremely efficient emitters. A radiated THz power as high as 112 µW ± 7 µW was detected with a calibrated pyroelectric detector, which is an increase by a factor of 100 compared to emitters made of LTG-InGaAs/InAlAs.

The optimized photoconductive emitter and receiver materials allowed for the development of compact THz-TDS systems with up to 6 THz bandwidth and more than 90 dB dynamic range.

The THz performance of an integrated transceiver with a bandwidth of 4.5 THz developed for THz reflection measurements was presented in Sec. 5. The transceiver comprised the THz emitter and receiver in a distance of only 45 µm on the same photoconductive chip. Due to the optical fiber coupling and a radiation pattern similar to individual THz emitters, this transceiver is directly compatible to commercially available THz-TDS systems. Therefore, it is a crucial step toward the application of THz-TDS in out-of-lab environments.

However, the THz photoconductor applied for this first transceiver was Be-doped LTG-InGaAs/InAlAs, originally developed for broadband THz receivers. Thus, the performance of THz-transceivers may be significantly increased by using a photoconductor, which is competitive to the optimized individual emitters *and* receivers. For this purpose, iron (Fe) doped InGaAs grown by MBE at temperatures close to 400 °C was studied. Homogenous Fe doping profiles with a concentration of up to 5×10^{20} cm^{-3} were obtained at these growth conditions. In contrast to iron doped InGaAs grown by MOVPE at temperatures around 650 °C, the MBE grown samples remain n-conductive even at the highest doping concentrations. The incorporation of iron into InGaAs was investigated in detail in Sec. 6. The relatively low growth temperature leads to modified incorporation properties in the MBE-grown material. A carrier lifetime of 300 fs combined with a Hall resistivity of 2 kΩ cm and a mobility of 918 cm^{2}V^{-1}s^{-1} was obtained for a Fe concentration of 5×10^{20} cm^{-3}. Applied as a photoconductive emitter, 75 µW ± 5 µW radiated THz power was measured. As a receiver, broadband THz pulses with up to 6 THz bandwidth and more than 90 dB dynamic range were detected. Thus, Fe-doped InGaAs is well suited for the application as THz-emitter and receiver and, therefore, bears great potential for the application in THz transceivers and similar integrated THz devices.

With regard to future work in the field of THz-TDS, the transceiver concept developed in this thesis may pave the way for novel applications of THz-TDS in out-of-lab environments. In particular, the Fe-doped InGaAs should be applied in fiber-coupled THz-transceivers, in order to increase the device performance. However, a THz transceiver is just the first step toward highly integrated THz devices. The combination of passive polymer components as optical waveguides or phase shifters and active THz photoconductors allows for the fabrication of THz emitter and detector arrays. On the emitter side, the array concept has the potential to enhance the output power of the device, which enables the measurement of absorptive materials. THz receiver arrays in combination with sophisticated image reconstruction algorithms have the potential for future high resolution THz imaging in NDT. Since polymer based devices become more and more prominent in many industrial fields, the demand for non-destructive inspection technologies will increase in the near future. Since THz-TDS is a contact-free measurement technique with a depth-resolution of several 10 µm it has great potential for applications in this field.

The photoconductive concepts investigated in this dissertation may also be applicable for continuous-wave (CW) THz-systems. State-of-the-art CW systems rely on a photodiode (PD) as the THz-emitter and a photoconductive THz-receiver [119]. Due to its unique properties InGaAs:Fe has the potential to replace the relatively complex PD-emitter. In contrast to pulsed THz-system, in which the high peak power and the dispersion of the exciting femtosecond laser pulse prevents the use of complex waveguide networks, the existing optical integration technology can be exploited immediately for CW THz-systems. Applications in field like THz-imaging, NDT and THz-communications are possible. Here, efficient photoconductors are the prerequisite for high performance CW-THz-systems.

Regarding novel photoconductive materials, transition metals like ruthenium (Ru) or rhodium (Rh) might serve as an efficient deep-level dopant in MBE-grown InGaAs. Previous studies on MOVPE grown InGaAs doped with these transition metals showed electrical properties superior to InGaAs:Fe [120], [121]. Hence, these dopants could further increase the bandwidth and the emitted THz power of future photoconductive antennas designed for the excitation with 1550 nm femtosecond pulses.

Publications

This thesis is a review of the following eight publications. The author's contributions to each of these publications are indicated below.

[I] R. J. B. Dietz, B. Globisch, M. Gerhard, A. Velauthapillai, D. Stanze, H. Roehle, M. Koch, T. Göbel, and M. Schell, "64 μW pulsed terahertz emission from growth optimized InGaAs/InAlAs heterostructures with separated photoconductive and trapping regions," Appl. Phys. Lett., vol. 103, no. 6, pp. 1–5, 2013.

- ❒ Most of the measurements together with R. J. B. Dietz
- ❒ Most of the data analysis together with R. J. B. Dietz
- ❒ Parts of the writing

[II] B. Globisch*, R. J. B. Dietz*, D. Stanze, T. Göbel, and M. Schell, "Carrier dynamics in Beryllium doped low-temperature-grown InGaAs/InAlAs," Appl. Phys. Lett., vol. 104, no. 17, 2014.

- ❒ All measurements
- ❒ Derivation of the rate equation model together with R. J. B. Dietz
- ❒ Most of the data analysis together with R. J. B. Dietz
- ❒ Most of the writing of the publication

* The authors contributed equally to the publication

[III] R. J. B. Dietz*, B. Globisch*, H. Roehle, D. Stanze, T. Göbel, and M. Schell, "Influence and adjustment of carrier lifetimes in InGaAs/InAlAs photoconductive pulsed terahertz detectors : 6 THz bandwidth and 90dB dynamic range," Opt. Express, vol. 22, no. 16, pp. 19411–19422, 2014.

- ❒ Parts of the measurements
- ❒ Data analysis together with R. J. B. Dietz
- ❒ Parts of the writing of the publication

* The authors contributed equally to the publication

[IV] B. Globisch, R. J. B. Dietz, T. Göbel, M. Schell, W. Bohmeyer, R. Müller, and A. Steiger, "Absolute terahertz power measurement of a time-domain spectroscopy system," Opt. Lett., vol. 40, no. 15, p. 3544, 2015.

- ❒ Design of the photoconductive THz emitter
- ❒ All measurements
- ❒ Data analysis
- ❒ Most of the writing of the publication

[V] S. Sawallich, B. Globisch, C. Matheisen, M. Nagel, R. J. B. Dietz, and T. Göbel, "Photoconductive Terahertz Near-Field Detectors for Operation With 1550-nm Pulsed Fiber Lasers," IEEE Trans. Terahertz Sci. Technol., vol. 6, no. 3, pp. 365–370, 2016.

- ❒ Design of the photoconductive material
- ❒ Measurements, data analysis and writing of the publication together with S. Sawallich

[VI] B. Globisch, R. J. B. Dietz, S. Nellen, T. Göbel, and M. Schell, "Terahertz detectors from Be-doped low-temperature grown InGaAs/InAlAs: Interplay of annealing and terahertz performance," AIP Advances, vol. 6, 125011, 2016.

- ❒ Design of the samples series
- ❒ Parts of the measurements
- ❒ Most of the data analysis and writing of the publication

[VII] B. Globisch, R. J. B. Dietz, R. B. Kohlhaas, S. Nellen, M. Kleinert, T. Göbel, and M. Schell, "Fiber-coupled transceiver for terahertz reflection measurements with a 4.5 THz bandwidth", Opt. Lett., vol. 41, no. 22, pp. 5262-5265, 2016.

- ❒ Design of the photoconductive material and the transceiver chip
- ❒ Design of the transceiver module
- ❒ Concept of the polymer waveguide coupler
- ❒ Most of the measurements, data analysis and writing of the publication

[VIII] B. Globisch, R. J. B. Dietz, R. B. Kohlhaas, T. Göbel, M. Schell, M. Semtsiv, D. Alcer and W. T. Masselink, "Iron doped InGaAs: Competitive THz emitters and detectors fabricated from the same photoconductor", J. Appl. Phys., vol. 121, 053102, 2017.

- ❒ Design of the samples series
- ❒ Parts of the measurements together with R. B. Kohlhaas
- ❒ Most of the data analysis
- ❒ Development of the rate equation model
- ❒ Most of the writing of the publication

Bibliography

[1] M. Czerny, "Über eine neue Form der Rubensschen Reststrahlenmethode," *Zeitschrift für Phys.*, vol. 16, pp. 321–331, 1923.

[2] W. Woltersdorff, "Über die optischen Konstanten dünner Metallschichten im langwelligen Ultrarot," *Zeitschrift für Phys.*, vol. 91, no. 3–4, pp. 230–252, 1934.

[3] A. Mitsuishi, "Progress in far-infrared spectroscopy: Approximately 1890 to 1970," *J. Infrared, Millimeter, Terahertz Waves*, vol. 35, pp. 243–281, 2014.

[4] D. H. Auston, K. P. Cheung, and P. R. Smith, "Picosecond photoconducting Hertzian dipoles," *Appl. Phys. Lett.*, vol. 45, no. 3, pp. 284–286, 1984.

[5] D. M. Mittleman, M. Gupta, R. Neelamani, R. G. Baraniuk, J. V. Rudd, and M. Koch, "Recent advances in terahertz imaging," *Appl. Phys. B Lasers Opt.*, vol. 68, pp. 1085–1094, 1999.

[6] B. S. Williams, "Terahertz quantum-cascade lasers," *Nat. Photonics*, vol. 1, pp. 517–525, 2007.

[7] D. M. Mittleman and R. A. Cheville, "Terahertz Generation and Applications," *Ultrafast Opt. Textb.*, pp. 1–58, 2008.

[8] S. Preu, G. H. Döhler, S. Malzer, L. J. Wang, and A. C. Gossard, "Tunable, continuous-wave Terahertz photomixer sources and applications," *J. Appl. Phys.*, vol. 109, no. 61301, 2011.

[9] P. U. Jepsen, D. G. Cooke, and M. Koch, "Terahertz spectroscopy and imaging - Modern techniques and applications," *Laser Photonics Rev.*, vol. 5, no. 1, pp. 124–166, 2011.

[10] K. Sakai, Ed., *Terahertz Optoelectronics*. Springer Berlin Heidelberg, 2005.

[11] C. A. Schmuttenmaer, "Exploring dynamics in the far infrared with terahertz spectroscopy," *Chem. Rev.*, vol. 104, pp. 1759–1780, 2004.

[12] R. Ulbricht, E. Hendry, J. Shan, T. F. Heinz, and M. Bonn, "Carrier dynamics in semiconductors studied with time-resolved terahertz spectroscopy," *Rev. Mod. Phys.*, vol. 83, pp. 543–586, 2011.

[13] C. Fattinger and D. Grischkowsky, "Terahertz beams," *Applied Physics Letters*, vol. 54, no. 6. pp. 490–492, 1989.

[14] M. Tonouchi, "Cutting-edge terahertz technology," *Nat. Photonics*, vol. 1, pp. 97–105, 2007.

[15] R. Huber, F. Tauser, A. Brodschelm, M. Bichler, G. Abstreiter, and A. Leitenstorfer, "How many-particle interactions develop after ultrafast excitation of an electron-hole plasma," *Nature*, vol. 414, no. 6861, pp. 286–289, 2001.

[16] R. Huber, C. Kübler, S. Tübel, A. Leitenstorfer, Q. T. Vu, H. Haug, F. Köhler, and M. C. Amann, "Femtosecond formation of coupled phonon-plasmon modes in InP: Ultrabroadband THz experiment and quantum kinetic theory," *Phys. Rev. Lett.*, vol. 94, p. 27401, 2005.

[17] D. M. Mittleman, Ed., *Sensing with Terahertz Radiation*. Springer-Verlag Berlin Heidelberg, 2003.

[18] T. Hochrein, "Markets, Availability, Notice, and Technical Performance of Terahertz Systems: Historic Development, Present, and Trends," *J. Infrared, Millimeter, Terahertz Waves*, vol. 36, no. 3, pp. 235–254, 2014.

[19] F. W. Smith, H. Q. Le, V. Diadiuk, M. A. Hollis, A. R. Calawa, S. Gupta, M. Frankel, D. R. Dykaar, G. A. Mourou, and T. Y. Hsiang, "Picosecond GaAs-based photoconductive optoelectronic detectors," *Appl. Phys. Lett.*, vol. 54, pp. 890–892, 1989.

[20] S. C. Warren, N. Katzenellenbogen, D. Grischkowsky, J. M. Woodall, M. R. Melloch, and N. Otsuka, "Subpicosecond, freely propagating electromagnetic pulse generation and detection using GaAs:As epilayers," *Appl. Phys. Lett.*, vol. 58, no. 14, p. 1512, 1991.

[21] A. Krotkus, "Semiconductors for terahertz photonics applications," *J. Phys. D. Appl. Phys.*, vol. 43, p. 273001, 2010.

[22] M. Suzuki and M. Tonouchi, "Fe-implanted InGaAs photoconductive terahertz detectors triggered by 1.56 μm femtosecond optical pulses," *Appl. Phys. Lett.*, vol. 86, no. 163504, 2005.

[23] O. Hatem, J. Cunningham, E. H. Linfield, C. D. Wood, A. G. Davies, P. J. Cannard, M. J. Robertson, and D. G. Moodie, "Terahertz-frequency photoconductive detectors fabricated from metal-organic chemical vapor deposition-grown Fe-doped InGaAs," *Appl. Phys. Lett.*, vol. 98, p. 121107, 2011.

[24] C. D. Wood, O. Hatem, J. E. Cunningham, E. H. Linfield, A. G. Davies, P. J. Cannard, M. J. Robertson, and D. G. Moodie, "Terahertz emission from metal-organic chemical vapor deposition grown Fe:InGaAs using 830 nm to 1.55 nm excitation," *Appl. Phys. Lett.*, vol. 96, p. 194104, 2010.

[25] A. Takazato, M. Kamakura, T. Matsui, J. Kitagawa, and Y. Kadoya, "Detection of terahertz waves using low-temperature-grown InGaAs with 1.56 μm pulse excitation," *Appl. Phys. Lett.*, vol. 90, p. 101119, 2007.

[26] A. Takazato, M. Kamakura, T. Matsui, J. Kitagawa, and Y. Kadoya, "Terahertz wave emission and detection using photoconductive antennas made on low-temperature-grown InGaAs with 1.56 μm pulse excitation," *Appl. Phys. Lett.*, vol. 91, p. 11102, 2007.

[27] H. Kuenzel, J. Boettcher, K. Biermann, H. Hensel, H. Roehle, and B. Sartorius, "Low temperature MBE-grown In (Ga, Al) As/InP structures for 1.55 μm THz photoconductive antenna applications," in *20th International Conference on Indium Phosphide and Related Materials (IPRM)*, 2008.

[28] B. Sartorius, H. Roehle, H. Künzel, J. Böttcher, M. Schlak, D. Stanze, H. Venghaus, and M. Schell, "All-fiber terahertz time-domain spectrometer operating at 1.5 microm

telecom wavelengths.," *Opt. Express*, vol. 16, no. 13, pp. 9565–9570, 2008.

[29] H. Roehle, R. J. B. Dietz, H. J. Hensel, J. Böttcher, H. Künzel, D. Stanze, M. Schell, and B. Sartorius, "Next generation 1.5µm terahertz antennas: mesa-structuring of InGaAs/InAlAs photoconductive layers.," *Opt. Express*, vol. 18, no. 3, pp. 2296–2301, 2010.

[30] A. Schwagmann, Z. Y. Zhao, F. Ospald, H. Lu, D. C. Driscoll, M. P. Hanson, A. C. Gossard, and J. H. Smet, "Terahertz emission characteristics of ErAs:InGaAs-based photoconductive antennas excited at 1.55 µm," *Appl. Phys. Lett.*, vol. 96, p. 141108, 2010.

[31] J. Sigmund, C. Sydlo, H. L. Hartnagel, N. Benker, H. Fuess, F. Rutz, T. Kleine-Ostmann, and M. Koch, "Structure investigation of low-temperature-grown GaAsSb, a material for photoconductive terahertz antennas," *Appl. Phys. Lett.*, vol. 87, p. 252103, 2005.

[32] R. J. B. Dietz, "Photoconductive THz emitters and detectors on the basis of InGaAs / InP for terahertz time domain spectroscopy," Philipps Universität Marburg, 2015.

[33] P. U. Jepsen, R. H. Jacobsen, and S. R. Keiding, "Generation and detection of terahertz pulses from biased semiconductor antennas," *J. Opt. Soc. Am. B*, vol. 13, no. 11, pp. 2424–2436, 1996.

[34] M. Tani, M. Herrmann, and K. Sakai, "Generation and detection of THz pulsed radiation with photoconductive antennas," *Meas. Sci. Technol.*, vol. 13, pp. 1739–1745, 2002.

[35] J. Shan and T. F. Heinz, "Terahertz radiation from semiconductors," in *Ultrafast Dynamical Processes in Semiconductors, Topics Appl. Phys.*, vol. 92, K.-T. Tsen, Ed. Berlin Heidelberg: Springer, 2004, pp. 1–59.

[36] P. U. Jepsen and S. R. Keiding, "Radiation patterns from lens-coupled terahertz antennas.," *Opt. Lett.*, vol. 20, no. 8, pp. 807–809, 1995.

[37] L. Duvillaret, F. Garet, J.-F. Roux, and J.-L. Coutaz, "Analytical Modeling and Optimization of Terahertz Time-Domain Spectroscopy Experiments, Using Photoswitches as Antennas," *IEEE J. Sel. Top. Quantum Electron.*, vol. 7, no. 4, pp. 615–623, 2001.

[38] P. U. Jepsen, J. K. Jensen, and U. Møller, "Characterization of aqueous alcohol solutions in bottles with THz reflection spectroscopy.," *Opt. Express*, vol. 16, no. 13, pp. 9318–9331, 2008.

[39] M. Tani, S. Matsuura, K. Sakai, and S. Nakashima, "Emission characteristics of photoconductive antennas based on low-temperature-grown GaAs and semi-insulating GaAs," *Appl. Opt.*, vol. 36, no. 30, pp. 7853–7859, 1997.

[40] R. H. Jacobsen, K. Birkelund, T. Holst, P. U. Jepsen, and S. R. Keiding, "Interpretation of photocurrent correlation measurements used for ultrafast photoconductive switch characterization," *J. Appl. Phys.*, vol. 79, no. 5, pp. 2649–2657, 1996.

[41] M. Ashida, "Ultra-broadband terahertz wave detection using photoconductive antenna," *Jpn. J. Appl. Phys.*, vol. 47, no. 10, pp. 8221–8225, 2008.

[42] A. Othonos, "Probing ultrafast carrier and phonon dynamics in semiconductors," *J. Appl. Phys.*, vol. 83, no. 4, pp. 1789–1830, 1998.

[43] N. Vieweg, F. Rettich, A. Deninger, H. Roehle, R. Dietz, T. Göbel, and M. Schell, "Terahertz-time domain spectrometer with 90 dB peak dynamic range," *J. Infrared Millim. Terahz Waves*, vol. 35, no. 10, pp. 823–832, 2014.

[44] S. Gupta, J. F. Whitaker, and G. a. Mourou, "Ultrafast carrier dynamics in III-V semiconductors grown by molecular-beam epitaxy at very low substrate temperatures," *IEEE J. Quantum Electron.*, vol. 28, no. 10, pp. 2464–2472, 1992.

[45] M. R. Melloch, J. M. Woodall, E. S. Harmon, N. Otsuka, F. H. Pollak, D. D. Nolte, R. M. Feenstra, and M. A. Lutz, "Low-Temperature Grown III-V Materials," *Ann. Rev. Mater. Sci.*, vol. 25, pp. 547–600, 1995.

[46] M. Kaminska, "Stoichiometry-related defects in GaAs grown by molecular-beam epitaxy at low temperatures," *J. Vac. Sci. Technol. B Microelectron. Nanom. Struct.*, vol. 7, no. 4, p. 710, 1989.

[47] R. M. Feenstra, J. M. Woodall, and G. D. Pettit, "Observation of bulk defects by scanning tunneling microscopy and spectroscopy: Arsenic antisite defects in GaAs," *Phys. Rev. Lett.*, vol. 71, no. 8, pp. 1176–1179, 1993.

[48] D. C. Look, D. C. Walters, M. O. Manasreh, J. R. Sizelove, C. E. Stutz, and K. R. Evans, "Anomalous Hall-effect results in low-temperature molecular-beam-epitaxial GaAs: Hopping in a dense EL2-like band," *Phys. Rev. B*, vol. 42, no. 6, pp. 3578–3581, 1990.

[49] D. E. Bliss, W. Walukiewicz, J. W. Ager, E. E. Haller, K. T. Chan, and S. Tanigawa, "Annealing studies of low-temperature-grown GaAs:Be," *J. Appl. Phys.*, vol. 71, no. 4, pp. 1699–1707, 1992.

[50] Z. Liliental-Weber, X. W. Lin, J. Washburn, and W. Schaff, "Rapid thermal annealing of low-temperature GaAs layers," *Appl. Phys. Lett.*, vol. 66, p. 2086, 1995.

[51] T. E. M. Staab, R. M. Nieminen, M. Luysberg, and T. Frauenheim, "Agglomeration of As antisites in as-rich low-temperature GaAs: Nucleation without a critical nucleus size," *Phys. Rev. Lett.*, vol. 95, p. 125502, 2005.

[52] E. S. Harmon, M. R. Melloch, J. M. Woodall, D. D. Nolte, N. Otsuka, and C. L. Chang, "Carrier lifetime versus anneal in low temperature growth GaAs," *Appl. Phys. Lett.*, vol. 63, no. 16, pp. 2248–2250, 1993.

[53] I. S. Gregory, C. M. Tey, A. G. Cullis, M. J. Evans, H. E. Beere, and I. Farrer, "Two-trap model for carrier lifetime and resistivity behavior in partially annealed GaAs grown at low temperature," *Phys. Rev. B*, vol. 73, p. 195201, 2006.

[54] J. K. Luo, H. Thomas, D. V. Morgan, and D. Westwood, "Thermal annealing effect on low temperature molecular beam epitaxy grown GaAs: Arsenic precipitation and the change of resistivity," *Appl. Phys. Lett.*, vol. 64, no. 1994, pp. 3614–3616, 1994.

[55] B. I. Shklovskii and A. L. Efros, “Electronic Properties of Doped Semiconductors,” in *Electronic Properties of Doped Semiconductors*, vol. 45, M. Cardona, Ed. Berlin: Springer, 1984, pp. 72–93.

[56] A. C. Warren, J. M. Woodall, J. L. Freeouf, D. Grischkowsky, D. T. McInturff, M. R. Melloch, and N. Otsuka, “Arsenic precipitates and the semi-insulating properties of GaAs buffer layers grown by low-temperature molecular beam epitaxy,” *Appl. Phys. Lett.*, vol. 57, no. 13, pp. 1331–1333, 1990.

[57] A. C. Warren, J. M. Woodall, P. D. Kirchner, X. Yin, F. Pollak, M. R. Melloch, N. Otsuka, and K. Mahalingam, “Role of excess As in Low-temperature-grown GaAs,” *Phys. Rev. B*, vol. 46, no. 8, pp. 4617–4620, 1992.

[58] D. E. Bliss, W. Walukiewicz, and E. E. Haller, “Annealing of AsGa-related defects in LT-GaAs: The role of gallium vacancies,” *J. Electron. Mater.*, vol. 22, no. 12, pp. 1401–1404, 1993.

[59] J. Gebauer, R. Krause-Rehberg, S. Eichler, M. Luysberg, H. Sohn, and E. R. Weber, “Ga vacancies in low-temperature-grown GaAs identified by slow positrons,” *Appl. Phys. Lett.*, vol. 71, p. 638, 1997.

[60] J. C. Bourgoin, K. Khirouni, and M. Stellmacher, “The behavior of As precipitates in low-temperature-grown GaAs,” *Appl. Phys. Lett.*, vol. 72, no. 4, pp. 442–444, 1998.

[61] A. J. Lochtefeld, M. R. Melloch, J. C. P. Chang, and E. S. Harmon, “The role of point defects and arsenic precipitates in carrier trapping and recombination in low-temperature grown GaAs,” *Appl. Phys. Lett.*, vol. 69, pp. 1465–1467, 1996.

[62] M. Luysberg, H. Sohn, A. Prasad, P. Specht, Z. Liliental-Weber, and E. R. Weber, “Effects of the growth temperature and As/Ga flux ratio on the incorporation of excess As into low temperature grown GaAs,” *J. Appl. Phys.*, vol. 83, pp. 561–566, 1998.

[63] I. S. Gregory, C. Baker, W. R. Tribe, M. J. Evans, H. E. Beere, E. H. Linfield, A. G. Davies, and M. Missous, “High resistivity annealed low-temperature GaAs with 100 fs lifetimes,” *Appl. Phys. Lett.*, vol. 83, pp. 4199–4201, 2003.

[64] A. Krotkus, K. Bertulis, L. Dapkus, U. Olin, and S. Marcinkevičius, “Ultrafast carrier trapping in Be-doped low-temperature-grown GaAs,” *Appl. Phys. Lett.*, vol. 75, no. 21, pp. 3336–3338, 1999.

[65] J. Gebauer, R. Zhao, P. Specht, E. R. Weber, F. Börner, F. Redmann, and R. Krause-Rehberg, “Does beryllium doping suppress the formation of Ga vacancies in nonstoichiometric GaAs layers grown at low temperatures?,” *Appl. Phys. Lett.*, vol. 79, pp. 4313–4315, 2001.

[66] H. Künzel, J. Böttcher, R. Gibis, and G. Urmann, “Material properties of Ga0.47In0.53As grown on InP by low-temperature molecular beam epitaxy,” *Appl. Phys. Lett.*, vol. 61, pp. 1347–1349, 1992.

[67] R. A. Metzger, A. S. Brown, L. G. McCray, and J. A. Henige, “Structural and electrical properties of low temperature GaInAs,” *J. Vac. Sci. Technol. B*, vol. 11, no. 3, pp. 798–801, 1992.

[68] B. Grandidier, H. Chen, R. M. Feenstra, D. T. McInturff, P. W. Juodawlkis, and S. E. Ralph, "Scanning tunneling microscopy and spectroscopy of arsenic antisites in low temperature grown InGaAs," *Appl. Phys. Lett.*, vol. 74, no. 10, pp. 1439–1441, 1999.

[69] H. Kuenzel, K. Biermann, D. Nickel, and T. Elsaesser, "Low-temperature MBE growth and characteristics of InP-based AlInAs/GaInAs MQW structures," *J. Cryst. Growth*, vol. 227–228, pp. 284–288, 2001.

[70] A. Claverie, K. M. Yu, W. Swider, Z. Liliental-Weber, M. O'Keefe, R. Kilaas, J. Pamulapati, and P. K. Bhattacharya, "Structural characterization of low-temperature molecular beam epitaxial In0.52Al0.48As/InP heterolayers," *Appl. Phys. Lett.*, vol. 60, no. 8, pp. 989–991, 1992.

[71] K. Biermann, "Untersuchungen an auf InP basierenden Halbleitern mit sub-ps Responsezeiten," Humboldt-Universität zu Berlin, 2007.

[72] R. Takahashi, Y. Kawamura, T. Kagawa, and H. Iwamura, "Ultrafast 1.55-μm photoresponses in low-temperature-grown InGaAs/InAlAs quantum wells," *Appl. Phys. Lett.*, vol. 65, no. 14, pp. 1790–1792, 1994.

[73] Y. Chen, S. S. Prabhu, S. E. Ralph, and D. T. McInturff, "Trapping and recombination dynamics of low-temperature-grown InGaAs/InAlAs multiple quantum wells," *Appl. Phys. Lett.*, vol. 72, no. 4, pp. 439–441, 1998.

[74] K. Biermann, D. Nickel, K. Reimann, M. Woerner, T. Elsaesser, and H. Künzel, "Ultrafast optical nonlinearity of low-temperature-grown GaInAs/AlInAs quantum wells at wavelengths around 1.55μm," *Appl. Phys. Lett.*, vol. 80, no. 11, pp. 1936–1938, 2002.

[75] I. Kostakis, D. Saeedkia, and M. Missous, "Terahertz Generation and Detection Using Low Temperature Grown InGaAs-InAlAs Photoconductive Antennas at 1.55 μm Pulse Excitation," *IEEE Trans. Terahertz Sci. Technol.*, vol. 2, no. 6, pp. 617–622, 2012.

[76] P. W. Juodawlkis, D. T. McInturff, and S. E. Ralph, "Ultrafast carrier dynamics and optical nonlinearities of low-temperature-grown InGaAs/InAlAs multiple quantum wells," *Appl. Phys. Lett.*, vol. 69, no. 26, pp. 4062–4064, 1996.

[77] I. Kostakis, D. Saeedkia, and M. Missous, "Characterization of low temperature InGaAs-InAlAs semiconductor photo mixers at 1.55 μm wavelength illumination for terahertz generation and detection," *J. Appl. Phys.*, vol. 111, no. 103105, 2012.

[78] W. Shockley and W. T. Read, "Statistics of the Recombination of Holes and Electrons," *Phys. Rev.*, vol. 87, no. 46, pp. 835–842, 1952.

[79] Y. A. Goldberg and N. N. Schmidt, *Handbook Series on Semiconductor Parameters*. London: World Scientific, 1999.

[80] D. V. Lang and C. H. Henry, "Nonradiative recombination at deep levels in GaAs and GaP by lattice-relaxation multiphonon emission," *Phys. Rev. Lett.*, vol. 35, no. 22, pp. 1525–1528, 1975.

[81] C. H. Henry and D. V. Lang, "Nonradiative capture and recombination by multiphonon

emission in GaAs and GaP," *Phys. Rev. B*, vol. 15, no. 2, pp. 989–1016, 1977.

[82] R. Pässler, "Capture and Ejection Properties of Deep Traps in Semiconductors," *Phys. Status Solidi*, vol. 203, pp. 203–215, 1978.

[83] R. Pässler, "Temperature Dependences of the Nonradiative Multiphonon Carrier Capture and Ejection Properties of Deep Traps in Semiconductors. II. Interpretation and Extrapolation of Capture Data," *Phys. Status Solidi*, vol. 103, pp. 673–686, 1981.

[84] R. J. B. Dietz, A. Brahm, A. Velauthapillai, A. Wilms, C. Lammers, B. Globisch, M. Koch, G. Notni, A. Tünnermann, T. Göbel, and M. Schell, "Low temperature grown photoconductive antennas for pulsed 1060 nm excitation : Influence of excess energy on the electron relaxation," *J. Infrared Millim. Terahz Waves*, vol. 36, pp. 60–71, 2015.

[85] A. J. L. Adam, "Review of near-field Terahertz measurement methods and their applications: How to achieve sub-wavelength resolution at THz frequencies," *J. Infrared, Millimeter, Terahertz Waves*, vol. 32, pp. 976–1019, 2011.

[86] A. J. Macfaden, J. L. Reno, I. Brener, and O. Mitrofanov, "3 µm aperture probes for near-field terahertz transmission microscopy," *Appl. Phys. Lett.*, vol. 104, p. 11110, 2014.

[87] A. J. Huber, F. Keilmann, J. Wittborn, J. Aizpurua, and R. Hillenbrand, "Terahertz near-field nanoscopy of mobile carriers in single semiconductor nanodevices," *Nano Lett.*, vol. 8, no. 11, pp. 3766–3770, 2008.

[88] M. Wächter, M. Nagel, and H. Kurz, "Tapered photoconductive terahertz field probe tip with subwavelength spatial resolution," *Appl. Phys. Lett.*, vol. 95, no. 41112, 2009.

[89] M. Nagel, A. Safiei, S. Sawallich, C. Matheisen, T. M. Pletzer, A. A. Mewe, N. van der Borg, I. Cesar, and H. Kurz, "THz microprobe system for contact-free high-resolution sheet resistance imaging," in *Proc. 28th Eur. Photovoltaic Sol. Energy Conf. Exhib.*, 2013, pp. 856–860.

[90] J. Lloyd-Hughes, E. Castro-Camus, and M. B. Johnston, "Simulation and optimisation of terahertz emission from InGaAs and InP photoconductive switches," *Solid State Commun.*, vol. 136, pp. 595–600, 2005.

[91] J. Lloyd-Hughes, E. Castro-Camus, M. D. Fraser, C. Jagadish, and M. B. Johnston, "Carrier dynamics in ion-implanted GaAs studied by simulation and observation of terahertz emission," *Phys. Rev. B - Condens. Matter Mater. Phys.*, vol. 70, no. 235330, 2004.

[92] E. Castro-Camus, J. Lloyd-Hughes, and M. B. Johnston, "Three-dimensional carrier-dynamics simulation of terahertz emission from photoconductive switches," *Phys. Rev. B - Condens. Matter Mater. Phys.*, vol. 71, no. 195301, 2005.

[93] Z. S. Piao, M. Tani, and K. Sakai, "Carrier dynamics and THz radiation in biased semiconductor structures," *Proceedings of SPIE - The International Society for Optical Engineering*, vol. 3617. pp. 49–56, 1999.

[94] R. J. B. Dietz, M. Gerhard, D. Stanze, M. Koch, B. Sartorius, and M. Schell, "THz generation at 1.55 µm excitation: six-fold increase in THz conversion efficiency by separated photoconductive and trapping regions," *Opt. Express*, vol. 19, no. 27, p. 25911, 2011.

[95] J. E. Oh, P. K. Bhattacharya, Y. C. Chen, O. Aina, and M. Mattingly, "The Dependence of the Electrical and Optical Properties of Molecular Beam Epitaxial In 0.52Al0.48As on Growth Parameters : Interplay of Surface Kinetics and Thermodynamics," *J. Electron. Mater.*, vol. 19, no. 5, pp. 435–441, 1990.

[96] A. Hase, H. Künzel, D. R. T. Zahn, and W. Richter, "Assessment of clustering induced internal strain in AlInAs on InP grown by molecular beam epitaxy," *J. Appl. Phys.*, vol. 76, pp. 2459–2465, 1994.

[97] H. Hoenow, H.-G. Bach, J. Böttcher, F. Gueissaz, H. Künzel, F. Scheffer, and C. Schramm, "Deep level analysis of Si doped MBE grown AlInAs layers," in *4th International Conference on Indium Phosphide and Related Materials*, 2002, pp. 136–139.

[98] W. P. Hong, P. K. Bhattacharya, and J. Singh, "Nonrandom alloying in In0.52Al0.48As/InP grown by molecular beam epitaxy," *Appl. Phys. Lett.*, vol. 50, pp. 618–620, 1987.

[99] D. V. Lang, "Deep-level transient spectroscopy: A new method to characterize traps in semiconductors," *J. Appl. Phys.*, vol. 45, no. 7, pp. 3023–3032, 1974.

[100] J. S. Weiner, D. S. Chemla, D. A. B. Miller, T. H. Wood, D. Sivco, and A. Y. Cho, "Room-temperature excitons in 1.6-µm band-gap GaInAs/AlInAs quantum wells," *Appl. Phys. Lett.*, vol. 46, no. 7, pp. 619–621, 1985.

[101] R. J. B. Dietz, N. Vieweg, T. Puppe, A. Zach, B. Globisch, T. Göbel, P. Leisching, and M. Schell, "All fiber-coupled THz-TDS system with kHz measurement rate based on electronically controlled optical sampling," *Opt. Lett.*, vol. 39, no. 22, pp. 6482–6485, 2014.

[102] T. Jung, R. Dietz, A. Chernikov, F. Kuik, B. Sartorius, M. Schell, M. Koch, and S. Chatterjee, "Photoluminescence study of (GaIn)As/(AlIn)As-based THz antenna materials for 1.55 µm excitation," *J. Lumin.*, vol. 138, no. 100, pp. 179–181, 2013.

[103] R. Müller, W. Bohmeyer, M. Kehrt, K. Lange, C. Monte, and A. Steiger, "Novel detectors for traceable THz power measurements," *J. Infrared, Millimeter, Terahertz Waves*, vol. 35, pp. 659–670, 2014.

[104] R. Müller, B. Gutschwager, J. Hollandt, M. Kehrt, C. Monte, R. Müller, and A. Steiger, "Characterization of a Large-Area Pyroelectric Detector from 300 GHz to 30 THz," *J. Infrared, Millimeter, Terahertz Waves*, vol. 36, no. 7, pp. 654–661, 2015.

[105] A. Steiger, M. Kehrt, C. Monte, and R. Müller, "Traceable terahertz power measurement from 1 THz to 5 THz.," *Opt. Express*, vol. 21, no. 12, pp. 14466–14473, 2013.

[106] A. Steiger, B. Gutschwager, M. Kehrt, C. Monte, R. Müller, and J. Hollandt, "Optical

methods for power measurement of terahertz radiation.," *Opt. Express*, vol. 18, no. 21, pp. 21804–21814, 2010.

[107] M. Tani, Z. Jiang, and X.-C. Zhang, "Photoconductive terahertz transceiver," *Electron. Lett.*, vol. 36, no. 9, pp. 804–805, 2000.

[108] C. Jördens, N. Krumbholz, T. Hasek, N. Vieweg, B. Scherger, L. Bähr, M. Mikulics, and M. Koch, "Fibre-coupled terahertz transceiver head," *Electron. Lett.*, vol. 44, no. 25, 2008.

[109] S. Busch, T. Probst, M. Schwerdtfeger, R. Dietz, J. Palací, and M. Koch, "Terahertz transceiver concept," *Opt. Express*, vol. 22, no. 14, pp. 16841–16846, 2014.

[110] M. Tani, M. Watanabe, and K. Sakai, "Photoconductive twin dipole antennas for THz transceiver," *Electron. Lett.*, vol. 38, no. 1, p. 5, 2002.

[111] H. S. Bark, Y. Bin Ji, S. J. Oh, S. K. Noh, and T. Jeon, "Optical Fiber Coupled THz Transceiver," in *40th International Conference on Infrared, Millimeter, and Terahertz Waves (IRMMW-THz)*, 2015.

[112] M. Kleinert, Z. Zhang, D. de Felipe, C. Zawadzki, A. Maese Novo, W. Brinker, M. Möhrle, and N. Keil, "Recent progress in InP/polymer-based devices for telecom and data center applications," in *Proc SPIE9365, Integrated Optics: Devices, Materials, and Technologies XIX*, 2015, p. 93650R.

[113] A. Zunger, "Electronic structure of 3d transition-atom impurities in semiconductors," *Solid State Phys.*, vol. 39, pp. 276–462, 1986.

[114] A. Zunger, "Theroy of 3d Transition Atom Impurities in Semiconductors," *Ann. Rev. Mater. Sci.*, vol. 15, pp. 411–453, 1985.

[115] B. Tell, U. Koren, and B. I. Miller, "Metalorganic vapor-phase-epitaxial growth of Fe-doped In0.53Ga0.47As," *J. Appl. Phys.*, vol. 61, no. 3, pp. 1172–1175, 1987.

[116] G. Guillot, G. Bremond, T. Benyattou, F. Ducroquet, B. Wirth, M. Colombet, A. Louati, and A. Bencherifa, "Identification Of The Fe Acceptor Level In Ga0.47In0.53As," *Semicond. Sci. Technol.*, vol. 5, pp. 391–394, 1990.

[117] B. Srocka, H. Scheffler, and D. Bimberg, "Fe2+-Fe3+ level as a recombination center in In0.53Ga0.47As," *Phys. Rev. B*, vol. 49, no. 15, pp. 10259–10268, 1994.

[118] J. Bourgoin and M. Lannoo, *Point Defects in Semiconductors II: Experimental Aspects*, Springer. Berlin: Springer, 1983.

[119] T. Göbel, D. Stanze, B. Globisch, R. J. B. Dietz, H. Roehle, and M. Schell, "Telecom technology based continuous wave terahertz photomixing system with 105 decibel signal-to-noise ratio and 3.5 terahertz bandwidth," *Opt. Lett.*, vol. 38, no. 20, pp. 4197–4199, 2013.

[120] B. Srocka, H. Scheffler, and D. Bimberg, "Rhodium and iridiumrelated deep levels in In0. 53Ga0 .47As," *Appl. Phys. Lett.*, vol. 64, pp. 2679–2681, 1994.

[121] A. Dadgar, O. Stenzel, A. Näser, M. Zafar Iqbal, D. Bimberg, and H. Schumann,

"Ruthenium: A superior compensator of InP," *Appl. Phys. Lett.*, vol. 73, pp. 3878–3880, 1998.

[122] M. Tani, K. Sakai, and H. Mimura, "Ultrafast photoconductive detectors based on semi-insulating GaAs and InP," *Japanese J. Appl. Physics, Part 2 Lett.*, vol. 36, pp. L1175–L1178, 1997.

Scientific curriculum vitae

PERSONAL DATA

Name	Björn Globisch
Date of Birth	September 16th 1986
Place of Birth	Damme, Germany
Nationality	German

SCIENTIFIC INTERESTS

Opto-electronic generation and detection of THz radiation

Micro-structuring of devices based on InP

Epitaxy of III/V semiconductors

THz spectroscopy in the time and the frequency domain

Sub-picosecond carrier dynamics in semiconductors

Non-linear dynamics in semiconductors lasers

PUBLICATIONS IN PEER REVIEWED JOURNALS

[1] B. Globisch, R. J. B. Dietz, R. B. Kohlhaas, T. Göbel, M. Schell, M. Semtsiv, D. Alcer and W. T. Masselink, "Iron doped InGaAs: Competitive THz emitters and detectors fabricated from the same photoconductor", accepted by *J. Appl. Phys.*, Jan. 2017.

[2] B. Globisch, R. J. B. Dietz, R. B. Kohlhaas, S. Nellen, M. Kleinert, T. Göbel, and M. Schell, "Fiber-coupled transceiver for terahertz reflection measurements with a 4.5 THz bandwidth," *Opt. Lett*. vol 41, no. 22, pp. 5262-5265, 2016.

[3] B. Globisch, R. J. B. Dietz, S. Nellen, T. Göbel, and M. Schell, "Terahertz detectors from Be-doped low-temperature grown InGaAs/InAlAs: Interplay of annealing and terahertz performance," AIP Advances, vol. 6, 125011, 2016.

[4] S. Sawallich, B. Globisch, C. Matheisen, M. Nagel, R. J. B. Dietz, and G. Thorsten, "Photoconductive Terahertz Near-Field Detectors for Operation With 1550-nm Pulsed Fiber Lasers," *IEEE Trans. Terahertz Sci. Technol.*, vol. 6, no. 3, pp. 365–370, 2016.

[5] B. Globisch, R. J. B. Dietz, T. Göbel, M. Schell, W. Bohmeyer, R. Müller, and A. Steiger, "Absolute terahertz power measurement of a time-domain spectroscopy system," *Opt. Lett.*, vol. 40, no. 15, p. 3544, 2015.

[6] R. J. B. Dietz, A. Brahm, A. Velauthapillai, A. Wilms, C. Lammers, B. Globisch, M. Koch, G. Notni, A. Tünnermann, T. Göbel, and M. Schell, "Low temperature grown photoconductive antennas for pulsed 1060 nm excitation: Influence of excess energy on the electron relaxation", *J. Infrared Millim. Terahz Waves,* vol. 36, pp. 60–71, 2015.

[7] D. Stanze, B. Globisch, R. Dietz, and H. Roehle, "Multilayer Thickness Determination Using Continuous Wave THz Spectroscopy", *IEEE Trans. Terahertz Sci. Technol.*, vol. 4, no. 6, pp. 696–701, 2014.

[8] R. J. B. Dietz, B. Globisch, H. Roehle, D. Stanze, T. Göbel, and M. Schell, "Influence and adjustment of carrier lifetimes in InGaAs/InAlAs photoconductive pulsed terahertz detectors : 6 THz bandwidth and 90dB dynamic range", *Opt. Express*, vol. 22, no. 16, pp. 19411–19422, 2014.

[9] R. J. B. Dietz, N. Vieweg, T. Puppe, A. Zach, B. Globisch, T. Göbel, P. Leisching, and M. Schell, "All fiber-coupled THz-TDS system with kHz measurement rate based on electronically controlled optical sampling", *Opt. Lett.*, vol. 39, no. 22, pp. 6482–5, 2014.

[10] B. Globisch, R. J. B. Dietz, D. Stanze, T. Göbel, and M. Schell, "Carrier dynamics in Beryllium doped low-temperature-grown InGaAs/InAlAs", *Appl. Phys. Lett.*, vol. 104, no. 17, 2014.

[11] T. Göbel, D. Stanze, B. Globisch, R. J. B. Dietz, H. Roehle, and M. Schell, "Telecom technology based continuous wave terahertz photomixing system with 105 decibel signal-to-noise ratio and 3.5 terahertz bandwidth", *Opt. Lett.*, vol. 38, no. 20, pp. 4197–4199, 2013.

[12] R. J. B. Dietz, B. Globisch, M. Gerhard, A. Velauthapillai, D. Stanze, H. Roehle, M. Koch, T. Göbel, and M. Schell, "64 µW pulsed terahertz emission from growth optimized InGaAs/InAlAs heterostructures with separated photoconductive and trapping regions", *Appl. Phys. Lett.*, vol. 103, no. 6, pp. 1–5, 2013.

[13] R. J. B. Dietz, R. Wilk, B. Globisch, H. Roehle, D. Stanze, S. Ullrich, S. Schumann, N. Born, M. Koch, B. Sartorius, and M. Schell, "Low temperature grown Be-doped InGaAs/InAlAs photoconductive antennas excited at 1030 nm", *J. Infrared Millim., Terahz Waves*, vol. 34, pp. 231–237, 2013.

[14] B. Globisch, C. Otto, E. Schöll, and K. Lüdge**,** "*Influence of carrier lifetimes on the dynamical behavior of quantum-dot lasers subject to optical feedback*", *Phys. Rev. E*, vol. 86, no. 4, 046201, 2012.

[15] C. Otto, B. Globisch, K. Lüdge, E. Schöll, and T. Erneux, **"***Complex dynamics of semiconductor quantum dot lasers subject to delayed optical feedback*", *Int. J. Bifurcation Chaos* 22, 1250246, 2012.

PATENTS

PCT/EP 2014/53631	Photoconductor for emitting and/or receiving electromagnetic waves, Ultrafast quantum photoconductor.
AKZ 10 2016 202 216.4	Terahertz-Antenne und Verfahren zum Herstellen einer Terahertz-Antenne.
PCT/EP 2016/072775	THz transceivers.

CONFERENCE CONTRIBUTIONS

[1] B. Globisch, R. J. B. Dietz, R. B. Kohlhaas, M. Kleinert, H. Roehle, T. Göbel, M. Schell, "Fully-integrated THz transceiver with 4.5 THz bandwidth and 70 dB dynamic range", 41th International Conference on Infrared, Millimeter, and Terahertz Waves (IRMMW-THz), 2016.

[2] R. B. Kohlhaas, B. Globisch, R. J. B. Dietz, T. Göbel, M. Schell, "Fe doped InGaAs for the generation and detection of pulsed THz radiation", 41th International Conference on Infrared, Millimeter, and Terahertz Waves (IRMMW-THz), 2016.

[3] R. J. B. Dietz, B. Globisch, H. Roehle, T. Göbel, M. Schell, "Fiber coupled terahertz time domain spectroscopy system based on InGaAs/InAlAs photoconductors with 100 dB dynamic range", 40th International Conference on Infrared, Millimeter, and Terahertz Waves (IRMMW-THz), 2015.

[4] B. Globisch, R. J. B. Dietz, A. Steiger, W. Bohmeyer, T. Göbel, M. Schell, "First absolute power measurement of a terahertz time domain spectroscopy system based on InGaAs/InAlAs photoconductors", 40th International Conference on Infrared, Millimeter, and Terahertz Waves (IRMMW-THz), 2015.

[5] B. Globisch, R. J. B. Dietz, D. Stanze, H. Roehle, T. Göbel, M. Schell, “Improved InGaAs/InAlAs photoconductive THz receivers: 5.8 THz bandwidth and 80 dB dynamic range”, Conference on Lasers and Electro-Optics (CLEO) - Laser Science to Photonic Applications, 2014.

[6] T. Göbel, D. Stanze, R. J. B. Dietz, B. Globisch, H. Roehle, M. Schell, “1.5µm cw THz photomixing system with 105 dB signal-to-noise ratio”, 38th International Conference on Infrared, Millimeter, and Terahertz Waves (IRMMW-THz), 2013.

[7] D. Stanze, T. Göbel, R. J. B. Dietz, B. Globisch, M. Schell, “Photoconductive Cw THz receiver with 20-fold increased THz conversion efficiency”, 38th International Conference on Infrared, Millimeter, and Terahertz Waves (IRMMW-THz), 2013.

[8] B. Globisch, D. Stanze, R. J. B. Dietz, T. Göbel, M. Schell, “Bandwidth improvement of cw THz receivers by Be doping of low-temperature-grown InGaAs/InAlAs heterostructures”, 38th International Conference on Infrared, Millimeter, and Terahertz Waves (IRMMW-THz), 2013.

[9] R. J. B. Dietz, B. Globisch, M. Gerhard, D. Stanze, M. Koch, B. Sartorius, T. Göbel, M. Schell, “32 µW pulsed terahertz emission from high mobility InAlAs/InGaAs multi-nanolayer structures”, Conference on Lasers and Electro-Optics (CLEO) - Laser Science to Photonic Applications, 2013.

[10] D. Stanze, T. Göbel, B. Globisch, R. J. B. Dietz, B. Sartorius, M. Schell, “High Speed Coherent Continuous Wave Terahertz Imaging System Based on Photomixing”, 37th International Conference on Infrared, Millimeter, and Terahertz Waves (IRMMW-THz), 2012.

[11] R. J. B. Dietz, R. Wilk, B. Globisch, H. Roehle, D. Stanze, S. Ullrich, S. Schumann, N. Born, N. Voss, M. Stecher, M. Koch, B. Sartorius, M. Schell, “Pulsed THz emission from low temperature grown Be-doped InGaAs/InAlAs photoconductive switches at 1030 nm excitation”, 37th International Conference on Infrared, Millimeter, and Terahertz Waves (IRMMW-THz), 2012.

Appendix: Scientific Publications

Publication I

R. J. B. Dietz, B. Globisch, M. Gerhard, A. Velauthapillai, D. Stanze, H. Roehle, M. Koch, T. Göbel, and M. Schell, “64 µW pulsed terahertz emission from growth optimized InGaAs/InAlAs heterostructures with separated photo-conductive and trapping regions,” Appl. Phys. Lett., vol. 103, no. 6, pp. 1–5, 2013.

64 µW pulsed THz emission from growth optimized InGaAs/InAlAs heterostructures with separated photoconductive and trapping regions

Roman J. B. Dietz,[1,a)] Björn Globisch,[1] Marina Gerhard,[2] Ajanthkrishna Velauthapillai,[2] Dennis Stanze,[1] Helmut Roehle,[1] Martin Koch,[2] Thorsten Göbel[1] and Martin Schell[1]

[1]*Fraunhofer Instiute for Telecommunications, Heinrich-Hertz-Institute, Einsteinufer 37,10587 Berlin, Germany*
[2]*Department of Physics, Philipps-Universität Marburg, Renthof 5, 35032 Marburg, Germany*

Abstract: We present results on optimized growth temperatures and layer structure design of high mobility photoconductive THz emitters based on molecular beam epitaxy (MBE) grown $In_{0.53}Ga_{0.47}As/In_{0.52}Al_{0.48}As$ multilayer heterostructures (MLHS). The photoconductive antennas (PCA) made of these MLHS are evaluated as THz emitters in a THz time domain spectrometer and with a Golay cell. We measured a THz bandwidth in excess of 4 THz and average THz powers of up to 64 µW corresponding to an optical power-to-THz power conversion efficiency of up to 2×10^{-3}.

Terahertz time domain spectroscopy (THz TDS) is among the most promising methods for industrial and scientific applications within the rapidly developing and promising field of terahertz technology.[1] In order to find widespread applications, THz TDS systems have to be compact, stable and cost effective. Therefore, various attempts have been made to exploit readily available Er-doped femtosecond fiber lasers at 1550 nm wavelength, of-the-shelf telecom components as well as efforts to design suitable InGaAs based PCAs.[2,3,4,5,6] However, great potential remains for further improvement of InGaAs based PCAs concerning their efficiency and output power. It has recently been shown that InAlAs/InGaAs MLHS grown by MBE at substrate temperatures of approx. 400 °C exhibit a high optical-to-THz conversion efficiency and broadband THz emission.[7] In this growth temperature range InGaAs shows a minimum of defect incorporation with a residual carrier concentration on the order of $n = 10^{16}$ cm^{-3}.[8] On the contrary, InAlAs exhibits increased defect incorporation in this temperature range, associated with alloy clustering due to the interplay of surface kinetics and thermodynamics during the MBE growth process.[9] By exploiting above characteristics it is possible to obtain InAlAs/InGaAs MLHS with low defect density and high mobility InGaAs layers adjacent to high defect InAlAs layers for carrier trapping at the same growth temperature.

For further understanding and optimization of these MLHS for THz generation we investigated the influence of growth temperature and InAlAs layer thickness on the defect incorporation, carrier relaxation dynamics and THz emission characteristics.

[a)] Electronic mail: Roman.Dietz@hhi.fraunhofer.de. Tel.:+493031002522

Therefore, we performed differential transmission (DT) measurements, THz time domain spectroscopy (TDS) and determined the emitted THz power with a Golay cell. To investigate the influence of the MBE growth temperature two sample series were grown. The first one with substrate temperatures ranging from $T_g = 325$ °C to $T_g = 450$ °C in steps of 25 °C with 30 periods of 12 nm InGaAs and 8 nm InAlAs (T_g-series 1), and the second series (T_g-Series 2) with temperatures ranging from $T_g = 350$ °C to $T_g = 425$ °C in 25 °C steps grown with 100 periods and the same layer thicknesses as in T_g-Series 1.

In order to probe the carrier relaxation dynamics we performed DT measurements using an Er-doped femtosecond fiber laser with 100 MHz repetition rate and a center wavelength of 1560 nm as excitation source. The pump and probe beam were focused on the sample with a spot size of approx. 15 µm diameter. Their polarizations were kept orthogonal to avoid interference effects between pump and probe beam. The probe power was kept constant at 0.1 mW while the pump power was varied between 1 mW and 16 mW in order to investigate possible trap saturation effects. Fig. 1(a) shows an example of the measured DT signals for a pump power of 16 mW for T_g-Series 2 as well as the DT measurement of a low temperature (LT) grown ($T_g = 130$ °C) and Beryllium doped MLHS sample. This sample will serve as a reference, since LT-grown Be-doped MLHS are known to exhibit very fast carrier trapping and have been demonstrated to be suitable materials for THz PCAs.[6] The LT-grown Be-doped MLHS sample shows a fast mono-exponential decay with a decay time of approx. 550 fs for 1 mW (not shown) and approx. $\tau_1 = 770$ fs at 16 mW of pump power. This fast decay in the DT signal is governed by electron trapping out of the conduction band (CB) into As_{Ga}-anti-site defect related trap states inside the InGaAs layers.[10,11]

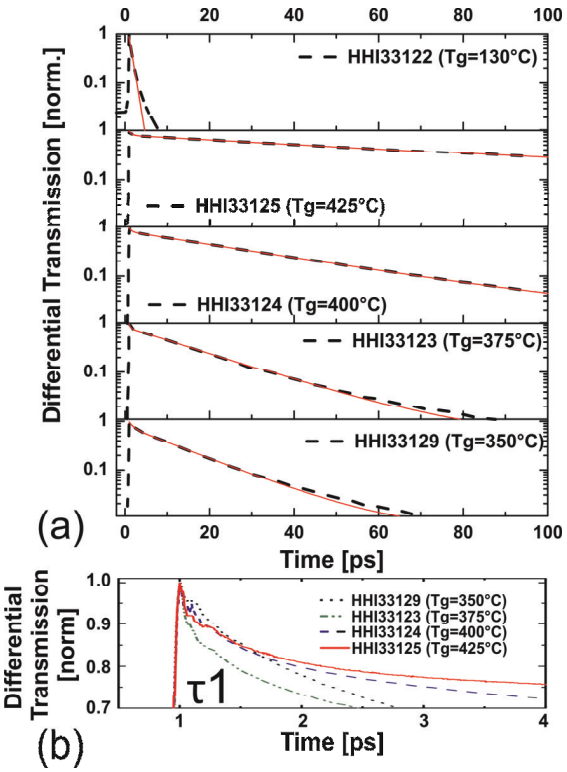

FIG. 1. Example of differential transmission signals measured with 16 mW pump power and at 0.1 mW probe power for samples of T_g-series 2 and a LT-grown Be-Doped MLHS as reference sample. (b) Example of the short decay component τ_1 for samples of T_g-series 2. The thin red solid lines in (a) indicate the fit functions, mono-exponential for the LT-grown reference and bi-exponential for all other samples.

The slight increase of the decay time for increased pump powers, which also leads to a deviation from a purely mono-exponential decay, is assumed to be due to partial trap state filling. Trap state filling occurs because of the relatively slow recombination of electrons within trap states with holes in the valence band (VB), for which the time constant is assumed to be on the order of several tens of picoseconds. The samples of T_g-Series 1 and 2 on the other hand show two distinct decay components: A relatively small component with a very fast decay time (τ_1) on the order of a few hundred femtoseconds (example in Fig. 1(b)) and a dominating decay component with a relatively slow decay time (τ_2) of several tens of picoseconds. The origin of the short time constant τ_1 is manifold: Part of the signal is due to the coherent interaction of pump and probe beam that is present despite the thoroughly crossed polarization. Furthermore, some of the absorption recovery is due to the redistribution of the carrier population in the CB via carrier-carrier scattering and phonon emission. Another part is assumed to originate from fast carrier trapping into a small amount of As_{Ga}-related defects in the InGaAs layers that exist even for these elevated growth temperatures. This contribution becomes slightly more dominant for samples grown at $T_g \leq 375$ °C. However, there is no strong correlation of this combined short decay τ_1 with growth temperature or THz dynamics of the samples. The second time constant τ_2 is associated with electron trapping into defect states within the InAlAs layer and shows a strong dependence on growth temperature (Fig. 2). Furthermore we see a strong correlation between THz dynamics and τ_2, as will be shown later on. As visible in Fig. 2 there is a minimum of τ_2 for samples grown at $T_g = 375$ °C and $T_g = 350$ °C, for series 1 and 2, respectively. This indicates the expected maximum of defect incorporation in the InAlAs layers at these growth temperatures. The two growth series seem to be shifted in temperature with respect to each other. This is supposed to originate from a systematic error in the calibration of T_g that is constant over each growth series. The temperature calibration was performed via the observation of oxide desorption from the InP substrate on the RHEED signal at $T_g \approx 500$ °C. We assume an uncertainty of up to $\Delta T_g = \pm 15$ °C in this calibration, especially for growth series that were not grown in direct succession as it is the case for T_g-series 1 and 2. The vertical shift, i.e. the on average faster decay times for samples from T_g-Series 2, is attributed to the increased number of periods, i.e. 100 versus 30, thus offering a higher total amount of traps.

The fastest decay time with $\tau_2 = 12.78 \pm 0.04$ ps for sample HHI33129 is still at least one order of magnitude higher than for LT-grown samples. This indicates that the capture cross section and/or the density of the trap states in the InAlAs layers is still small compared to arsenic anti-site related trap states obtained via LT-growth of InGaAs. We see a minor influence of the pump power on the slow decay component τ_2 tending towards faster relaxation for higher pump powers and for samples with high defect densities, i.e. $T_g = 350$-400 °C. Higher electron excitation densities result, after thermalization with the lattice, in a higher phonon density that in turn increases the carrier trapping probability into defects states within the InAlAs layers.

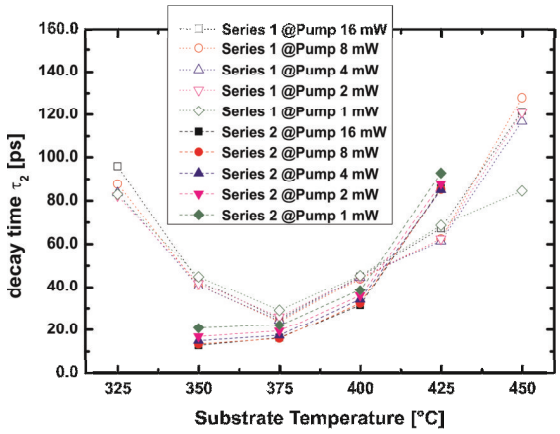

FIG. 2. Fit results for slow decay time constant τ_2 extracted from bi-exponential fits on DT measurements for T_g-series 1 (empty symbols) and T_g-series 2 (filled symbols) at various pump powers.

For a detailed analysis of the carrier capture into trap states associated with defects in the InAlAs barrier, we investigated the influence of the barrier thickness (d_B) on carrier relaxation dynamics. Therefore, samples with 2 nm, 4 nm, 8 nm, 16 nm of InAlAs layer thickness were grown while keeping the InGaAs thickness fixed at 12 nm (d_B-Series). All samples consisted of 100 periods and where grown at substrate temperature of approx. T_g = 400 °C.

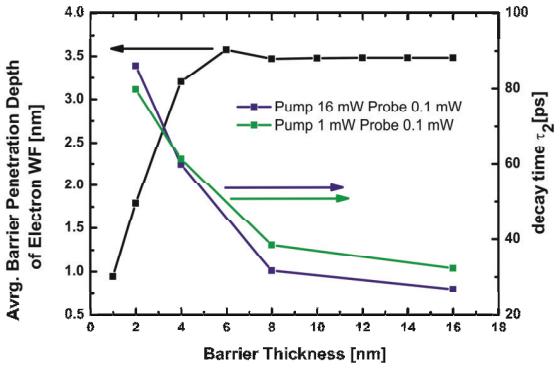

FIG. 3. Fit results for decay time constant τ_2 from bi-exponential fit on differential transmission signals for samples with different barrier thicknesses (right) and the calculated average penetration depth of the electron wave-function in to the barrier as a function of barrier thickness (left). The lines are guidelines for the eyes.

Additionally, we calculated the electron wave functions (WF) solving one dimensional (1D) Schroedinger equation for a 30 period MLHS. The WF was used to calculate an averaged penetration depth of the WF into the barrier, by summing over all positions within the barrier with non-zero WF values and averaging over all 30 (in 1D) degenerate energy eigenvalues of the first sub-band. Considering a homogeneous trap density within the barrier, this quantity gives a measure of how many defect states are "reachable" by an electron. The results from the DT measurements on the samples and the results from the above mentioned calculation are shown in Fig. 3. As can be seen from the measurements, an increased barrier thickness leads to a faster decay. This is due to the higher absolute number of available and/or reachable trap states in the InAlAs barrier assuming that the trap state density is independent of the barrier thickness and solely dependent on T_g. The slightly reduced slope of the curve for 1 mW pump supports this assumption if possible trap saturation at higher carrier densities is taken into account.

In order to investigate the THz emission the samples were structured with mesa-type strip-line antennas with gap sizes of 100 µm and employed as emitters in a THz-TDS setup.[6] The applied receiver was a mesa-type dipole antenna with a gap size of 10 µm and a contact line separation of 25 µm made from the LT Be-doped reference sample HHI33122 shown in Fig. 1(a). For the sake of brevity we only show pulse traces and spectra for four of the samples. The sample parameters and the measured τ_2 are given in Table I. As visible in Fig. 4(b) the THz-TDS spectrum of the fast LT-sample shows a slight shift of the spectral maximum towards higher frequencies compared to the other samples. However, no significant difference in overall bandwidth or dynamic range is evident. This strongly suggests that the bandwidth of the generated THz radiation is mainly governed by the rising edge of the carrier density, i.e. the exiting laser pulse duration, and not trapping or recombination dynamics. This is in agreement with studies conducted on Si:GaAs by Liu et al.[12]

Sample	T_g [°C]	Be-doping [cm^{-3}]	d_B [nm]	decay time [ps]
33122	130	3×10^{18}	8	0.77±0.07 (τ_1)
33129	350	no doping	8	12.78±0.04 (τ_2)
33124	400	no doping	8	31.53±0.04 (τ_2)
33141	400	no doping	2	86.0±0.2 (τ_2)

Table I. List of samples measured in THz-TDS Setup with respective growth and DT parameters.

Furthermore, the samples with slower decay time show strongly increased THz emission amplitudes under equal excitation conditions as visible from the THz pulse traces in Fig. 4(a).

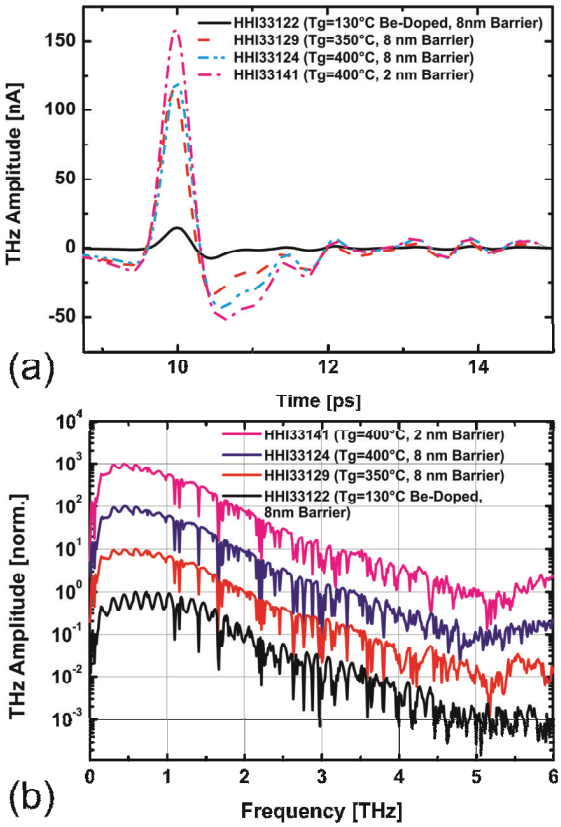

FIG. 4. Pulse traces (a) and corresponding Fourier spectra (b) obtained for 100 µm strip-line antennas made of samples listed in Table I. The receiver was a 10 µm dipole antenna made from sample HHI33122. Emitter bias was 10 kV/cm and 16 mW optical power for both, emitter and receiver. The spectra are shifted vertically for clarity.

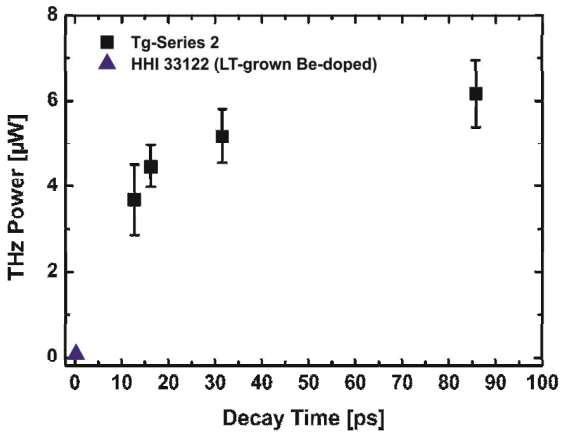

FIG. 5. Measured average THz power obtained from samples of T_g-Series 2 and the LT-grown Be-doped sample in dependence on the decay time obtained from DT measurements. The bias field strength was 10 kV/cm and 16 mW of optical power were used for all measurements.

In order to quantify the emitted THz power, the coherent receiver, i.e. the dipole antenna, was substituted with a Golay cell. For each sample of T_g-Series 2 and the d_B-Series several 100 µm strip-line antennas were tested in this setup to eliminate adjustment errors and possible fluctuations of antenna quality. We observe a clear increase of the average emitted THz power for samples with increasing decay time τ_2 for both sample series as shown in Figure 5 and 6.

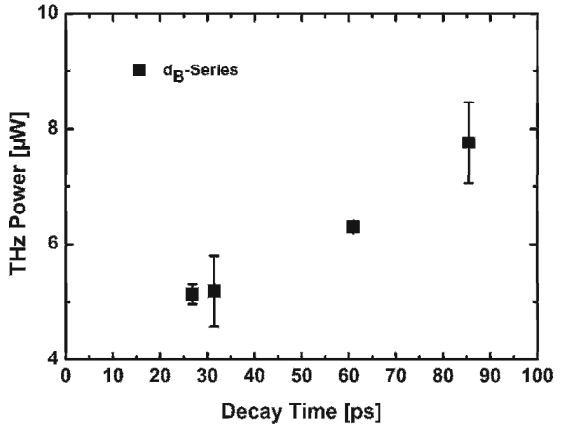

FIG. 6. Measured average THz power obtained from samples of the d_B-Series in dependence on the decay time obtained from DT measurements. The bias field strength was 10 kV/cm and 16 mW of optical power were used for all measurements.

Considering that the measured decay time of all samples (except HHI33122) is long compared to the time scale on which the THz radiation is produced, i.e. < 2 ps, this result is counterintuitive. However, this correlation does not necessarily mean that the underlying physical process is carrier capture. The decay time τ_2 can be considered an adequate measure of the trap state density in the InAlAs layers. Considering this, the decrease in THz emission can be explained in terms of an elastic scattering process of electrons that is trap density related and hence limiting the carrier mobility. There are two possible mechanisms for this scattering process. One is scattering due to surface roughness at the interfaces between InAlAs and InGaAs layers that is increased for increased clustering in the InAlAs layers. However, in case of the d_B-series this explanation would only be valid if surface roughness is strongly dependent on the InAlAs layer thickness which we assume is not the case. More plausible is elastic scattering directly at the defects within the InAlAs barrier. Other than a capture process, an elastic scattering process does not require the emission of phonons for the sake of energy conservation. An elastic scattering process is thus assumed to have a much higher probability than a capture process at the same defect state.

We like to point out, that complete removal of the InAlAs layers, i.e. bulk InGaAs, increases dark conductivity by several orders of magnitude due to the relatively high residual carrier concentration of InGaAs of $n \approx 10^{16}$ cm^{-3} and thus would render the application of sufficiently strong bias fields impossible. This is also the case for growth temperatures of $T_g \geq 450$ °C where the reduced density in the InAlAs barriers does not suffice to obtain an overall semi-insulating sample.

The maximum applicable field strength for 100 µm strip-line antennas reached up to 15 kV/cm. The dependence of the THz power on the optical excitation power emitted by antennas from samples HHI33122 and 33141 are given in Fig. 7. At 32 mW optical excitation we measured an average THz output power for the antenna from HHI33141 of 64 µW corresponding to an optical power-to-THz power conversion efficiency of 2×10^{-3}.

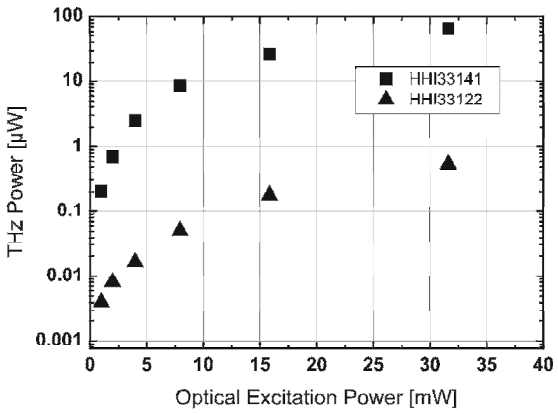

FIG. 7. Emitted THz power of a 100 µm strip-line antenna from sample HHI33141 and HHI33122 in dependence on the optical excitation power at a bias field of 15 kV/cm.

In conclusion we have shown that the carrier relaxation shows a (local) minimum at a growth temperature of around T_g = 350-375°C. Additionally the carrier relaxation time decreases when the barrier thickness is decreased. However, the emitted THz bandwidth has been shown to be mostly independent on the carrier relaxation time in the semiconductor and is hence governed by the excitation laser pulse width. Furthermore, the THz emission efficiency is reduced for increasing trap densities, which is associated with trap related elastic carrier scattering.

For optimal growth parameters of the semiconductor material we measured 64 µW of emitted average THz power for 32 mW of optical excitation. This corresponds to an achieved optical-to-THz conversion efficiency of 2×10^{-3} which is two orders of magnitude higher than values accessible with LT-grown Be-doped InGaAs/InAlAs MLHS and the highest value for InGaAs based emitters reported so far. This work was funded by the German Research Foundation (DFG).

[1] P.U. Jepsen, D.G. Cooke, and M. Koch, Laser & Photonics Reviews **5**, 124 (2011).
[2] M. Suzuki and M. Tonouchi, Applied Physics Letters **86**, 051104 (2005).
[3] B. Sartorius, H. Roehle, H. Künzel, J. Böttcher, M. Schlak, D. Stanze, H. Venghaus, and M. Schell, Optics Express **16**, 9565 (2008).
[4] A. Schwagmann, Z.-Y. Zhao, F. Ospald, H. Lu, D.C. Driscoll, M.P. Hanson, a. C. Gossard, and J.H. Smet, Applied Physics Letters **96**, 141108 (2010).
[5] C.D. Wood, O. Hatem, J.E. Cunningham, E.H. Linfield, a. G. Davies, P.J. Cannard, M.J. Robertson, and D.G. Moodie, Applied Physics Letters **96**, 194104 (2010).
[6] H. Roehle, R.J.B. Dietz, H.J. Hensel, J. Böttcher, H. Künzel, D. Stanze, M. Schell, and B. Sartorius, Optics Express **18**, 2296 (2010).
[7] R.J.B. Dietz, M. Gerhard, D. Stanze, M. Koch, B. Sartorius, and M. Schell, Optics Express **19**, 122 (2011).
[8] H. Künzel, J. Böttcher, R. Gibis, and G. Urmann, Applied Physics Letters **61**, 1347 (1992).
[9] J.E. Oh, P.K. Bhattacharya, and Y.C. Chen, Journal of Electronic Materials **19**, (1990).
[10] K. Biermann, D. Nickel, K. Reimann, M. Woerner, T. Elsaesser, and H. Künzel, Applied Physics Letters **80**, 1936 (2002).
[11] B. Grandidier, H. Chen, R.M. Feenstra, D.T. McInturff, P.W. Juodawlkis, and S.E. Ralph, Applied Physics Letters **74**, 1439 (1999).
[12] T.-A. Liu, M. Tani, and C.-L. Pan, Journal of Applied Physics **93**, 2996 (2003).

Publication II

B. Globisch, R. J. B. Dietz, D. Stanze, T. Göbel, and M. Schell, "Carrier dynamics in Beryllium doped low-temperature-grown InGaAs/InAlAs," Appl. Phys. Lett., vol.104, no. 17, 2014.

Carrier dynamics in Beryllium doped low-temperature-grown InGaAs/InAlAs

B. Globisch,[a),b)] R. J. B. Dietz,[a)] D. Stanze, T. Göbel, M. Schell
Fraunhofer Institute for Telecommunications, Heinrich Hertz Institute, Einsteinufer 37, 10587 Berlin, Germany

The electron and hole dynamics in low-temperature-grown (LTG) InGaAs/InAlAs multiple quantum well structures are studied by optical pump-probe transmission measurements for Beryllium (Be) doping levels between 3×10^{17} cm^{-3} and 4×10^{18} cm^{-3}. We investigate electron dynamics in the limit cases of unsaturated and completely saturated electron trapping. By expanding a rate equation model in these limits the details of carrier dynamics are revealed. Electrons are trapped by ionized arsenic antisites whereas recombination occurs between trapped electrons and holes trapped by negatively charged Be dopants.

Low-temperature (LT) growth of III-V compounds such as LTG-GaAs and LTG-InGaAs has become a widespread technique to fabricate semiconductors with sub-picosecond carrier lifetime.[1] The reduction of growth temperature leads to the incorporation of excess arsenic as point defects on Ga lattice sites (antisite defect, As_{Ga}), which form deep donor levels in the material.[1] In LTG-GaAs these defects are mid-bandgap[1,2] whereas As_{Ga} defects in LTG-InGaAs lie energetically close to the conduction band (CB) edge with activation energies around 30-40 meV.[3] The reduction of the electron lifetime in LTG material compared to standard temperature grown semiconductors is attributed to electron capture by ionized arsenic antisites (As_{Ga}^{+}). In LTG-GaAs the arsenic antisites are ionized by Ga vacancies[4] whereas ionization in LTG-InGaAs is mainly thermal due to the low activation energy of the defect.[3] This leads to highly n-conductive material at room temperature.[3] For compensation LTG-InGaAs is usually p-doped with Beryllium (Be). While LTG-GaAs has been studied extensively within the last decades, there are only few investigations of the carrier dynamics in Be doped LTG-InGaAs based structures. However, photoconductors fabricated from LTG-InGaAs/InAlAs have become a standard emitter and detector material for THz time domain spectroscopy (THz-TDS) within the last years.[5,6] In LTG-InGaAs/InAlAs the fast carrier capture is supposed to occur in the InGaAs, whereas the InAlAs barriers increase the resistivity of the structure by trapping of the residual carriers.[5,7] Since THz-TDS bears great potential for future applications in industrial processes improved photoconductors are highly desirable.

In this letter we reveal the fundamental processes of electron and hole capture in Be-doped LTG-InGaAs/InAlAs heterostructures by combining pump power dependent differential transmission (DT) measurements with a rate equation model. In our experiments we investigate a series of five samples of 130 °C MBE grown InGaAs/InAlAs structures. Each sample features 100 periods of 12 nm InGaAs and 8 nm InAlAs grown on top of an InAlAs buffer layer and a semi-insulating InP substrate. The InGaAs/InAlAs layers were homogeneously Be-doped with nominal concentrations of 3×10^{17} cm^{-3}, 9×10^{17} cm^{-3}, 2×10^{18} cm^{-3}, 4×10^{18} cm^{-3} and an undoped reference. After MBE growth the samples were in-situ annealed for 60 min. at 500°C.

The electron density obtained from Hall measurements is shown in Fig. 1. The horizontal, dashed line indicates the free electron concentration of an undoped, standard temperature grown (STG, $T_G \approx 500$°C), 1.1 µm thick InGaAs sample. Since no excess arsenic is incorporated at 500°C this line indicates the background doping level. The free electron concentration of the undoped LTG material is more than two orders of magnitude higher than in the STG material. This is caused by thermally ionized arsenic antisite defects.[3] Be-doping with a nominally concentration of 3×10^{17} cm^{-3} reduces the electron density to the level of the STG sample. Since the reduction of free electron density and the doping concentration between the undoped and the 3×10^{17} cm^{-3} doped sample features the same order of magnitude Be compensates the excess arsenic. For higher doping levels the electron concentration is further reduced but no transition to p-conductivity is observed. Grandidier et al.[8] explained this effect by the additional compensatory behavior of Beryllium. The authors estimated the total number of As_{Ga} defects in p-doped LTG-InGaAs material to 3×10^{19} cm^{-3}.

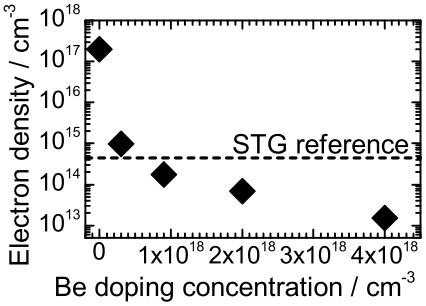

Fig. 1. Electron density vs. Be doping concentration of LTG-InGaAs/InAlAs. The horizontal, dashed line indicates the free electron concentration of undoped, 500 °C grown, 1.1 µm thick InGaAs.

[a)] B. Globisch and R. J. B. Dietz contributed equally to this work.
[b)] Electronic mail: Bjoern.Globisch@hhi.fraunhofer.de.

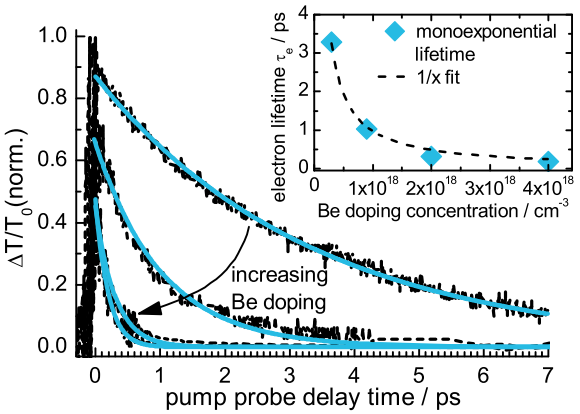

Fig. 2. Low pump power (≈2 pJ) DT-signals of LTG-InGaAs/InAlAs (a) and extracted mono-exponential electron lifetime vs. Be doping concentration (inset). Light blue lines indicate mono-exponential fits. Dashed line in the inset is 1/x fit to the data.

Hence, Be-doping concentrations higher than the density of free electrons in the undoped material lead to the ionization of additional arsenic antisites. This lowers the Fermi-level of the material but the conductivity remains n-type. In contrast, the authors of Ref. 5 observed a transition to p-type conductivity for increased Be-doping. We attribute this to the increased growth temperature of 200°C for their samples. This leads to a higher concentration of Gallium vacancies which facilitates the redistribution of As_{Ga} defects during anneal.

In order to investigate the influence of Be-doping on carrier dynamics after transient optical excitation wavelength degenerate DT measurements were performed. We used a 1550 nm erbium doped fiber laser with 100 MHz repetition rate and 90 fs optical pulse width for pump and probe, respectively. All samples had been processed into 10 µm mesa-type structures according to Ref. 6. This ensures homogenous illumination of the sample for laser spot diameters of about 12 µm. Pump and probe beam were cross polarized and incident under an angle of 15° to the surface normal. The transmission change of the probe beam was measured by an InGaAs photodetector via lock-in detection.

Since the ionized arsenic antisite is the dominant trapping center in the material, we expect the lifetime of electrons in the CB to decrease for higher As_{Ga}^{+} density. Since the Hall results of our samples suggest that increased Be-doping increases the As_{Ga}^{+} density a lifetime decrease proportional to the Be-doping concentration is expected. In order to measure this in DT experiments the number of electrons excited by the pump pulse has to be small compared to the total number of electron traps in order to avoid any saturation or carrier accumulation effects. Therefore, the optical pump pulse energy in the subsequent DT experiments was set to 2 pJ corresponding to about 3.0×10^{16} cm^{-3} of excited electrons. This is at least one order of magnitude smaller than the Be-doping concentration of all samples.

The normalized low power DT signals are plotted in Fig. 2. Light blue lines correspond to mono-exponential fits. The exponential decay time τ_e was extracted from each fit and plotted against Be doping concentration in the inset. The reduction of τ_e from 3.3 ps for Be: 3×10^{17} cm^{-3} to below 200 fs for Be: 4×10^{18} cm^{-3} is nicely described by a 1/x-fit (dashed black line). This confirms that electron trapping becomes faster for higher Be-doping. Hence, the doping concentration is a direct measure of the density of electron traps, i.e. As_{Ga}^{+} defects.[9]

The electron capture process saturates when the optical pump pulse excites electron densities in the CB that exceed the number of traps since the trapping is orders of magnitudes faster than the recombination of trapped electrons. In our DT experiments 160 pJ pump pulse energy corresponds to approximately 4×10^{18}cm^{-3} of excited electrons. Hence, strong saturation of the DT-signal can be observed for the samples with the lowest concentration of electron traps, i.e. lowest Be-doping, in Fig. 3(a). The signal decay time for the 3×10^{17} cm^{-3} and 9×10^{17} cm^{-3} doped samples increases to values above 200 ps and 100 ps, respectively, whereas the highest doped samples keep their picosecond or sub-picosecond decay. In order to investigate the development of this saturation Figs. 3(b)-(c) show DT-signals for various pump pulse energies (dashed black lines). Two regimes can be identified for the highest pump pulse energies: An initial fast decay within the first few picoseconds and a slow linear feature (i.e. mono-exponential decay in a linear plot) for pump probe delays above 20 ps. Since the initial fast decay is attributed to electron trapping the fraction of the fast decay scales with the difference between excited electrons and available As_{Ga}^{+} defects. In Fig. 3(b) higher optical pump power reduces the fraction of the fast decay component due to the faster saturation of trapping centers when more electrons are optically excited. The higher Be doping concentration of 9×10^{17}cm^{-3} in Fig. 3(c) attenuates the onset of saturation features since the increased number of trapping centers reduces the difference between traps and electrons in the CB. Hence, the behavior of the fast component in the DT-signals of Figs. 3 can be described within the picture of trapping saturation. The slow, linear features in the DT-signals, which appear for low doping and high optical pump power, are interpreted as complete filling of trapping centers. In this regime the slope of the saturation is a direct measure for the recombination time in the corresponding sample. Fig. 3(a) suggests that higher Be doping accelerates recombination. This is unexpected within the common model of electron recombination. When all the As_{Ga}^{+} defects are occupied by trapped electrons recombination is supposed to take place between neutral arsenic antisites (As_{Ga}) and free holes in the valence band (VB). Since Be doping does not enhance the number of As_{Ga} defects[7] nor the density of free holes a faster recombination for higher doping is not expected. In order to explain the results of Figs. 3 Be dopants have

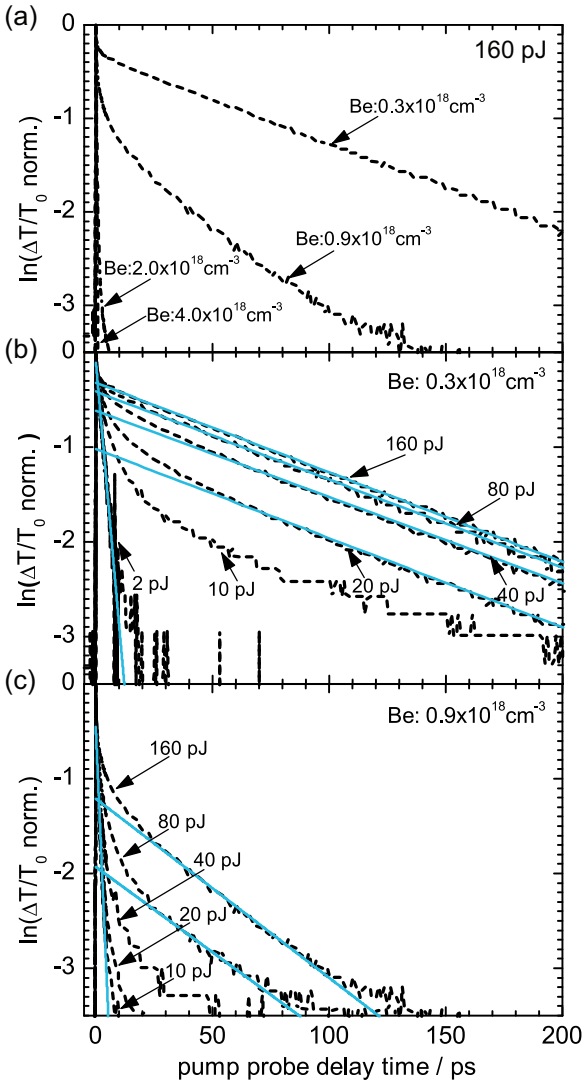

Fig. 3. Natural logarithm of normalized DT-signals for 160 pJ pump pulse energy (a). Curves are labeled by the corresponding Be-doping concentration. Pump power dependent DT-signals for LTG-InGaAs/InAlAs with Be doping concentration of 0.3×10^{18}cm^{-3} (b) and 0.9×10^{18}cm^{-3} (c). Bold lines are linear fits to the long time tail of each signal. Curves are labeled by the energy of the pump pulse.

to assist in electron recombination. This is most probably due to direct recombination between electrons captured by ionized antisites and holes captured by negatively charged Be dopants. In order to confirm this conclusion and to analyze the electron and hole dynamics we developed a rate equation model, which is described in the following.

The time dependent transmission of a semiconductor with thickness L and linear absorption coefficient α can be written as:

$$T(t) = T_0 \exp(\alpha L\, n(t)/N_0). \qquad (1)$$

Here, the constant N_0 is the saturation carrier density, i.e. the density of states in the CB integrated over the laser bandwidth. $T_0 = \exp(-\alpha L)$ denotes static, linear transmission and $n(t)$ is the time dependent occupation of the CB. Thus, the DT reads:

$$\frac{\Delta T(t)}{T_0} = \frac{T(t)-T_0}{T_0} = \exp\left(\alpha L \frac{n(t)}{N_0}\right) - 1, \qquad (2)$$

where $n(t)$ is determined via the following coupled rate equations:

$$\frac{dn}{dt} = G(t,n) - \frac{n}{\tau_e}\left(1 - \frac{n_T}{N_{As}^+}\right) \qquad (3a)$$

$$\frac{dn_T}{dt} = \frac{n}{\tau_e}\left(1 - \frac{n_T}{N_{As}^+}\right) - B_R\left(N_{As} - N_{As}^+ + n_T\right)n_{Be} \qquad (3b)$$

$$\frac{dn_{Be}}{dt} = \frac{h}{\tau_h}\left(1 - \frac{n_{Be}}{N_{As}^+}\right) - B_R\left(N_{As} - N_{As}^+ + n_T\right)n_{Be} \qquad (3c)$$

$$\frac{dh}{dt} = G(t,n) - \frac{h}{\tau_h}\left(1 - \frac{n_{Be}}{N_{As}^+}\right). \qquad (3d)$$

Here, $n_T(t)$ denotes the occupation of the ionized arsenic antisites (electron traps) and $n_{Be}(t)$ is the occupation of ionized Be dopants (hole traps). We assume that the total number of electron and hole traps is determined by the Be doping concentration and use the parameter N_{As}^+ for both quantities. The number of free holes in the VB is given by $h(t)$. All parameters appearing in Eqs. 3 are listed in Table I. Electrons in the CB and holes in the VB are created by an optical femtosecond laser pulse via the electron/hole generation rate $G(t,n)$. The density dependence of G accounts for the limited density of states in the CB. Free electrons in the CB and free holes in the VB are trapped by ionized arsenic antisites and ionized Be dopants, respectively. The terms $1-n_T/N_{As}^+$ and $1-n_{Be}/N_{As}^+$ account for the partial filling of these traps. Carrier recombination is modeled as a two particle process with recombination rate B_R between neutral arsenic antisites ($N_{As}-N_{As}^+ + n_T$) and neutral Be dopants (n_{Be}). In order to model the results of our DT measurements Eqs. 3 were analyzed in three limit cases. First, we considered low-power optical excitation comparable to the experimental situation of Fig. 2. Here, the density of excited carriers in the CB is small compared to the density of electron traps, i.e. $n_T(t)/N_{As}^+ << 1$ for all t. In this regime Eq. (3a) and Eq. (3b) decouple since the saturation term $1-n_T/N_{As}^+$ reduces to unity. Hence, $n(t)$ decays mono-exponentially with time constant τ_e. In addition, Eq.(2) can be expanded for small exponents since $n_T(t)/N_0 << 1$:

$$\Delta T(t) \approx \alpha L\, n(t)/N_0 \propto \exp(-t/\tau_e). \qquad (4)$$

Hence, in the low power regime, the DT signal decays

TABLE I: Parameters of Eqs. 3.

N_{As}	total number of arsenic antisites
N_{As}^+	number of initially ionized antisites
G	electron/hole generation rate
B_R	electron/hole recombination rate
τ_e	electron capture time
τ_h	hole capture time

mono-exponentially and the decay time is the electron capture time τ_e. Together with the results of Fig. 2 the electron capture cross section σ_e^{As+} of the ionized arsenic antisite can be deduced from Shockley-Read-Hall theory:[11]

$$\tau_e = \left(\sigma_e^{As^+} v_e^{th} N_{As}^+\right)^{-1}, \qquad (5)$$

where $v_e^{th} = 5.5\times10^7$ cm/s is the thermal velocity of electrons in the CB, yielding $\sigma_e^{As+} \approx 2\times10^{-14}$ cm^2. Lochtefeld et al.[12] determined the electron capture cross section of the ionized arsenic antisite in LTG-GaAs to $\sigma_e^{As+} \approx 0.7\times10^{-14}$ cm^2. Since electrons in LTG-GaAs and LTG-InGaAs/InGaAs are captured by the same defect, similar values of σ_e^{As+} are reasonable.

Next, Eqs. 3(a-d) were expanded under trap saturation conditions in order to model the experimental situation of Figs. 3. In this regime the density of electrons excited by the optical pump pulse is considerably higher than the number of electron traps N_{As}^+. Since electron and hole trapping is assumed to be more than one order of magnitude faster than electron/hole recombination trapping centers will fill up continuously. The limit of this trap saturation process is reached when each electron/hole trap is occupied. In this regime the decay of the electron population in the CB is determined by the electron/hole recombination rate B_R, since each recombined electron-hole pair is directly replaced by a free electron/hole. When Eqs. 3 are expanded in this limit case, i.e. $dn_T/dt = dn_{Be}/dt = 0$, the following expression for the density of electrons in the CB is obtained:[13]

$$n^{sat}(t) \approx n_0^{sat} - B_r N_{As}^+ N_{As} t\,. \qquad (6)$$

Here, n_0^{sat} denotes the occupation of the CB when complete saturation of the As_{Ga}^+ traps occurs. The superscript *sat* indicates that Eq. (6) is only valid when electron and hole traps are saturated. Eq. (6) predicts a linear decrease of the electron density in the CB. The decay becomes faster when the number of electron traps (N_{As}^+) and the number of antisites (N_{As}) increases. In addition, the carrier recombination rate B_R determines the electron dynamic in the CB instead of τ_e. Combining Eq. (6) and Eq. (2) a mono-exponential decay of the DT is predicted and the decay constant is proportional to N_{As}^+ and hence the Be doping concentration. This is identical to the behavior observed in the measurements. The saturation tail of the DT in Figs. 3 decays mono-exponentially and the decay time decreases for higher doping. Hence, the modeling together with the experimental data suggest that negatively charged Be dopants capture holes from the VB and recombination occurs between trapped electrons and trapped holes.

Finally, Eqs.(3) were analyzed in the regime of partial trap filling. In this case the number of excited electrons in the CB is supposed to be smaller than N_{As}^+ but high enough to reduce the number of electron traps significantly. Since electron trapping is still fast compared to the recombination process the last term on the right hand side of Eq. (3b) does not contribute on the timescale of the electron dynamics. Therefore, the coupling of Eq. (3b) and Eq. (3c) is resolved and Eq. 3(a) and Eq. 3(b) can be solved analytically:[13]

$$n(t) \approx n_{ex} \exp\left\{-\left(1-\frac{n_{ex}}{N_{As}^+}\right)\frac{t}{\tau_e}\right\}, \qquad (7)$$

with n_{ex} being the number of electrons excited by the optical pump pulse. The factor $1-n_{ex}/N_{As}^+$ describes the enhancement of the electron lifetime τ_e when n_{ex} is on the order of N_{As}^+. This behavior is illustrated in Fig. 4 for the LTG-InGaAs/InAlAs sample with 4×10^{18}cm^{-3} Be doping concentration.

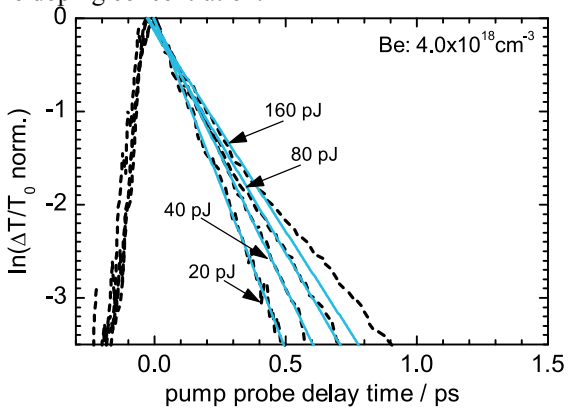

Fig. 4. Natural logarithm of the normalized DT signal for the LTG-InGaAs/InAlAs sample with 4×10^{18}cm^{-3} Be doping concentration. Symbols are equal to Fig. 3(b),(c).

Due to the high doping of this sample the condition of partial trap filling is valid even for high optical pump pulse energy. For 160 pJ, the DT-signal deviates from the mono-exponential trend indicating that a significant number of electron traps are filled and the approximations of Eq. (7) loose validity.

In summary, we have analyzed the carrier dynamics of Be doped LTG-InGaAs/InAlAs samples by power dependent DT measurements. Our results show that electrons are captured by ionized arsenic antisite defects with capture cross section $\sigma_e^{As+} \approx 2\times10^{-14}$ cm^2. High power DT measurements, which induce strong trap saturation in the material, imply that trapped electrons do not recombine with free holes in the VB as has been commonly assumed. Instead, recombination occurs with neutral Be dopants, that have captured the VB holes. Hence, Be doping does not only compensate the high electron density in LTG-InGaAs/InAlAs, but accelerates electron capture and electron recombination in the material. Therefore, it is an important mechanism to fabricate semiconductors with low carrier lifetime and high resistivity, properties that are desired for fast photoconductive switches.

[1] S. Gupta, J. F. Whitaker, G. A. Mourou, IEEE J. Quantum Electron., **28** (10), pp. 2464-2472 (1992).
[2] S. D. Benjamin, H. S. Loka, A. Othonos, P. W. E. Smith, Appl. Phys. Lett., **68,** 2544 (1996).
[3] H. Künzel, J. Böttcher, R. Gibis, G. Urmann, Appl. Phys. Lett **61**, 1347 (1992).
[4] M. Luysberg, H. Sohn, A. Prased, P. Specht, Z. Liliental-Weber, E. R. Weber, J. Gebauer, R. Krause-Rehberg, J. Appl. Phys. **83**, 561-566 (1998).

[5] B. Sartorius, H. Roehle, H. Künzel, J. Böttcher, M. Schlak, D. Stanze, H. Venghaus, M. Schell, Opt. Express, 16 (13), 9565 (2008).
[6] H. Roehle, R. J. B. Dietz, H. J. Hensel, J. Böttcher, H. Künzel, D. Stanze, M. Schell, B. Sartorius, Opt. Express, **18** (3), 2296 (2010).
[7] R. J. B. Dietz, B. Globisch, M. Gerhard, A. Velauthapillai, D. Stanze, H. Roehle, M. Koch, T. Göbel, M. Schell, Appl. Phys. Lett. **103** 061103 (2013).
[8] B. Grandidier, Huajie Chen, R. M. Feenstra, D. T. McInturff, P. W. Juodawlkis, S. E. Ralph, Appl. Phys. Lett. **74**, 1439 (1999).
[9] In Ref. 10 the same relation between absorption recovery time and Be doping concentration was observed. However, the authors assumed that carrier trapping occurs by complexes consisting of Be acceptors and excess arsenic donors. In scanning tunneling microscopy experiments Grandidier et. al[8] have not observed any of these Be-As complexes. Instead, the authors suggested the theory of additional compensation by Be acceptors. Therefore, we interpret our DT data on the basis of this theory.
[10] R. Takahashi, Y. Kawamura, T. Kagawa, H. Iwamura, Appl. Phys. Lett. **65**, 1790 (1994).
[11] W. Shockley, W. T. Read, Phys. Rev. **87** (5), 835 (1952).
[12] A. J. Lochtefeld, M. R. Melloch, J. C. P. Chang, E. S. Harmon, Appl. Phys. Lett. **69**, 1465 (1996).
[13] See supplemental material for details of the derivation of Eq. (6) and Eq. (7).

Publication III

R. J. B. Dietz, B. Globisch, H. Roehle, D. Stanze, T. Göbel, and M. Schell, "Influence and adjustment of carrier lifetimes in InGaAs/InAlAs photoconductive pulsed terahertz detectors: 6 THz bandwidth and 90dB dynamic range," Opt. Express,vol. 22, no. 16, pp. 19411–19422, 2014.

Influence and adjustment of carrier lifetimes in InGaAs/InAlAs photoconductive pulsed terahertz detectors: 6 THz bandwidth and 90dB dynamic range

Roman J.B. Dietz,[1,2,*] Björn Globisch,[1,2] Helmut Roehle,[1] Dennis Stanze,[1] Thorsten Göbel,[1] and Martin Schell[1]

[1]*Fraunhofer Institute for Telecommunications, Heinrich-Hertz-Institute, Einsteinufer 37,10587 Berlin, Germany*
[2]*Authors contributed equally*
[*]*Roman.Dietz@hhi.fraunhofer.de*

Abstract: We investigate the influence of Beryllium (Be) doping on the performance of photoconductive THz detectors based on molecular beam epitaxy (MBE) of low temperature (LT) grown $In_{0.53}Ga_{0.47}As/In_{0.52}Al_{0.48}As$ multilayer heterostructures (MLHS). We show how the optical excitation power affects carrier lifetime, detector signal, dynamic range and bandwidth in THz time domain spectroscopy (TDS) in dependence on Be-doping concentration. For optimal doping we measured a THz bandwidth in excess of 6 THz and a dynamic range of up to 90 dB.

OCIS codes: (040.2235) Far infrared or terahertz; (260.5150) Physical optics: Photoconductivity; (300.6495) Spectroscopy: Spectroscopy, terahertz; (320.7130) Ultrafast processes in condensed matter, including semiconductors.

References and links

1. H. Roehle, R. Dietz, B. Sartorius, and M. Schell, "Fiber-coupled terahertz TDS combining high speed operation with superior dynamic range," 37th Int. Conf. Infrared, Millimeter, Terahertz Waves, 1-2 (2012).
2. P. Jepsen, D. G. Cooke, M. Koch, "Terahertz spectroscopy and imaging – Modern techniques and applications," Laser Photonics Rev. **5**, 124 (2011), http://onlinelibrary.wiley.com/doi/10.1002/lpor.201000011/abstract.
3. M. Suzuki, M. Tonouchi, "Fe-implanted InGaAs terahertz emitters for 1.56 μm wavelength excitation," Appl. Phys. Lett. **86** (5), 051104 (2005). http://link.aip.org/link/doi/10.1063/1.1861495.
4. B. Sartorius, H. Roehle, H. Künzel, J. Böttcher, M. Schlak, D. Stanze, H. Venghaus, and M. Schell, "All-fiber terahertz time-domain spectrometer operating at 1.5 μm telecom wavelengths," Opt. Express **16** (13), 9565-9570 (2008) http://www.opticsinfobase.org/abstract.cfm?URI=oe-16-13-9565.
5. A. Schwagmann, Z.-Y. Zhao, F. Ospald, H. Lu, D. C. Driscoll, M. P. Hanson, A. C. Gossard, and J. H. Smet," Terahertz emission characteristics of ErAs:InGaAs-based photoconductive antennas excited at 1.55μm," Appl. Phys. Lett. **96** (14), 41108 (2010) http://link.aip.org/link/doi/10.1063/1.3374401.
6. C. D. Wood, O. Hatem, J. E. Cunningham, E. H. Linfield, A. G. Davies, P. J. Cannard, M. J. Robertson, and D. G. Moodie, "Terahertz emission from metal-organic chemical vapor deposition grown Fe:InGaAs using 830 nm to 1.55 μm excitation," Appl. Phys. Lett. **96** (19), 194104 (2010).
7. H. Roehle, R. J. B. Dietz, H. J. Hensel, J. Böttcher, H. Künzel, D. Stanze, M. Schell, and B. Sartorius, "Next generation 1.5 μm terahertz antennas: mesa-structuring of InGaAs/InAlAs photoconductive layers," Opt. Express **18** (3), 2296–2301 (2010) http://www.opticsinfobase.org/oe/abstract.cfm?URI=oe-18-3-2296.
8. R.J.B. Dietz, M. Gerhard, D. Stanze, M. Koch, B. Sartorius, and M. Schell, "THz generation at 1.55 μm excitation: six-fold increase in THz conversion efficiency by separated photoconductive and trapping regions," Opt. Express **19** (27), 122-126 (2011).

9. R.J.B. Dietz, B. Globisch, M. Gerhard, A. Velauthapillai, D. Stanze, H. Roehle, M. Koch, T. Göbel, and M. Schell, "64 µW pulsed THz emission from growth optimized InGaAs/InAlAs heterostructures with separated photoconductive and trapping regions," Appl. Phys. Lett. **103** (6), 061103 (2013).
10. P. Uhd Jepsen, R. H. Jacobsen, and S. R. Keiding, "Generation and detection of terahertz pulses from biased semiconductor antennas," J. Opt. Soc. Am. B **13** (11), 2424-2436 (1996) http://www.opticsinfobase.org/abstract.cfm?URI=josab-13-11-2424.
11. L. Duvillaret, F. Garet, J. F. Roux, and J.-L. Coutaz, "Influence of noise on the characterization of materials by terahertz time-domain spectroscopy," IEEE J. Quantum Electron., **7** (4), 615-623 (2001).
12. E. Castro-Camus, M. B. Johnston, J. Lloyd-Hughes, "Simulation of fluence-dependent photocurrent in terahertz photoconductive receivers," Semicond. Sci. Technol. **27** (11), 115011 (2012).
13. B. Globisch, R.J.B. Dietz, D. Stanze, R. Roehle, T. Göbel, and M. Schell, "Carrier dynamics in Beryllium doped low-temperature-grown InGaAs/InAlAs," Appl. Phys. Lett. **104** (17), 172103 (2014).
14. B. Grandidier, Huajie Chen, R. M. Feenstra, D. T. McInturff, P. W. Juodawlkis, and S.E. Ralph, "Scanning tunneling microscopy and spectroscopy of arsenic antisites in low temperature grown InGaAs," Appl. Phys. Lett. **74** (10), 1439 (1999).
15. L. Duvillaret, F. Garet, and J. Coutaz, "Influence of noise on the characterization of materials by terahertz time-domain spectroscopy," J. Opt. Soc. Am. B **17** (3), 452-461 (2000).
16. P. Jepsen, B. Fischer, "Dynamic range in terahertz time-domain transmission and reflectionspectroscopy," Opt. Lett. **30** (1), 29-31 (2005).
17. M. Van Exter, D. Grischkowsky, "Characterization of an optoelectronic terahertz beam system," IEEE Trans. Microw. Theory Techn., **38** (11), 1684-1691 (1990).
18. E. Castro-Camus, L. Fu, J. Lloyd-Hughes, H. H. Tan, C. Jagadish, and M. B. Johnston, "Photoconductive response correction for detectors of terahertz radiation," J. Appl. Phys., **104** (5), 053113 (2008).

1. Introduction

Over the past decade, terahertz time domain spectroscopy (THz TDS) has matured from pure scientific research and expensive laboratory sized setups to industrial applications and compact, portable THz-TDS systems [1]. Therefore, many future applications for terahertz technology have come into close reach [2]. A great portion of this development originates from the utilization of readily available Er-doped femtosecond fiber lasers at 1550 nm wavelength, of-the-shelf telecom components, and the design of suitable photoconductive antennas (PCAs) [3-7]. More recently, progress has been made concerning photoconductive THz emitters based on InGaAs/InAlAs multi-layer heterostructures (MLHS) [8]. Here, MBE growth at substrate temperatures of approx. 375-400 °C together with an adjusted heterostructure design led to good optical-to-THz conversion efficiencies with output powers up to 64 µW [9]. However, the results of principal physical models of THz generation and detection predict that material development for emitters and receivers has to be done separately, since the main requirements are different [10-12]. The goal of this paper is the careful investigation of how the interplay of carrier lifetime and carrier mobility in PCA detectors influences THz bandwidth, dynamic range and detector noise. Therefore, we investigated four different samples of low temperature (LT) grown Beryllium (Be)-doped InGaAs/InAlAs MLHS with different nominal Be-doping concentrations of 0.3×10^{18} cm^{-3}, 0.9×10^{18} cm^{-3}, 2.0×10^{18} cm^{-3} and 4.0×10^{18} cm^{-3} (cf. Table 1). To obtain a detailed picture of the carrier trapping, carrier recombination and trap saturation dynamics, the samples were probed via differential transmission (DT) measurements at different pump pulse powers. A detailed presentation of the results on the DT measurements performed with these samples and their theoretical interpretation has been published in [13]. After giving a brief overview on these DT results for illustration, this paper focuses on the influence of carrier dynamics and carrier lifetime on PCA detector performance in a THz-TDS system made from the exact same samples.

2. Influence of Beryllium Doping on the Carrier Lifetime

The dominating mechanism of electron relaxation from the conduction band (CB) in LT-grown Be-doped InGaAs/InAlAs MLHS is phonon-assisted electron capture into arsenic anti-

site defects (As_{Ga}) and subsequent recombination with a hole. More precisely, electron capture is dominated by the part of the arsenic antisite defects that has been positively ionized (As_{Ga}^{+}) due to doping with Be-acceptors and hence lowering the Fermi level. Since, to a good approximation, every Be-dopant ionizes one As_{Ga} defect, the density of fast traps is equal to the Be-doping concentration [13, 14]. The time constants for the electron capture process are typically on the order of a few hundred femtoseconds (fs) to picoseconds (ps) depending on the As_{Ga}^{+} density. The time constant for the recombination process of electrons captured in As_{Ga} defects with holes is on the order of a few tens of ps to hundreds of ps. As pointed out in [13], there is strong evidence that the recombination occurs with holes captured by Be-dopants rather than with free holes in the valence band (VB) and hence is also dependent on the Be-doping concentration. However, even for high doping concentrations the recombination time remains on the order of several tens of picoseconds. The excitation source for all DT and THz-TDS measurements was a mode-locked fiber ring laser with a center wavelength of 1550 nm, a pulse width of approx. 90 fs and 100 MHz repetition rate. The excitation spot size was approx. 12 µm for both DT and THz TDS measurements in order to obtain similar excitation conditions for a quantitative comparison between both measurements. Additionally, all the samples were structured with mesa-type dipole antennas with a 10 µm×10 µm photoconductive gap. Hence, the optically excited photoconductive region was precisely defined for both measurement methods.

The results obtained from DT measurements at 1550 nm pump and probe wavelength are given in Fig. 1(a), Fig. 1(b) and Fig. 1(c) for a low (0.25 mW), intermediate (2 mW) and a high pump power (16 mW), respectively. These excitation powers correspond to carrier densities in the CB directly after fs-excitation of approx. $1\times10^{17}\,cm^{-3}$, $6.5\times10^{17}\,cm^{-3}$ and $1.28\times10^{18}\,cm^{-3}$, respectively. For the calculation of these carrier densities, the absorption saturation due to the limited density of states in the CB over the photon energies covered by the excitation laser pulse was taken into account.

For 0.25 mW pump power none of the samples shows significant trap filling as the induced carrier density in the CB is a least a factor of three smaller than the As_{Ga}^{+} density of every sample. Thus the absorption relaxation, i.e. the DT signal, can be fitted by assuming a mono exponentially declining carrier density within the CB. The respective fit results for the electron lifetime from the DT data are given in Table 1, the corresponding capture cross section according to Shockley-Read-Hall theory for the As_{Ga}^{+} defects was determined to $\sigma_e^{As+}\approx2\times10^{-14}\,cm^2$ [13].

Sample	T_g [°C]	Be-doping [cm^{-3}]	Unsaturated capture time [ps]	Scattering time from Hall mobility data [fs]
MLHS 1	130	0.3×10^{18}	3.29	50.15
MLHS 2	130	0.9×10^{18}	1.03	24.76
MLHS 3	130	2×10^{18}	0.32	10.36
MLHS 4	130	4×10^{18}	0.19	6.882

Table 1. List of samples used as detectors in THz-TDS Setup with respective growth and DT parameters.

For the intermediate pump power of 2 mW MLHS 1 already shows a very slow absorption recovery. This is because the induced carrier density in the CB is on the same order as the available As_{Ga}^{+} trap density, i.e. $\approx0.3\times10^{18}\,cm^{-3}$. Hence, the DT signal is dominated by the recombination time of electrons in As_{Ga} defects with holes captured by Be-dopants, since this process forms a bottleneck for the carrier relaxation. MLHS 2 shows a slightly increased absorption recovery time which is caused by partial filling of the available As_{Ga}^{+} traps.

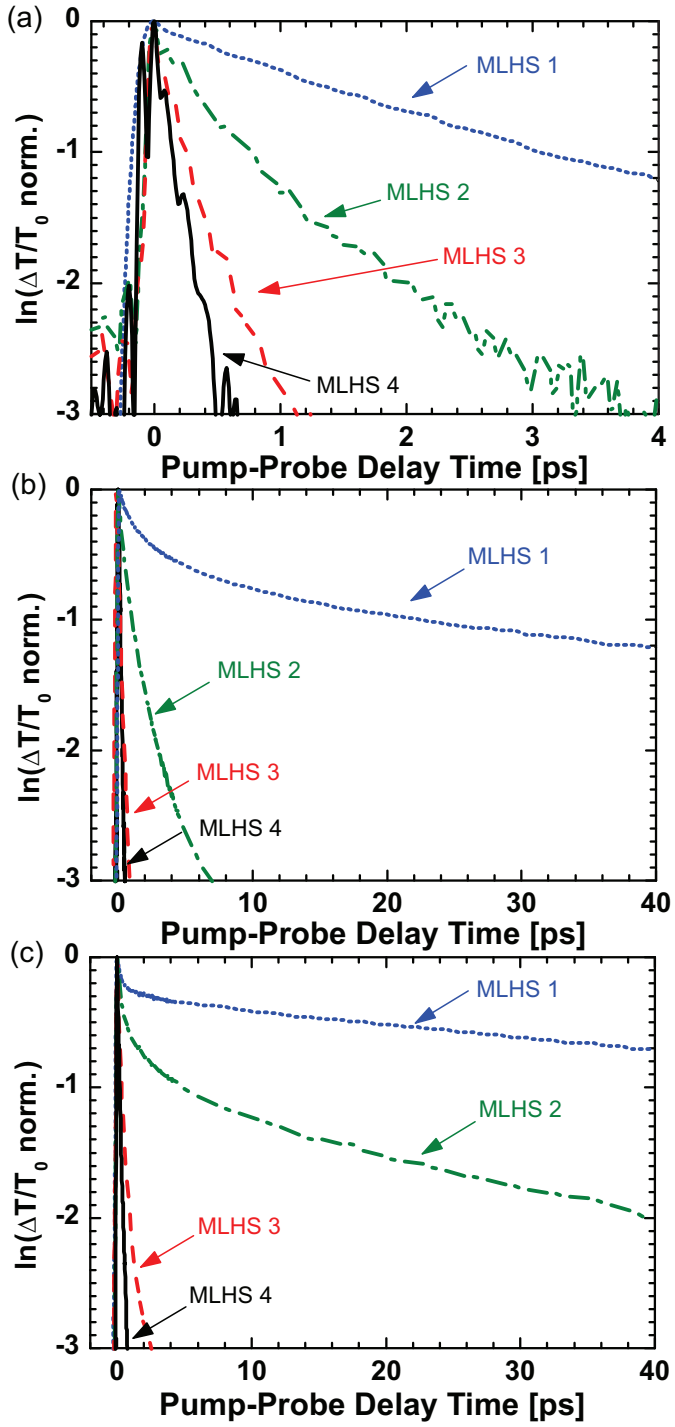

Fig 1. Plot of the logarithmic DT signals measured for (a) 0.25 mW, (b) 2 mW and (c) 16 mW pump power for all four different doping levels. At 0.25 mW all signals decay mono-exponentially. At 2 mW, there is an onset of trap saturation for MLHS 2 and 1, respectively. For 16 mW, both MLHS 1 and 2 show strong trap saturation, while MLHS 3 and 4 only show minor partial trap filling.

MLHS 3 and 4 show no significant increase of absorption recovery time due to the high amount of As_{Ga}^{+} that still exceeds the density of electrons in CB at this excitation power.
For 16 mW pump power [Fig. 1(c)], the samples MLHS 1 and 2 both show strong As_{Ga}^{+} trap saturation and thus very long relaxation times in the DT signal, again governed by the electron-hole recombination time. The DT signal of MLHS 3 shows a slight deviation from a mono-exponential decay and an increased carrier lifetime due to partial trap filling. MLHS 4 still shows almost no change in the DT signal since the density of As_{Ga}^{+} traps, i.e. $n_t \approx 4\times10^{18}\,cm^{-3}$, is still significantly higher than the excited carrier density in the CB of $n_e \approx 1.28\times10^{18}\,cm^{-3}$.

3. Influence of the Optical Power on the detected THz Signal and Bandwidth

For further investigation of the influence of the Be-doping concentration and the resulting carrier dynamics on the THz detection properties, we performed THz-TDS measurements in dependence of the optical power at the detector. The photoconductive THz emitter used for the measurements in this chapter was a strip-line mesa-antenna with 25 µm gap made from the $4.0\times10^{18}\,cm^{-3}$ Be-doped sample MLHS 4. For all measurements the applied bias was 50 V at an optical excitation power of 25 mW. For an efficient out-coupling of the THz radiation, the emitter and the respective detectors were attached to hyper-hemispherical HRFZ silicon substrate lenses. Furthermore, two off-axis parabolic mirrors for THz collimation and focusing were used.
The peak-to-peak signals obtained from THz-TDS measurements for the case of low excitation power (0.25 mW) are given in Fig. 2. In this low carrier density regime, the potential influence of THz field screening by free carriers in the CB and VB can be safely neglected leaving only two main influences to the current signal. One is the carrier scattering time (cf. Table 1) which limits carrier velocity and hence the detector current. The other influence is the carrier capture time which limits the integrated detector current, i.e. the value of the convolution integral in TDS detection Eq. (1). The scattering time extracted from Hall mobility data and the unsaturated carrier capture time from DT measurements at 0.25 mW are also shown in Fig. 2. It should be noted that the carrier capture time enters the carrier scattering time via Matthiessens rule since carrier capture is inelastic scattering.

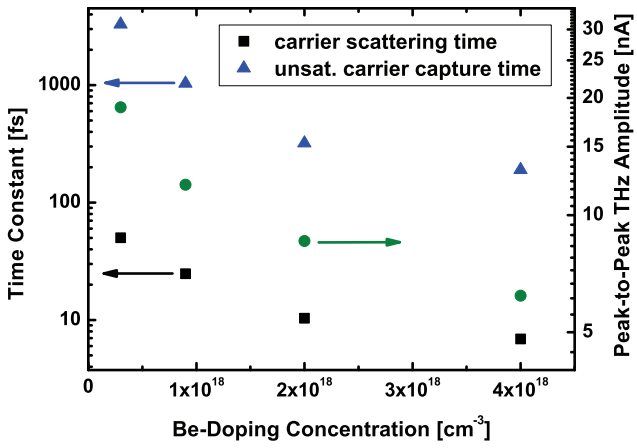

Fig. 2. Measured scattering time constants (black squares), unsaturated capture time constants (blue triangles) for DT measurements and THz peak-to-peak detector current (green circles) from THz-TDS measurements at an optical excitation of 0.25 mW.

However, because scattering mechanisms such as phonon scattering and more importantly elastic ionized impurity scattering due to the Be-doping are dominant in our case, the contribution of carrier capture to the carrier scattering time can be safely neglected.
For an understanding of the influence of carrier capture time on the frequency behavior of a PCA detector, it is instructive to consider two simplified limiting cases:

1. An infinitely *short* carrier lifetime, i.e. a Dirac delta function like carrier density in the CB: $n(t) = \delta(t)$.
2. An infinitely *long* carrier lifetime, i.e. a theta function like carrier density in the CB: $n(t) = \theta(t)$.

The TDS current of the detector for a linear response with respect to the electric field, i.e. neglecting influences such as THz field screening by charged carriers, can be described by the convolution:

$$j(\tau) = \sigma(t) * E_{THz}(t) = \mathrm{e}\cdot \mathrm{n(t)} * \mu(\mathrm{t}) * E_{THz}(t) \,, \tag{1}$$

which in Fourier space is given by

$$j(\omega) = \mathrm{e}\cdot \mathrm{n}(\omega) \cdot \mu(\omega) \cdot E_{THz}(\omega) \,. \tag{2}$$

Here σ is the conductivity, E_{THz} is the incident THz field, n is the carrier density, μ is the mobility, $*$ denotes the convolution operation and e is the elementary charge.
For the first case Eq. (2) yields

$$j_{delta}(\omega) = \mathrm{e}\cdot \, {}^{1}\!\Big/\!_{\sqrt{2\pi}} \cdot \mu(\omega) \cdot E_{THz}(\omega) \,, \tag{3}$$

where for second case Eq. (2) yields

$$j_{theta}(\omega) = \mathrm{e}\cdot \left({}^{i}\!\Big/\!_{\sqrt{2\pi}\omega} + \delta(\omega) \right) \cdot \mu(\omega) \cdot E_{THz}(\omega) \,. \tag{4}$$

From Eq. (3) and Eq. (4) it is obvious that for a slow, integrating detector one would expect a nonzero DC component in the signal and a faster roll-off towards higher frequencies as compared to a Dirac-like sampling detector. To investigate the effects of partial trap filling and trap saturation on the THz detector performance in terms of dynamic range and bandwidth we performed THz-TDS measurements in dependence of the optical excitation at the receiver. The obtained THz-TDS spectra for 0.25 mW, 2 mW and 16 mW excitation power are given in Fig. 3. The measurement time for each trace was approx. 1 minute (average over 1000 pulse traces measured at 16 Hz).
In case of the 0.25 mW, i.e. without trap saturation, MLHS 1 shows the highest THz peak-to-peak amplitude (cf. Fig. 2). When compared with the other samples it is obvious that the amplitude increase is mostly due to an increase of lower frequency components, i.e. < 2 THz. At higher frequencies, e.g. 2-4 THz, the detected amplitudes are smaller as compared to the other MLHS. We attribute this to the slow trapping time (cf. Table 1). A closer investigation of the results in Fig. 2 reveals that, in general, longer carrier lifetimes in the detector shift the center frequency towards lower frequencies and enhance the frequency roll-off, as expected from Eq. (3) and Eq. (4). Furthermore, it agrees with predictions from more sophisticated Monte Carlo calculations in [12].

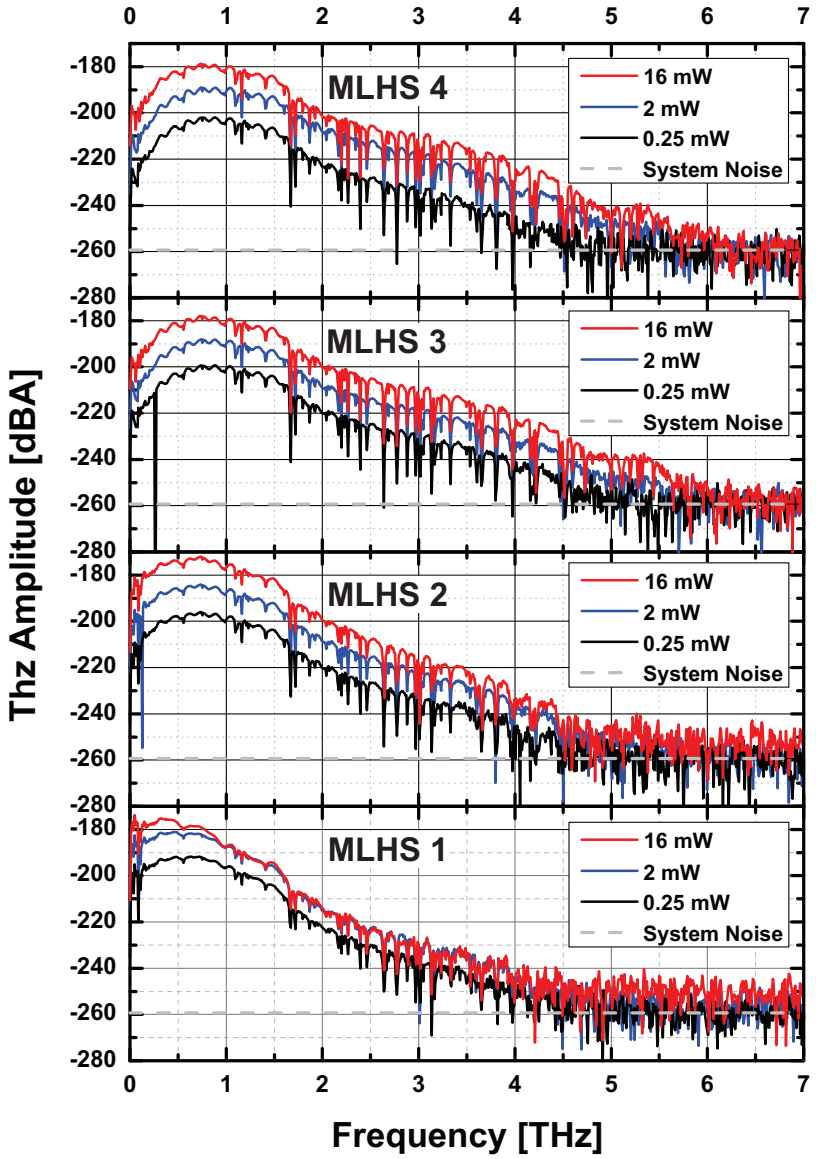

Fig. 3 THz-TDS spectra obtained from detectors made from the different MLHS samples for 0.25 mW, 2 mW and 16 mW of optical excitation power at the detector. The grey striped line indicates the noise of the detection electronics without a connected antenna.

The 2.0×10^{18} cm^{-3} doped MLHS 3 shows the highest signal in the frequency range of 2-4 THz at this low excitation power, indicating a trade-off between fast trapping and high mobility. The dynamic range for all detectors under this excitation condition was limited by the noise of the detection system itself and not the respective MLHS. The system noise amplitude measured with an open circuit, i.e. without an antenna, is depicted as a grey line in Fig. 3.For medium optical excitation power of 2 mW, the frequency roll-off for MLHS 2-4 remains almost equal to the roll-off at 0.25 mW. For MLHS 1, a minor shift of the center frequency towards lower frequencies and a slightly steeper roll-off is visible. Considering the prolonged carrier lifetime of MHLS 1 at this excitation condition (cf. Fig. 1(b)) the change of the

frequency roll-off is weaker than what would be expected from Eq. (4). The relative increase of the THz signal amplitude as compared to the other samples is small indicating the onset of a saturation behavior, as will be discussed later in more detail.
At 16 mW MLHS 1 shows a further red shift of the center frequency as expected for this long carrier lifetime and hence a mostly integrating antenna behavior. The peak in the frequency components around 5-30 GHz originates from resonances in the contact metallization. The damping of these resonances is reduced for long carrier lifetimes. MLHS 2 also shows a steeper frequency roll-off due to the prolonged carrier lifetime at 16 mW. However the effect is not as pronounced as for the MLHS 1. MLHS 3-4 show almost no difference in the roll-off behavior and MLHS 3 shows only a slight shift of the center frequency and thus a superior bandwidth. These results indicate that the benefit of a short carrier capture time outweigh the lower detector signals due to the simultaneous increase of the carrier scattering time for higher Be doping concentrations. Furthermore, in case of MLHS 1 we observed a strong saturation and even reduction of the detector peak-to-peak pulse amplitude for higher excitation powers which can be seen in Fig. 4. We assume that the decrease is due to screening of the incident THz field by free and trapped carriers which in case for MLHS 1 gets relevant due to the long carrier capture and recombination lifetimes. In this case the detector response is not linear in the electric field since the carrier acceleration becomes dependent on the CB carrier density and Eq. (1) loses its validity. A model describing carrier screening effects in the semiconductor response of a PCA has been proposed by Jepsen et al. [10].

The peak-to-peak amplitudes of MLHS 2 to 4 do not show such a saturation behavior even at higher optical excitation powers suggesting a linear response. The slight sub-linear behavior of the peak-to-peak amplitude with respect to the optical power is assumed to be due to absorption saturation. The amplitudes of MLHS 2-4 are therefore determined by the carrier scattering time and the carrier capture lifetime which enters via the convolution integral [Eq. (1)] as explained before.

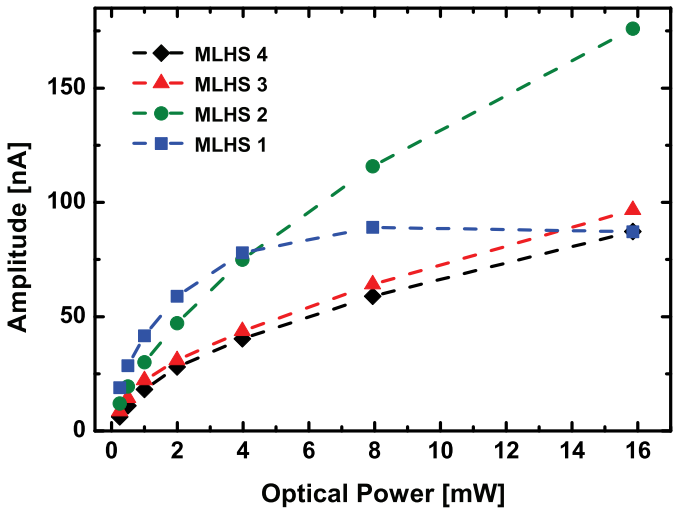

Fig. 4. Peak-to-peak amplitude of the detected THz-TDS pulse in dependence of the optical excitation power at the detectors made form MLHS 1-4. The striped lines are guidelines for the eyes.

4. Noise and Bandwidth

Another important characteristic of THz detectors is the electronic detector noise which potentially limits the dynamic range and thus the detectable bandwidth. Duvillaret et al. [15] and Jepsen et al. [16] have analyzed how noise limits the extractable data in THz-TDS spectroscopy. Even though, the authors of [15] show that emitter noise dominates the noise in TDS measurements they find that detector noise contributions are not negligible. Grischkowsky and Van Exter [17] as well as Castro-Camus et al. [18] have shown that the major detector noise contribution arises from thermal Nyquist noise. Shot noise and generation-recombination (GR) noise are found to have only minor influence as they scale with the square root of the THz field induced detector current which is generally relatively small. The Nyquist noise current is given by:

$$I_N = \sqrt{4 \cdot K_B \cdot T \cdot \Delta f \cdot R^{-1}} \tag{5}$$

where K_B, T and Δf are Boltzmann constant, absolute temperature and measurement bandwidth, respectively. R is the detector resistance. Since the measurement of the signal in TDS detection is essentially a DC or very low frequency current measurement, the time average resistance of the detector is sufficient for analysis.

We measured the average root-mean-square (rms) noise current in the detector, without an incident THz field, in dependence of the optical power at the detector. Additionally, we calculated the Nyquist noise currents from PCA resistances by numerically solving the carrier density equations given in [13]. Both results are given in Fig. 5. For MLHS 1 and 2 there is a strong increase (~factor 7) in the measured and calculated Nyquist noise current for higher excitation powers, which is due to the long carrier lifetimes in the saturation regimes and hence a low average resistivity. For MLHS 1 and 2 the general behavior of the Nyquist noise as a function of optical excitation power, is covered quite well by the simulation results. However, the absolute values differ by a factor of approx. 2. Here, it should be noted that thermal re-excitation of carriers from trap states into to the CB and the VB was not included in the calculation. After the optical excitation and until electrons and holes in trap states have recombined, only Quasi Fermi levels are defined.

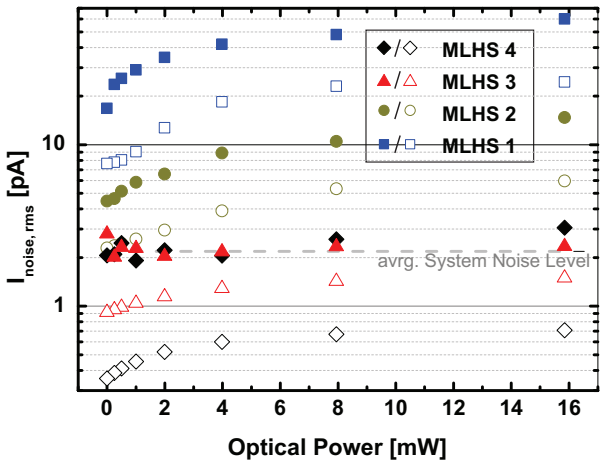

Fig. 5 Measured (full symbols) root mean square noise current and calculated Nyquist noise current (open symbols) shown in dependence of the optical excitation power for four different detectors made form MLHS 1-4. The grey striped line indicates the system noise measured with an open circuit.

During this time the probability for thermal re-excitation is increased, leading to a further reduction of the samples resistance. This effect could explain the discrepancy between measurement and simulation.
For MLHS 3 and 4 the measured noise currents seem to show a minor increase (~ factor 1.5). However, since the measured noise currents are very close to the average system noise level (measured with an open circuit) the result is inconclusive. The prediction of the simulation for MLHS 3 is within the margin of the factor 2 discrepancy. The simulation of MLHS 4, however, is significantly lower than the measured one, suggesting that the system noise could be the limiting factor in this case.

To further examine the influence of the Be-doping level, we extracted the dynamic range and measureable bandwidth from all measured TDS spectra at different detector excitation powers for each of the MLHS samples. The noise floor for the dynamic range calculation was defined as the average value of the spectral amplitude between 6.5 and 10 THz. The detectable bandwidth was defined as the highest frequency component with an amplitude 6 dB above the noise floor in the respective THz power spectrum. The obtained results are given in Figs. 6(a) and 6(b). For MLHS 1, the dynamic range decreases for excitation powers in excess of 4 mW due to the amplitude saturation and the increase in Nyquist noise. In conjunction with the strong frequency roll-off, the detectable bandwidth is significantly limited at high excitation powers. Similarly, MLHS 2 shows a saturation behavior of the dynamic range for the highest excitation power due to an increased noise level (cf. Fig. 5) and a decrease of the detectable bandwidth for higher excitation. Both MLHS 3 and 4 show no saturation in the dynamic range or bandwidth as expected from their short carrier lifetime for all excitation levels. Interestingly, the highest measurable bandwidth is not obtained for MLHS 4 which features the shortest carrier lifetime. Instead, the slightly higher carrier lifetime and scattering time of MLHS 3 leads to an increase of the detected THz current. Since the noise level is defined by the system noise for these samples, the THz bandwidth increases for higher detector currents as long as the carrier lifetime is short enough. Considering the noise calculations shown in Fig. 5, MLHS 4 could potentially exceed the dynamic range of MLHS 3 if the system noise could be further reduced.

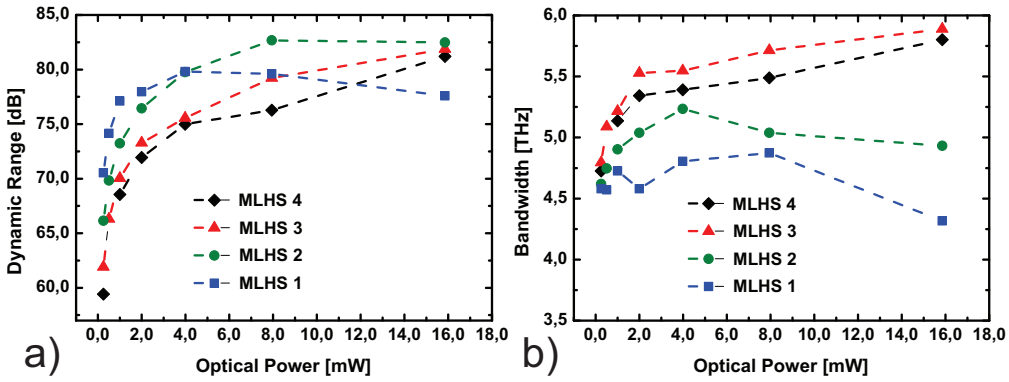

Fig. 6. (a) Dynamic range and (b) detectable bandwidth of the THz-TDS signal in dependence of the optical excitation power for four different detectors made form MLHS 1-4. The striped lines are guidelines for the eyes.

In an attempt to overcome the system noise limitation and increase the dynamic range, we employed a 100 µm strip-line emitter fabricated from a high mobility MLHS which has a significantly higher THz output than LT-grown Be-doped MLHS [8, 9]. The bias of the emitter was 100 V and the optical excitation was set to 25 mW. As detector we employed MLHS 4, which features the fastest trapping time. The average noise floor in the spectra was

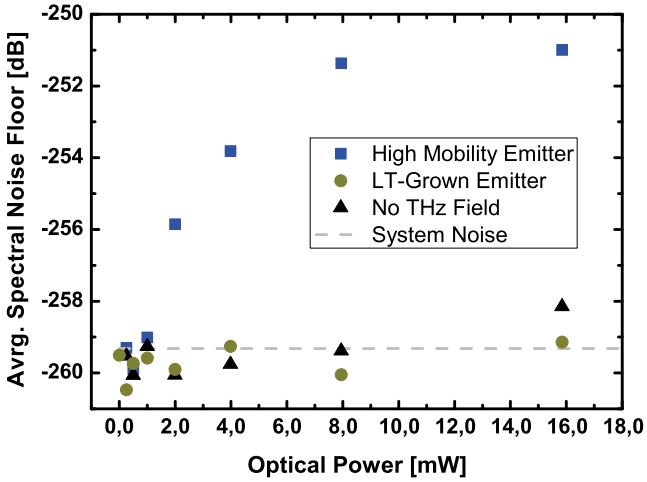

Fig. 7. Average noise floor in THz-TDS spectra taken between 6.5 THz and 10THz in dependence of the optical excitation power at the detector made form MLHS 4 and for a high mobility MLHS emitter at 100 V bias (blue squares), a LT-grown emitter made from MLHS 4 at 50 V bias (green circles) and without an incident THz field (black triangles).

extracted for different excitation powers at the detector for the high mobility emitter, the LT-grown emitter and without a THz field present, which is shown in Fig. 7. In accordance with our previous results the noise of the LT grown emitter is on the order of the system noise level. However, there is an increase of the noise floor for higher excitation levels if a THz field is present in case of the high mobility emitter. The square root like behavior strongly suggests that the increase is due to shot noise from the detector current which in turn, to a good approximation, is directly proportional to the optical excitation power at the detector and is given by:

$$I_N = \sqrt{2 \cdot e \cdot I_{THz}} \propto \sqrt{2 \cdot e \cdot P_{opt,\mathrm{det}}} \tag{6}$$

Here I_{THz} is the THz-field induced detector current, $P_{opt,\mathrm{det}}$ is the optical power at the detector and e is the elementary charge. Since for the high mobility emitter the detector currents have much higher values (approx. 285 nA for 16 mW excitation at the detector) the shoot noise contribution appears to become significant. However, since the shoot noise scales with the square root of the detector current were as the signal scales linear with the detector current the dynamic range is further increased as compared to the previous emitter.

Finally we increased the emitter bias to 120 V and averaged over ten thousand trace taken at 16 Hz (approx. 10 min) resulting in a measureable bandwidth of over 6 THz and approx. 90 dB dynamic range as can be seen in Fig. 8. For this emitter and detector combination the spectrum of a single pulse trace with a measurement time of 62.5 ms still shows a dynamic range in excess of 65 dB and a bandwidth >4.5 THz (not shown).

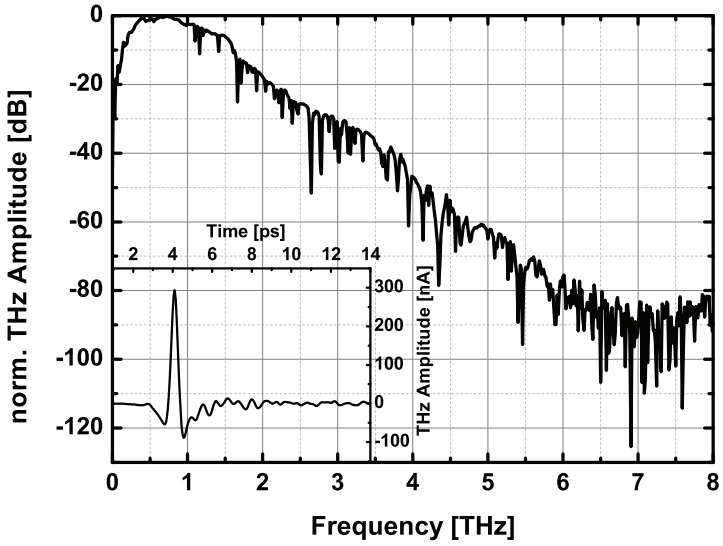

Fig. 8. FFT spectrum obtained for a high mobility MLHS emitter at 120 V bias and 25 mW optical excitation and a detector made from MLHS 4 at 16 mW optical excitation. The spectrum is obtained by averaging ten thousand pulse traces at 16 Hz measurement rate (approx. 10 min). The corresponding THz Pulse trace is shown in the inset.

5. Conclusion and Outlook

We have shown that knowledge of the influence of Beryllium doping on carrier dynamics in LT-grown InGaAs/InAlAs MLHS is crucial for the design of THz-TDS detectors made from this material. We have found that trap saturation, i.e. long carrier lifetime, limits the detector dynamic range and bandwidth because of increased frequency roll-off and Nyquist noise. Furthermore, we have shown that in case of detectors with short carrier lifetimes and sufficiently strong THz fields the shot noise in the detector becomes a relevant noise source. Finally, it was demonstrated that for fast LT-grown InGaAs/InAlAs detectors, i.e. with appropriate Be doping concentration, together with highly efficient THz emitters it is possible to obtain PCA based THz-TDS measurement systems at 1550 nm excitation with 90 dB dynamic range and more than 6 THz bandwidth.

Publication IV

B. Globisch, R. J. B. Dietz, T. Göbel, M. Schell, W. Bohmeyer, R. Müller, and A. Steiger, "Absolute terahertz power measurement of a time-domain spectroscopy system," Opt. Lett., vol. 40, no. 15, p. 3544, 2015.

First absolute terahertz power measurement of a time-domain spectroscopy system

Björn Globisch,[1,*] Roman J. B. Dietz,[1] Thorsten Göbel,[1] Martin Schell,[1] Werner Bohmeyer,[2] Ralf Müller,[3] and Andreas Steiger[3]

[1]*Fraunhofer Institute for Telecommunications, Heinrich Hertz Institute (HHI), Einsteinufer 37, 10587 Berlin, Germany*
[2]*Sensor und Lasertechnik (SLT), Schulstr.15, 15366 Neuenhagen, Germany*
[3]*Physikalisch-Technische Bundesanstalt (PTB), Abbestr. 2-12, 10587 Berlin, Germany*
**Corresponding author: Bjoern.Globisch@hhi.fraunhofer.de*

We report on the first absolute terahertz (THz) power measurement of a photoconductive emitter developed for time-domain spectroscopy (TDS). The broad-band THz radiation emitted by a photoconductor optimized for the excitation with 1550 nm femtosecond pulses was measured by an ultrathin pyroelectric thin-film (UPTF) detector. We show that this detector has a spectrally flat transmission between 100 GHz and 5 THz due to special conductive electrodes on both sides of the UPTF. Its flat responsivity allows the calibration with a standard detector which is traceable to the International System of Units (SI) at the THz detector calibration facility of PTB. Absolute THz power in the range from below 1 µW to above 0.1 mW was measured.

Terahertz time-domain spectroscopy (THz-TDS) systems have been widely utilized tools in science since nearly 30 years [1,2]. Continuous progress in the development of THz-TDS especially by employing femtosecond fiber lasers operating at 1550 nm central wavelength and photoconductive antennas based on InGaAs lead to several promising applications in industrial environments [3,4]. In spite of all the improvements in THz-TDS system performance, reliable THz power measurements do still not exist. Instead, THz-TDS systems are commonly characterized by quantities like detected pulse amplitude or maximum signal to noise ratio. This complicates the direct comparison of TDS systems from different manufacturers since the aforementioned quantities depend on the specific spectroscopic setup. The challenge in the development of absolute THz power detectors for TDS systems is caused by of the broad spectrum of the emitted radiation combined with the low (<100 µW [5]) THz power.

The Physikalisch-Technische Bundesanstalt (PTB, the German national metrology institute), in collaboration with Sensor und Lasertechnik (SLT), has recently developed ultrathin pyroelectric thin-film (UPTF) detectors which are well suited for absolute power measurements of THz-TDS systems. In [6] the authors showed that a frequency independent absorption from 100 GHz to 5 THz could be realized by special conductive coatings as read-out electrodes on both sides of a pyroelectric thin-film. This structure led to a spectrally flat absorption of 50 % of the THz radiation accompanied by 25 % transmission and 25 % reflection [6]. The fundamentals of the above mentioned absorption properties of thin metallic films have been investigated already by W. Woltersdorff in 1934 [8]. In order to fulfill the second demand on absolute power detectors for TDS emitters, the ability to measure THz power in the µW range, a new ultrathin pyroelectric film was used with 4 µm thickness only. Due to an improved mounting technology these new ultrathin pyroelectric thin-film detectors can still be manufactured with a diameter of 20 mm, which is large enough to ensure that all emitted THz radiation can be captured easily.

In this paper we describe the first quantitative determination of the total THz power generated by an advanced TDS emitter developed by Fraunhofer Heinrich Hertz Insititute (HHI) by using a UPTF detector. First, we show by THz transmission spectroscopy that the responsivity of the UPTF is constant within the whole TDS spectrum. Next, we demonstrate that the signal detected by the UPTF has its origin in the absorption of THz radiation and is not caused by any other source like the exciting laser or thermal radiation. Finally, the absolute output power of a fiber-coupled THz emitter module excited with a 1550 nm femtosecond pulsed laser is determined by the UPTF detector and compared to the results obtained with a coherent detector in THz-TDS. This successful field test proves the applicability of the

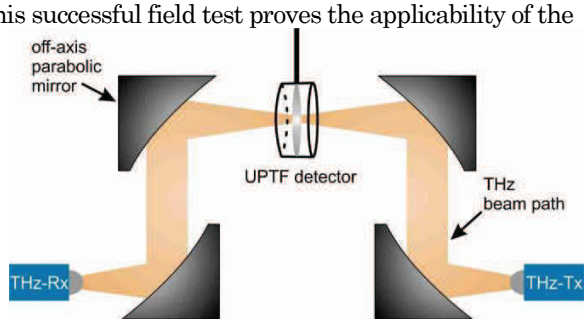

Fig. 1. Schematic of a THz setup with intermediate focus. Four 90 ° off-axis parabolic mirrors guide the THz beam from the fiber coupled emitter (THz-Tx) to the receiver (THz-Rx). For THz transmission spectroscopy and absolute power measurements the UPTF was set into the intermediate focus.

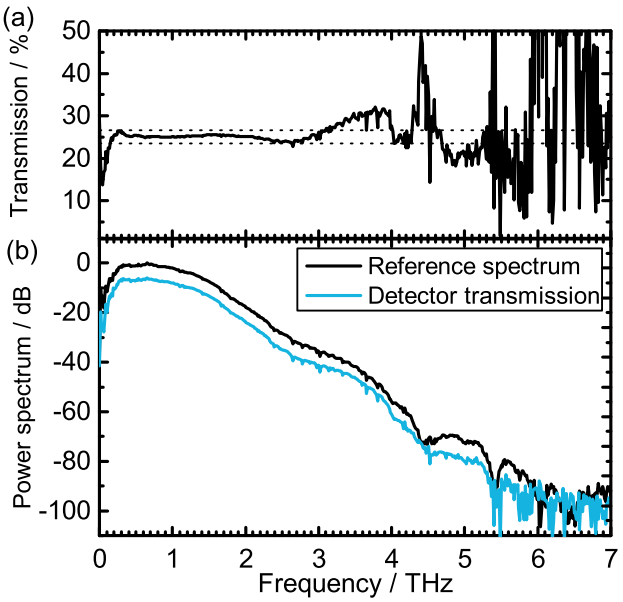

Fig. 2. Results of THz-transmission spectroscopy on the UPTF-detector with removed metallic backside plate. Power spectra in (b) were obtained by fast Fourier transformation (FFT) of the corresponding THz pulses. The light blue line shows the power spectrum after transmission through the UPTF detector. The black line is the reference when the UPTF detector was removed from the intermediate focus in Fig 1. Measurements were performed under dry nitrogen purge. Both spectra were normalized to the maximum of the reference spectrum. The THz transmission in (a) is calculated by dividing the detector transmission by the reference spectrum. Dashed lines in (a) show the uncertainty range calculated from the calibrated sensitivity of the detector, which is 160 ± 10 V/W.

UPTF detector for absolute THz-TDS power measurements. Since its responsivity was calibrated with a standard detector at PTB the results are directly traceable to the International System of Units (SI) [8].

In order to characterize the transmission properties of the UPTF we employed THz-TDS. The THz beam path of the experimental setup is shown in Fig. 1. The THz radiation is generated by a growth optimized photoconductor consisting of 100 periods of an InGaAs/InAlAs heterostructure mounted in a fiber-coupled transmitter module (THz-Tx). The semiconductor material is designed for efficient emission of THz radiation when illuminated with a 1550 nm femtosecond fiberlaser [5]. An intermediate THz focus is created by a set of four 90 ° off-axis parabolic mirrors (cf. Fig. 1). The photoconductor used in the THz receiver (THz-Rx) consists of a low-temperature-grown InGaAs/InAlAs heterostructure with optimized Beryllium doping for maximum signal to noise ratio [10, 11]. Both emitter and detector are optically excited by an Erbium-doped fiber laser with 100 MHz repetition rate, 90 fs pulse width (FWHM) and 1550 nm central wavelength. The average optical power at THz-Tx and THz-Rx is controlled by an optical attenuator. The THz time domain spectrometer employed in all subsequent experiments is described in detail in [9].

In order to perform the THz transmission experiments and the subsequent absolute THz power measurements with the same thin-film we used a UPTF detector with removable backside plate. When this metallic plate is removed from the housing the detector foil is accessible from both sides and allows THz transmission as schematically shown in Fig. 1. During operation as an absolute power detector the metallic plate ensures electrical shielding of the housing and prevents backside illumination of the UPTF. Additionally, the plate is covered by an absorption layer for THz radiation on its inner side in order to prevent multiple reflections of the 25 % of transmitted radiation inside the detector housing.

Fig. 2 shows the results of the transmission experiments. The power spectra in Fig. 2(b) were obtained by fast Fourier transformation of the corresponding pulse traces. The light blue line is the power spectrum after transmission through the UTPF whereas the black spectrum serves as the reference measurement for which the UPTF had been removed from the setup. Both spectra are normalized to the maximum of the reference spectrum. The THz transmission shown in Fig. 2(a) is calculated from the ratio of the detector transmission and the reference spectrum. In order to reduce the influence of water vapor absorption these measurements were performed under dry nitrogen purge. The power spectra in Fig. 2(b) show the broadband emission of the THz emitter reaching from 100 GHz to above 5 THz. The calculated THz transmission in Fig. 2(a) is centered around 25 %. The dashed lines indicate the interval of uncertainty ranging from 23.4 – 26.6 % derived from the uncertainty of the detector calibration at PTB (160 ± 10 V/W). From 100 GHz to 3.2 THz the transmission of the UPTF detector amounts to 25.0 ± 1.6 %. For higher frequencies residual water vapor absorption and the relatively low THz power lead to slightly higher deviations from 25 %. Nevertheless, the results shown in Fig. 2 confirm a spectrally flat transmission of 25 % as predicted by [7]. Detailed spectroscopic measurements with the pyroelectric material used for the UPTF can be found in [6].

Apart from the ability to detect broadband THz radiation the UPTF detector is also sensitive for infrared light with 1550 nm central wavelength and thermal infrared radiation. Hence, the next section describes how it was ensured that the signal detected by the UPTF was solely caused by THz radiation generated in the TDS emitter. For this purpose, we systematically ruled out other signal sources: The residual light of the exciting laser, which was not absorbed by the THz photoconductor, was blocked by coating the Silicon lens of the emitter module with a layer opaque for 1550 nm. In addition, we used electrical bias modulation and optical chopping as two different THz modulation techniques to ensure that the detector signal is not influenced by the modulation itself. (Since the thermal relaxation time of the UPTF detector amounts to less than 100 ms the amplitude of the THz signal has to be modulated with a frequency of 10 Hz at least.) The black lines in Fig. 3 show the UPTF signal amplified by a transimpedance amplifier (10^8 V/A) and read out by an oscilloscope when the exciting femtosecond laser light was chopped with a frequency of 16 Hz. The average optical power was set to 20 mW. The large amplitude signal corresponds to 120 V emitter bias

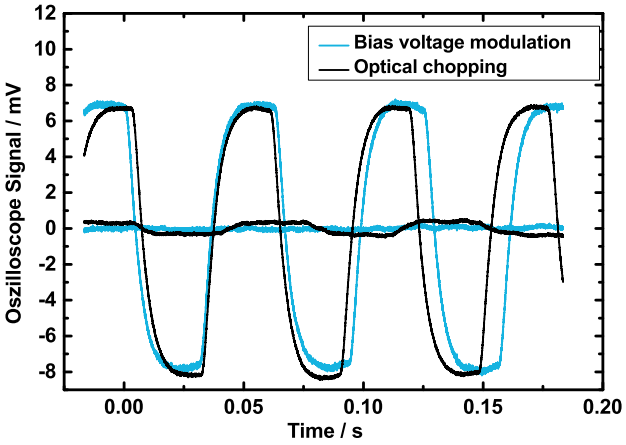

Fig. 3. Waveform of the UPTF detector output recorded by an oscilloscope. The signal was amplified by a transimpedance amplifier (10^8 V/A). The detected THz signal was optically chopped with 16 Hz (black line) and electrically modulated with the bias voltage of the emitter (14 Hz, light blue line). Large amplitude signals correspond to 120 V bias and 20 mW optical power. Small amplitude signals are the background for 0 V bias (optical chopping) and 0 mW optical power (bias voltage modulation).

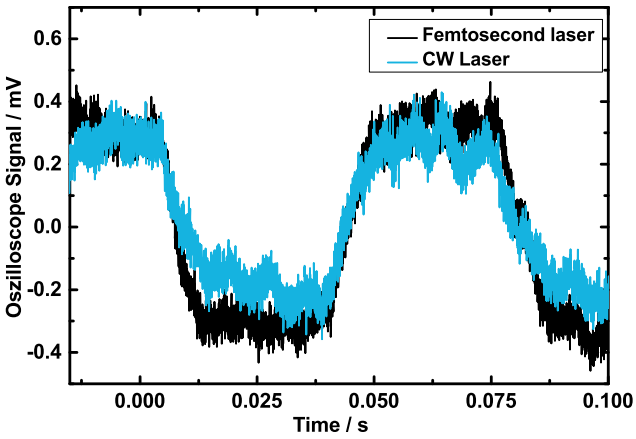

Fig. 4. Waveform of the amplified UPTF detector. The black line corresponds to excitation with an optically chopped femtosecond laser with 20 mW average optical power and 0 V emitter bias. The light blue line corresponds to the excitation with a 1550 nm cw-laser with 20 mW optical power and 30 V emitter bias.

whereas the small amplitude signal is detected for 0 V bias. The light blue lines in Fig. 3 correspond to bias voltage modulation between 0 V and 120 V with a frequency of 14 Hz. The large amplitude signal is obtained when the emitter is illuminated with 20 mW optical power whereas the small amplitude signal corresponds to 0 mW of optical illumination power. For the high amplitude signal optical chopping and bias voltage modulation led to a detected amplitude of 15.35 mV and 14.66 mV which corresponds to an absolute power of 95.9 ± 6 µW and 91.6 ± 5.7 µW, respectively. Since these amplitudes agree within the calibration uncertainties the detector signal is independent of the modulation technique for equal operation conditions of the THz emitter. In contrast, the small amplitude signal is zero for bias voltage modulation whereas it has finite amplitude for optical chopping. The principal difference between these measurements is that in the case of voltage modulation the optical illumination power is switched off whereas the optical chopping modulates the light of the exciting femtosecond laser. Hence, we attribute the finite signal detected for 0 V bias and 20 mW optical power to a small amount of 1550 nm light that is transmitted through the THz emitter module although the Silicon lens had been coated.

In order to determine if any thermal radiation contributes to the detector signal, which may be generated by heating the photoconductor with the femtosecond laser or by the average current flow in the THz emitter, we used a single-mode, continuous-wave (cw) laser emitting at 1550 nm for the optical illumination. The average optical power of the cw-laser was set to 20 mW, equal to the average power of the femtosecond laser in our previous experiments. The bias voltage of the emitter was set to 30 V which caused a photocurrent in the THz emitter similar to 120 V bias for pulsed excitation. In this configuration the heat generated by the optical illumination and/or by the current in the photoconductor should be equal for pulsed and cw-excitation. However, no THz radiation is generated when the emitter is illuminated with cw-light. The light blue line in Fig. 4 shows the waveform of the UPTF detector for cw-excitation. The amplitude of this signal is about a factor of 20 smaller than the signal generated by the corresponding femtosecond laser excitation with 120 V bias and 20 mW optical illumination (large amplitude signals in Fig. 3). Hence, the main part of the detector signal in Fig. 3 is caused by THz radiation from the emitter and not by any different type of radiation. The finite signal detected by the UPTF when the THz emitter is illuminated with cw-light can be explained by the optical background identified previously in Fig. 3, i.e. the signal caused by the residual light transmitted through the emitter. For this purpose the black line in Fig. 4 shows the magnification of the small amplitude signal of Fig. 3 for optical chopping and 0 V bias voltage. Note, that the amplitude of both signals in Fig. 4 is almost identical. This suggests that the signal generated by the cw-laser is also due to residual light transmitted through the THz emitter module. For further verification, we changed the optical power of the cw-laser and observed the same variation in the amplitude of the UPTF signal. In contrast, the detector signal did not scale with the bias voltage of the THz emitter as long as the cw-laser power was kept constant (not shown). These results prove that the detector signal generated by cw-excitation of the THz emitter is caused by residual light and not by any thermal radiation. Hence, the combination of all the above mentioned procedures demonstrates that the signal measured by the UPTF-detector originates from THz radiation generated in the photoconductive emitter module. Nevertheless, the prior discussion emphasizes the necessity of protecting the UPTF from illumination with infrared light from the exciting laser in order to obtain accurate results.

After having shown that the UPTF detector meets all the demands on absolute THz power detection, we

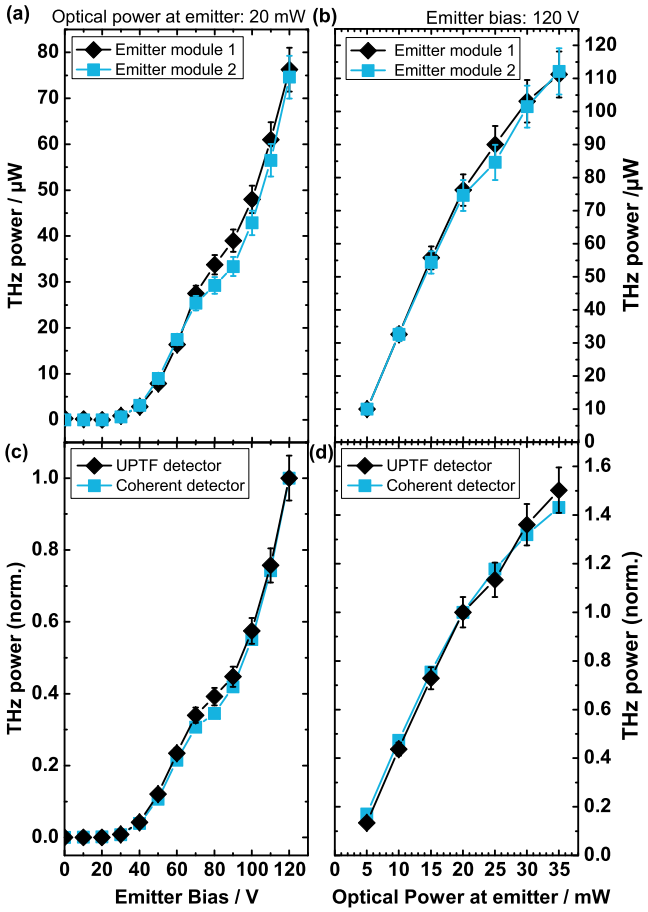

Fig. 5. Absolute THz power versus emitter bias (a) and optical power (b) for two different emitter modules. Error bars were calculated from the sensitivity of the PFT detector (160 ± 10 V/W) obtained by the calibration at PTB. (c) and (d) show a comparison between the absolute power measurement with the PTF detector (black diamonds) and the results from coherent detection with a photoconductive receiver in THz-TDS (blue circles). The TDS pulse trace was squared and integrated over time to obtain a quantity proportional to THz power. The signals in (c) and (d) were normalized to their respective values at 20 mW optical power and 120 V bias.

measured the THz output of two fiber-coupled TDS emitters which are equal in construction. Fig. 5 (a) and (b) show the absolute THz power versus bias voltage and optical power at the emitter. THz modulation was achieved by chopping the femtosecond laser with a frequency of 16 Hz. The background signal caused by residual light was subtracted from each data point. Error bars were calculated from the uncertainty of the detector calibration, which measured 160 ± 10 V/W. The detected THz power increases from below 1 µW for 30 V bias and 20 mW optical power to above 70 µW at 120 V bias voltage. In addition, the emitted THz power exceeds 0.1 mW when the optical illumination power is higher than 30 mW. This corresponds to an optical-to-THz conversion efficiency of 0.33 %.

Finally, we compared the results of the absolute THz power measurements with the signal measured by a coherent detector in TDS. We employed the emitter module 1 of Fig. 5 (a) and (b) as the THz source in TDS and varied bias voltage and optical power accordingly. In order to obtain a quantity proportional to THz-power from the TDS experiments the time integral of the squared pulse trace was calculated. Since the THz responsivity of the coherent detector was unknown, we normalized the absolute THz power as well as the quantity derived from THz-TDS with respect to their values at 120 V bias and 20 mW average optical power. The results are shown in Fig. 5 (c) and (d). Here, the shape of both plots coincides for the two different detection schemes. This agreement originates from the fact that the emission spectrum of the THz emitter is almost constant for increased bias voltage and optical illumination power. Since the sensitivity of the coherent THz detector is higher in the low frequency range of the spectrum and not spectrally flat the results of both measurement techniques would not agree if the emission spectrum changed with optical power or bias voltage. However, the results of Fig. 5 (c) and (d) show that the calibrated UPTF detector and the InGaAs/InAlAs photoconductor measure the same quantity, which is the THz radiation generated in the photoconductive emitter.

In conclusion, we demonstrated for the first time absolute power measurements of THz-TDS emitters with recently developed ultrathin pyroelectric thin-film detectors. Their responsivity can be calibrated traceable to SI-units at PTB. From now on, these new detectors enable a direct comparison of various THz-TDS systems from different manufacturers. We verified that these detectors feature a spectrally flat responsivity from 100 GHz to 5 THz and are able to measure THz power down to 1 µW. By systematically investigating the origin of the detector signal we ensured that the measured absolute THz power was exclusively caused by the THz radiation generated in the TDS emitter. A THz power exceeding 0.1 mW was measured for the latest generation of photoconductive emitters designed for 1550 nm excitation.

The work of SLT and PTB was in part funded by the "Zentrales Innovationsprogramm Mittelstand" of the German Federal Ministry of Economic Affairs and Energy.

References

1. K. P. Cheung, D. H. Auston, Infrared Phys. 26, 23 (1986).
2. M. Tonouchi, Nature Photonics 1, 97 (2007).
3. J. L. M. van Mechelen, Langmuir 30, 12748 (2014).
4. T. Hochrein, J Infrared Milli Terahz Waves 36, 235 (2015).
5. R. J. B. Dietz, B. Globisch, M. Gerhard, A. Velauthapillai, D. Stanze, H. Roehle, T. Göbel, M. Schell, Appl. Phys. Lett. 103, 061103 (2013).
6. R. Müller, W. Bohmeyer, M. Kehrt, K. Lange, C. Monte, A. Steiger, J Infrared Milli Terahz Waves 35, 659 (2014).
7. W. Woltersdorff, Z. Physik 54, 230 (1934).
8. A. Steiger, M. Kehrt, C. Monte, R. Müller, Opt. Express 21, 14466 (2013).
9. N. Vieweg, F. Rettich, A. Deninger, H. Roehle, R. J. B. Dietz, T. Göbel, J Infrared Milli Terahz Waves 35, 823 (2014).
10. R. J. B. Dietz, B.Globisch, H. Roehle, D. Stanze, T. Göbel, M. Schell, Opt. Express 22 (16), 19411 (2014).
11. B. Globisch, R. J. B. Dietz, D. Stanze, T. Göbel, M. Schell, Appl. Phys. Lett. 104, 172103 (2014).

Publication V

S. Sawallich, B. Globisch, C. Matheisen, M. Nagel, R. J. B. Dietz, and T. Göbel, "Photoconductive Terahertz Near-Field Detectors for Operation With 1550-nm Pulsed Fiber Lasers," IEEE Trans. Terahertz Sci. Technol., vol. 6, no. 3, pp. 365–370, 2016.

Photoconductive THz near-field detectors for operation with 1550 nm pulsed fiber lasers

Simon Sawallich, Björn Globisch, Christopher Matheisen, Michael Nagel, Roman J. B. Dietz, and Thorsten Göbel

***Abstract*— We present a new generation of photoconductive (PC) Terahertz (THz) near-field probes based on freestanding Beryllium-doped, low-temperature-grown InGaAs/InAlAs cantilevers. The PC probes are compatible to optical sampling with femtosecond-laser pulses having a center-wavelength of 1550 nm. Therefore, they are well-suited for a cost-efficient direct integration with fiber-coupled THz time domain spectroscopy (TDS) systems. The photoconductor material features electron lifetimes of 500 fs allowing for broadband detection up to 2 THz, which is comparable to existing LT-GaAs-based near-field detectors requiring, however, 800 nm wavelength excitation. We demonstrate the detector operation in a state-of-the-art fiber based TDS system with fast and coherent data acquisition and show obtained sheet-resistance mappings of conductive thin-films featuring sub-wavelength resolution.**

***Index Terms*— time domain spectroscopy, terahertz (THz), near-field imaging, near-field microscopy, photoconductor**

I. Introduction

The unique properties of terahertz (THz) radiation have stimulated a multitude of applications and research activities. THz-based methods have seen a rapid development in the past and have been successfully exploited to inspect solar cells [1], to identify gases or explosives by their spectroscopic fingerprints in this specific frequency range or to detect damages in packaged chip-structures [2]. By now, THz research has left its infancy. Time domain systems and spectroscopy kits are commercially available and THz imaging is involved in a wide range of topics [3]. Despite of the relatively long THz wavelengths λ, enormous results in terms of deep sub-wavelength spatial resolution have been achieved by various near-field imaging techniques [4][3]. With metallic apertures, a spatial resolution of λ/100 at 1 THz has been demonstrated [5]. Using atomic-force-microscope tips as scattering elements for THz radiation in scanning near-field optical microscopy (SNOM) systems even allowed THz imaging of nanoscopic structures [6], [7].

Manuscript submitted January 15th, 2016;

Simon Sawallich, Christopher Matheisen and Michael Nagel are with Protemics GmbH, Otto-Blumenthal-Straße 25, 52074 Aachen, Germany (e-mail: Sawallich@protemics.com, Matheisen@protemics.com, Nagel@protemics.com).

Björn Globisch, Roman J. B. Dietz, and Thorsten Göbel are with the Photonic Components Department of Fraunhofer Institute for Telecommunications, Heinrich Hertz Institute, Einsteinufer 37, 10587 Berlin, Germany (e-mail: Bjoern.Globisch@hhi.fraunhofer.de, Roman.Dietz@hhi.fraunhofer.de, Thorsten.Goebel@hhi.fraunhofer.de).

Photoconductive (PC) near-field detectors [8] based on free-standing cantilever microstructures made of low-temperature-grown Gallium Arsenide (LT-GaAs) have been developed as an alternative to scattering-type and aperture-based approaches. With a maximum resolution of a few µm they range between sub-µm SNOM-approaches and conventional THz spectroscopy far-field systems with a diffraction-limited resolution of several hundred µm to millimeters. Taking advantage of their high-sensitivity and capability for high-speed scanning they were recently introduced for wafer-scale inspection tasks [9]. The PC micro-probe detectors sample the amplitude and phase information of a THz field signal and have been used for miscellaneous temporally and spectrally resolved THz near-field imaging applications. Examples include the characterization of THz emitting nano-photonic devices [10], or meta-material characterization [11].

For efficient photo-carrier generation, GaAs requires an excitation wavelength around 800 nm, which is usually provided by a free-space optical beam. In order to configure more compact and flexible imaging systems fiber-coupled probe excitation is highly desirable. An 800 nm operation wavelength implies not only a comparably high cost of the required femtosecond source but also increased effort to set up a dispersion compensation for fiber-based pulse transmission. The majority of commercially available THz-TDS systems rely on cheap and highly integrated Erbium (Ytterbium) doped fiber lasers emitting at 1550 nm (1060 nm) central wavelength. The combination of these well-developed TDS

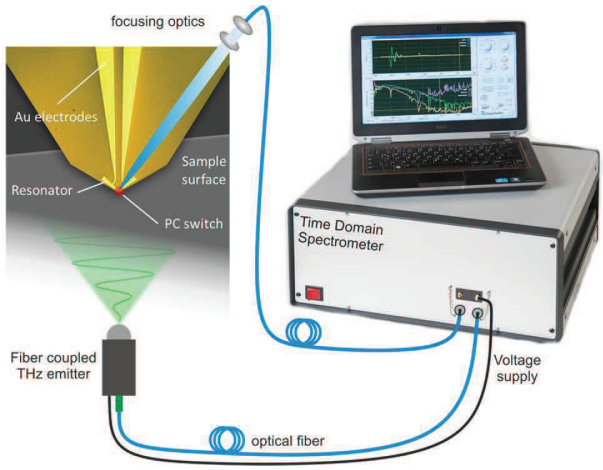

Fig. 1. Schematic of the THz near-field setup including a magnified image of the near-field microprobe detector in close vicinity to the sample surface. The fiber coupled THz-spectrometer allows for fast and easy access to the entire pulse trace.

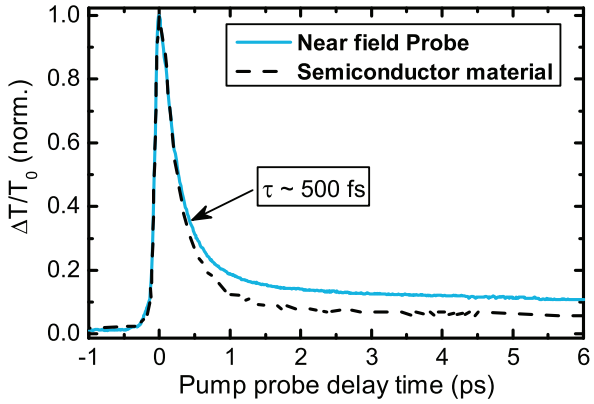

Fig. 2. Normalized differential transmission signal of the photoconductive material before and after fabrication of the near-field probe. The sub-picosecond electron lifetime is preserved after the fabrication process.

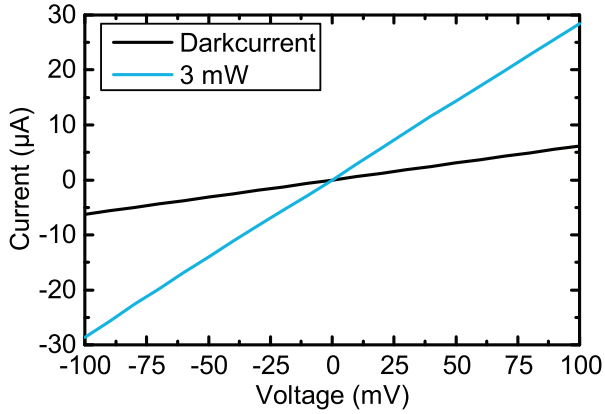

Fig. 3. Current-Voltage characteristics of the near-field probe. Both I-V curves for dark current (black) and photocurrent under optical illumination of the photo-switch with 3 mW (blue) indicate ohmic contacts.

systems with a LT-GaAs based detector is possible by placing a second-harmonic generation (SHG) module between the output of the fiber and the PC probe. However, since the SHG requires high optical power as well as additional optical components, the development of a near-field probe suitable for direct illumination with femtosecond pulses centered on 1550 nm is highly desirable.

In this work, we present the first photoconductive THz near-field micro-probe for operation at $\lambda = 1550$ nm and demonstrate its direct combination with a fully fiber-coupled THz-TDS system developed by the Fraunhofer Heinrich Hertz Institute [12], [13]. The fast data acquisition of this spectrometer allows us to acquire a 25 ps long pulse trace within 25 ms. We investigate the potential of this configuration and demonstrate a fast near-field imaging system featuring amplitude and phase information for each pixel. We will show that the system is well suited for wafer-scale THz transmission measurements with a spatial resolution of some 10 µm.

The outline of this paper is as follows: In the following chapter, we describe the detector layout and investigate the semiconductor properties of the raw material and the readily processed near-field probe. In chapter III, we focus on the measurement performance of the THz near-field detector in combination with the THz time domain spectrometer. Exemplarily, we evaluate this technique for sheet resistance measurements on a 6-inch silicon wafer with sub-wavelength metal-based microstructures.

II. THz NEAR-FIELD PROBE

The near-field detector device is based on a free-standing Beryllium-doped LT-InGaAs/InAlAs [14] cantilever only 1 µm thin to achieve minimum field invasiveness. Gold-electrodes forming a resonant near-field antenna are structured on top of the photoconductor. A 5-µm-wide photo-switch in the center of the antenna is located at the very tip. In order to enable highest spatial resolution the tip is placed in a few micrometer distance to the surface of interest (cf. Fig. 1).

The photoconductor material itself is designed to have electron lifetimes significantly below 1 ps, to allow for the detection of broadband THz radiation. Fig. 2 shows the normalized 1550 nm differential transmission (DT) signal of the photoconductor before and after fabrication of the near-field probe. A detailed description of the measurement technique can be found in [15]. For optical excitation, we used a fiber laser with 100 MHz repetition rate and 90 fs pulse duration which was focused to a spot with a diameter of 15 µm. The optical power was kept constant at 3 mW for both samples in order to characterize the semiconductor under the same conditions as it will be applied in the subsequent near-field imaging setup. The DT signal, as seen in Fig. 2, decays mono-exponentially with a time-constant of 500 fs before as well as after processing of the near-field probe indicating that the fabrication process does not influence the fundamental properties of the photoconductor. Nevertheless, the DT signal of the final near-field probe shows a slowly decaying component after the initial sub-picosecond decay in contrast to the raw photoconductor. We attribute this additional, slow decay to increased thermal heating of the free-standing 1-µm-thick probe-tip. The DT measurement of the raw semiconductor was done with a 350 µm semi-insulating InP substrate underneath the photoconductive layer. This served as a thermal heat sink. During the fabrication process of the free-standing cantilever, this substrate was removed such that the thermal conductivity of the probe tip is significantly reduced compared to the raw photoconductor.

In order to verify the functionality of the structured photoconductive switch and the quality of the metal-semiconductor-contact of the deposited electrodes, we measured the detector's current-voltage (I-V) characteristics without the presence of any THz field. Fig. 3 shows the dark current in dependence of the applied bias voltage as well as the photocurrent for an optical illumination power of 3 mW. In both cases, the expected ohmic behavior is observed.

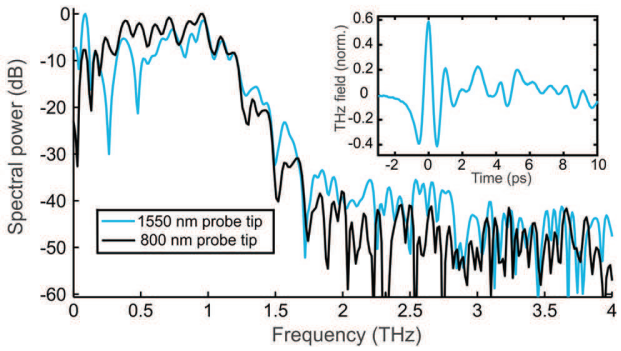

Fig. 4. Normalized power spectrum measured with the LT-InGaAs near-field probe (blue) under illumination with 1550 nm femtosecond pulses and the corresponding THz pulse trace (inset). The THz transient was averaged 100 times corresponding to a total acquisition time of 2.5 s. For comparison, the spectrum obtained with a LT-GaAs near-field detector, operated with 800nm fs-laser pulses, is shown in black.

Before we applied the photoconductive near-field probe as an imaging tool, we recorded THz pulse traces with a distance of 15 mm between the detector probe and a fiber coupled THz emitter without employing any further THz optics. The emitter was illuminated with 20 mW optical power and biased at 120 V resulting in broadband THz emission with an overall power of approximately 75 µW [15]. In Fig. 4 the normalized power spectrum (blue) as well as the corresponding pulse trace (inset) recorded with the near-field probe as photoconductive receiver are depicted. The pulse trace was averaged 100 times leading to a total acquisition time of 2.5 s. The bandwidth of 2 THz confirms the broadband detection capability of the device. For comparison, a typical power spectrum acquired with an LT-GaAs near-field probe illuminated with 800 nm laser pulses of 100 fs duration is shown by the black line in Fig. 4. Although the data was recorded with a completely different spectroscopic setup, the frequency roll-off as well as the dynamic range is similar for both detectors. In particular, the strong decrease of spectral power for frequencies above 1.5 THz is a typical characteristic for the applied resonant detector design with a resonance frequency at approx. 1 THz. As for other LT-GaAs based probes, we expect that a further increased bandwidth of the InGaAs probe with a continuous roll-off from 1 to 4 THz will be obtained by using a non-resonant antenna design.

III. Near-field imaging

In this section we present the results of our THz near-field imaging experiments using the above described microprobe detector operated at 1550 nm. All measurements are based on the fiber-coupled THz TDS system which has been described earlier [12], [13]. The system is used for data acquisition and THz generation in combination with the micro-probe for THz near-field detection, as schematically depicted in Fig. 1. For near-field microscopy measurements with some 10 µm of spatial resolution the tip-to-sample distance is set to a few µm. Spatial scanning is enabled by a motorized xyz-stage moving the sample between the THz emitter and the near-field detector. During scanning, we force the detector-to-sample distance to be constant by dynamically following the sample topography, as measured with an optical height sensor. Height variations of up to 2 mm can be compensated, limited by the applied height sensor. To avoid unnecessary de- and acceleration movements, which would result in prolonged measurement runs, the sample is continuously xy-scanned below the detector and the position is recorded at a fixed rate. Synchronously to the sample movement, the THz time domain data acquisition gathers full time transients of 25 ps duration at a rate of 40 Hz. In frame of the THz near-field imaging experiments we record the peak-to-peak amplitude and the temporal position of the THz pulse peak and map this data to the corresponding xy-sample coordinates.

Exemplarily, we apply this technique for conductivity measurements of a 40 nm Chromium (Cr) thin-film on top of a 6-inch high-resistivity float-zone (HRFZ) silicon wafer. Such sheet resistance measurements of thin conductive layers are needed e.g. for graphene inspection tasks [16] or solar cell development. The Cr-top-layer of our test sample is structured to a grid of bars with different sizes, ranging from a few µm to several mm. Fig. 5 (a) displays a photograph of the wafer, while the THz image obtained by near-field microscopy is shown in Fig. 5 (b). The scanned area measures 100 mm x 85 mm and is sampled with a lateral resolution of 250 µm in a vertical distance of approx. 120 µm, acquiring THz pulse traces with a duration of 25 ps for each pixel. While the amplitude of the transmitted THz signal is mainly determined by the conductivity of the top layer, the substrate thickness is the main factor influencing the signal phase. Both parameters are separately available for each pixel of the near-field image.

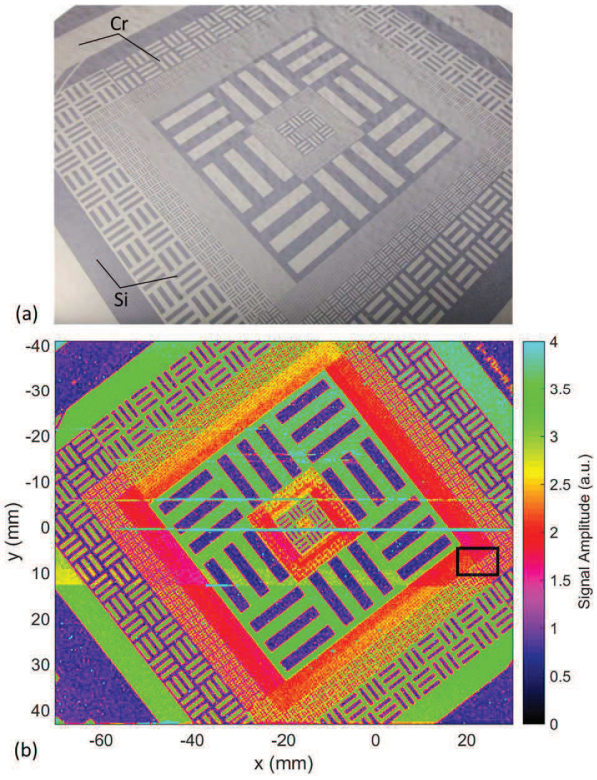

Fig. 5. Photograph (a) and THz near-field image (b) of a HRFZ silicon wafer covered with a 40 nm layer of Chromium, structured lithographically into bars of variable sizes and spacing. Half a million THz pulse traces of 25 ps duration were recorded for the full image.

The top-layer structures of the sample shown in the photograph of Fig. 5 (a) are easily found in the THz image. Here, the color-coding is as follows: Light green to red color refers to areas of high THz transmission corresponding to the bare HRFZ silicon substrate. Violet to black color indicates those parts covered with the Cr thin-film leading to low THz transmission. The horizontal light-blue lines in the THz image are measurement artifacts caused by dust particles, which adhered to the sample surface during the measurement and touched the detector tip.

In Fig. 6 (a), a high-resolution measurement of the area framed in Fig. 5 (b) is shown. The size of this field measures 7.5 mm x 3 mm. The lateral scan resolution was increased to 20 µm and the vertical sample-to-tip distance was set to 15 µm. The data acquisition rate and the length of the THz pulse trace remained unchanged. In the right part of Fig. 6 (a) the bar-shaped areas in light green refer to areas of bare HRFZ-Si. They are clearly distinguishable from the adjacent areas covered with Cr, which are characterized by a strongly reduced THz transmission amplitude. Next to this area, in the lower part of the image the inverted structure is depicted: Bars of low THz transmission become visible due to the high conductivity of the Cr layer compared to the surrounding bare substrate. The nominal width of these clearly resolved bars measures 300 µm. In the THz transmission image the apparent transition between substrate and Cr-bars occurs within five pixels, i.e. within 80 µm. The upper part of Fig. 6 (a) shows a smaller structure with 100 µm wide bars of Cr and HRFZ-Si, which are barely recognizable. Concluding from this data, we estimate our resolution limit to be about 100 µm under this configuration. Up to 20 µm resolution, can be expected for the applied probe antenna design using a vertical probe/sample distance in the range of 1-2 µm. Optimized semiconductor and antenna designs should lead to even better resolution as observed for LT-GaAs based counterparts.

The sheet resistance R_{SH} of the Cr-layer we can calculate from the THz data by using the Tinkham formula [17]:

$$T = \frac{T_{SL}}{T_S} = \frac{1}{1 + \frac{Z_0}{R_{sh} \cdot (n+1)}}.$$

Here, T_{SL} is the signal amplitude transmitted through the sample areas covered by the conductive Cr layer, whereas T_S is the reference transmission value for the bare silicon substrate. Further constants are the substrate refractive index $n \approx 3.42$ and the free-space impedance $Z_0 = 377\ \Omega$. Fig 6 (b) shows the calculated sheet resistance map based on the transmission image in Fig. 6 (a). Here, the black areas correspond to the highly resistive silicon and the blue to green areas indicate the conductive Cr thin-film. The mean sheet resistance of the complete Cr layer is $R_{SH} = (24.6 \pm 3.2)\ \Omega$/sq. Local sheet resistance variations in the Cr-layer, structure dimensions below the resolution limit and measurement noise contribute to the specified uncertainty of ± 3.2 Ω/sq. In order to confirm the sheet resistance value deduced from the THz near-field image we applied a 4-point-probe (4pp) measurement in the larger outer areas of the sample. The measured result of 25 Ω/sq. is clearly within the standard deviation obtained by THz near-field imaging.

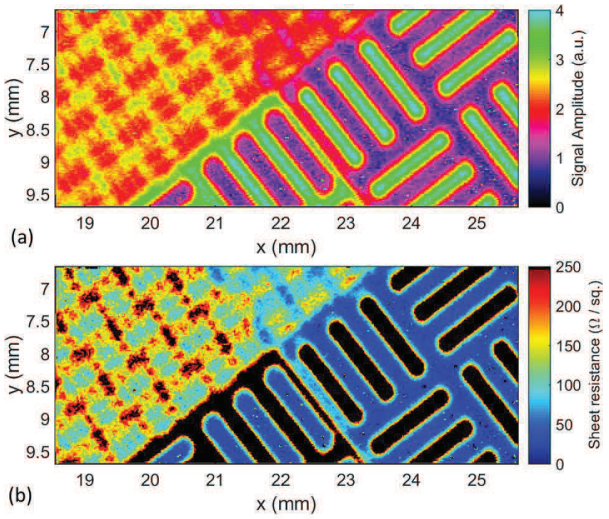

Fig. 6. High resolution near-field image of the framed area in Fig. 5 (b). The distance between probe tip and sample surface was 15 µm and the lateral resolution of this measurement 20 µm. The clearly resolved green and violet bars in (a) are 300 µm wide. In (b) the corresponding sheet resistance values calculated from the THz transmission data are shown, indicating a sheet resistance around R_{SH} = 25 Ω/sq. for the Cr-areas.

However, sheet resistance measurements of conductive thin-films are just one possible application for THz near-field imaging. The benefits of this measurement technique in fields like non-destructive testing of semiconductor devices or the development of meta-materials have also been demonstrated [18], [10]. The developed LT-InGaAs/InAlAs detector in combination with a fully fiber-coupled TDS system opens up the door for a more flexible and cost-efficient utilization of THz near-field microscopy at large scale. Practical advantages of fiber-coupled detectors and emitters for near-field measurements are evident: For applications like pulse tracing on a THz waveguide it is often required to freely move the THz emitter or detector device instead of moving a sample only. The use of fiber-coupled emitter and detector devices facilitates these measurement procedures significantly.

IV. Conclusion and Outlook

In this work, we presented a LT-InGaAs-based photoconductive THz near-field probe, designed for the direct operation with 1550 nm femtosecond laser pulses. We demonstrated that the semiconductor features sub-picosecond electron lifetimes resulting in a detectable bandwidth of up to 2 THz. The main advantage of the new 1550 nm near-field probe compared to existing 800 nm LT-GaAs probes is its direct compatibility with fiber-coupled THz-TDS systems. This enables stable and fast data acquisition of the entire THz pulse trace for each pixel of a near-field image without the need of time-consuming lock-in measurements. We demonstrated a first fully fiber-coupled THz near-field microscopy system, which combines operational flexibility, measurement speed and high spatial resolution.

V. REFERENCES

[1] H. Nakanishi, S. Fujiwara, K. Takayama, I. Kawayama, H. Murakami, M. Tonouchi,"Imaging of a Polycrystalline Silicon Solar Cell Using a Laser Terahertz Emission Microscope". *Applied Physics Express*. 2012, vol 5, no. 11, p. 112301.

[2] M. Tonouchi, "Cutting-edge terahertz technology". Nature Photonics. 2007, vol 1, no. 2, p. 97-105.

[3] W. L. Chan, J. Deibel, D. M. Mittleman,, "Imaging with terahertz radiation". *Reports on Progress in Physics*. 2007, vol. 70, no. 8, p. 1325.

[4] A. Adam, "Review of Near-Field Terahertz Measurement Methods and Their Applications", *Journal of Infrared, Millimeter, and Terahertz Waves* 2011, vol. 32, p. 976-1019

[5] A. J. MacFaden, J. L. Reno, I. Brener, O. Mitrofanov, "3um aperture probes for near-field terahertz transmission microscopy". *Appl. Phys. Lett*. 2014, vol. 104, no. 1.

[6] A. J. Huber, F. Keilmann, J. Wittborn, J. Aizpurua, R. Hillenbrand, "Terahertz Near-Field Nanoscopy of Mobile Carriers in Single Semiconductor Nanodevices". *Nano Letters*. 2008, vol. 8, no. 11, p. 3766-3770.

[7] K. Moon, E. Jung, M. Lim, Y. Do H. Han, "Terahertz Near-Field Microscope: Analysis and Measurements of Scattering Signals", *Terahertz Science and Technology, IEEE Transactions on* 2011, vol. 1, no. 1, p. 164-168,

[8] M. Wächter, M. Nagel, H. Kurz, "Tapered photoconductive terahertz field probe tip with subwavelength spatial resolution". *Appl. Phys. Lett*. 2009, vol. 95, no. 4, p. 041112.

[9] M. Nagel, A. Safiei, S. Sawallich, C. Matheisen, T. M. Pletzer, A. A. Mewe, N. J. C. M. van der Borg, I. Cesar, H. Kurz, "THz microprobe system for contact-free high-resolution sheet resistance imaging". *28th European Photovoltaic Solar Energy Conference and Exhibition*. 2013, pp. 856-860.

[10] M. Nagel, C. Matheisen and H. Kurz, "Novel techniques in terahertz near-field imaging and sensing" in, *Handbook of terahertz technology for imaging, sensing and communications*, ed. D. Saeedkia, Woodhead Publishing Series in Electronic and Optical Materials, no 34, 2013, p. 374 - 402,

[11] A. Bhattacharya, G. Georgiou, S. Sawallich, C. Matheisen, M. Nagel and J. Gómez Rivas, "Large near-to-far field spectral shifts for terahertz resonances", *Phys. Rev. B* 2016, vol. 93, p. 035438

[12] "Terawave time domain spectrometer," available: http://www.hhi.fraunhofer.de/fileadmin/Terahertz/Flyer_LasserWorld2015_Terawave-Time_Domain-Spectrometer_web.pdf.

[13] N. Vieweg, F. Rettich, A. Deninger, H. Roehle, R.J.B. Dietz, T. Göbel, "Terahertz-time domain spectrometer with 80 dB peak dynamic range," *J. Infrared Milli Terahz Waves*, vol. 35, pp. 823–832, Jul. 2014.

[14] R.J.B. Dietz, B. Globisch, H. Roehle, D. Stanze, T. Göbel, M. Schell "Influence and adjustment of carrier lifetimes in InGaAs/InAlAs photoconductive pulsed terahertz detectors: 6 THz bandwidth and 90dB dynamic range," *Opt. Express*, vol. 22, no. 16, pp. 19411-19422, Aug. 2014.

[15] B. Globisch, R. J. B. Dietz, T. Göbel, M. Schell, W. Bohmeyer, R. Müller, A. Steiger, "Absolute terahertz power measurement of a time domain spectroscopy system," *Opt. Lett.*, vol. 40, no. 15, pp. 3544-3547, Aug. 2015.

[16] J. D. Buron, D. H. Petersen, P. Bøggild, D. G. Cooke, M. Hilke, J. Sun, E. Whiteway, P. F. Nielsen, O. Hansen, A. Yurgens, P. U. Jepsen, "Graphene Conductance Uniformity Mapping". *Nano Letters*. 2012, vol 12, no. 10, p. 5074-5081.

[17] M. Tinkham, "Energy Gap Interpretation of Experiments on Infrared Transmission through Superconducting Films". *Phys. Rev.* 1956, vol 104, p. 845–846.

[18] Y. Xu, X. Zhang, Z. Tian, J. Gu, C. Ouyang, Y. Li, J. Han, W. Zhang, "Mapping the near-field propagation of surface plasmons on terahertz metasurfaces". *Appl. Phys. Lett*., vol. 107, no. 2, p. 021105, 2015.

[19] C. Matheisen, M. Waldow, B. Chmielak, S. Sawallich, T. Wahlbrink, J. Bolten, M. Nagel and H. Kurz, "Electro-optic light modulation and THz generation in locally plasma-activated silicon nanophotonic devices", *Opt. Express* 2014, vol. 22, no. 5, p. 5252--5259,

Publication VI

B. Globisch, R. J. B. Dietz, S. Nellen, T. Göbel, and M. Schell, “Terahertz detectors from Be-doped low-temperature grown InGaAs/InAlAs: Interplay of annealing and terahertz performance,” AIP Advances, vol. 6, 125011, 2016.

Terahertz detectors from Be-doped low-temperature grown InGaAs/InAlAs: Interplay of annealing and terahertz performance

B. Globisch,[1,a)] R. J. B. Dietz,[1] S. Nellen,[1] T. Göbel,[1] M. Schell[1]

[1]Fraunhofer Institute for Telecommunications, Heinrich Hertz Institute, Einsteinufer 37, 10587 Berlin, Germany

The influence of post-growth annealing on the electrical properties, the transient carrier dynamics and the performance as THz photoconductive receiver of Beryllium (Be) doped InGaAs/InAlAs multilayer heterostructures grown at 130 °C in a molecular beam epitaxy (MBE) system was investigated. We studied samples with nominally Be doping concentrations of 8×10^{17} cm^{-3} – 1.2×10^{19} cm^{3} annealed for 15 min. – 120 min. at temperatures between 500 °C – 600 °C. In contrast to previous publications, the results show consistently that annealing increases the electron lifetime of the material. In analogy to the annealing properties of low-temperature grown (LTG) GaAs we explain our findings by the precipitation of arsenic antisite defects. The knowledge of the influence of annealing on the material properties allowed for the fabrication of broadband THz photoconductive receivers with an electron lifetime below 300 fs and varying electrical properties. We found that the noise of the detected THz pulse trace in time-domain spectroscopy (TDS) was directly determined by the resistance of the photoconductive receiver and the peak-to-peak amplitude of the THz pulse correlated with the electron mobility.

I. INTRODUCTION

Within the last decades low-temperature growth of III-V compounds has become an important technique for the fabrication of semiconductors with sub-picosecond carrier lifetime and semi-insulating properties. The most prominent examples of low-temperature grown (LTG) semiconductors are GaAs and InGaAs.[1] Whereas the properties of LTG-GaAs have been studied extensively within the last 35 years, only a few studies of LTG-InGaAs exist. Due to its compatibility with the telecommunication band around 1550 nm LTG-InGaAs has become an important photoconductive material. The principal applications are semiconductor saturable absorber mirrors (SESAMs)[2], which are applied for the passive mode-locking of femtosecond fiber-lasers, and photoconductors for the generation and detection of THz radiation.[3,4] LTG-InGaAs based photoconductors are the state-of-the art detector antennas in commercially available THz time-domain spectroscopy (THz-TDS) systems.[5,6] However, the improvement of devices fabricated from LTG-InGaAs based materials demands a fundamental understanding of

a) Electronic mail: Bjoern.Globisch@hhi.fraunhofer.de

the properties of the material itself.

In this publication we study the influence of post-growth annealing on the electrical and dynamical properties of Be-doped InGaAs/InAlAs multilayer structures. Previous investigations have not drawn a consistent picture of the annealing process (see Sec. II). We show that annealing increases the electron lifetime and the resistivity of the material. Since a sub-picosecond electron lifetime is a prerequisite for broadband detectors in THz-TDS the control of the annealing process offers a great possibility for the optimization of these devices. Exemplarily, we fabricated THz receivers with an electron lifetime below 300 fs and varying electrical properties and showed that the noise-level as well as the peak-to-peak amplitude of the THz pulse trace were directly influenced by the annealing.

Before we discuss our results in Sec. III - V of this publication we give a short summary of the state of knowledge about LTG-GaAs and LTG-InGaAs and point out similarities, differences and open questions in the next section.

II. LOW TEMPERATURE GROWTH

The MBE growth of GaAs at temperatures below 300 °C leads to the incorporation of excess arsenic on Gallium lattice sites.[7,8] The concentration of these arsenic antisite (As_{Ga}) defects increases for lower growth temperatures and can reach values of up to 3×10^{20} cm^{-3} with still good crystal quality.[7] The energetic position of the As_{Ga} in LTG-GaAs is approx. 0.75 eV below the conduction band minimum, which corresponds to a mid-bandgap position.[9] Due to the high concentration of point defects, as-grown GaAs is conductive at room temperature caused by hopping conductivity between arsenic antisites.[9,10] When LTG-GaAs is annealed at temperatures above 300 °C the excess arsenic starts to precipitate.[10–12] The density and the size of the precipitates depends strongly on the duration and the temperature of the annealing process.[13,14] Generally, temperatures higher than 400 °C lead to a strong increase in resistivity[14] since the probability for hopping conductivity decreases exponentially with the decreasing density of point defects due to precipitation.[15] In addition, the arsenic precipitates form Schottky-barriers in the crystal, which further increase the resistivity of the material.[16,17] The diffusion of excess arsenic during the annealing process occurs via Gallium vacancies (V_{Ga}), which are incorporated during low-temperature growth.[11,18–20] Equally to the As_{Ga} defect, the concentration of V_{Ga} increases for lower growth temperatures and reaches values of up to 1×10^{18} cm^{-3}.[19] The ultrashort carrier

lifetime of LTG-GaAs is due to carrier trapping by ionized As_{Ga} defects (As_{Ga}^{+}).[1,21] In LTG-GaAs arsenic antisites are ionized by Gallium vacancies.[22] Since annealing leads to the formation of arsenic precipitates and thus reduces the concentration of As_{Ga} defects, the electron lifetime of LTG-GaAs increases when the material is annealed at temperatures above 400 °C.[11,21] The formation of arsenic precipitates during the post-growth annealing process is significantly suppressed by p-doping of LTG-GaAs with Beryllium (Be).[8,10,23] First, it was believed that Be-doping reduced the concentration of V_{Ga} in the material and therefore impeded the diffusion of excess arsenic.[10] However, Gebauer and co-workers[24] showed by positron annihilation spectroscopy that the concentration of V_{Ga} was not influenced by Be-doping. Instead, the authors proposed that the relatively small Be dopant, incorporated on substitutional group III lattice sites, reduced the lattice strain caused by the As_{Ga} defects and therefore eliminated a driving force for the diffusion of As_{Ga} during the annealing.[24] Be-As complexes, which were proposed in several publications, could not be observed in LTG-GaAs.[8]

Whereas the influence of the Be-doping and the annealing on the material properties of LTG-GaAs is quite well understood, several points are still ambiguous for LTG-InGaAs. Similar to LTG-GaAs, the low temperature growth of InGaAs leads to the formation of AsGa defects.[25] One of the major differences between LTG-InGaAs and LTG-GaAs is the energetic position of the As_{Ga} defect in the bandgap. Whereas it is almost mid-bandgap in LTG-GaAs[9] the defect level in LTG-InGaAs is located only approx. 0.1 eV below the conduction band minimum.[25] Therefore, a considerable fraction of the As_{Ga} defects is thermally ionized at room temperature leading to n-conductive material with electron densities higher than 1×10^{17} cm^{-3}.[25] In contrast to LTG-GaAs, annealing of LTG-InGaAs does not produce highly resistive material although arsenic precipitates are formed.[1,25,26] This can be explained by the fundamentally different reason for the n-conductivity of the as-grown LT-InGaAs compared to the as-grown LT-GaAs. Whereas LTG-GaAs shows hopping conductivity that depends exponentially on the concentration of As_{Ga} defects, the n-conductivity of LTG-InGaAs is caused by thermal ionization of the arsenic antisites, which leads to a linear dependency of the n-conductivity on the As_{Ga} concentration.

In order to compensate the n-conductivity and increase the resistivity of the material, LTG-InGaAs is commonly p-doped with Beryllium.[27] Apart from the pure compensatory effect of Be-doping, the electron lifetime in LTG-InGaAs decreases for a higher Be-doping concentration due to the ionization of additional As_{Ga} defects by Be dopants.[28,29] Electron lifetimes below 0.5 ps were

measured in LTG-InGaAs:Be. However, carrier concentrations below 1×10^{14} cm^{-3} could only be obtained by an additional annealing step in combination with the growth of a multilayer heterostructure consisting of Be-doped InGaAs and Be-doped InAlAs.[30,31] Here, the LTG-InAlAs:Be layer, which contains mid-bandgap defect levels, is purely compensatory.[32] In contrast, the influence of the post-growth annealing step has not been resolved entirely. Only a few publications studied the annealing process of LTG-InGaAs and LTG-InGaAs/InAlAs and obtained partially inconsistent results. Whereas it was consistently shown that the resistivity increases after annealing[33,34], the influence of annealing on the carrier lifetime is indistinct. On the one hand it was reported that annealing increased the electron lifetime due to the formation of arsenic clusters, similarly to LTG-GaAs.[28,27,35] On the other hand a recent study on annealed Be-doped LTG-InGaAs/InAlAs multilayer structures revealed a decrease of the electron lifetime for annealing temperatures between 350 °C and 600 °C.[34] In this publication we address this inconsistency and show that annealing indeed increases the electron lifetime due to the precipitation of arsenic antisites.

III. SAMPLE GROWTH AND CHARACTERIZATION

We studied multilayer-heterostructures grown at 130 °C in an MBE system on 2-inch semi-insulating InP:Fe-substrates. The layer stack consists of 100 periods of 12 nm InGaAs and 8 nm InAlAs lattice matched to the InP substrate. This multilayer structure was grown on top of a lattice matched InAlAs buffer with a thickness of 700 nm. All samples were homogenously Be-doped during the growth process.

We investigated the influence of the annealing time (isothermal annealing) and the annealing temperature (isochronal annealing) on the electrical and dynamical properties of the material. For the isothermal annealing, samples with a nominally Be doping concentration of 1.0×10^{18} cm^{-3} were annealed at 500 °C under an arsenic atmosphere for 15, 30, 60 and 120 minutes within the MBE growth chamber. For the isochronal annealing, three 2-inch wafers with nominally Be doping concentrations of 0.8×10^{18} cm^{-3}, 4.0×10^{18} cm^{-3} and 12.0×10^{18} cm^{-3} were cleaved into eight samples. We annealed seven of them for 60 min. at 500 °C, 525 °C, 550 °C, 575 °C, 600 °C, 650 °C and 700 °C in a metal organic chemical vapor epitaxy (MOVPE) system and kept one samples as an unannealed reference. The annealing was done inside the MOVPE growth chamber in order to prevent the out-diffusion of As and P from the samples at temperatures above 500 °C.

The partial pressures of As and P achieved in the MOVPE were significantly higher than those obtained in the MBE system. We used an As and P flux of 100 sccm for annealing temperatures below 600 °C and 200 sccm for annealing temperatures of 600 °C and higher.

We controlled the surface morphology of all samples by difference interference contrast microscopy. For annealing temperatures up to 600 °C a smooth surface was obtained whereas the samples annealed at 650 °C and 700 C showed a strong degradation of the surface quality. Therefore, the latter two samples are not discussed in the remainder of this publication. XRD rocking curves revealed good crystallinity with sharp peaks for all other samples. In contrast to the findings for LT-GaAs,[14] annealing did not essentially affect the XRD data of the multilayer structures investigated in this paper. For the electrical characterization, room temperature Hall measurements in van-der-Pauw geometry were conducted.

In order to determine the carrier lifetime, wavelength degenerate differential transmission (DT) measurements were applied.[31] In our setup, a femtosecond fiber laser with two fiber-coupled output ports provided 90 fs-pulses with a repetition rate of 100 MHz and 1550 nm central wavelength. A fiber-coupled attenuator was used to set the optical power of the pump and the probe beam, respectively. For all measurements the optical power of the pump pulse was at least one order of magnitude higher than the probe pulse.

A. Isothermal annealing

In Fig. 1 (a) the electron lifetime (τ_e) determined from wavelength degenerate DT measurements is plotted as a function of the annealing time. The Be doping concentration of all samples was 1×10^{18} cm^{-3} and the annealing temperature measured 500 °C. The density of carriers excited by the pump pulse was 6.5×10^{16} cm^{-3}, which is more than an order of magnitude lower than the Be-doping concentration. In this regime, the density of trapping sites is significantly higher than the density of excited carriers such that the DT-signal decays mono-exponentially and the electron lifetime (τ_e) can be determined by mono-exponential fits to the data.[21,31] In Fig. 1 (a) a gradual increase of τ_e for longer annealing times is observed. According to Shockley-Read-Hall[36] theory of carrier trapping, τ_e increases when the density of trapping sites decreases. Hence, annealing of Be doped LTG-InGaAs/InAlAs at 500 °C reduced the density of trapping centers,

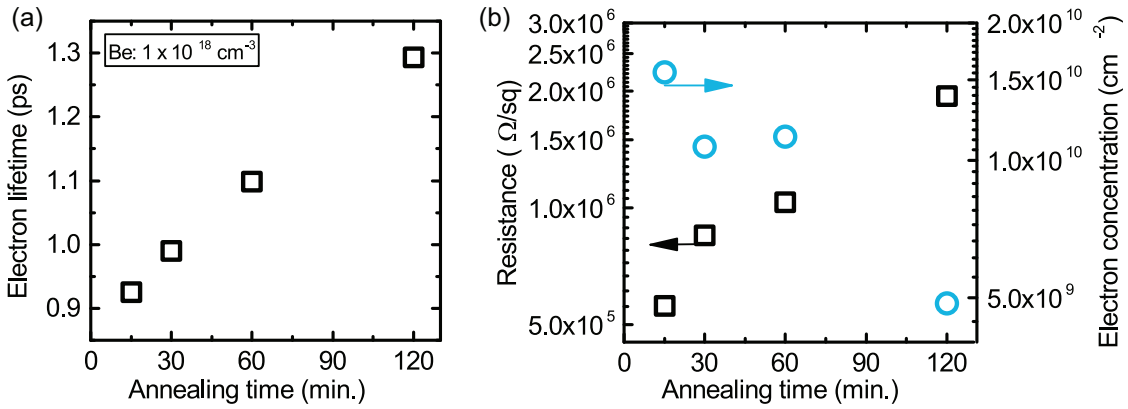

FIG.1. Electron lifetime (a) in dependence of the annealing time determined from wavelength degenerate differential transmission (DT) measurements. The excited carrier density was 6.5×10^{16} cm^{-3} in order to avoid the saturation of trapping sites. The electron lifetime was determined by mono-exponential fits to the DT signals. All samples were annealed at 500 °C in an arsenic atmosphere inside the MBE growth chamber. The Resistance and the electron concentration determined by room temperature Hall measurements are shown as a function of the annealing time in (b).

which is the As_{Ga}^{+} defect. In LTG-GaAs annealing at temperatures above 400 °C also increased the electron lifetime, which was explained by the formation of arsenic clusters (see Sec. II).[11,21] Thus, we attribute the lifetime increase in our samples to the precipitation of As_{Ga}^{+}.

In addition to the electron lifetime, we studied the electrical properties as a function of the annealing time. A semi-logarithmic plot of the resistance and the electron concentration obtained from room temperature Hall measurements is shown in Fig. 1 (b). The gradual increase of the resistance with longer annealing is also attributed to the precipitation of arsenic antisites. In Sec. II we showed that arsenic precipitates act as Schottky-barriers, which increase the resistance of the material. The decreasing electron concentration for longer annealing can be explained by the reduction of thermally ionized antisites due to the arsenic precipitation.

B. Isochronal annealing

In this section we investigate the influence of the annealing temperature on the resistance, the electron concentration and the electron lifetime. All samples were annealed in an MOVPE system for 60 min. with As and P stabilization. Fig. 2 shows (a) the resistance and (b) the electron concentration determined by room temperature Hall measurements as a function of the inverse annealing temperature for samples with a Be doping concentration of 0.8×10^{18}cm^{-3}, 4.0×10^{18}cm^{-3} and 12.0×10^{18}cm^{-3}. The annealing temperature of the as-grown samples was defined as room

temperature (20 °C). First, one observes that Beryllium acts as a p-dopant since the resistance increased and the electron concentration decreased for higher doping concentrations. Annealing between 500 °C – 600 °C further increased the resistance and decreased the electron concentration for all doping concentrations. Compared to the as-grown samples annealing at 600 °C changes the resistivity and the electron concentration by approx. three orders of magnitude. Hence, the post-growth annealing is an important technique for the adjustment of the electrical properties of the samples. Especially the annealing temperature has great influence on the material parameters.

The dashed lines in Fig. 2 (a) and (b) are linear fits to the data indicating that the resistivity decreases exponentially with the inverse annealing temperature whereas the electron concentration increases exponentially. This is the characteristic shape of a thermally activated diffusion process (Arrhenius plot). In agreement with the conclusion drawn from the results presented in Sec. III A we attribute this finding to the diffusion of As_{Ga} defects via Gallium vacancies during the annealing process.[11]

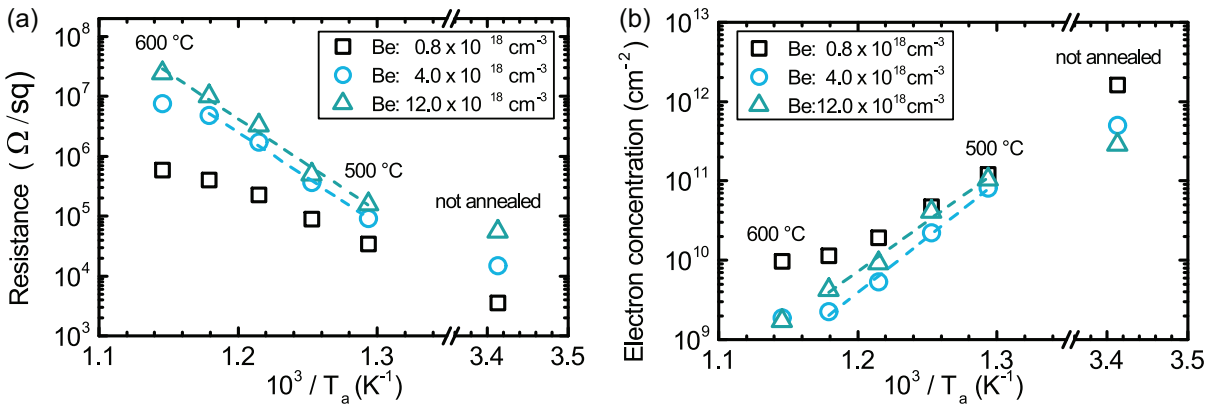

FIG. 2. (a) Resistance and (b) residual electron concentration determined by room temperature Hall measurements in van-der-Pauw geometry as a function of inverse annealing temperature for samples with Be doping concentration of 0.8×10^{18} cm^{-3} (black squares), 4.0×10^{18} cm^{-3} (blue circles) and 12.0×10^{18} cm^{-3} (green triangles). All samples were annealed in a MOVPE system in an As and P stabilized atmosphere. The annealing temperature corresponds to the temperature of the susceptor. The as-grown, samples are plotted for an annealing temperature of 20 °C.

Equally to the results discussed in Sec. III A we determined the electron lifetime (τ_e) by wavelength degenerate differential transmission measurements for an excited carrier density of 6.5×10^{16} cm^{-3}, in order to avoid any saturation of trapping defects. In Fig. 3 a semi-logarithmic plot of τ_e is shown as a function of the inverse annealing temperature. First, we notice that the electron lifetime decreases for higher Be doping concentrations since Be dopants ionize additional

antisite defects, which in turn increases the density of fast trapping centers.[28,29,31] Furthermore, the fact that Be dopants ionize additional antisites explains why the conductivity of all the samples shown in Fig. 2 was electron-like, although the Be doping concentration was up to two orders of magnitude higher than the residual electron concentration of the undoped material.[28,31] Apart from these well-known effects of Be-doping Fig. 3 shows that annealing increases the electron lifetime of all samples. Similar to Fig. 2 the dashed lines in Fig. 3 are linear fits to the data, which indicate a thermally activated diffusion process. Note that the slope of the linear fits decreases for higher doping concentrations, i.e. the diffusion of arsenic antisites is retarded when the density of Be dopants increases. The same effect was observed previously in LTG-GaAs: The precipitation of excess arsenic was reduced in Be-doped samples and could be explained by the relaxation of the lattice strain due to the small size of the substitutional Be dopants on group III lattice sites (see Sec. II and Ref. 24).

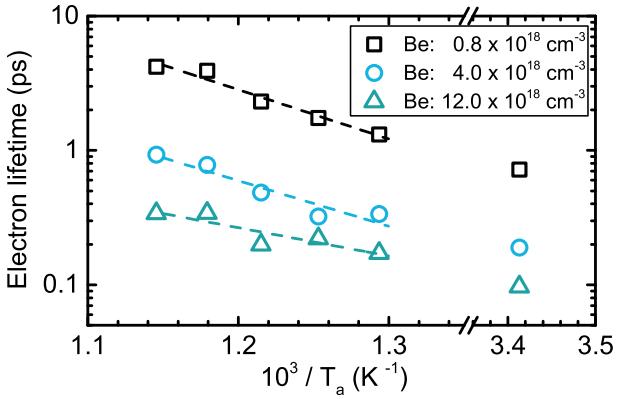

FIG. 3. Semi-logarithmic plot of the electron lifetime determined by wavelength degenerate differential transmission measurements as a function of the inverse temperature. Experimental conditions can be found in the caption of Fig. 1 (a). The electron lifetime increases for higher annealing temperatures and decreases with the Be doping concentration.

In summary, we have demonstrated that the annealing of Be doped LTG-InGaAs/InAlAs multilayer heterostructures had great impact on the electrical and dynamical properties of the material. In general, long-time annealing at higher temperatures increased the resistance and the electron lifetime whereas the electron concentration decreased. These effects were consistently explained by the precipitation of excess arsenic during the annealing process, analogously to LTG-GaAs.

IV. THZ CHARACTERIZATION

In the last 20 years, the influence of the carrier lifetime and the annealing of LT-GaAs on the performance as a THz photoconductor was extensively studied.[37–41] In contrast, comparably few investigations of the interplay between the material properties and the THz performance of photoconductors suitable for the illumination with 1550 nm radiation were conducted.[42–44] Recently, the influence of Be doping of LTG-InGaAs/InAlAs heterostructures on the performance as THz photoconductive detectors was described.[6] It was shown, that the spectral roll-off, the amplitude of the detected THz pulse and the noise-level were strongly influenced by this parameter. In this publication we studied samples with carrier lifetimes below 300 fs but significantly different electrical properties as THz photoconductive detectors. This was achieved by adjusting the Be-doping concentration and the post growth annealing temperature carefully which allowed us to study the influence of the electrical properties almost independent of the electron lifetime. Therefore, a detailed understanding of the principal parameters influencing the performance of photoconductors in THz-TDS can be obtained.

The electrical and the optical properties of the three samples are summarized in Table I.

TABLE I. Material properties of the samples selected for the fabrication of THz photoconductive detector antennas. The names are a combination of the prefix HHI, the doping concentration in units of 10^{18} cm^{-3} and the annealing temperature. The symbols denote: c_{Be} – Be-doping concentration, T_a – annealing temperature, ρ – resistance, n_e – electron concentration, μ_e – electron mobility, τ_e – electron lifetime.

Name	c_{Be} (10^{18} cm^{-3})	T_a (°C)	ρ (Ω / sq)	n_e (10^{11} cm^{-2})	μ_e (cm^2 V^{-1} s^{-1})	τ_e (ps)
HHI-4-0	4.0	-	1.5×10^4	8.1	517	0.16
HHI-4-500	4.0	500	1.1×10^5	1.1	517	0.27
HHI-12-500	12.0	500	3.3×10^5	0.9	194	0.14

The THz detector antennas were mesa-structured[45] as λ/2-dipoles with a length of 50 µm and a 10 µm × 10 µm photoconductive gap. For all subsequent experiments a commercially available THz time-domain spectrometer operating with femtosecond laser-pulses centered around 1550 nm was used.[5] The fiber-coupled THz emitter was illuminated with 20 mW of optical power and biased with 120 V.[46] For an individual measurement 1000 pulse trace with a

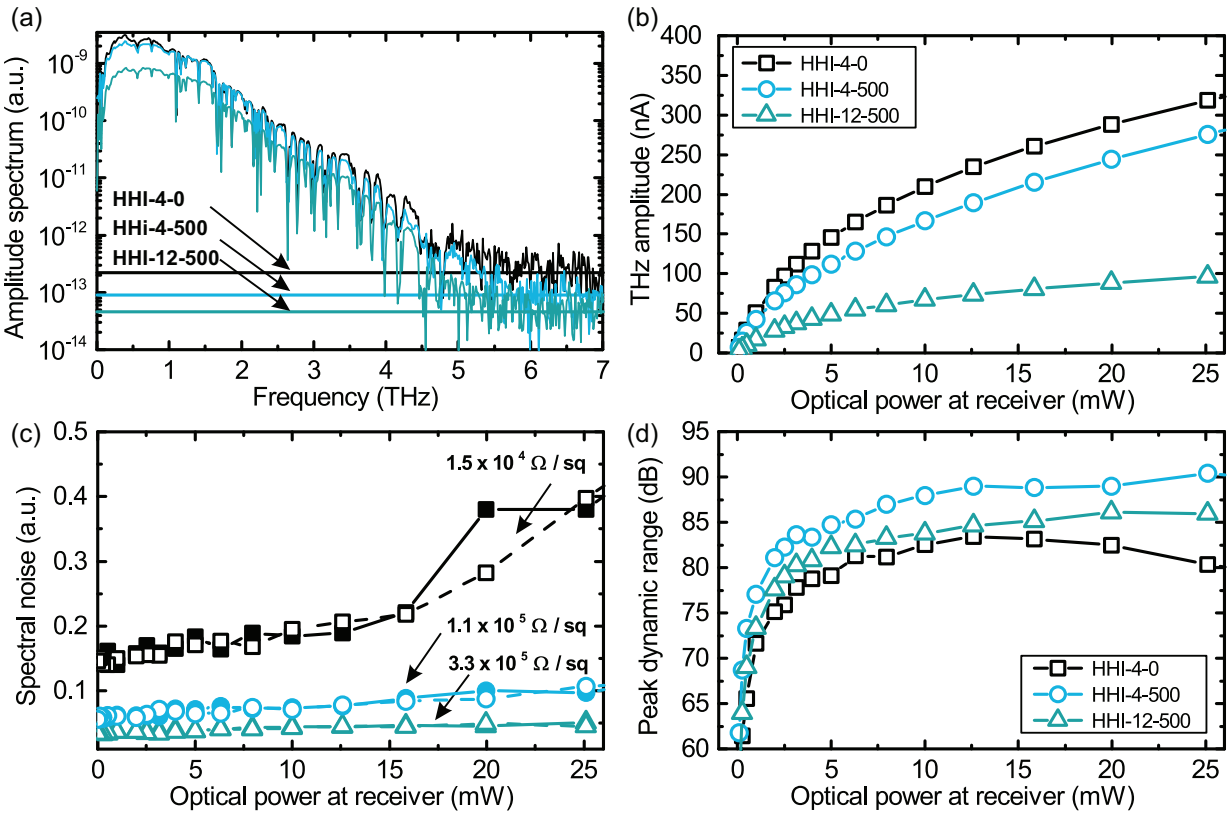

FIG. 4. (a) Amplitude spectrum obtained by Fast-Fourier-Transformation of pulse traces recorded for samples HHI-4-0, HHI-4-500 and HHI-12-500 as THz photoconductive receivers. The optical illumination power was 20 mW for all samples. The noise level obtained by averaging the spectral amplitudes from 7.5 THz – 10 THz are shown as horizontal lines. The peak-to-peak THz amplitude (b), the spectral noise-level (c) and the peak dynamic range (d) are shown as a function of the optical illumination power of the receiver. The THz emitter was illuminated with 20 mW of optical power and biased with 120V for all measurements. Pulse traces with a duration of 70 ps were recorded and averaged 1000 times for a single measurement leading to a total acquisition time of 60 s.

duration of 70 ps were recorded and averaged, leading to a total acquisition time of 60 s. The THz path consisted of two 2-inch 90 ° off-axis parabolic mirrors with a focal length of 3-inch. All measurements were done in ambient air. Similar to the emitter, the THz receiver antenna was attached to a hyper-hemispherical silicon lens and integrated into a fiber-coupled module. The optical illumination power of the receiver was controlled by a fiber-coupled attenuator.

A summary of the THz results is given in Fig. 4. The amplitude spectra, obtained by Fast Fourier Transformation (FFT) of the corresponding pulse trace, are shown in Fig. 4 (a). The optical illumination power at the receiver was set to 20 mW for these measurements. First, one observes that the spectral roll-off is almost identical for the three devices leading to a bandwidth of more

than 5 THz. Since the electron lifetime determines the spectral roll-off and therefore the bandwidth of the THz detector the principal reason for the shape of the THz-spectra in Fig. 4 (a) is the ultrashort electron lifetime of all samples. However, obvious differences in the amplitudes of the spectral components as well as the noise level, which is depicted as a horizontal line for each spectrum, can be observed. The samples with lower Be doping (HHI-4-0, HHI-4-500) show higher amplitudes for all frequencies, whereas the noise level is the lowest for sample HHI-12-500. In order to investigate the influence of the material properties on the receiver performance in more detail we plotted the peak-to-peak amplitude of the THz pulse and the noise-level as a function of the optical illumination power at the receiver in Figs. 4 (b) and (c), respectively. Here, the conclusions drawn in the analysis of Fig. 4 (a) are confirmed: The THz amplitude is approx. a factor of three higher for the samples HHI-4-0 and HHI-4-500 than for HHI-12-500. We explain this with an increased scattering on ionized defects for higher Be doping concentrations, which reduces the detector current.[6] The ratio between the electron mobility of these samples (cf. Table I) agree well with the increase of the THz amplitude. Therefore, a high mobility of the photoconductive material translates into high THz amplitudes.

In Fig. 4 (c) the noise level of the three samples are compared. Colors and symbols are equivalent to Fig. 4 (b). We averaged the spectral amplitudes from 7.5 THz to 10 THz and interpreted the value as the spectral noise. The open symbols in Fig. 4 (c) correspond to the spectral noise-level when the THz pulse is blocked, i.e. the noise-level generated by the receiver only. Since full and open symbols are in good agreement the receiver determines the noise level in our system. In order to relate the noise level of the THz-spectrum with the electrical properties of the photoconductors, we labeled each graph with the resistance determined from Hall measurements. Here, we observe that the Hall resistance correlates with the spectral noise of the receiver, i.e. the higher the resistance is the lower is the noise-level. This is directly expectable, since the duty cycle of the laser is 10^{-5} and the electron lifetime of all receiver devices is below 1 ps. Therefore, the receiver is unilluminated almost all the time, such that the noise current is simply determined by the resistance of the photoconductor.

After having analyzed the THz amplitude and the noise-level of each receiver separately, we finally investigated the combined parameter, which is the peak dynamic range. In Fig. 4 (d) we observe that HHI-4-0 - the sample with the highest THz amplitude - shows the lowest dynamic range due to the relatively high noise level. In contrast, the highest doped sample (HHI-12-500),

which had the lowest THz amplitude in Fig. 4 (b) shows an intermediate dynamic range due to the low noise-level. However, the sample HHI-4-500, with a Be doping concentration of 4×10^{18} cm^{-3} and 500 °C annealing has the highest dynamic range due to the optimal combination of signal amplitude and noise-level.

The results presented in this section underline that a detailed understanding of the interplay between material parameters and THz performance allows for the precise optimization of THz photoconductive receivers. Particularly, the post-growth annealing of the photoconductive material is a suitable parameter for tuning resistance, electron lifetime and electron mobility of the future device.

V. CONCLUSION

We investigated the influence of annealing on the electrical properties, the carrier dynamics and the performance as THz photoconductive receiver of Be-doped LTG-InGaAs/InAlAs multilayer heterostructures. We analyzed doping concentrations between 8×10^{17} cm^{-3} – 1.2×10^{17} cm^{-3}, annealing times between 15 min. – 120 min. and annealing temperatures between 500 C – 600 °C. In contrast to previously published results we found that annealing generally increases the resistivity and the electron lifetime of the material and decreases the residual carrier concentration. We explain these effects by the formation of arsenic clusters (precipitates) during the annealing process, similar to the annealing behavior of LTG-GaAs. Subsequently, we analyzed three selected samples as THz photoconductive receivers in a TDS system. The resistance and electron concentration of these devices differed by more than an order of magnitude, whereas all samples featured electron lifetimes below 300 fs. Hence, we could analyze the influence of the electrical properties on the performance as THz receiver without losing the broadband detection capability of the devices. We found that the noise-level of the THz spectrum was directly determined by the resistivity of the device: The higher the resistivity is, the lower is the noise-level. The peak-to-peak amplitude of the THz pulse increased for higher electron mobility. Since low noise and high amplitude lead to high dynamic range, the detailed understanding and precise control of the interplay between Be doping and post-growth annealing allows for the optimization of THz photoconductive receivers.

ACKNOWLEDGMENTS

This work was funded by the German Ministry for Education and Research under grant 13N13388.

REFERENCES

[1] S. Gupta, J.F. Whitaker, and G. a. Mourou, IEEE J. Quantum Electron. **28**, 2464 (1992).
[2] U. Keller, K.J. Weingarten, X.K. Franz, D. Kopf, B. Braun, I.D. Jung, R. Fluck, H. Clemens, N. Matuschek, and J. Aus der Au, IEEE J. Sel. Top. Quantum Electron. **2**, 435 (1996).
[3] A. Takazato, M. Kamakura, T. Matsui, J. Kitagawa, and Y. Kadoya, Appl. Phys. Lett. **90**, 101119 (2007).
[4] A. Takazato, M. Kamakura, T. Matsui, J. Kitagawa, and Y. Kadoya, Appl. Phys. Lett. **91**, 11102 (2007).
[5] N. Vieweg, F. Rettich, A. Deninger, H. Roehle, R. Dietz, T. Göbel, and M. Schell, J. Infrared Millim. Terahz Waves **35**, 823 (2014).
[6] R.J.B. Dietz, B. Globisch, H. Roehle, D. Stanze, T. Göbel, and M. Schell, Opt. Express **22**, 19411 (2014).
[7] M. Kaminska, J. Vac. Sci. Technol. B Microelectron. Nanom. Struct. **7**, 710 (1989).
[8] R.M. Feenstra, J.M. Woodall, and G.D. Pettit, Phys. Rev. Lett. **71**, 1176 (1993).
[9] D.C. Look, D.C. Walters, M.O. Manasreh, J.R. Sizelove, C.E. Stutz, and K.R. Evans, Phys. Rev. B **42**, 3578 (1990).
[10] D.E. Bliss, W. Walukiewicz, J.W. Ager, E.E. Haller, K.T. Chan, and S. Tanigawa, J. Appl. Phys. **71**, 1699 (1992).
[11] Z. Liliental-Weber, X.W. Lin, J. Washburn, and W. Schaff, Appl. Phys. Lett. **66**, 2086 (1995).
[12] T.E.M. Staab, R.M. Nieminen, M. Luysberg, and T. Frauenheim, Phys. Rev. Lett. **95**, 1 (2005).
[13] E.S. Harmon, M.R. Melloch, J.M. Woodall, D.D. Nolte, N. Otsuka, and C.L. Chang, Appl. Phys. Lett. **63**, 2248 (1993).
[14] I.S. Gregory, C.M. Tey, A.G. Cullis, M.J. Evans, H.E. Beere, and I. Farrer, Phys. Rev. B **73**, 195201 (2006).
[15] B.I. Shklovskii and A.L. Efros, in *Electron. Prop. Doped Semicond.*, edited by M. Cardona (Springer, Berlin, 1984), pp. 72–93.
[16] A.C. Warren, J.M. Woodall, J.L. Freeouf, D. Grischkowsky, D.T. McInturff, M.R. Melloch, and N. Otsuka, Appl. Phys. Lett. **57**, 1331 (1990).
[17] A.C. Warren, J.M. Woodall, P.D. Kirchner, X. Yin, F. Pollak, M.R. Melloch, N. Otsuka, and K. Mahalingam, Phys. Rev. B **46**, 4617 (1992).
[18] D.E. Bliss, W. Walukiewicz, and E.E. Haller, J. Electron. Mater. **22**, 1401 (1993).
[19] J. Gebauer, R. Krause-Rehberg, S. Eichler, M. Luysberg, H. Sohn, and E.R. Weber, Appl. Phys. Lett. **71**, 638 (1997).
[20] J.C. Bourgoin, K. Khirouni, and M. Stellmacher, Appl. Phys. Lett. **72**, 442 (1998).
[21] A.J. Lochtefeld, M.R. Melloch, J.C.P. Chang, and E.S. Harmon, Appl. Phys. Lett. **69**, 1465 (1996).
[22] M. Luysberg, H. Sohn, and a Prasad, J. Appl. Phys. **83**, 561 (1998).
[23] A. Krotkus, K. Bertulis, M. Kaminska, K. Korona, A. Wolos, J. Siegert, S. Marcinkevičius, J.-F. Roux, and J.-L. Coutaz, IEE Proc. - Optoelectron. **149**, 111 (2002).
[24] J. Gebauer, R. Zhao, P. Specht, E.R. Weber, F. Börner, F. Redmann, and R. Krause-Rehberg, Appl. Phys. Lett. **79**, 4313 (2001).

[25] H. Künzel, J. Böttcher, R. Gibis, and G. Urmann, Appl. Phys. Lett. **61**, 1347 (1992).
[26] R.A. Metzger, A.S. Brown, L.G. McCray, and J. a. Henige, J. Vac. Sci. Technol. B **11**, 798 (1992).
[27] H. Kuenzel, K. Biermann, D. Nickel, and T. Elsaesser, J. Cryst. Growth **227–228**, 284 (2001).
[28] B. Grandidier, H. Chen, R.M. Feenstra, D.T. McInturff, P.W. Juodawlkis, and S.E. Ralph, Appl. Phys. Lett. **74**, 1439 (1999).
[29] R. Takahashi, Y. Kawamura, T. Kagawa, and H. Iwamura, Appl. Phys. Lett. **65**, 1790 (1994).
[30] B. Sartorius, H. Roehle, H. Künzel, J. Böttcher, M. Schlak, D. Stanze, H. Venghaus, and M. Schell, Opt. Express **16**, 9565 (2008).
[31] B. Globisch, R.J.B. Dietz, D. Stanze, T. Göbel, and M. Schell, Appl. Phys. Lett. **104**, (2014).
[32] S. Gupta, P.K. Bhattacharya, J. Pamulapati, and G. Mourou, Appl. Phys. Lett. **57**, 1543 (1990).
[33] P.W. Juodawlkis, D.T. McInturff, and S.E. Ralph, Appl. Phys. Lett. **69**, 4062 (1996).
[34] I. Kostakis, D. Saeedkia, and M. Missous, J. Appl. Phys. **111**, (2012).
[35] K. Biermann, D. Nickel, K. Reimann, M. Woerner, T. Elsaesser, and H. Künzel, Appl. Phys. Lett. **80**, 1936 (2002).
[36] W. Shockley and W.T. Read, Phys. Rev. **87**, 835 (1952).
[37] Z.S. Piao, M. Tani, and K. Sakai, Proc. SPIE - Int. Soc. Opt. Eng. **3617**, 49 (1999).
[38] M. Tani, S. Matsuura, K. Sakai, and S. Nakashima, Appl. Opt. **36**, 7853 (1997).
[39] M. Tani, K. Sakai, and H. Mimura, Japanese J. Appl. Physics, Part 2 Lett. **36**, L1175 (1997).
[40] I.S. Gregory, C. Baker, W.R. Tribe, M.J. Evans, H.E. Beere, E.H. Linfield, A.G. Davies, and M. Missous, Appl. Phys. Lett. **83**, 4199 (2003).
[41] A. Krotkus, J. Phys. D. Appl. Phys. **43**, 273001 (2010).
[42] I. Kostakis, D. Saeedkia, and M. Missous, IEEE Trans. Terahertz Sci. Technol. **2**, 617 (2012).
[43] S. Preu, G.H. Döhler, S. Malzer, L.J. Wang, and A.C. Gossard, J. Appl. Phys. **109**, 61301 (2011).
[44] C. Baker, I. Gregory, M. Evans, W. Tribe, E. Linfield, and M. Missous, Opt. Express **13**, 9639 (2005).
[45] H. Roehle, R.J.B. Dietz, H.J. Hensel, J. Böttcher, H. Künzel, D. Stanze, M. Schell, and B. Sartorius, Opt. Express **18**, 2296 (2010).
[46] B. Globisch, R.J.B. Dietz, T. Göbel, M. Schell, W. Bohmeyer, R. Müller, and A. Steiger, Opt. Lett. **40**, 3544 (2015).

Publication VII

B. Globisch, R. J. B. Dietz, R. B. Kohlhaas, S. Nellen, M. Kleinert, T. Göbel, and M. Schell, “Fiber-coupled transceiver for terahertz reflection measurements with a 4.5 THz bandwidth”, Opt. Lett., vol. 41, no. 22, pp. 5262-5265, 2016.

Fiber-coupled transceiver for terahertz reflection measurements with 4.5 THz bandwidth

Björn Globisch,[1,*] Roman J. B. Dietz,[1] Robert B. Kohlhaas,[1] Simon Nellen,[1] Moritz Kleinert,[1] Thorsten Göbel,[1] Martin Schell[1]

[1]*Fraunhofer Institute for Telecommunications, Heinrich Hertz Institute, HHI, Einsteinufer 37, 10587 Berlin*
**Corresponding author: Bjoern.Globisch@hhi.fraunhofer.de*

Received XX Month XXXX; revised XX Month, XXXX; accepted XX Month XXXX; posted XX Month XXXX (Doc. ID XXXXX); published XX Month XXXX

We present a fiber-coupled transceiver for THz time domain spectroscopy which combines emitter and receiver on a single photoconductive chip. With a bandwidth of 4.5 THz and a peak dynamic range larger than 70 dB it allows for THz reflection measurements under normal incidence. This THz reflection head is a promising device for applications in fields like material inspection and non-destructive testing.

OCIS codes: *(040.2235) Far infrared or terahertz; (300.6495) Spectroscopy, terahertz; (120.4290) Nondestructive testing,*

http://dx.doi.org/10.1364/OL.99.099999

Within the last decade THz time-domain spectroscopy (THz-TDS) evolved from a purely scientific tool to a promising technology for future industrial applications.[1,2] Core enabling developments were femtosecond fiber-lasers emitting at a central wavelength of 1550 nm in combination with photoconductive antennas sensitive to this radiation.[3-7] These developments paved the way for compact, reliable and fully fiber-coupled THz spectrometers, which allowed for the transfer of the THz technology to industrial enviroments.[8] Nevertheless, many applications for THz-TDS in fields like non-destructive testing and in-line process monitoring permit only one-side access to the sample under test, which requires measurements in reflection geometry. Existing implementations of sensor heads are based on discrete emitters and detectors, which require an angled beam path or a THz beamsplitter in order to distribute the reflected THz signal to the receiver. Both concepts lead to bulky and expensive setups with low signals and limited bandwidth. In this paper we present a monolithically integrated THz transceiver, which allows for measurements under normal incidence and therefore overcomes the limitations mentioned above.

The concept of an integrated transceiver device, which combines THz emitter and detector on a single photoconductive chip, was proposed for the first time in the year 2000.[9] The authors employed a low-temperature-grown GaAs antenna with a common photoconductive gap for THz generation and detection, which allowed for THz reflection measurements under normal incidence. In the following years, THz transceivers remained a constant research topic and up to now two different transceiver designs have been proposed: Transceivers that use the same photoconductive gap for generation and detection[9-11] and those which employ two spatially separated gaps on the same chip[12,13]. The first concept permits a rather simple optical coupling since only a single photoconductive gap has to be illuminated. However, the photocurrent generated by the optical excitation beams as well as the bias voltage of the emitter contribute to the noise of the detector.[9] Therefore, the THz bandwidth and the maximum dynamic range obtained with this concept were limited to below 2 THz and 40 dB, respectively.[9,10] THz transceivers with two spatially separated photoconductive gaps reduce the unwanted crosstalk of the emitted THz signal measured by the detector. However, the optical fiber-coupling of the individual gaps is challenging in this transceiver concept. When each gap is directly connected to an optical fiber, the distance between emitter and receiver measures at least 125 µm, which corresponds to the diameter of a stripped single-mode fiber. Since the radiated THz spectrum of a photoconductive emitter typically contains frequencies in the range of 0.1 THz – 5 THz (3000 µm – 60 µm in wavelength), the minimum distance of 125 µm between emitter and detector leads to unwanted resonances in the spectrum[9] and a distorted radiation pattern. Published results for this transceiver concept report a bandwidth of up to 2 THz with a peak dynamic range of 30 dB.[12,13] Since individual THz emitters and receivers allow for the detection of THz pulses with a bandwidth of up to 6 THz and 90 dB dynamic range[8,14], THz transceivers have to be improved significantly in order to reach competitive performance.

The solution to this challenge is an integrated THz transceiver where the photoconductive gaps for emitter and detector are separated by 45 µm only. The fiber-optical coupling is enabled with a polymer waveguide chip, which reduces the distance of two polarization maintaining (PM) fibers to 45 µm. This transceiver concept allows for the detection of THz pulses with a bandwidth of up to 4.5 THz and more than 70 dB peak dynamic range. Due to the close proximity of the emitter and the detector on the chip, the radiation pattern of the transceiver is almost identical to individual

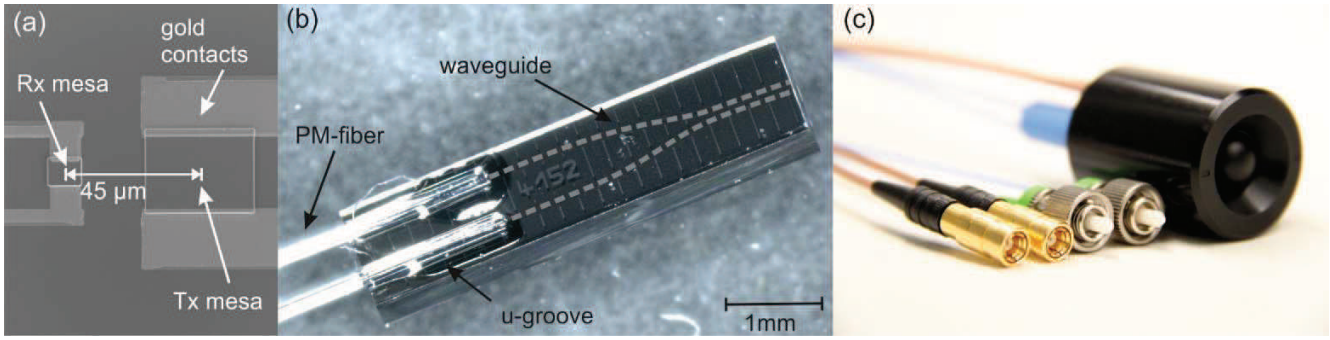

Fig. 1. Scanning electron micrograph of the THz transceiver chip (a). The distance between the centers of the receiver and emitter mesa measures 45 µm. Optical micrograph of the polymer coupler with two attached PM-fibers (b). The u-grooves fabricated into the polymer chip have a distance of 500 µm and support stripped PM fibers with a diameter of 125 µm. The two waveguides, highlighted by dashed lines, lead from the tip of each u-groove to the facet of the polymer chip and reduce the distance between the optical beams from 500 µm to 45 µm. The fiber-coupled THz transceiver module (c) has a diameter of 25 mm, which is equivalent to individual, fiber-coupled emitter and receiver devices. It provides two PM fibers for the illumination of emitter and receiver and two SMB connectors: One for the bias supply of the emitter and one for the current signal detected by the receiver.

THz emitters (cf. Fig. 3). Thus, this transceiver is a convenient device for THz reflection measurements under normal incidence. Due to the optical fiber coupling it can be directly combined with commercially available THz time-domain spectrometers.[8]

The key component of the novel THz transceiver chip is the photoconductor itself. Theoretical models and experimental results of the last 15 years revealed that the demands on photoconductors for THz emitters and detectors are different.[7,14-18] On the detector side, a sub-picosecond electron lifetime is required for the detection of broadband THz radiation with high dynamic range.[14,16,18] In contrast, photoconductive materials for THz emitters require high breakdown fields and carrier mobility, whereas the electron lifetime is of minor importance.[7] Therefore, specialized photoconductive materials were developed for THz emitters and detectors. Since a THz transceiver combines the two devices on a single chip, the same photoconductive material has to be used for THz emission and detection. (Here, we will not discuss the possibility to integrate two different photoconductors on the same chip via re-growth steps during the fabrication.) In this case the sub-picosecond carrier lifetime is the key parameter for THz transceivers: On the receiver side, it guarantees the broadband detection capability and in the emitter it prevents long-living carriers, which are a source of low-frequency crosstalk.

Therefore, we fabricated our THz transceiver from a photoconductor originally optimized for the application as an individual THz detector. The state-of-the art photoconductive material for 1550 nm excitation is low-temperature-grown, Beryllium doped InGaAs/InAlAs grown by molecular beam epitaxy.[14] We verified the sub-picosecond electron lifetime (~ 500 fs) by transient differential transmission measurements with femtosecond pulses centered around 1550 nm.[19] The transceiver-chip features two monolithically integrated photoconductive areas (mesas) formed by chemically assisted ion beam etching (CAIBE). Fig. 1 (a) shows a scanning electron micrograph of the chip. The THz emitter measures 25 µm × 40 µm and is contacted by a strip-line antenna. For the receiver, a dipole antenna with a length of 35 µm and a photosensitive area of 10 µm × 15 µm is applied. The centers of the emitter and detector mesa are separated by 45 µm. This distance was chosen as a first concept in order to facilitate the fabrication of the photoconductive chip and the polymer waveguide-coupler. The influence of the distance between emitter and detector on the performance of the transceiver will be investigated elsewhere.

The emitting and receiving areas were illuminated by femtosecond laser-pulses provided by two distinct PM-fibers. Due to the proximity of emitter and receiver on the chip the direct attachment of the fibers to the photoconductive gaps was impeded. To overcome this, we fabricated a passive polymer coupler from the ZPU-12 series of ChemOptics Inc. Two u-grooves spaced by 500 µm were structured lithographically into the polymer and a stripped PM fiber with a diameter of 125 µm was fixed in each of these u-grooves. An integrated waveguide leads from the tip of each u-groove to the facet of the polymer chip in order to reduce the distance of the optical beams to 45 µm. The refractive index contrast of the polymer waveguide is $\Delta n = 0.01$ with a cross section of 6 µm × 6 µm. The insertion loss between the PM fiber and the facet of the waveguide chip was below 1 dB.[20] A micrograph of the polymer chip with a size of 4 mm × 1 mm is depicted in Fig. 1 (b), the waveguides are highlighted by dashed lines.

For the integration into a fiber-coupled transceiver module (cf. Fig. 1 (c)) the photoconductive chip was placed on top of a hyper-hemispherical silicon lens with a diameter of 10 mm and the polymer waveguide chip was butt-coupled to the photoconductor. We employed wire bonds to connect the emitter and detector of the transceiver with an electric circuit board. Coaxial cables were used for the bias supply of the emitter and the extraction of the detector signal.

The transceiver was operated with a THz-TDS system supplying 100 fs pulses with a repetition rate of 100 MHz and 20 mW of optical power for the emitter and the receiver, respectively.[8] The emitter was biased with 35 V. The THz radiation emitted by the transceiver was collimated with a 90 °off-axis parabolic mirror and reflected by a plane, gold-coated mirror. The total length of the THz path measured 15 cm. For data acquisition, no lock-in detection was used. We recorded individual pulse traces with a length of

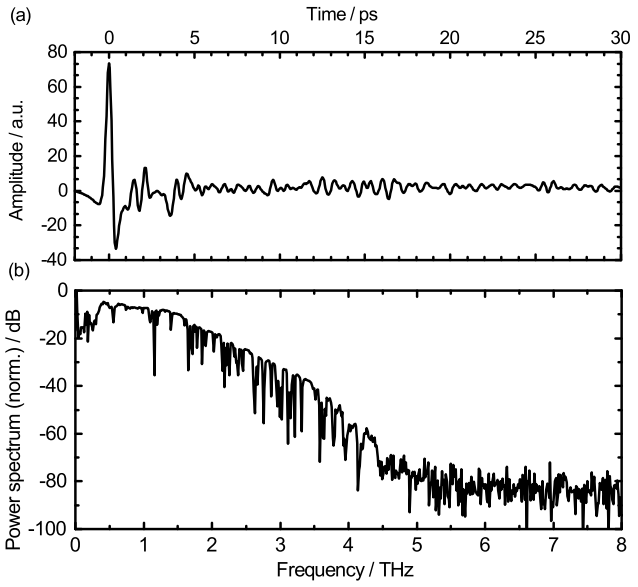

Fig. 2. Pulse trace (a) and normalized power spectrum (b) detected by the THz transceiver. The emitted THz pulse was collimated by a 90 ° off-axis parabolic mirror and reflected by a plane, gold-coated mirror. The total length of the THz path measured approx. 15 cm. Measurements were done in ambient air. The optical illumination power was 20 mW for the emitter and detector part of the transceiver. The electrical bias measured 35 V. The pulse trace shown in (a) is an average of 1000 traces acquired within 60 s. A bandwidth higher than 4.5 THz with a peak dynamic range of more than 70 dB can be observed (b).

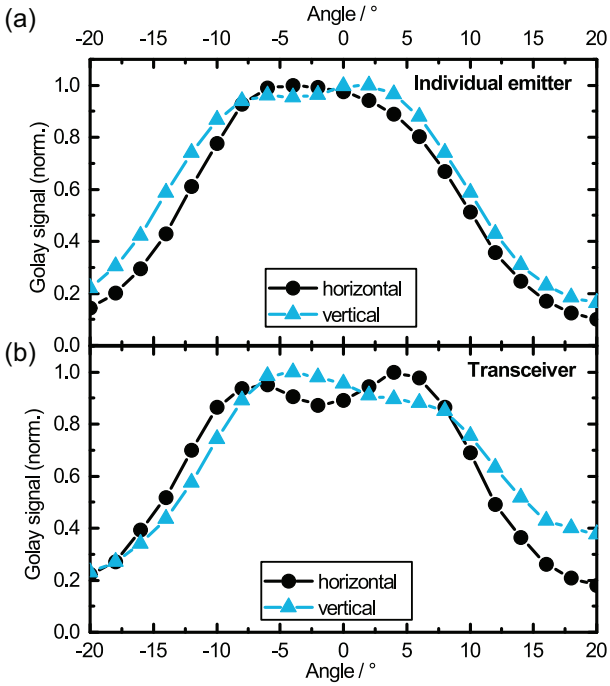

Fig. 3. Radiation pattern of an individual emitter (a) and the THz transceiver (b) recorded by a Golay cell. The fiber-coupled modules were rotated in a distance of 5 cm in front of the entrance cone of the Golay cell between -20 ° - 20 ° with respect to the aligned position. Measurements labeled horizontal (black dots) and vertical (blue triangles) correspond to the orientation of the respective module.

70 ps within 60 ms and averaged 1000 traces leading to a total acquisition time of 60 s.. In Fig. 2 (a) and (b) the THz pulse trace and the corresponding normalized power spectrum are shown. The bandwidth of the detected signal exceeds 4.5 THz and the peak dynamic range is larger than 70 dB. This is a significant improvement compared to all results published previously for any transceiver concept.[9-13] The pulse trace in Fig. 2 (a) shows a pronounced peak and adjacent undulations originating from water vapor absorption. Additional features suggesting significant cross-talk between emitter and detector are not observed.

Further, we studied the radiation pattern of the transceiver. Due to the spatial separation of emitter and receiver mesa, the focal point of the silicon lens is not perfectly aligned to the position of each gap. This could distort the radiation pattern of the device. We compared the radiation pattern of an individual fiber-coupled THz emitter[21] with the transceiver by aligning the respective device in a distance of approx. 5 cm in front of the entrance cone of a Golay cell. The optical excitation beam of the THz emitter was chopped with a frequency of 20 Hz and the signal of the Golay cell was measured via lock-in detection. From the aligned position we rotated the module successively between -20 ° and 20 ° in steps of 2 ° around its vertical axis and read out the Golay cell at each point. Afterwards, the module was turned by 90 ° around its horizontal axis and the measurements were repeated. Thus, radiation patterns for two orthogonal orientations were recorded, which are called horizontal and vertical, respectively. Due to the design of the hyper-hemispheric silicon lens a beam divergence of 12 ° - 15 ° is expected for both orientations. Fig. 3 (a) and (b) show the results for the individual emitter and the transceiver, respectively. One observes comparable radiation patterns for both orientations. The half-width at half maximum corresponds to the assumed 12 ° - 15 °. These results underline that the spatial separation of emitter and detector mesa on the transceiver chip has no significant influence on the radiation properties of this device. Note, that the beam divergence of the transceiver can be adjusted by the height of the silicon lens.[22] Hence, transceivers emitting a collimated THz beam can be designed for future applications.

In conclusion, we have realized a monolithically integrated, fiber-coupled THz transceiver with up to 4.5 THz bandwidth and more than 70 dB peak dynamic range. We employed a single Be-doped InGaAs/InAlAs photoconductor with individual emitter and detector mesas separated by 45 µm. The optical coupling with two individual PM-fibers was realized with the help of a polymer waveguide chip. Due to this compact design the fiber-coupled THz transceiver can be integrated in a 25 mm housing. We showed that the radiation pattern of the device is comparable to individual THz emitters. Therefore, it is directly compatible with commercially available THz time-domain spectrometers and bears great potential for THz applications in non-destructive testing and material inspection.

Funding German Ministry of Education and Research under grant 13N13388.

REFERENCES

1. P. U. Jepsen, D. G. Cooke , M. Koch, Laser Photonics Rev. **5** (1), 124 (2011).

2. T. Hochrein, J. Infrared. Milli. Terahz Waves **36**, 235 (2015).
3. M. Suzuki, M. Tonouchi, Appl. Phys. Lett. **86**, 163504 (2005).
4. B. Sartorius, H. Roehle, H. Künzel, J. Böttcher, M. Schlak, D. Stanze, H. Venghaus, M. Schell, Optics Exp. **16** (13), 9565 (2008).
5. H. Roehle, R. J. B. Dietz, H. J. Hensel, J. Böttcher, H. Künzel, D. Stanze, M. Schell, B. Sartorius, Optics Exp. **18** (3), 2296 (2010).
6. S. Preu, M. Mittendorff, H. Lu, H. B. Weber, S. Winnerl, and A. C. Gossard, Appl. Phys. Lett. **101**, 101105 (2012).
7. R. J. B. Dietz, B. Globisch, M. Gerhard, A. Velauthapillai, D. Stanze, H. Roehle, M. Koch, T. Göbel, M. Schell, Appl. Phys. Lett. **103**, 061103 (2013).
8. N. Vieweg, F. Rettich, A. Deninger, H. Roehle, R. J. B. Dietz, T. Göbel, J. Infrared. Milli. Terahz Waves **35**, 823 (2014).
9. M. Tani, Zhiping Jian, X.-C. Zhang, Electron. Lett., **36** (9), 804 (2000).
10. C. Jördens, N. Krumbholz, T. Hasek, N. Vieweg, B. Scherger, L. Bähr, M. Mikulics, M. Koch, Electron. Lett., **44**, (25) (2008).
11. S. Busch, T. Probst, M. Schwerdtfeger, R. Dietz, J. Palaci, M. Koch, Optics Exp. **22**, (14), 16841 (2014).
12. M. Tani, M. Watanabe, and K. Sakai, Electron. Lett. **38** (1), 5 (2002).
13. H. S. Bark, Y. B. Ji, S. J. Oh, S. K. Noh, T. I. Jeon, Proc. 40th International Conference on Infrared, Millimeter, and Terahertz Waves (IRMMW-THz), 2015.
14. R. J. B. Dietz, B. Globisch, H. Roehle, D. Stanze, T. Göbel, M. Schell, Optics Exp. **22** (16), 19411 (2014).
15. J. Lloyed-Hughes, E. Castro-Camus, M. B . Johnston, Solid State Comm. **136**, 595 (2005).
16. E. Castro-Camus, M. B. Johnston, J. Lloyd-Hughes, Semic. Sci. Technol. **27**, 115011 (2012).
17. P. U. Jepsen, R. H. Jacobsen, S. R. Keiding, J. Opt. Soc. Am. B **13** (11), 2424 (1996).
18. L. Duvillaret, F. Garet, J. F. Roux, J. L. Coutaz, IEEE J. Sel. Topics Quantum Electron. **7** (4), 615 (2001).
19. B. Globisch, R.J.B. Dietz, D. Stanze, T. Göbel, and M. Schell, Appl. Phys. Lett. **104**, 172103 (2014).
20. M. Kleinert, Z. Zhang, D. de Felipe, C. Zawadzki, A. M. Novo, W. Brinker, M. Möhrle, N. Keil, In: *SPIE OPTO*, pp. 93650R-93650R, International Society for Optics and Photonics (2015).
21. B. Globisch, R. J. B. Dietz, T. Göbel, M. Schell, W. Bohmeyer, R. Müller, A. Steiger, Opt. Lett. **40**, 3544 (2015).
22. J. Van Rudd, D. M. Mittleman, J. Opt. Soc. Am. B **19** (2), 319 (2002).

Publication VIII

B. Globisch, R. J. B. Dietz, R. B. Kohlhaas, T. Göbel, M. Schell, M. Semtsiv, D. Alcer and W. T. Masselink, “Iron doped InGaAs: Competitive THz emitters and detectors fabricated from the same photoconductor”, J. Appl. Phys., vol. 121, 053102, 2017

.

Iron doped InGaAs: Competitive THz emitters and detectors fabricated from the same photoconductor

B. Globisch,[1,a)] R. J. B. Dietz,[1] R. Kohlhaas,[1] T. Göbel,[1] M. Schell,[1] D. Alcer,[2] M. Semtsiv,[2] W. T. Masselink[2]
[1]*Fraunhofer Institute for Telecommunications, Heinrich Hertz Institute, Einsteinufer 37, 10587 Berlin, Germany*
[2]*Department of Physics, Humboldt University Berlin, Newtonstrasse 15, 12489 Berlin, Germany*

Per today, the optimum material systems for photoconductive emitters and receivers are different. In THz reflection measurements, this leads to complicated optics or performance compromises. We present photoconductive emitters and detectors fabricated from molecular beam epitaxy (MBE) grown iron (Fe) doped InGaAs, which are well suited for THz time-domain spectroscopy (THz-TDS) both as emitters and detectors. As a photoconductive emitter, 75 µW ± 5 µW of radiated THz power were measured. As a detector, THz pulses with a bandwidth of up to 6 THz and a peak dynamic range of 95 dB could be detected. These results are comparable to state-of-the-art THz photoconductors, which allows for simple reflection measurements without performance decrease. The incorporation of Fe in InGaAs during MBE growth is investigated by Secondary Ion Mass Spectroscopy (SIMS), Hall, and transient differential transmission measurements. Growth temperatures close to 400 °C allow for homogeneous Fe doping concentrations up to 5×10^{20} cm^{-3} and result in a photoconductor with an electron lifetime of 0.3 ps, a resistivity of 2 kΩ cm, and an electron mobility higher than 900 cm^2 V^{-1} s^{-1}. We show that iron dopants are incorporated up to a maximum concentration of 1×10^{17} cm^{-3} on substitutional lattice sites. The remaining dopants are electrically inactive and form defects that are anneal-stable up to a temperature of 600 °C. The fast recombination center in Fe-doped InGaAs is an unidentified defect representing ≈ 0.5 % of the nominal iron concentration. The electron and hole capture cross section of this defect are determined as $\sigma_e = 3.8 \times 10^{-14}$ cm^2 and $\sigma_h = 5.5 \times 10^{-15}$ cm^2, respectively.

I. INTRODUCTION

Photoconductive THz antennas excited by 1550 nm femtosecond lasers have become a standard component in commercial THz time-domain-spectroscopy (THz-TDS) systems within the last years.[1] On the one hand, this was enabled by the development of compact femtosecond fiber-lasers with integrated pre-compensation of dispersion. On the other hand, the photoconductive material was improved by several orders of magnitude in output power and signal-to-noise ratio within the last 10 years.[2–6] These improvements were enabled by using different materials for THz emitters and detectors. Whereas the emitter requires high resistivity in combination with high electron mobility for efficient acceleration of the photogenerated carriers[4], the crucial parameter for the detector is an electron lifetime below 1 ps for the accurate sampling of the THz pulse.[5,7–9] Several photoconductive materials have been investigated as THz emitters and detectors sensitive to 1550 nm excitation.[10] These include iron-doped or iron implanted InGaAs,[11–14] low-temperature grown (LTG) InGaAs,[15,16] Beryllium-doped LTG-InGaAs/InAlAs superlattices,[2,3,17,18] ErAs:InGaAs superlattices,[19] and LTG-GaAsSb[20]. However, a single photoconductive material that is sensitive to 1550 nm excitation and that combines a sub-picosecond lifetime with high carrier mobility and high resistivity has not been found.

The combination of these properties in one photoconductive material can be especially interesting for integrated THz devices: A single chip containing THz emitter and detector would allow for a compact THz reflection head applicable in material inspection and in-line process monitoring. Therefore, the quest for new THz photoconductive materials, suitable for the excitation with 1550 nm radiation, remains an important field of study.

A promising candidate, which may combine all the desired properties, is iron (Fe) doped InGaAs grown lattice matched to InP. Iron is incorporated as a deep acceptor in the middle of the bandgap of InGaAs and acts as a recombination center.[21,22] THz emitters and detectors made of InGaAs:Fe grown by metal organic vapor phase epitaxy (MOVPE) at temperatures around 650 °C showed a bandwidth of up to 2.5 THz and a signal-to-noise ratio of 50 dB.[13,14] These results demonstrate the potential of the material although the bandwidth and the signal-to-noise ratio have to be increased to about 5 THz and 90 dB for competitive

THz devices.[1,5]

In this publication, we show that Fe-doped InGaAs grown by gas-source molecular beam epitaxy (MBE) at temperatures close to 400 °C features sub-picosecond electron lifetime, high resistivity and high mobility for Fe concentrations exceeding 10^{20} cm^{-3}. Compared to MOVPE growth, the MBE permits essentially lower growth temperatures, which leads to modified incorporation properties of iron in InGaAs and, therefore, allows for significantly higher doping concentrations. THz emitter and receiver antennas fabricated from this material are competitive to the respective state-of-the-art photoconductors.

The paper is organized as follows: In Sec. II we summarize the properties of Fe-doped InGaAs determined by previous publications. Temperature-dependent Hall measurements of as-grown and annealed samples are discussed in Sec. III and the electron and hole dynamics after transient optical excitation are investigated in Sec. IV. The results of InGaAs:Fe as photoconductive THz emitter and detector are presented in Sec. V.

II. PROPERTIES OF INGAAS:FE.

Transition metal doping of semiconductors has been studied extensively in the last decades.[23–25] The unique properties of transition metals stem from their partially filled d-orbitals, which determine their electrical and optical properties. Generally, impurities can be incorporated as a point defect on two stable lattice sites in the host crystal: The substitutional and the interstitial position. In sphalerite crystals substitutional 3d impurities are incorporated exclusively on the cation lattice site[24], which corresponds to the In or Ga position in InGaAs. As the cation site in III-V semiconductors is trivalent a neutral substitutional iron impurity is symbolized as Fe^{3+} since three electrons are needed to repair the dangling bonds of the host crystal. Consequently, when substitutional iron has trapped an electron it is labeled Fe^{2+}. Oxidation states other than Fe^{2+} and Fe^{3+} have not been reported for Fe-doped InGaAs.[21] In general, impurities are called electrically active when they occupy substitutional lattice sites.[24]

For the interstitial lattice site two positions are possible: The tetrahedral interstitial and the hexagonal interstitial. In III-V semiconductors only the tetrahedral interstitial has been observed whereas iron interstitials in InGaAs have not been found.[24] In contrast, iron is almost exclusively incorporated on interstitial lattice sites in Silicon.[26]

For the energetic position of the Fe^{3+} acceptor level in the bandgap of InGaAs values of 0.15 eV[27], 0.3 eV[28] up to 0.38 eV[29] above the valence band maximum have been published. This large variation is mainly caused by different growth conditions and a relatively low doping concentration of the samples. The three most recent publications consistently determined the Fe^{3+} acceptor at 0.39 eV – 0.40 eV above the valence band maximum in InGaAs grown by liquid phase epitaxy (LPE)[21,22] and MOVPE[30]. With this value the authors could successfully describe the band offset of the interface between InGaAs/InP in the framework of the internal reference rule.[22,31]

Regarding the electron lifetime and the electrical properties of InGaAs:Fe previous investigations have not drawn a consistent picture. One of the reasons is that these parameters have not been studied on the same samples, yet. In addition, the results published for LPE-, MOVPE- and MBE-grown samples differ significantly. Nevertheless, some important conclusions can be drawn from previous publications: Fe-doped InGaAs grown by MOVPE at temperatures of 650 °C – 680 °C changes its conductivity from n-type to p-type for doping concentrations higher than 1×10^{17} cm^{-3}.[13,14,30] Here, the substitutional iron dopants compensate the residual electron concentration of InGaAs up to an Fe concentration of 1×10^{17} cm^{-3}. For higher doping, the substitutional Fe-acceptor leads to p-type conductivity.[13,30]

Electron lifetimes of 8.1 ps and 0.3 ps were measured in Fe-doped InGaAs/InP quantum-wells grown via MBE at 450 °C for Fe-concentrations of 2.5×10^{18} cm^{-3} and 2.0×10^{19} cm^{-3}, respectively.[32,33] These results show that sub-picosecond lifetimes can be obtained in Fe-doped InGaAs. However, the electrical properties of these samples were not published and, therefore, the conductivity type, the mobility and the resistivity of the samples are unknown.

A resistivity above 10^7 Ω cm, an electron mobility of 2395 cm^{2}V^{-1}s^{-1}, and an electron lifetime of 0.3 ps was demonstrated for Fe-doped $Ga_{0.69}In_{0.31}As$ with a bandgap of 1.0 eV grown by a hybrid vertical Bridgman and gradient freezing directional solidification process.[34,35] Although this material cannot be efficiently excited with 1550 nm femtosecond fiber lasers these results underscore that iron doping of InGaAs may result in high resistivity, high mobility, and sub-picosecond electron lifetime in a single photoconductor.

The electron capture cross section σ_e of Fe-doped InGaAs grown by LPE was determined via deep-level transient spectroscopy (DLTS).[21,22] From Shockley-Read-Hall theory of carrier capture the cross section σ_e determines the electron lifetime τ_e via[36]:

$$\tau_e = (v_{th}\ \sigma_e\ N_T)^{-1}. \qquad (1)$$

Here, v_{th} is the thermal velocity and N_T is the concentration of trapping centers. Guillot and co-workers[21] published $\sigma_e = (3 \pm 2) \times 10^{-16}$ cm^2 whereas Srocka and co-workers[22] measured $\sigma_e = (8 \pm 5) \times 10^{-18}$ cm^2. The relatively large difference

between these two values is not directly clear from the results presented. Nevertheless, with the help of Eq. (1) we conclude that sub-picosecond lifetimes in InGaAs:Fe can be obtained for doping levels in the range of (10^{19}-10^{20}) cm^{-3} and an electron capture cross section higher than 10^{-16} cm^2.

In this publication we show that the incorporation of iron in InGaAs depends strongly on the growth temperature. In contrast to the MOVPE results presented above we do not observe p-type conductivity for samples grown by MBE at temperatures around 400 °C. In contrast, we obtain homogenous doping profiles up to a concentration of 5×10^{20} cm^{-3} with n-type conductivity and 0.3 ps electron lifetime. We attribute this to different incorporation properties of iron in InGaAs grown at 400 °C compared to temperatures of 650 °C – 680 °C.

III. SAMPLE GROWTH AND ELECTRICAL CHARACTERIZATION

We investigated a series of five two-inch wafers grown by gas-source molecular-beam epitaxy (GSMBE) on a RIBER compact 21 system. The structures consist each of two layers grown on top of a semi-insulating InP:Fe substrate: A nominally undoped InAlAs buffer with a thickness of 0.7 - 1.0 µm followed by a Fe-doped InGaAs layer with nominal doping concentration in the range of 1×10^{18} cm^{-3} - 5×10^{20} cm^{-3} and a thickness between 1.0 µm and 1.2 µm. The compositions of all layers were such that they were lattice matched to the InP substrate, as verified by x-ray diffraction. The growth temperature was set between 350 °C and 450 °C. Table I summarizes the properties of all samples.

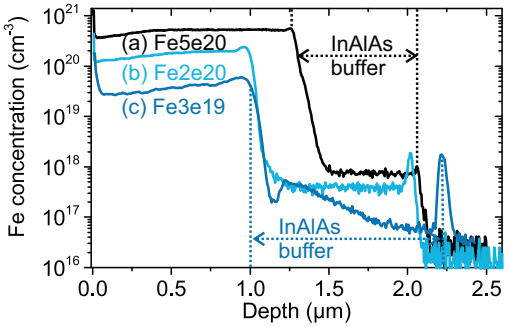

FIG. 1. SIMS profiles of Fe in three Fe-doped InGaAs layers with a thickness of 1.2 µm (a) and 1.0 µm (b), (c). The underlying InAlAs buffer layer is nominally undoped. The vertical dashed lines indicate the beginning and the end of the buffer layer for samples Fe5e20 and Fe3e19. Iron concentrations of 5×10^{20} cm^{-3} (a), 1.5×10^{20} cm^{-3} (b), 3.0×10^{19} cm^{-3} (c) were obtained.

The surface morphology was checked by differential interference contrast microscopy. We observed slightly rough surfaces for all samples with no significant increase for higher Fe doping concentrations.

The nominal Fe-doping concentration was verified by SIMS measurements. Fig. 1 shows the Fe concentration profiles of samples (a) Fe5e20, (b) Fe2e20 and (c) Fe3e19. Measurements were conducted by Evans Analytical Group, Santa Clara, CA, USA, who claim an uncertainty of 10 % on their results. Almost flat doping profiles with Fe-concentrations of 5×10^{20} cm^{-3} (a), 1.5×10^{20} cm^{-3} (b) and 0.3×10^{20} cm^{-3} (c) were obtained within the first 1.2 µm (a) and 1.0 µm (b), (c) of the InGaAs layer. The transition between the nominally undoped InAlAs buffer and the Fe doped InGaAs is marked by a sharp drop of the Fe concentration to values below 10^{18} cm^{-3}. We attribute the unintended doping of the buffer layer to diffusion of iron dopants from the InGaAs layer into the buffer during the growth process. The Fe-concentration of the InP substrate could not be determined due to the resolution limit of the SIMS measurement. One observes an accumulation of Fe-dopants between buffer and substrate, which is most probably caused by Fe-clustering on interface states. Due to the location deep inside the buffer these clusters will not influence the properties of the Fe-doped InGaAs layer.

A. Room temperature Hall Results

The results of Hall measurements at room temperature are shown in Fig. 2. Ohmic contacts were obtained by soldering In droplets on top of square samples. In Fig. 2 (a) the resistivity (black triangles) and the carrier mobility (blue circles) are shown as functions of the Fe doping concentration. The resistivity increases by more than three orders of magnitude from undoped InGaAs to Fe doping concentrations of 5.0×10^{20} cm^{-3}. The maximum resistivity of 2038 Ω cm is obtained for Fe5e20. The mobility decreases for higher Fe doping from 3655 $cm^2 V^{-1} s^{-1}$ of undoped InGaAs to 984 $cm^2 V^{-1} s^{-1}$ and 912 $cm^2 V^{-1} s^{-1}$ for samples Fe2e20 and Fe5e20, respectively. Considering the high doping concentrations of these samples a mobility of nearly 1000 $cm^2 V^{-1} s^{-1}$ is still very high. Note that the mobility of sample Fe3e19 is rather low compared to all other samples. We assume that a slightly higher impurity concentration in this sample, maybe from incomplete oxide desorption or unintended contamination of the substrate, decreased the mobility. However, this effect is not attributed to Fe doping concentration.

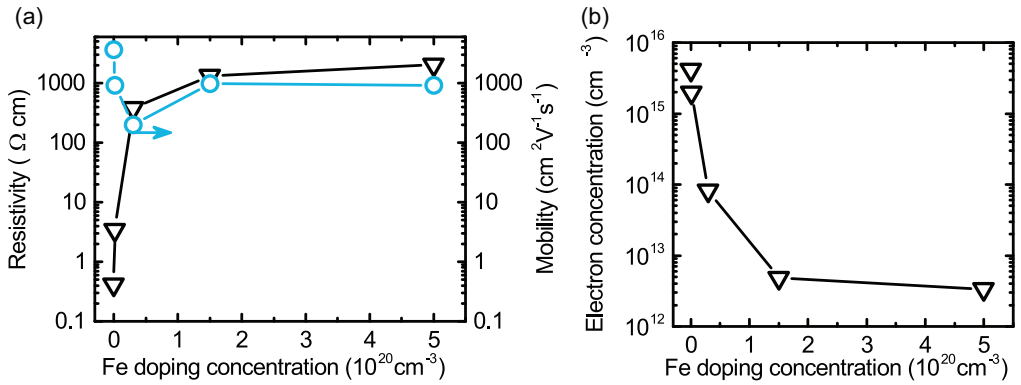

FIG. 2. Resistivity, electron mobility (a) and electron concentration (b), versus Fe doping concentration of MBE grown InGaAs. Solid lines are guides for the eye. The correspondence between the Fe doping concentration and the sample names can be deduced from Table I. Note that the conductivity remains n-type for all doping levels. This is in contrast to Hall data of MOVPE grown, Fe-doped InGaAs that shows p-type material for doping levels higher than 10^{18} cm^{-3}.

The resistivity increases by more than three orders of magnitude from undoped InGaAs to Fe doping concentrations of 5.0 ×10 20 cm-3. The maximum resistivity of 2038 Ω cm is obtained for Fe5e20. The mobility decreases for higher Fe doping from 3655 cm2 V-1 s-1 of undoped InGaAs to 984 cm2 V-1 s-1 and 912 cm2V-1s-1 for samples Fe2e20 and Fe5e20, respectively. Considering the high doping concentrations of these samples a mobility of nearly 1000 $cm^2V^{-1}s^{-1}$ is still very high. Note that the mobility of sample Fe3e19 is rather low compared to all other samples. We assume that a slightly higher impurity concentration in this sample, maybe from incomplete oxide desorption or unintended contamination of the substrate, decreased the mobility. However, this effect is not attributed to Fe doping.

In Fig. 2 (b) the residual carrier concentration is plotted as a function of the Fe doping concentration. The undoped sample shows n-type conductivity with an electron concentration of 4×10^{15} cm^{-3}. Residual carrier concentrations of a few 10^{15} cm^{-3} are commonly observed in nominally undoped InGaAs due to shallow impurities. For higher Fe doping the residual carrier concentration decreases more than three orders of magnitude to 3×10^{12} cm^{-3} for sample Fe5e20, which is close to the intrinsic carrier concentration of InGaAs at room temperature (6.7×10^{11} cm^{-3}). This stands in contrast to all results reported on Fe-doped InGaAs grown by MOCVD. In that case, the material changed from n-type to p-type conductivity for doping concentrations above 10^{17} cm^{-3}.[13,14] Tell and coworkers modeled the electron and hole concentration in Fe-doped InGaAs and showed that the transition to p-type conductivity is expected for doping densities above 1×10^{17} cm^{-3}.[30] The authors assumed that iron was the

Table I. Sample series, results of room temperature Hall measurements, and carrier lifetimes derived from Fig. 5. The unsaturated carrier lifetime of the undoped sample, Fe1e18, and Fe1e19 could not be determined (see Sec. III B 1). The legend of the symbols is: T_G – growth temperature, c_{Fe} – Fe doping concentration, n_{Hall} – residual electron concentration, ρ – Hall resistivity, μ – Hall mobility, τ_e – unsaturated electron lifetime.

Sample name	T_G (°C)	c_{Fe} (cm^{-3})	n_{Hall} (cm^{-3})	ρ (Ω cm)	μ ($cm^2V^{-1}s^{-1}$)	τ_e (ps)
Fe5e20	350	5.0×10^{20}	3.4×10^{12}	2038.0	912	0.3
Fe2e20	400	1.5×10^{20}	4.8×10^{12}	1328.0	984	0.9
Fe3e19	400	3.0×10^{19}	8.2×10^{13}	379.0	201	-
Fe1e18	450	1.0×10^{18}	2.0×10^{15}	3.0	928	-
undoped	350	n.i.d.	4.0×10^{15}	0.4	3655	-

dominant acceptor in the material with an ionization energy of 0.35 eV. Hence, the n-type conductivity in our MBE grown samples with Fe concentrations above 10^{20} cm^{-3} indicates that the majority of dopants is not incorporated on substitutional lattice sites. We assume that the growth temperature around 400 °C leads to the incorporation on interstitial lattice sites, where the dopants are electrically inactive. Therefore, the relatively high electron mobility at doping concentrations above 10^{20} cm^{-3} (see Fig. 2 (a)) can be explained by the low concentration of electrically active and, therefore, ionized Fe impurities. In contrast, the higher temperatures during MOVPE growth (650 °C – 680 °C) favor the incorporation on substitutional lattice sites. The difference in growth temperature leads to different kinetics on the surface of the substrate, which has direct influence on the incorporation of dopants into the lattice

B. Temperature dependent Hall results

In this subsection we analyze the temperature dependent resistivity, electron concentration, and electron mobility of sample Fe3e19, doped with a nominal Fe concentration of 3×10^{19} cm^{-3}. In order to investigate the thermal stability of the Fe dopants in the material, we performed post-growth annealing studies. Two pieces of sample Fe3e19 were annealed at 550 °C and 600 °C for 60 min. in a MOVPE growth chamber under arsenic and phosphorous atmospheres. This stabilization is necessary in order to prevent the outgassing of As from the InGaAs and InAlAs layers and P from the substrate. The Hall measurements were performed between room temperature and 400 °C. In Fig. 3, the residual carrier concentration (a) and the resistivity (b) of the as-grown (black triangles) and the 600 °C-annealed sample (blue circles) are plotted as functions of the inverse temperature. Both quantities show almost identical values within the entire temperature range, which indicates that annealing up to 600 °C has no influence on the electrical properties of the material. The insensitivity towards annealing indicates that the Fe dopants occupy thermally stable positions in the lattice. In particular, annealing up to 600 °C cannot activate additional Fe dopants, which would increase the residual carrier concentration and lead to p-conductivity. Annealing at higher temperatures was impeded since the required As overpressure could not be provided by the MOVPE system. The logarithmic plot in Fig. 3 (a) shows a linear dependence of the residual carrier concentration on the inverse temperature. This is indicative of a thermally activated defect level.[30,37] The dashed lines in Fig. 3 (a) are linear fits to the data.

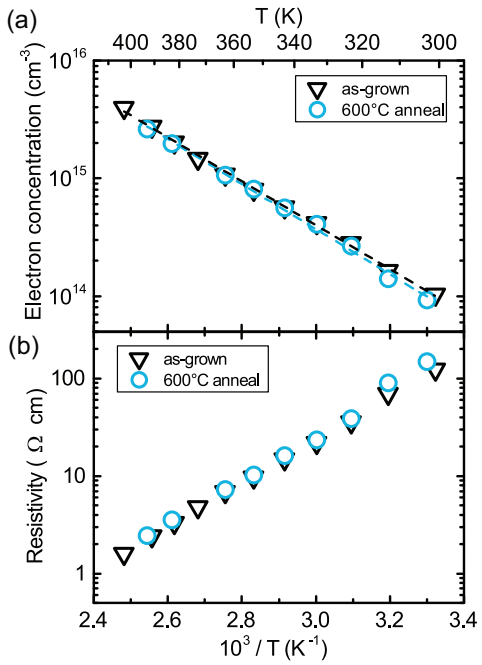

FIG. 3. Residual electron concentration (a) and Hall resistance (b) versus inverse temperature of the as-grown (black triangles) and the 600 °C-annealed (blue dots) sample Fe3e19. Dashed lines in (a) are linear fits to the data. An activation energy of 0.33 eV is calculated from the data, which compares well to the activation energy of substitutional Fe dopants in InGaAs ($E_A = 0.35 \pm 0.02$ eV)[21,22].

We calculated the activation energy of the defect $E_A = 0.33$ eV by assuming no compensation, so that $n \propto \exp(-E_A/(2k_BT))$. This result compares well to the ionization energy of substitutional Fe dopants in InGaAs determined from previous studies ($E_A = 0.35$ eV $\pm$ 0.02 eV).[21,22,30]

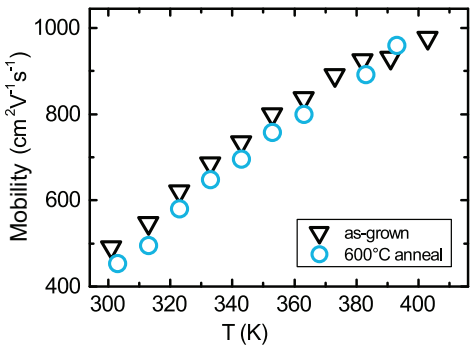

FIG. 4. Hall mobility versus temperature for the as-grown (black triangles) and 600 °C-annealed (blue dots) sample Fe3e19. The increasing mobility for higher temperatures indicates ionized impurity scattering as the dominant scattering mechanism in Fe-doped InGaAs. In contrast to the room temperature Hall measurements presented in Fig. 2, the temperature dependent measurements were performed on different samples in different setups and different laboratories. The slightly different mobility values are most likely caused by the soldered In contacts.

The resistivity of the as-grown and annealed sample is shown in Fig. 3 (b). One observes an exponential increase as a function of the inverse temperature, which is again indicative of a thermally activated defect level. Finally, the electron mobility is plotted as a function of the temperature in Fig. 4. The mobility increases for higher temperatures, which indicates that ionized impurity scattering is the dominant scattering mechanism in the material. Since ionized substitutional Fe-dopants carry positive charge (Fe^{3+}) the ionized impurity scattering increases when substitutional Fe dopants are thermally ionized ($Fe^{2+} \rightarrow Fe^{3+}$). In conclusion, the results of temperature dependent Hall measurements indicate that substitutional iron is the electrically active dopant in MBE-grown InGaAs:Fe with an activation energy of 0.33 eV.

IV. CARRIER DYNAMICS AFTER OPTICAL EXCITATION

The carrier lifetime after optical excitation by femtosecond laser pulses is one of the most important parameters for THz photoconductive devices. Especially the detector requires an electron lifetime below 1 ps for an almost instantaneous sampling of the incoming THz pulse.[5,7] We analyzed the depopulation of the conduction band after transient optical excitation by wavelength degenerate differential transmission (DT) measurements. This measurement technique has become a standard for the investigation of ultrashort carrier lifetimes in photoconductors.[38–40] An intense femtosecond pump pulse excites electrons from the valence band into the conduction band of the material while the transmission of a time-delayed probe pulse is measured. Due to Pauli-blocking, the transmission of the probe pulse increases directly after the excitation by the pump. Trapping of electrons and holes in defects of the fast photoconductor reduces the transmission of the probe pulse to its level before the excitation. In our setup a femtosecond fiber laser with two fiber-coupled output ports provided 90 fs-pulses with a repetition rate of 100 MHz and a 1550 nm central wavelength. A fiber-coupled attenuator was used to set the optical power of the pump and the probe beam, respectively. For all measurements the optical power of the pump pulse was at least one order of magnitude higher than the probe pulse. In order to avoid interference on the sample surface we assured orthogonal polarization of pump and probe beam by polarization filters. The diameter of the laser spot on the sample surface was 15 µm. We measured the transmission change of the probe beam via lock-in detection. Before we discuss the results of our DT experiments, the carrier dynamics are modeled via rate equations in the next subsection.

A. Modeling of DT experiments

We use rate equations in order to model the electron dynamics after transient optical excitation, analogously to previous studies.[38,41]

$$\frac{dn}{dt} = G - \frac{n}{\tau_e}\left(1 - \frac{n_T}{N_T^0}\right), \tag{2}$$

$$\frac{dn_T}{dt} = \frac{n}{\tau_e}\left(1 - \frac{n_T}{N_T^0}\right) - \frac{n_T}{\tau_r}. \tag{3}$$

Here, the dynamic variables n and n_T describe the density of electrons in the conduction band and the occupation of the recombination centers, respectively. Due to the charge neutrality condition we omitted a dynamic equation for the holes. The generation of electrons by the optical excitation is described by the parameter G. The electron trapping time and the recombination time of trapped electrons with holes from the valence band are symbolized as τ_e and τ_r, respectively. The total density of trapping centers in the material is N_T^0, and the term $1 - (n_T/N_T^0)$ accounts for the fraction of unoccupied traps.

The unknown parameters in Eqs. (2) – (3) are τ_e, τ_r, and N_T^0. Together with the Shockley-Read-Hall relation Eq. (1), these parameters allow for the calculation of the capture cross section of electrons σ_e and holes σ_h. In contrast to a numerical solution of Eqs. (2) – (3), which requires the fitting of all three parameters to a large number of DT signals, τ_e, τ_r and N_T^0 can be determined independently from the experimental data by studying three limit cases: The unsaturated regime, the partial trap filling, and the saturated regime.[38] First, we introduce dimensionless quantities in order to facilitate the subsequent analysis. Time is measured in units of the electron trapping time $t' \equiv t/\tau_e$ and carrier densities are normalized to the density of trapping centers $N \equiv n/N_T^0$ and $N_T \equiv n_T/N_T^0$. Hence, Eqs. (2) - (3) read:

$$\frac{dN}{dt'} = -N\left(1 - N_T\right), \tag{4}$$

$$\frac{dN_T}{dt'} = N\left(1 - N_T\right) - \gamma N_T, \tag{5}$$

$$N(t'=0) = N_{ex}; \quad N_T(t'=0) = 0. \tag{6}$$

Here, $\gamma = \tau_e/\tau_r$ is the ratio of electron capture and electron recombination time. Moreover, we defined the time of the optical excitation by the pump pulse at $t = 0$ and included the density of excited electrons N_{ex} in the initial conditions shown in Eq. (6). Here, the time dependence of the optical excitation is neglected, which

is a minor inaccuracy since the pulse duration in our experiments was 90 fs only. Note that N_{ex} is normalized to N_T^0 and, thus, a dimensionless quantity. For the analysis of the three limit cases we exploit that γ is a small quantity, i.e. the recombination time is much longer than the trapping time. It will be shown during the analysis of the experimental data that this assumption is valid.

1. The unsaturated regime

For unsaturated electron capture, the density of carriers excited by the pump pulse N_{ex} is much smaller than the density of available traps N_T^0, i.e. $N_{ex} \ll 1$. In this case the occupation of trapping centers is low at all times ($N_T \ll 1$) and Eq. (4) can be written as:

$$\frac{dN}{dt'} = -N \,. \tag{7}$$

The solution of this equation is an exponential function of the form:

$$n(t) = n(t=0)\exp(-t/\tau_e) \,. \tag{8}$$

For clarity, we transformed back to variables with dimensions. From Eq. (8) we deduce that the population of the conduction band decays mono-exponentially with the electron trapping time τ_e. Hence, τ_e can be determined by a mono-exponential fit to the DT signal in the unsaturated regime.

2. Partial trap filling

For partial trap filling the density of excited carriers is smaller but on the same order of magnitude as the density of available trapping centers, i.e. $N_{ex} < 1$. Hence, Eqs. (4) – (5) can be written in the form:

$$\frac{dN}{dt'} = -N\left(1 - N_T\right) \tag{9}$$

$$\frac{dN_T}{dt'} = N\left(1 - N_T\right). \tag{10}$$

Here, we assumed that γ is a small quantity, i.e. the recombination process is slow compared to carrier trapping. Eq. (9) – (10) can be solved analytically and one obtains:

$$N(t') = \frac{\left(N_{ex} - 1\right)}{1 - 1/N_{ex}\exp\left\{-\left(N_{ex} - 1\right)t'\right\}}. \tag{11}$$

In the next step the condition of partial trap filling is applied, i.e. $-1 < N_{ex} - 1 < 0$, such that Eq. (11) can be simplified to:

$$N(t') \approx N_{ex}\left(1 - N_{ex}\right)\exp\left\{-\left(1 - N_{ex}\right)t'\right\}. \tag{12}$$

By neglecting the term quadratic in N_{ex} and transforming back to unscaled quantities one obtains:

$$n(t) \approx n_{ex}\exp\left\{-\left(1 - n_{ex}/N_T^0\right)\left(t/\tau_e\right)\right\} \tag{13}$$

From Eq. (13) a modified carrier lifetime due to partial trap filling is defined as:

$$\tau_{pt} \equiv \tau_e\left(1 - \frac{n_{ex}}{N_T^0}\right)^{-1} \,. \tag{14}$$

When the unsaturated time constant τ_e as well as the density of excited carriers n_{ex} are given, N_T^0 can be obtained by a mono-exponential fit to the DT signal when the condition of partial trap filling holds.

3. The saturated regime

In the saturated regime the density of excited carriers is much higher than the density of trapping centers ($N_{ex} \gg 1$). The available traps fill up relatively fast after the optical excitation. Since we assumed that carrier trapping is much faster than carrier recombination the remaining $N_{ex} - 1$ electrons in the conduction band can only be trapped if a trapped electron recombines with a hole in the valence band. Hence, the electron dynamic in the conduction band is completely determined by the carrier recombination. In Eq. (5) we write $1 - N_T \approx 0$ as long as the saturation condition $N_{ex} \gg 1$ holds and obtain:

$$\frac{dN_T}{dt'} = -\gamma\, N_T \,. \tag{15}$$

In analogy to Eq. (7) and Eq. (8), the solution of Eq. (15) can be written as an exponential function with decay time τ_r by inserting unscaled quantities. Hence, the recombination of trapped electrons is mono-exponential in this regime. Since the trapping dynamics is completely determined by the recombination process a mono-exponential fit to the DT signal delivers the carrier recombination time. A mathematically more rigorous derivation of Eq. (15) can be found in one of our previous publications.[38]

B. Experimental results

In this subsection the three regimes are studied experimentally and τ_e, τ_r and N_T^0 of iron-doped InGaAs are derived from the data.

1. The unsaturated regime

In order to induce the unsaturated regime, in which the carrier density excited by the pump pulse is supposed to be much lower than the density of trapping centers, we applied the lowest optical pump power that

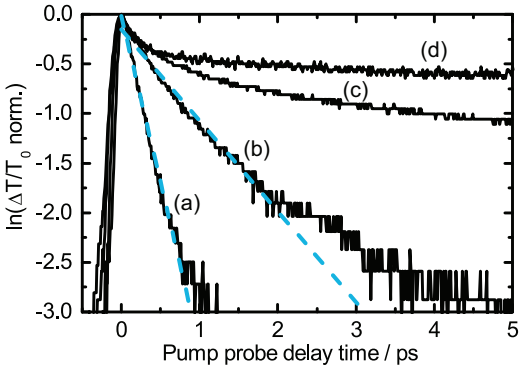

FIG. 5. Natural logarithm of the normalized differential transmission signal of samples Fe5e20 (a), Fe2e20 (b), Fe3e19 (c) and Fe1e18 (d). The excitation power of the pump beam was 0.2 mW for all samples which corresponds to 5×10^{16} cm^{-3} of excited carriers. The signal decay time decreases for higher Fe-doping. Dashed lines are linear fits to the signals.

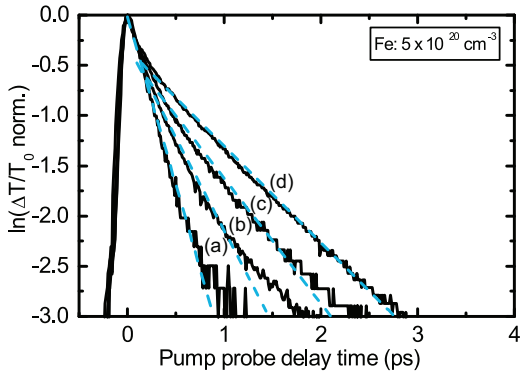

FIG. 6. Natural logarithm of the normalized differential transmission of sample Fe5e20 for an increasing carrier density excited by the pump pulse: (a) 5×10^{16} cm^{-3}, (b) 5×10^{17} cm^{-3}, (c) 1×10^{18} cm^{-3}, (d) 2×10^{18} cm^{-3}. The increase of the exponential decay time for higher excitation densities is attributed to partial trap filling.

induced a measurable DT signal in our setup. This was 0.2 mW corresponding to 5×10^{16} cm^{-3} of excited electrons in the conduction band. In Fig. 5 the natural logarithm of the normalized differential transmission signal is plotted for the samples Fe5e20 (a), Fe2e20 (b), Fe3e19 (c) and Fe1e18 (d). The dashed lines in Fig. 5 are linear fits to the data. First, one observes that the decay time of the signal is faster for higher Fe doping concentrations. Hence, electron trapping can be directly related to defects inducedby Fe doping. However, one also notices that the signal decay is mono-exponential only for samples Fe5e20 and Fe2e20. The deviation of line (b) from the mono-exponential decay for delay times higher than 1.5 ps is attributed to the relatively high noise caused by the low optical excitation density. From the linear fits in Fig. 5 an electron trapping time of 0.9 ps and 0.3 ps was calculated for Fe2e20 and Fe5e20, respectively.

The signals of the samples Fe3e19 (c) and Fe1e18 (d) consist of two components: An initially fast decay within the first 0.5 ps followed by a second, slowly decaying component. This signal shape is indicative of saturation of trapping centers, which occurs when the density of excited carriers exceeds the concentration of available traps. This result is rather unexpected since the doping concentrations of 3×10^{19} cm^{-3} (c) and 1×10^{18} cm^{-3} (d) are more than an order of magnitude higher than the density of excited carriers of 5×10^{16} cm^{-3}. If all Fe dopants served as active electron traps saturation should not occur for the samples Fe3e19 and Fe1e18. Thus, the DT signals in Fig. 5 suggest that only a small fraction of all Fe dopants contributes to the trapping process. In order to quantify the density of active trapping centers we investigate the regime of partial trap filling in the next subsection

.

2. *Partial trap filling*

For partial trap filling in a DT experiment the density of carriers excited by the pump pulse has to be of the same magnitude as the density of trapping centers. We study this regime on sample Fe5e20 since the unsaturated decay shown in Fig. 5 (a) should gradually disappear due to partial trap filling when the optical pump power is increased. Fig. 6 shows the natural logarithm of the normalized differential transmission signal of sample Fe5e20 for excitation densities of 5×10^{16} cm^{-3} (a), 5×10^{17} cm^{-3} (b), 1×10^{18} cm^{-3} (c) and 2×10^{18} cm^{-3} (d). The signal decay maintains mono-exponential for all excitation densities, whereas the signal decay time increases gradually. The dashed lines in Fig. 6 are linear fits to the data and the corresponding decay times τ_{pt} measure 0.30 ps (a), 0.54 ps (b), 0.80 ps (c) and 1.04 ps (d). In agreement with the results of the unsaturated DT measurements in the last subsection we assume that 0.3 ps is the unsaturated decay time τ_e. By using Eq. (14), the density of trapping centers can be calculated as $N_T^0 = (1.9 \pm 0.7) \times 10^{18}$ cm^{-3}. The uncertainty is obtained by averaging the values of N_T^0 derived from lines (b) - (d) in Fig. 6. Note, that the calculated density of active trapping centers N_T^0 corresponds to a fraction of 0.38 % ± 0.14 % of all Fe dopants in sample Fe5e20. The nature of this trapping defect could not be identified so far. Experiments like electron paramagnetic resonance (ESR) spectroscopy would be helpful to specify the defect, which were not within the scope of this paper. For all subsequent investigations, it is assumed that 0.5 % of the nominal Fe-doping concentration serves as an active trapping center in Fe-doped InGaAs.

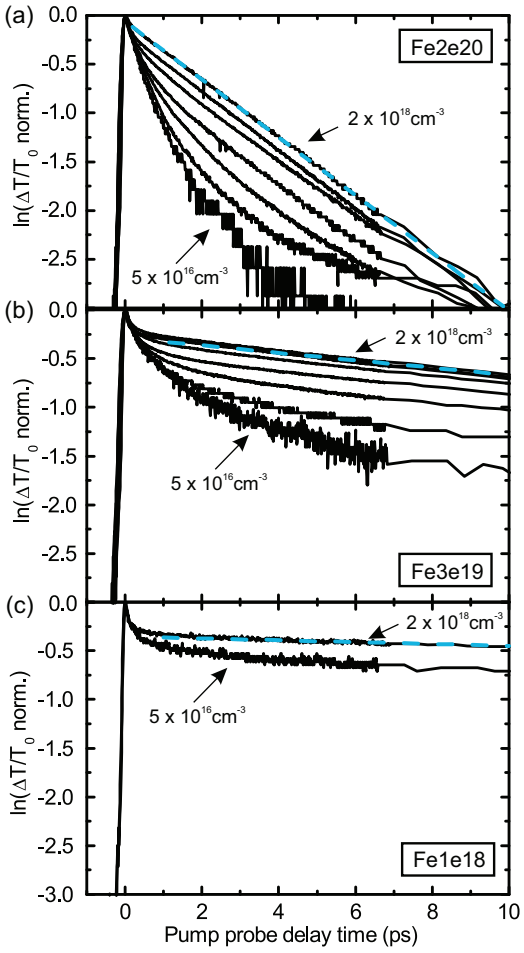

FIG. 7. Natural logarithm of the normalized differential transmission signal of samples Fe2e20 (a), Fe3e19 (b) and Fe1e18 (c). The fastest and slowest decaying signal in each panel correspond to an excited carrier density of 5×10^{16} cm^{-3} and 2×10^{18} cm^{-3}. For the signals in-between the optical pump power was gradually increased. For clarity, only two signals are shown in (c). The dashed, light-blue lines correspond to a linear fit to the saturated DT signal of each sample.

3. *The saturated regime*

In the saturated regime the density of carriers excited by the pump pulse exceeds the concentration of trapping centers by more than an order of magnitude. As a consequence the DT signal features two components: An initially fast decaying component due to trap filling followed by a slowly decaying component arising from the recombination of trapped electrons with holes from the valence band. Fig. 7 shows the natural logarithm of the normalized DT signals of samples Fe2e20, Fe3e19 and Fe1e18 for increasing optical pump power. The fastest and slowest decaying signal of each plot correspond to an excited carrier density of 5×10^{16} cm^{-3} and 2×10^{18} cm^{-3}, respectively. One observes that the signal decay time increases when the Fe doping concentration decreases. In addition, Fig. 7 (a) shows the transition from the unsaturated decay for the lowest excitation density to the saturated regime for the highest excitation. In Fig. 7 (b) and (c) the saturated regime can be clearly identified by the initially fast decay followed by a slowly decaying component for pump probe delay times above 1.5 ps. In agreement with the results of our rate equation model in Sec. II A 3.,the signal corresponding to the highest excitation density shows the strongest saturation and decays exponentially for delay times longer than 1.5 ps. The dashed, light-blue lines are linear fits to this part of the signals. In Fig. 8 the slope of this linear fit is plotted as a function of the Fe doping concentration. In agreement with Eq. (15) this parameter is interpreted as the hole trapping rate. One observes a linear increase for higher Fe doping in Fig. 8, which indicates that the recombination process involves electrons trapped by Fe-related defects and holes from the valence band.

We studied pump-power dependent DT measurements in the unsaturated regime, for partial trap filling and in the saturated regime and determined the electron trapping time τ_e, the density of active trapping centers N_T^0 and the recombination time of trapped electrons τ_r in Fe-doped InGaAs. Together with Eq. (1) the capture cross section of electrons $\sigma_e = 3.8\times 10^{-14}$ cm^2 and holes $\sigma_h = 5.5\times 10^{-15}$ cm^2 was calculated from these results. Here, we used the thermal velocity of electrons and holes $v_{th}^e = 5.5\times 10^7$ cm/s and $v_{th}^h = 2.0\times 10^7$ cm/s, respectively. In contrast to previously published results we considered only 0.5 % of all Fe dopants as active recombination centers. Therefore, the calculated capture cross sections are significantly higher than those obtained in former studies. Although the nature of these trapping centers could not be determined from the data, we unambiguously showed that their density is proportional to the concentration of Fe dopants in the material.

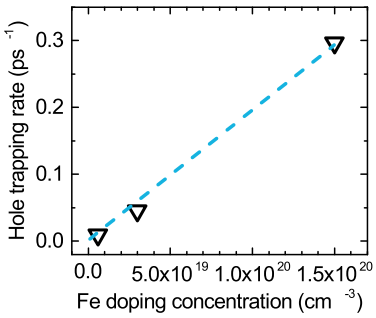

FIG. 8. The slope of the linear fits to the saturated DT signals in Fig. 7 is plotted as a function of the Fe doping concentration. This parameter corresponds to the hole trapping rate (cf. Eq. (15)) and increases for higher Fe doping. The dashed line is a linear fit to the data.

In summary, the results of the last three sections show that photoconductive materials with sub-picosecond electron lifetime combined with high mobility and high resistivity were obtained in Fe-doped InGaAs grown at temperatures close to 400 °C in a MBE system. The relatively low growth temperature compared to MOVPE and LPE allows for doping concentrations above 10^{20} cm^{-3} with preserved n-type conductivity. The sub-picosecond lifetime can be explained by electron and hole recombination via Fe-related defects. In the next section we demonstrate the potential of this photoconductive material for emitters and detectors in THz-TDS.

V. THZ RESULTS

We selected wafers Fe5e20 and Fe2e20 for the fabrication of THz antennas due to their promising electrical and optical properties. Photoconductive emitters (detectors) were structured as strip-line (dipole) antennas with 25 µm × 25 µm (10 µm × 10 µm) mesas.[3] The total length of the dipole antenna of the THz detector measured 50 µm. All THz measurements were done in ambient air. Two 90 °-off-axis parabolic mirrors with a focal length of 3 inch and a diameter of 2 inch guided the THz radiation from the emitter to the detector. The total length of the THz path measured 25 cm. A fiber-laser providing femtosecond pulses with a duration of 100 fs and 100 MHz repetition rate was used for the optical excitation. The optical delay line as well as the data acquisition was part of a commercially available THz spectroscopy system.[1] The operation mode of this system was identical for all following THz experiments: We averaged 1000 pulse traces with a length of 70 ps each. A single trace was recorded in 60 ms. No lock-in amplification was used for data acquisition.

A. THz detector

For the characterization of InGaAs:Fe as a detector in THz-TDS, we used the same fiber coupled THz emitter for all measurements, which was illuminated with 20 mW of optical power and biased with 120 V. Under these conditions the THz output power measures approx. 75 µW.[6] Fig. 9 (a) shows the detected THz peak-to-peak amplitude as a function of the optical illumination power at the detector. For sample Fe2e20 one observes a steep rise of the amplitude to approx. 800 nA when the optical power increases from 0 mW to 5 mW. For higher levels of optical illumination a constant plateau is seen before the amplitude decreases gradually for an illumination power above 10 mW. In contrast, the THz amplitude detected by Fe5e20 shows no decrease for higher optical powers. After a steep rise from 0 mW to 5 mW the amplitude increases gradually for higher optical illumination. However, the absolute value of the detected amplitude differs significantly between both detectors: Fe2e20 detects THz pulses with 50 % higher amplitudes than Fe5e20. This behavior can be directly understood by analyzing the THz spectra obtained via Fast Fourier Transformation (FFT) of the corresponding pulse trace. Fig. 9 (b) shows two THz spectra detected by Fe5e20 for an optical power of 5 mW and 32 mW, respectively. The equivalent spectra detected with Fe2e20 are shown in Fig. 9 (d). A bandwidth higher than 5.5 THz is obtained in all cases, which is comparable to optimized THz detectors made from Be-doped LTG-InGaAs/InAlAs heterostructures.[5] The comparison of Fig. 9 (b) and (d) reveals several important differences: First, the frequency at which the spectrum shows its largest amplitude is lower for Fe2e20 than for Fe5e20. This indicates a higher percentage of low-frequency components in the spectrum of Fe2e20. Second, the roll-off in the spectrum of Fe2e20 changes strongly compared to Fe5e20 when the optical power is increased from 5 mW to 32 mW. Additionally, the noise level, highlighted by a horizontal line in each spectrum, becomes higher for the Fe2e20 detector illuminated with 32 mW than for the Fe5e20. All these features can be explained by the results obtained from electron lifetime measurements in Sec. IV. The saturation of carrier trapping was more pronounced for sample Fe2e20 than for Fe5e20 when the optical excitation power was increased. This was directly connected to the lower density of trapping states in Fe2e20 due to the reduced Fe doping concentration. These long living carriers increase the average conductivity of sample Fe2e20 after the optical excitation, which translates into a higher noise level (see Fig. 9 (d)).[5] Additionally, the relatively long carrier lifetime broadens the THz pulse, resulting in the suppression of high frequency components in the THz spectrum. On the other hand, the lower density of trapping centers in Fe2e20 decreases the probability for elastic electron scattering on ionized defect sites. This increases the detected-peak-to-peak amplitude of Fe2e20 compared to the higher doped sample Fe5e20 in Fig. 9 (a). In Fig. 9 (c) the maximum dynamic range is plotted as a function of the optical illumination power. This parameter is defined as the distance between the maximum frequency in the THz spectrum and the noise level. Hence, the dynamic range is a combined parameter, which accounts for changes of the detected THz amplitude and changes of the noise level. First, one observes that the maximum dynamic range is higher than 90 dB for an optical power exceeding 2 mW, which is competitive to values obtained for LTG-InGaAs/InAlAs detectors.[1,5] Fe2e20 shows up to 6 dB higher dynamic range than Fe5e20 between 2 mW and 10 mW. For an optical excitation above 10 mW the

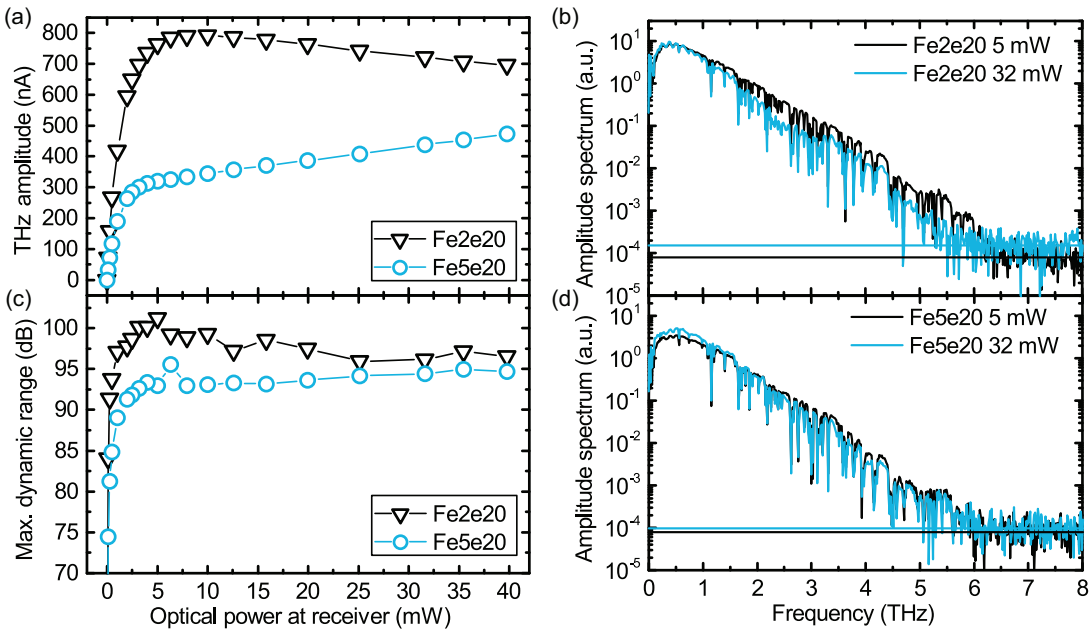

Fig. 9. Peak-to-peak THz amplitude (a) and maximum dynamic range (c) as a function of optical excitation power for THz detectors fabricated from Fe5e20 and Fe2e20. THz spectra for 5 mW and 32 mW of optical excitation power are shown in (b) and (d) for Fe5e20 and Fe2e20. The horizontal lines in (b) and (d) indicate the noise level of the spectrum, which is calculated by averaging all frequency components higher than 7 THz in each spectrum. All measurements were done in ambient air. Hence, the dips in the spectra stem from water vapor absorption

dynamic range of Fe2e20 decreases due to an increasing noise level combined with a decay in the THz amplitude. A detailed analysis of the influence of carrier lifetime and trap saturation on the performance of THz detectors can be found in previous publications.[5,8,9]

In summary, the results of this section underscore the suitability of Fe-doped InGaAs as broadband THz detectors. The doping range between 1.5×10^{20} cm^{-3} and 5×10^{20} cm^{-3} offers flexibility for adjusting the properties of the detector to the desired optical illumination power.

B. THz emitter

The most remarkable property of the samples Fe2e20 and Fe5e20 is the combination of high resistivity and mobility with an electron lifetime below 1 ps. Whereas the ultrashort carrier lifetime is a crucial parameter for THz detectors, the high resistivity allows for high bias fields on the emitter site. In fiber-coupled THz-TDS systems the maximum optical power is commonly limited due to optical nonlinearities in the fiber that increase quadratically with the optical power. Therefore, increasing the THz output of photoconductive emitters without increasing the optical power is a principal aim in the development of THz emitters. Here, the bias voltage can be a suitable parameter if the resistivity of the material, or more precisely, the breakdown field, is sufficiently high. Since the Hall resistivity of samples Fe2e20 and Fe5e20 is higher than 1500 Ω cm and the mobility measures almost 1000 cm^2 V^{-1} s^{-1}, high breakdown fields can be expected. Fig. 10 shows the peak-to-peak THz amplitude detected with a fiber-coupled LTG-InGaAs/InAlAs detector as a function of the bias field

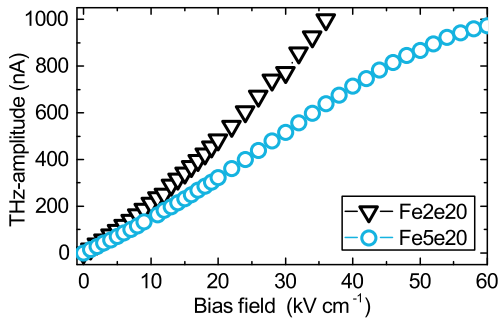

FIG. 10. THz peak-to-peak amplitude versus bias field for photoconductive emitters fabricated from Fe2e20 (black triangles) and Fe5e20 (blue circles). A fiber-coupled module with an LTG-InGaAs/InAlAs photoconductor served as the detector. The optical excitation power for emitter and detector was 20 mW. Due to a high resistivity combined with high mobility, bias fields of up to 36 kV/cm respectively 60 kV/cm can be applied. high as 36 kV/cm and 60 kV/cm were applied to Fe2e20 and Fe5e20, respectively. This is significantly higher than all values reported previously for 1550 nm photoconductors.

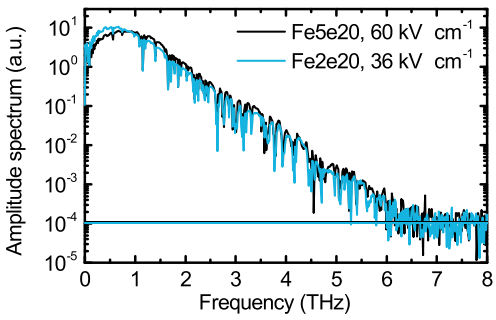

FIG. 11. THz spectra obtained with a bias field of 60 kV/cm (Fe5e20) and 36 kV/cm (Fe2e20) at the THz emitter. The horizontal lines indicate the noise level of each spectrum, which was calculated by averaging the spectral amplitudes between 7 THz – 10 THz.

at the emitter. The optical illumination power of the emitter and the detector was 20 mW throughout all measurements. Bias fields as high as 36 kV/cm and 60 kV/cm were applied to Fe2e20 and Fe5e20, respectively. This is significantly higher than all values reported previously for 1550 nm photoconductors. Bias fields higher than 60 kV/cm could not be applied to sample Fe5e20 due to limitations of our voltage supply. The breakdown field of sample Fe2e20 was approx. at 40 kV/cm such that 36 kV/cm corresponds to the maximal bias field.

Fig. 11 shows the THz spectra corresponding to bias fields of 36 kV/cm (Fe2e20) and 60 kV/cm (Fe5e20). In both cases the bandwidth is as high as 6 THz and the maximum dynamic range measures almost 100 dB in power. Although the spectral roll-off is nearly identical the frequency of the maximum in the spectrum of Fe2e20 is shifted towards lower frequencies compared to Fe5e20. In general, the spectrum of the Fe5e20-emitter contains a higher amount of high frequency components compared to

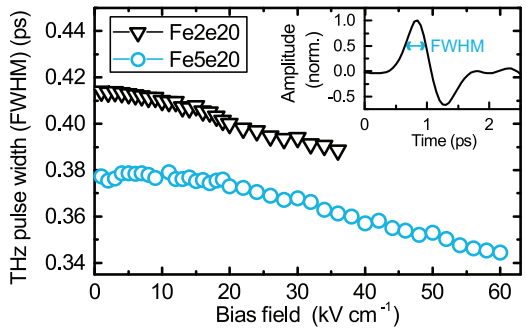

FIG. 12. Full width at half maximum (FWHM) of THz pulses as a function of bias field at the emitter. The inset illustrates the data extraction from a representative THz pulse. Due to the combination of sub-picosecond electron lifetime and high electron mobility the pulses emitted by Fe5e20 (blue circles) are 30 fs shorter than those of Fe2e20 (black triangles).

Fe2e20. Again, we attribute this to the ultra-short electron lifetime of Fe5e20. On the emitter side, long-living carriers screen the externally applied bias field and, therefore, decrease the acceleration of carriers, which broadens the THz pulse. Fig. 12 shows the full width at half maximum (FWHM) of the THz pulses emitted by Fe2e20 (black triangles) and Fe5e20 (blue circles) as a function of the bias field. The THz-pulses emitted by Fe5e20 are approx. 30 fs shorter than those generated by Fe2e20. For increasing bias fields the pulse-width decreases to about 340 fs for the Fe5e20-emitter. These short pulses explain the high bandwidth of the signals displayed in Fig. 11.

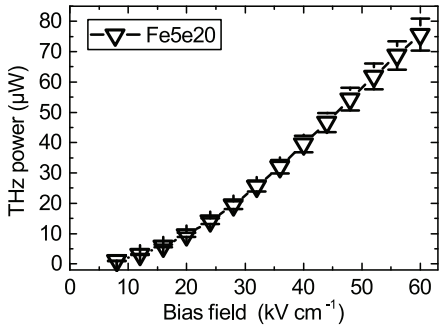

FIG. 13. Absolute THz power measured with a calibrated pyroelectric detector by Sensor- und Lasertechnik GmbH as a function of the bias field at the emitter. The optical excitation power was 20 mW for all measurements. The maximum value of 75 µW ± 5 µW is competitive to recently published values of photoconductive emitters based on InGaAs/InAlAs heterostructures.

In order to give quantitative results on the output power, we used a THz detector calibrated by the German National Metrology Institute.[42,43] Due to its unique properties this detector can be traced back to a national standard detector, which allows us to measure absolute power values with calibrated uncertainties for the entire frequency range of the emitter.[6] Results are shown in Fig. 13. The maximum output power obtained at a bias field of 60 kV/cm measures 75.6 µW ± 5.2 µW. Recently published values of photoconductive emitters based on an InGaAs/InAlAs heterostructures state 70 µW - 80 µW for the same optical illumination power of 20 mW. Hence, Fe-doped InGaAs is a competitive alternative to existing THz emitters.

VI. CONCLUSION

We studied Fe doped InGaAs grown by MBE at temperatures around 400 °C as photoconductive material for THz-TDS. Homogenous doping profiles with concentrations up to 5×10^{20} cm^{-3} were obtained. Room temperature Hall measurements show that even the highest doped samples are n-conductive. This is in

contrast to all results published for Fe-doped InGaAs grown by MOVPE and LPE. We assume that the low temperature during MBE growth prevents the incorporation of more than 1×10^{17} cm^{-3} of Fe on substitutional lattice sites. The activation energy of the electrically active, substitutional dopants was determined by temperature dependent Hall measurement to be $E_A = 0.33$ eV, which agrees well with the activation energy of substitutional iron in InGaAs. The remaining dopants are electrically inactive – probably as tetrahedral interstitials. Post-growth annealing at 550 °C and 600 °C had no impact on the electrical properties of the material, which indicates that both the substitutional and the electrically inactive dopants occupy thermally stable lattice sites. From pump-power dependent differential transmission experiments with 1550 nm femtosecond pulses the capture cross section of electrons and holes as well as the density of active trapping sites in the material were determined. For this analysis, we expanded a rate equation model in three limit cases which allowed us to determine the desired parameters independently. We found that approx. 0.5 % of all Fe dopants serve as recombination centers with an electron and hole capture cross section of $\sigma_e = 3.8 \times 10^{-14}$ cm^2 and $\sigma_h = 5.5 \times 10^{-15}$ cm^2, respectively. This suggest a hitherto unknown recombination defect in iron doped InGaAs, which is electrically inactive.

The samples with Fe doping concentrations of 1.5×10^{20} cm^{-3} and 5.0×10^{20} cm^{-3} comprise a resistivity higher than 1000 Ω cm, a residual carrier concentration around 4×10^{12} cm^{-3}, an electron mobility above 900 cm^2 V^{-1} s^{-1} and an electron lifetimes below 1 ps. To the best of our knowledge, this is the first time that sub-picosecond carrier lifetime and the aforementioned electrical properties were obtained in a single photoconductive material suitable for the illumination with 1550 nm-femtosecond lasers.

Due to these unique properties, Fe-doped InGaAs shows compatible performance to state-of-the art photoconductive emitters *and* detectors. The combination of high resistivity and high mobility allows for bias fields of 60 kV/cm at InGaAs:Fe emitters resulting in a calibrated THz power of 75 µW ± 5 µW. Used as a THz-detector, peak signal-to-noise ratios of 95 dB and a THz bandwidth exceeding 5.5 THz were obtained. Whereas state-of the art photoconductive antennas rely on different photoconductive materials for THz emission and detection, Fe-doped InGaAs combines the desired properties of THz emitters and detectors in a single material. Therefore, it is a convenient photoconductor for the development of integrated THz devices and compact reflection heads.

ACKNOWLEDGMENTS

This work was funded by the German Research Foundation (DFG) under grant GO 2533/2-1.

[1] N. Vieweg, F. Rettich, A. Deninger, H. Roehle, R. Dietz, T. Göbel, and M. Schell, J. Infrared Millim. Terahz Waves **35**, 823 (2014).
[2] B. Sartorius, H. Roehle, H. Künzel, J. Böttcher, M. Schlak, D. Stanze, H. Venghaus, and M. Schell, Opt. Express **16**, 9565 (2008).
[3] H. Roehle, R.J.B. Dietz, H.J. Hensel, J. Böttcher, H. Künzel, D. Stanze, M. Schell, and B. Sartorius, Opt. Express **18**, 2296 (2010).
[4] R.J.B. Dietz, B. Globisch, M. Gerhard, A. Velauthapillai, D. Stanze, H. Roehle, M. Koch, T. Göbel, and M. Schell, Appl. Phys. Lett. **103**, 61103 (2013).
[5] R.J.B. Dietz, B. Globisch, H. Roehle, D. Stanze, T. Göbel, and M. Schell, Opt. Express **22**, 19411 (2014).
[6] B. Globisch, R.J.B. Dietz, T. Göbel, M. Schell, W. Bohmeyer, R. Müller, and A. Steiger, Opt. Lett. **40**, 3544 (2015).
[7] L. Duvillaret, F. Garet, J.-F. Roux, and J.-L. Coutaz, IEEE J. Sel. Top. Quantum Electron. **7**, 615 (2001).
[8] S. Rihani, R. Faulks, H. Beere, H. Page, I. Gregory, M. Evans, D.A. Ritchie, and M. Pepper, Appl. Phys. Lett. **95**, 51106 (2009).
[9] E. Castro-Camus, M.B. Johnston, and J. Lloyd-Hughes, Semicond. Sci. Technol. **27**, 115011 (2012).
[10] A. Krotkus, J. Phys. D. Appl. Phys. **43**, 273001 (2010).
[11] M. Suzuki and M. Tonouchi, Appl. Phys. Lett. **86**, 163504 (2005).
[12] O. Hatem, J.R. Freeman, J.E. Cunningham, P.J. Cannard, M.J. Robertson, E.H. Linfield, A.G. Davies, and D.G. Moodie, J. Infrared Millim. Terahz Waves **37**, 415 (2016).
[13] C.D. Wood, O. Hatem, J.E. Cunningham, E.H. Linfield, A.G. Davies, P.J. Cannard, M.J. Robertson, and D.G. Moodie, Appl. Phys. Lett. **96**, 194104 (2010).
[14] O. Hatem, J. Cunningham, E.H. Linfield, C.D. Wood, A.G. Davies, P.J. Cannard, M.J. Robertson, and D.G. Moodie, Appl. Phys. Lett. **98**, 121107 (2011).
[15] A. Takazato, M. Kamakura, T. Matsui, J. Kitagawa, and Y. Kadoya, Appl. Phys. Lett. **90**, 101119 (2007).
[16] A. Takazato, M. Kamakura, T. Matsui, J. Kitagawa, and Y. Kadoya, Appl. Phys. Lett. **91**, 11102 (2007).
[17] H. Kuenzel, J. Boettcher, K. Biermann, H. Hensel, H. Roehle, and B. Sartorius, in *Indium Phosphide Relat. Mater. 2008. IPRM 2008. 20th Int. Conf.* (2008).
[18] I. Kostakis, D. Saeedkia, and M. Missous, IEEE Trans. Terahertz Sci. Technol. **2**, 617 (2012).
[19] A. Schwagmann, Z.Y. Zhao, F. Ospald, H. Lu, D.C. Driscoll, M.P. Hanson, A.C. Gossard, and J.H. Smet, Appl. Phys. Lett. **96**, 141108 (2010).
[20] J. Sigmund, C. Sydlo, H.L. Hartnagel, N. Benker, H. Fuess, F. Rutz, T. Kleine-Ostmann, and M. Koch, Appl. Phys. Lett. **87**, 252103 (2005).
[21] G. Guillot, G. Bremond, T. Benyattou, F. Ducroquet, B. Wirth, M. Colombet, A. Louati, and A. Bencherifa, Semicond. Sci. Technol. **5**, 391 (1990).
[22] B. Srocka, H. Scheffler, and D. Bimberg, Phys. Rev. B **49**, 10259 (1994).
[23] H.H. Woodbury and G.W. Ludwig, Phys. Rev. **117**, 102 (1960).
[24] A. Zunger, Solid State Phys. **39**, 276 (1986).
[25] F.X. Zach, J. Appl. Phys. **75**, 7894 (1994).
[26] A.A. Istratov, H. Hieslmair, and E.R. Weber, Appl. Phys. A Mater. Sci. Process. **69**, 13 (1999).
[27] K.-H. Goetz, D. Bimberg, K.-A. Brauchle, H. Jürgensen, J. Selders, M. Razeghi, and E. Kuphal, Appl. Phys. Lett. **46**, 277 (1985).
[28] Z. Chen, T. Wolf, W. Korb, and D. Bimberg, J. Appl. Phys. **64**, 4574 (1988).
[29] M. Sugawara, M. Kondo, T. Takanohashi, and K. Nakajima", Appl.Phys.Lett. **51**, 834 (1987).
[30] B. Tell, U. Koren, and B.I. Miller, J. Appl. Phys. **61**, 1172 (1987).

[31] J.M. Langer, C. Delerue, M. Lannoo, and H. Heinrich, Phys. Rev. B **38**, 7723 (1988).
[32] M. Guézo, S. Loualiche, J. Even, A. Le Corre, H. Folliot, C. Labbé, O. Dehaese, and G. Dousselin, Appl. Phys. Lett. **82**, 1670 (2003).
[33] M. Gicquel-Guézo, S. Loualiche, J. Even, C. Labbé, O. Dehaese, A. Le Corre, H. Folliot, and Y. Pellan, Appl. Phys. Lett. **85**, 5926 (2004).
[34] S. Sengupta, I. Wilke, and P.S. Dutta, Appl. Phys. Lett. **95**, 211102 (2009).
[35] S. Sengupta, I. Wilke, and P.S. Dutta, J. Appl. Phys. **107**, 33104 (2010).
[36] W. Shockley and W.T. Read, Phys. Rev. **87**, 835 (1952).
[37] J. Bourgoin and M. Lannoo, *Point Defects in Semiconductors II: Experimental Aspects*, Springer (Springer, Berlin, 1983).
[38] B. Globisch, R.J.B. Dietz, D. Stanze, T. Göbel, and M. Schell, Appl. Phys. Lett. **104**, 172103 (2014).
[39] A.J. Lochtefeld, M.R. Melloch, J.C.P. Chang, and E.S. Harmon, Appl. Phys. Lett. **69**, 1465 (1996).
[40] A. Othonos, J. Appl. Phys. **83**, 1789 (1998).
[41] S.D. Benjamin, H.S. Loka, A. Othonos, and P.W.E. Smith, Appl. Phys. Lett. **68**, 2544 (1996).
[42] A. Steiger, M. Kehrt, C. Monte, and R. Müller, Opt. Express **21**, 14466 (2013).
[43] R. Müller, B. Gutschwager, J. Hollandt, M. Kehrt, C. Monte, R. Müller, and A. Steiger, J. Infrared, Millimeter, Terahertz Waves **36**, 654 (2015).